



**On the Precise Generation of Textured and Profiled Resin
Bond Diamond Grinding Wheels via Laser Ablation:
Understanding the Laser Ablation Law on Composites**

by

KEGE XIE
MEng (Hons)

A thesis submitted to the University of Nottingham in partial fulfilment of
the requirements for the Degree of
Doctor of Philosophy

Under the supervision of

A/Prof Adam Rushworth

A/Prof Hao Chen

Prof Dragos Axinte

MARCH 2022

Abstract

High-quality structures featuring functional planes (e.g., machine tool guide trail with unique textures) and non-flat surfaces (e.g., aircraft engine tenon tooth with low tolerance) are essential parts of high value-added industrial equipment components. They usually need grinding as the finishing process to meet the severe requirements like high precision for assembling, high efficiency for industrial production, high profile accuracy keeping ability and lower cost for large batch orders. Typically, textured and profiled grinding wheels are expected to be the two most capable tools to be selected for these demanding structures in many cases. Therefore, the need to find appropriate methods to develop these high-performance structured grinding tools has been highly emphasised.

Among these existing machining or dressing strategies (e.g., mechanical, chemical, thermal or energy beam), laser ablation has been keeping considered the most promising way for the fabrication process of these special tools thanks to the advantages like high efficiency, no tool wear, environmentally friendly. Nevertheless, the precise fabrication of these structured (textured and profiled) grinding wheels has kept an open question as it would be pretty challenging to remove the ultra-high hardness of abrasives embedded in porous bond agents in a controllable way. Therefore, solving the widely concerned particular fabrication-induced issues has a significant sense.

To this end, a systematic research scheme including theoretical analysis,

model simulation and experimental study is formulated in this research based on the previous studies. Firstly, an analytical model regarding the temperature field distribution and ablation depth involved in the ablation process is calculated, and the fundamental law is experimentally validated. Secondly, a controllable electromechanical laser ablation system with a stable CO₂ laser beam generator and a precise positioning platform is established, and the functional performance is evaluated by generating irregular patterns (e.g., sine slots and variable depth zigzag groove). Then, the strategies to remove target materials on the grinding wheel in a controllable and optimum way are investigated based on the model and the laser ablation system. Afterwards, the flat grinding wheels with regular patterns (e.g., tilt slots, parallelogram, triangle, hexagon and rectangle) are generated after the experimental work regarding the ablation law of laser feed rate and laser power on ablation depth and width is carried out. Finally, the topographies of the ablated slots changing with laser power, duty cycle, feed rate and track overlap rate are studied. The possibilities to generate precise profiled grinding wheels (including stepped wheels and curved surface wheels) respectively by a single pass, multiple-pass, and a combination of feed rate, overlap rate, and focal length are addressed. The research in the thesis is anticipated to solve the urgent precise fabrication-related issues in machining high-performance abrasive tools, which has significant value in both academic research and industrial application.

Research Achievements

Research Publications

Hao Nan Li, **Ke Ge Xie**, Bo Wu, Wei Qiang Zhu. Generation of textured diamond abrasive tools by continuous-wave CO₂ laser: Laser parameter effects and optimization. Journal of Material Processing Technology. 2020, 275: 116279. (**SCI, JCR 1, ESI High Cited Paper, Co-first Author**)

Adam Rushworth, **Ke Ge Xie**, Benli Fang, Yi Xiu Shen, Zhi Pei Huang, Xiang Yu Zhang. Generating Profile Diamond Grinding Wheels by 2,000 W Fibre Laser: On the Understanding of Laser Ablation Law with High Power and Establishment of Predictive Model. Journal of Advanced Manufacturing Technology. 2022, 120: 3045-3063. (**SCI, JCR 2, Co-first author**)

Ke Ge Xie, Adam Rushworth, Hao Chen, Xiang Yu Zhang, Zhi Pei Huang, Yi Xiu Shen. Generating Precise Non-Flat Grinding Wheel Surfaces via CO₂ Laser Ablation: Understanding the Relationship between Overlap Rate and Feed Rate on Composite Materials. Journal of Manufacturing Processes. (**SCI, JCR 2, Co-first author**)

Patent Applications

Ke Ge Xie, Adam Rushworth, etc. A curved surface grinding device and method (一种曲面磨削加工装置及方法). 202110641731.4 (**Innovation patent, Temporary approved**)

Adam Rushworth, **Ke Ge Xie**, etc. An Electromagnetic heating device and control method (一种电磁加热装置及控制方法). 202110642893.X (**Innovation patent, Temporary approved**)

Adam Rushworth, **Ke Ge Xie**, etc. A 3D printing device and its control method (一种 3D 打印设备及其控制方法). 202010838514.X (**Innovation patent, Temporary approved**)

Adam Rushworth, **Ke Ge Xie**, etc. A 3D printing device (一种 3D 打印设备). 202021744183.5 (**Utility model patent, Final approved**)

Adam Rushworth, **Ke Ge Xie**, etc. A droplet generation device (一种熔滴生成装置). 202021744184.X (**Utility model patent, Final approved**)

Major Research Projects Involved

Structured profile grinding wheel manufacturing system (**Team leader**, under supervision of Dr Adam Rushworth)

--- Innovation Lab project (I01201200027), RMB 25,000

A Novel Low-Cost 3D Printer for Stainless Steel and Aluminium Alloy (**Membership**, led by Dr Adam Rushworth)

--- Li Dak Sum Innovation Fellowship (E06211200008), RMB 500,000.

Acknowledgement

Firstly, the author would like to thank the supervision team formed by Dr Adam Rushworth, Dr Hao Chen, and Prof. Dragos Axinte. They provided the author with much help when preparing the thesis, from the research contents, via approaches, to writing skills.

Dr Rushworth is the author's principal supervisor, whose modest character benefits the author the most. Unlike the style of most Chinese teachers, Dr Rushworth is more like a friend whom we can directly call each other's name. Furthermore, he shows great respect, understanding, and patience to his students, and he never forces them to do things they do not like. In his consciousness, everyone is equal, and he is never stingy to express his thanks to those who have helped him. In such an atmosphere, the author can fully devote himself to his studies and feel fully developed over the past few years.

Meanwhile, the author sincerely thanks Dr Chen and Prof Axinte. They helped the author with the idea generation of the thesis, provided the author with experimental convenience for the author's project research, and helped fix the thesis structures to make the paper more readable. Thank them for the continuous efforts they dedicated to helping!

The author would also like to thank the support from the technician team members at the University of Nottingham, Ningbo, China, like Mr John Zhu, Mr Benli Fang, Mr Bo Wu, Mr Jason Wang, and Mr Dawei Chen. They provided the author with solid support to access the experimental facilities and spared no trouble to help the author with the sample preparation and manufacturing

of the critical mechanical components.

The author also thanks the PhD candidates from the Advanced and Intelligent Manufacturing Research Group (AIMRG). Mr Jinyi Li and Ms Yoland Yang helped the author with the mathematical modelling and the generation of the Matlab codes in the author's simulation works. Ms Xiao Han helped formulate the testing and validation plan and the operation of the experimental equipment. Besides, the author thanks Mr Mengshen Yang from Ningbo Institute of Materials Technology and Engineering, Chinese Academy of Sciences (CAS), who helped with the material's physical performance test. The author sincerely thanks them for the great time they spent with the author.

The author also wants to thank the undergraduate students, Mr Zhipei Huang, Mr Xiangyu Zhang, Mr Yixiu Shen, Mr Wensong Hu and Mr Hanxuan Wang, who volunteered involved in this research project, helped the author with the experiment preparation and part of the data processing.

The author also sincerely thanks A/Pro Nicholas Hamm and A/Pro Lily Cai, who provided exceptional care and attention for the author's life and PhD studies and rescued the author from the darkest hours.

Thanks to the reviewers taking time out of their busy schedules to provide valuable help to improve the quality of the thesis.

Finally, a special and unique thanks to the author's family, that supported the author with love and care although in the distance, and to all of the author's special friends in Nottingham. Thanks to the school and author's country provided with the chance. Thanks to all of them!

Contents

Abstract	i
Research Achievements	iii
Acknowledgement	v
Contents	vii
List of Figures	xv
List of Tables.....	xxxv
List of Abbreviations	xxxvi
List of Nomenclature	xxxviii
Chapter 1 Introduction.....	1
1.1 Research Background.....	1
1.2 Problem Definition.....	5
1.3 Objectives of this Study.....	7
1.4 Outline of this Thesis	9
Chapter 2 Literature Review.....	13
2.1 Introduction to Abrasive Tools.....	13
2.1.1 Conventional Abrasive Tools.....	15
2.1.2 Superhard Abrasive Tools	17
2.1.3 Structured Abrasive Tools	20
2.2 Introduction to Dressing Strategies on Abrasive Tools	31
2.2.1 Dressing by Mechanical Methods.....	32
2.2.2 Dressing by Electrochemical Methods.....	34

2.2.3 Dressing by Energy Beam Methods.....	36
2.3 Introduction to Laser Processing Technology	42
2.3.1 Laser Classification	43
2.3.2 Laser Beam	44
2.3.3 Interaction of Laser Beam with Target Materials	47
2.3.4 Key Factors Affect Laser Processing	52
2.4 Introduction to Ablation Results Evaluation and Control.....	65
2.4.1 Topography Measurement Technologies.....	65
2.4.2 Morphology Observation Strategies.....	72
2.4.3 Heat Affected Zone Identification and Control	74
2.5 Introduction to Simulation Models for Laser Processing.....	79
2.5.1 Empirical Model.....	80
2.5.2 Numerical Model	81
2.5.3 Analytical Model	83
2.6 Electromechanical Systems for Laser Manipulation	86
2.6.1 Positioning System and Electromechanical Control	86
2.6.2 Laser Beam Manipulation	94
2.7 Summary and Research Gaps.....	97
Chapter 3 Methodology.....	101
3.1 Methodology Background	101
3.2 Preliminary Research Preparation.....	103
3.2.1 Selection of Grinding Wheels.....	103
3.2.2 Selection of Dressing Strategy.....	103

3.2.3 Selection of Laser Source.....	105
3.3 Modelling Study	106
3.3.1 Preliminary Modelling Analysis.....	106
3.3.2 Simulation Model Selection	108
3.3.3 Determination of Composite Material Properties.....	116
3.3.4 Simulation Results Analysis.....	120
3.4 Experimental Investigation	121
3.4.1 Experimental Scheme Design	124
3.4.2 Experimental Platform Establishment.....	126
3.4.3 Experimental Procedures	127
3.5 Conclusions and Discussions.....	131
Chapter 4 Ablation Process Modelling Based on Finite Difference Method: Understanding the Ablation Parameters Effect on the Temperature Field.....	133
4.1 Introduction.....	133
4.2 Theoretical Analysis.....	134
4.3 Modelling Process	136
4.3.1 Model description.....	136
4.3.2 Flowchart	143
4.4 Simulation Results and Analysis	145
4.4.1 Temperature Filed Responds to Time	145
4.4.2 Laser Power Effects on the Temperature Field.....	148
4.4.3 Laser Power Effects on Ablation Depth.....	153
4.4.4 Feed Rate Effects on the Temperature Field	156

4.4.5 Feed Rate Effects on the Ablation Depth.....	161
4.5 Application	164
4.6 Conclusions and Discussions	167
Chapter 5 On the Establishment of the Electromechanical Ablation System and Motion Evaluation.....	169
5.1 Introduction.....	169
5.2 Establishment of the Ablation System Prototype	169
5.2.1 Positioning Platform	170
5.2.2 Laser Beam Generation System	174
5.2.3 Electromechanical Control System	175
5.3 Positioning Evaluation.....	175
5.3.1 Positioning Accuracy.....	176
5.3.2 Speed Accuracy	178
5.3.3 Acceleration Performance.....	180
5.3.4 Adjusting Time.....	183
5.4 Applications	184
5.5 Conclusions and Discussions	185
Chapter 6 Generation of Textured Diamond Abrasive Tools by Continuous-Wave CO₂ Laser: Understanding the Laser Parameter Effects and Optimisation	187
6.1 Introduction.....	187
6.2 Experimental Strategy.....	188
6.3 Experimental Results on the Ablated Structure Topography	192

6.3.1 Effects of Laser Powers	192
6.3.2 Effects of Laser Feed Rates	194
6.4 Experimental Results on the Ablated Structure Morphology.....	197
6.4.1 Effects of Laser Powers.....	197
6.4.2 Effects of Laser Feed Rates	200
6.5 Applications	202
6.5.1 Laser Ablation Parameters Selection for Texturing Diamond Abrasive Tools...	202
6.5.2 Precise Generation of Textures on Flat Grinding Wheels	204
6.6 Conclusions and Discussions.....	205
Chapter 7 Generating Profile Diamond Grinding Wheels by Single Pass of High-Power Fibre Laser: Understanding the Ablation Law with High Laser Power and Predictive Model Establishment	207
7.1 Introduction.....	207
7.2 Experimental Strategy.....	208
7.3 Experimental Results and Analysis	212
7.3.1 Effect of Duty Cycle Changes under Different Laser Power on the Ablation Law...	212
7.3.2 Effect of Feed Rate Changes under Different Laser Power on the Ablation Law	213
7.3.3 Effect of Laser Power Changes under Different Duty Cycles on the Ablation Law.	214
7.3.4 Effect of Laser Power Changes under Different Feed Rates on the Ablation Law	215
7.4 Analytical Modelling Analysis	216
7.4.1 Modelling Process Background	216

7.4.2 Model Description.....	216
7.4.3 Calculation Results and Analysis	219
7.5 Empirical Modelling Analysis.....	221
7.5.1 Model Description.....	221
7.5.2 Modelling Results	222
7.6 Prediction Results Validation.....	228
7.6.1 Validation of Ablation Results under the Laser Power of 2,000 W	228
7.6.2 Validation of Ablation Results Changed with Laser Power under the Duty Cycle of 100%.....	229
7.6.3 Validation of Ablation Results Changed with Laser Power under the Feed Rate of 100 mm/s	230
7.7 Error Analysis	230
7.8 Applications	232
7.9 Conclusions and Discussions	233
Chapter 8 Generating Profile Diamond Grinding Wheels by Multiple Pass of Fibre Laser: On the Understanding of Laser Ablation Law with Pass Number and Feed Rate	235
8.1 Introduction.....	235
8.2 Theoretical Analysis.....	236
8.3 Experimental Strategy.....	237
8.4 Experimental Results and Analysis	240
8.4.1 Ablation Width Affected by Laser Pass Number and Feed Speed	240
8.4.2 Ablation Depth Affected by Laser Pass Number and Feed Speed.....	241
8.4.3 Ablation Morphology Affected by Laser Pass Number and Feed Speed.....	242

8.4.4 Parameters Selection for Multi-pass Ablation of Abrasive Tools.....	245
8.5 Applications	246
8.6 Conclusions and Discussions.....	247
Chapter 9 Generating Precise Non-flat Diamond Grinding Wheels via a Combination of CO₂ Laser Ablation: Understanding the relationship between Overlap Rate and Feed Rate on Composite Materials.....	249
9.1 Introduction.....	249
9.2 Theoretical Analysis.....	250
9.2.1 Laser Ablation Process.....	250
9.2.2 Parallel Overlap	251
9.3 Experimental Strategy.....	256
9.4 Experimental Results and Analysis.....	260
9.4.1 Effect of Feed Rates and Overlap Rates on the Ablated Topography	260
9.4.2 Effect of Overlap Rate Changes on the Ablation Law under Different Feed Rates	262
9.4.3 Effect of Feed Rate Changes on the Ablation Law under Different Overlap Rates	264
9.5 Establishment of Empirical Prediction Model.....	265
9.5.1 Prediction Model for Ablated Width and Depth.....	266
9.5.2 Prediction Model for Ablated Topography	269
9.6 Applications	271
9.7 Conclusions and Discussions.....	277
Chapter 10 Research outcomes and further work.....	279
10.1 Summary of research findings and conclusions.....	279

10.2 Further work.....	281
References	283

List of Figures

Figure 1.1 Present situation of abrasive tools. (a) Global abrasive tools market size prediction and (b) current consumption condition of high-end abrasive tools [1].	1
Figure 1.2 Downstream application of abrasive tools worldwide in 2020 [1]. .	2
Figure 1.3 Proportions of resin bond diamond abrasive tools used in the different regions [2].	3
Figure 1.4 Flow chart representing the outline of the thesis and each chapter.	12
Figure 2.1 Typical abrasive tools. Conventional abrasive tools, including (a) aluminium oxide [25] and (b) silicon carbide [26] abrasive tools. Super-abrasive tools, including (c) diamond [27] and (d) Cubic Boron Nitride (CBN) [28] abrasive tools. Structured abrasive tools, including (e) textured [29] and (f) profiled [30] abrasive tools.	14
Figure 2.2 Conventional abrasives [31]. (a) Green silicon carbide and (b) white aluminium oxide.	15
Figure 2.3 Standard marking system for aluminium oxide and silicon carbide wheels [35].	17
Figure 2.4 Superhard abrasives. (a) Synthetic diamond [36] and (b) CBN [37].	18
Figure 2.5 Standard marking system for diamond and cubic boron nitride grinding wheels and other bonded abrasives [35].	20
Figure 2.6 Structures on pad abrasive tools. (a) Phyllotactic pattern [40]; (b) tilt slot pattern [41]; (c) straight slot pattern [42]; (d) centrifugal channel pattern [43]; (e) cone slot pattern [44].	21
Figure 2.7 Structures on flat abrasive tools. (a) Wedge angle pattern [46]; (b)	

cutting edge pattern [23]; (c) hexagon, square and triangle pattern [47]; (d) square frustum pattern [48]; (e) V-shape groove pattern [49]. 23

Figure 2.8 Structures on abrasive wheel tools. (a) Straight slots; (b) helical slots; (c) zigzag slots and parallelogram patterns; (d) milled slots; (e) blind micro-hole; (f) protruding grains with defined requirement. 25

Figure 2.9 The definition of uniform and non-uniform arranged ablation slots 26

Figure 2.10 Applications of profiled abrasive tools [57]. 27

Figure 2.11 Form grinding of gear. (a) Error compensation method to improve the form grinding accuracy [58], (b) function-oriented form-grinding approach to producing outstanding cylindrical gears [69], (c) heat conduction mechanism analyses in grinding of involute gears [70], and (d) simulation study of temperature field distribution in gear form-grinding [71]. 28

Figure 2.12 Grinding of free form profile. (a) Turbine disk slots [76], (b) profile-adapted needle nozzle for good grinding performance [77], (c) ultra-precision grinding of the biconical free-form optics [64], and (d) errors compensation to directly used for 3D curved wheel [78]. 30

Figure 2.13 Dressing by mechanical method. (a) Single point tool [89], (b) dressing tool controlled excitation [91], and (c) fly-cutting [93]. 33

Figure 2.14 Dressing by electrochemical method. (a) Schematic diagram [101], (b) and (c) microscopes of electroplating method [98, 100]; (d) Schematic diagram [102] and (e) digital microscope [103] of brazing method. 35

Figure 2.15 Diagrams of two leading energy beam methods [107]. (a) Abrasive waterjet and (b) laser beam. 37

Figure 2.16 (a) Schematic diagram of AWJ turning; (b) grooved and scalloped grinding wheel [116]. 38

Figure 2.17 (a) Photo of micro-structured wheels and its morphology [119]; (b)

experimental setup for micro-structuring grinding wheel and the grain morphology processed by 300 mm/s laser scanning [120].	40
Figure 2.18 Different types of laser. (a) Solid [127], (b) gas [128], (c) liquid [129], and (d) semiconductor [130].	43
Figure 2.19 Interpretation of the atomic excitation [131]. (a) An electron absorbs input energy and moves from an orbit with lower energy to a higher one; (b) an excited electron decays, it emits a light photon; (c) photons clash with other energised atoms in stimulated emission.....	45
Figure 2.20 Generation of laser beam [132]. (a) The fundamental design of a laser device lies in its excited state; (b) a laser beam is formed when the stimulated photons travel through the mirror.....	46
Figure 2.21 A ruby laser in action with a set of simple components [127]....	46
Figure 2.22 Interaction of laser beam with materials in macro-level view [134].	47
Figure 2.23 Absorption of two different unpolarised beams from CO ₂ and solid-state laser light measured as a function of the incident angle from a molten iron surface [135].	49
Figure 2.24 Definition of glancing angle (left) and absorptivity as a function of glancing angle (right) [136]	50
Figure 2.25 CO ₂ laser absorption coefficient of steel utilising oxygen as a function of material thickness [141]......	51
Figure 2.26 Micro-behaviours in the laser processing zone [143].....	52
Figure 2.27 Absorption wavelength spectrum for different materials [145]. .	54
Figure 2.28 Mechanism of CW or PW beam creation. (a) The basic mechanism of the laser resonator and (b) CW vs Pulsed laser [145]......	55
Figure 2.29 Damage effects of different wave modes [149]. (a) Damaging	

effects of a long pulse laser beam on the surface and surrounding material; (b) ultrashort laser pulses do not affect the surface, minimize heat transfer to surrounding material and avoid micro-cracks and a melt zone..... 57

Figure 2.30 Laser power range fits the application scopes [145]..... 59

Figure 2.31 (a) Diagram of a typical laser-material interaction geometry; (b) the absorptivity of CO₂ laser affected by perpendicular and parallel [151]. 60

Figure 2.32 Radial and circular polarizations affect the cutting speed of CO₂ laser for 2 mm stainless steel [151]. 61

Figure 2.33 Definition of parameters for beam propagation and beam characterization formulas [154]..... 62

Figure 2.34 Diagram for the definition of M^2 and its influence on the beam diameter. The functions are generated from Equation (2.4). 63

Figure 2.35 Focused beam profile affected by beam parameter product [156]. 63

Figure 2.36 Intensity distribution of two different laser types. (a) CO₂ and (b) disk laser beam [158]. 64

Figure 2.37 Effect of BPP on beam diameter and power density [160]. 65

Figure 2.38 Depth measurement technologies. 66

Figure 2.39 Diagram of optics principles of an SPR angular sensor [164]. Rays back from an objective lens and a mirror are (a) parallel, (b) converging, and (c) diverging..... 67

Figure 2.40 Principle of MSMI [166]. 68

Figure 2.41 The robot calibration system [167]. (a) Machine vision measurement, (b) mechanical measurement. 69

Figure 2.42 Schematic of the measurement principle [168]..... 69

Figure 2.43 Experimental setups for absolute measurements: (a) calibration, (b) nonlinearity measurement.	70
Figure 2.44 Diagram for locating process of reading head [171].....	71
Figure 2.45 Morphologies observed by SEM and optical images. (a) Single-crystal silicon carbide [172] and (b) CFRP [173]; (c) Ti-6Al-4V [126] and (d) CFRP [174].	73
Figure 2.46 Metallography changes with temperature observed by ESEM [175].	74
Figure 2.47 HAZ detection by (a) SEM and (b, c) optical image. (a) Titanium (Ti) and carbon fibre reinforced plastic [178], (b) single crystal 4H-SiC wafer [172], and CFRP [174].	75
Figure 2.48 HAZ detected by the thermal infrared camera. (a) Temperature field distribution with time [173], (b) calculated and the thermal infrared camera measured results comparison [180], and (c) prediction of temperature distribution [126].....	77
Figure 2.49 The hybrid cutting head. (a) Experimental platform and (b) working diagram [172].	79
Figure 2.50 Prediction results of the empirical model. Results for HAZ (a) cutting speed vs power, laser power vs gas pressure, and (c) cutting speed vs gas pressure; (d) validation of response surface models with experimental results [191].	81
Figure 2.51 (a) Ablation depth (H) against feed rate (v) in FEA simulation and experimental validation (F_0 set as 5.0 kJ/m^2 and f set as 30 kHz). Simulation time (b) 298.34 ns, (c) 342.86 ns, (d) 407.54 ns, and (e) 744.83 ns [198]. ..	82
Figure 2.52 (a) Gaussian distribution of the laser beam. The bottom of the thermal simulation model (b) before and (c) after the death of the elements [10].	83

Figure 2.53 (a) Comparison of experimental and predicted microchannel profiles with 95% pulse overlapping under different conditions [199]; (b) surface temperature and ablation depth during trench ablation for heat buildup and temperature-dependent absorption [200]; (c) sensitivity analysis with various determinations of cell size Δd and time step Δt [201].	85
Figure 2.54 The schematic diagram of the single-axis stage [204].	87
Figure 2.55 The screw based position system. (a) 3D positioning system [206]; (b) running bench for ball screws [207].	88
Figure 2.56 Piezoelectric actuator. (a), (b) and (c) linear movement types [208] [210] [211]; (d), (e) and (f) rotary movement types [212] [213] [214].	89
Figure 2.57 Schematic diagram and photo of the flexible beam driven by a ball-screw stage [205].	90
Figure 2.58 The structure of the position control system with observers and compensators [215].	90
Figure 2.59 Nano-positioning motion stage [217].	91
Figure 2.60 Impedance control design with a delay in the outer admittance control loop [223].	92
Figure 2.61 Stepper motor wiring of XYZ System [206].	93
Figure 2.62 Shutters. (a) Stepper motor, (b) relay and (c) piezoelectric actuator [229].	95
Figure 2.63 Shutters. (a) DC motor shutter [230]; (b) motor-shield shutter [231]; (c) piezoelectric cantilever shutter [232].	96
Figure 3.1 Flow chart of the methodology for the research programme.	102
Figure 3.2 Selected resin bond diamond grinding wheels.	103
Figure 3.3 Schematics of incidence of laser beams in the (a) tangential and (b)	

radial directions.....	104
Figure 3.4 The calculation diagram of laser fluence.....	107
Figure 3.5 The laser beam profile model.	109
Figure 3.6 The GB and SGB laser beam model. (a) GB model and (b) SGB model.	110
Figure 3.7 The diagram illustrating heat transfer from the laser beam to the workpiece. (a) The front and (b) top view.....	111
Figure 3.8 Nodes physical situations (Dashed lines indicate volume element). (a) Interior node; (b) convection boundary node; (c) exterior corner with convection boundary; (d) interior corner with convection boundary.	112
Figure 3.9 Melt pool geometry and energy flows in a quasi-stationary case [202].....	114
Figure 3.10 The ingredients and percentages of the diamond abrasive wheel. (a) The grinding wheel block and ingredients; (b) ingredients elements detecting EDS; (c) the weight percentage and (d) volume percentage determination in the grinding wheel.	116
Figure 3.11 Ablation process. (a) The left view and (b) the front view of the grinding wheel; (c) the top view of the sample; (d) the lateral section, and (e) the cross-section of the slot on the sample.....	121
Figure 3.12 Experimental equipment. (a) 5-axis manufacturing centre; (b) Han's Nd: YAG laser machine; (c) Hongfan CO2 laser machine; (d) EDM; (e) grinder; (f) handsaw; (g) 3D coordinate measurement machine; (h) optical microscope; (i) SEM.....	123
Figure 3.13 Path plan for some typical textures. (a) Straight line, (b) tilt line, (c) zigzag line and (d) square block.	124
Figure 3.14 Ablation scheme for the profiled grinding wheels. Remove target	

materials by (a) single pass, (b) multiple passes and (c) a combination of ablation strategies.	125
Figure 3.15 The overall scheme design of the manufacturing system.....	126
Figure 3.16 Sample Preparation. (a) Cutting through the abrasive layer by hand saw, (b) cutting the samples from the grinding wheel by EDM, (c) polishing both sides of the samples, and (d) drying the samples.....	128
Figure 4.1 The surface characteristics generation mechanism. (a) Exposure (most of the diamond part is still under the resin)/loosening (most of the diamond part was in the air), (b) breakage and (c) deterioration.	135
Figure 4.2 The diagram of the calculation position.	138
Figure 4.3 Diagram of the different cases in the heat transfer solution [268].	142
Figure 4.4 Flowchart for the theoretical model, solving the temperature field distribution and ablation depth estimation by inputting processing parameters of laser power and feed rate.	145
Figure 4.5 Temperature field responses to time during laser ablation under the laser power of 24 W and feed rate of 3 mm/s. The transient temperature field of the slot cross section for (a) the time at 0, 0.5, 1.0, 1.5 and 2.0 s, (b) the time at 0.01, 0.02, 0.03, 0.04 and 0.05 s, (c) the time at 0.06, 0.07, 0.08, 0.09 and 0.1 s, (d) the time at 0.1, 0.2, 0.3, 0.4 and 0.5 s, and (e) the time at 0.6, 0.7, 0.8, 0.9 and 1.0 s.....	146
Figure 4.6 Simulation results of temperature field distribution response to laser powers from 24 to 60 W with an interval of 12 W under the feed rate of 3.0 mm/s. (a), (c), (e) and (g) are the lateral section view (from the x-z plane) and (b), (d), (f) and (h) are the cross-section view (from the y-z plane) for the laser powers of 24 W, 36 W, 48 W and 60 W, respectively.....	149
Figure 4.7 Simulation results of temperature field distribution response to laser powers from 24 to 60 W with an interval of 12 W under the feed rate of 4.0	

mm/s. (a), (c), (e) and (g) are the lateral section view (from the x-z plane) and (b), (d), (f) and (h) are the cross-section view (from the y-z plane) for the laser powers of 24 W, 36 W, 48 W and 60 W, respectively. 150

Figure 4.8 Simulation results of temperature field distribution response to laser powers from 24 to 60 W with an interval of 12 W under the feed rate of 5.0 mm/s. (a), (c), (e) and (g) are the lateral section view (from the x-z plane) and (b), (d), (f) and (h) are the cross-section view (from the y-z plane) for the laser powers of 24 W, 36 W, 48 W and 60 W, respectively. 151

Figure 4.9 Simulation results of temperature field distribution response to laser powers from 24 to 60 W with an interval of 12 W under the feed rate of 6.0 mm/s. (a), (c), (e) and (g) are the lateral section view (from the x-z plane) and (b), (d), (f) and (h) are the cross-section view (from the y-z plane) for the laser powers of 24 W, 36 W, 48 W and 60 W, respectively. 152

Figure 4.10 Simulation results of the ablation depth response to laser powers from 24 W to 60 W with an interval of 12 W under the feed rate of 3.0 mm/s. (a), (b), (c) and (d) are the ablation depth for the laser power of 24 W, 36 W, 48 W and 60 W, respectively. 153

Figure 4.11 Simulation results of the ablation depth response to laser powers from 24 to 60 W with an interval of 12 W under the feed rate of 4.0 mm/s. (a), (b), (c) and (d) are the ablation depth for the laser power of 24 W, 36 W, 48 W and 60 W, respectively..... 154

Figure 4.12 Simulation results of the ablation depth response to laser powers from 24 to 60 W with an interval of 12 W under the feed rate of 5.0 mm/s. (a), (b), (c) and (d) are the ablation depth for the laser power of 24 W, 36 W, 48 W and 60 W, respectively..... 155

Figure 4.13 Simulation results of the ablation depth response to laser powers from 24 to 60 W with an interval of 12 W under the feed rate of 6.0 mm/s. (a), (b), (c) and (d) are the ablation depth for the laser power of 24 W, 36 W, 48 W and 60 W, respectively..... 155

Figure 4.14 Simulation results of temperature field distribution response to feed rates from 3.0 to 6.0 mm/s with an interval of 1.0 mm/s under the laser power of 24 W. (a), (c), (e) and (g) are the lateral section view (from x-z plane) and (b), (d), (f) and (h) are the cross-section view (from y-z plane) for the feed rate of 3.0 mm/s, 4.0 mm/s, 5.0 mm/s and 6.0 mm/s, respectively..... 157

Figure 4.15 Simulation results of temperature field distribution response to feed rates from 3.0 to 6.0 mm/s with an interval of 1.0 mm/s under the laser power of 36 W. (a), (c), (e) and (g) are the lateral section view (from x-z plane) and (b), (d), (f) and (h) are the cross-section view (from y-z plane) for the feed rate of 3.0 mm/s, 4.0 mm/s, 5.0 mm/s and 6.0 mm/s, respectively..... 158

Figure 4.16 Simulation results of temperature field distribution response to feed rates from 3.0 to 6.0 mm/s with an interval of 1.0 mm/s under the laser power of 48 W. (a), (c), (e) and (g) are the lateral section view (from x-z plane) and (b), (d), (f) and (h) are the cross-section view (from y-z plane) for the feed rate of 3.0 mm/s, 4.0 mm/s, 5.0 mm/s and 6.0 mm/s, respectively..... 159

Figure 4.17 Simulation results of temperature field distribution response to feed rates from 3.0 to 6.0 mm/s with an interval of 1.0 mm/s under the laser power of 60 W. (a), (c), (e) and (g) are the lateral section view (from x-z plane) and (b), (d), (f) and (h) are the cross-section view (from y-z plane) for the feed rate of 3.0 mm/s, 4.0 mm/s, 5.0 mm/s and 6.0 mm/s, respectively..... 160

Figure 4.18 Simulation results of the ablation depth response to feed rate from 3.0 mm/s to 6.0 mm/s with an interval of 1.0 mm/s under the laser power of 24 W. (a), (b), (c) and (d) are the ablation depth for the feed rate of 3.0 mm/s, 4.0 mm/s, 5.0 mm/s and 6.0 mm/s, respectively..... 161

Figure 4.19 Simulation results of the ablation depth response to feed rate from 3.0 mm/s to 6.0 mm/s with an interval of 1.0 mm/s under the laser power of 36 W. (a), (b), (c) and (d) are the ablation depth for the feed rate of 3.0 mm/s, 4.0 mm/s, 5.0 mm/s and 6.0 mm/s, respectively..... 162

Figure 4.20 Simulation results of the ablation depth response to feed rate from

3.0 mm/s to 6.0 mm/s with an interval of 1.0 mm/s under the laser power of 48 W. (a), (b), (c) and (d) are the ablation depth for the feed rate of 3.0 mm/s, 4.0 mm/s, 5.0 mm/s and 6.0 mm/s, respectively.....	163
Figure 4.21 Simulation results of the ablation depth response to feed rate from 3.0 mm/s to 6.0 mm/s with an interval of 1.0 mm/s under the laser power of 60 W. (a), (b), (c) and (d) are the ablation depth for the feed rate of 3.0 mm/s, 4.0 mm/s, 5.0 mm/s and 6.0 mm/s, respectively.....	164
Figure 4.22 Application for heat-affected zone control on resin-bond diamond grinding wheels. Section views of the ablation result from the feed rate of 3.0 mm/s under laser powers of (a) 24 W, (b) 36 W and (c) 48 W; section views of the ablation result from the feed rate of 6.0 mm/s under laser powers of (d) 24 W, (e) 36 W and (f) 48 W. Section views of the ablation result from the feed rate of 8.0 mm/s under laser powers of (d) 24 W, (e) 36 W and (f) 48 W...	165
Figure 4.23 Evaluation of the ablation results on resin-bond diamond grinding wheels. (a) The heat-affected zone index (W_m/D_w ratio) and (b) aspect ratio (D_m/W_m ratio) change with feed rate under different laser power.....	166
Figure 5.1 Overview of the newly designed ablation system. (a) The main ablation system; (b) the positioning; (c) the electromechanical control system.....	170
Figure 5.2 Initial version of the design. (a) Solidworks model and (b) the physical prototype.....	171
Figure 5.3 Improved version of the platform. (a) Solidworks model and (b) the physical prototype.	173
Figure 5.4 Overall view of the whole positioning platform.....	174
Figure 5.5 Positioning for different moving distances under various speeds. Positioning for moving distance of (a) 1 mm, (b) 10 mm, (c) 100 mm and (d) 1,000 mm.....	177

Figure 5.6 Stable error and maximum overshoot for different moving distances under various speeds. Positioning for moving distance of (a) 1 mm, (b) 10 mm, (c) 100 mm and (d) 1,000 mm. 178

Figure 5.7 Moving speed varies with time under different conditions. Moving speed varies with time under (a) lower and (b) higher feed rates. 179

Figure 5.8 Stable error and percentage vary with speed under different conditions. Stable error and percentage under (a) lower and (b) higher feed rate. 179

Figure 5.9 Acceleration performance under relatively lower speed. Acceleration performance for moving speed of (a) 1 mm/s, (b) 5 mm/s, (c) 10 mm/s, (d) 15 mm/s and 20 mm/s. 181

Figure 5.10 Acceleration performance under relative higher speed. Acceleration performance for moving speed of (a) 20 mm/s, (b) 40 mm/s, (c) 60 mm/s, (d) 80 mm/s and 100 mm/s. 182

Figure 5.11 Adjusting time for the positioning system motion. Adjusting time for (a) moving different distances, (b) quasi/stable speeds and quasi/stable accelerations. 183

Figure 5.12 Ablated diamond grinding wheels with irregular-shaped textures. Grinding wheels with (a) continuously changed depths and (b) sine-line textures. 185

Figure 6.1 Experiment methodology. (a) Experimental setup including the laser and motion control PCs (left), the specially-designed positioning system (middle) and the laser ablation system setup (right), (b) the ablation strategy where the wheel was equally divided into eight segments (A-H) and in each segment there were seven ablated tracks along the wheel axis direction (X1-X7 where X refers to A-H). The laser feed rate was incrementally increased from segment A to H, while the laser power was incrementally increased from track X1 to X7, and (c) the quadratic function fitting by the least square method based on the nine key points (P1-P9). 189

Figure 6.2 The effects of laser power on the ablated structure topography. (a) The fitting profile of the ablated structure cross-section profile when the feed rate was 3.0 mm/s and the laser powers were 54 W (specimen A), 48 W (specimen B), 42 W (specimen C), 36 W (specimen D), 30 W (specimen E), and 24 W (specimen F), (b) the SEM micrographs of the cross-sections of the specimens from A to F, and the effects of laser power on the (c) top width (red) and depth (blue), and (d) bottom width (red) and side edge tilt angle (blue).
 194

Figure 6.3 The effects of laser feed rate on the ablated structure topography. (a) The fitting profile of the ablated structure cross-section profile when the laser power was 54 W and the feed rates were 3.0 mm/s (specimen A), 4.0 mm/s (specimen B), 5.0 mm/s (specimen C), 6.0 mm/s (specimen D), 7.0 mm/s (specimen E), and 8.0 mm/s (specimen F), (b) the SEM micrographs of the cross-sections of the specimens from A to F, and the effects of feed rate on the (c) top width (red) and depth (blue), and (d) bottom width (red) and side edge tilt angle (blue).
 196

Figure 6.4 The effects of laser power on the ablated structure morphology. (a) The fitted profile of the ablated structure cross-section profile when the feed rate was 3.0 mm/s and the laser power was separately 24 W (specimen A), 42 W (specimen B), 54 W (specimen C) and the SEM micrographs of the top views from specimen C, and the SEM micrographs, the XRD patterns, and the EDS analysis results of the specimen A (b, c, d), B (e, f, g) and C (h, i, j). 199

Figure 6.5 The effects of feed rates on the ablated structure morphology. (a) The fitting profile of the ablated structure cross-section profile when the laser power was 54 W and the feed rate was separately 8.0 mm/s (specimen A), 5.0 mm/s (specimen B), 3.0 mm/s (specimen C) and the SEM micrographs of the top views from specimen C; and the SEM micrographs, the XRD patterns, and the EDS analysis results of the specimen A (b, c, d), B (e, f, g) and C (h, i, j).
 201

Figure 6.6 Diagram for the selection of laser ablation parameters for proper

diamond grinding wheel texturing.204

Figure 6.7 Ablated diamond abrasive tools with different-shaped textures (including tilt line, parallelogram, hexagonal, triangular, and rectangular structures). (a) The parameters selected by the proposed method (the laser power of 54 W and the feed rate of 5.5 mm/s) and (b) the improper parameters (the laser power of 54 W and the feed rate of 2.0 mm/s).....205

Figure 7.1 Experimental methodology. (a) The grinding wheel is divided into eight segments from segment A to segment H, for each segment includes ten laser power parameters, (b) the side view of the grinding wheel and (c) view A of the ablated area and (d) the measurement.....209

Figure 7.2 Experimental setup and procedure. (a) The experimental setup; (b) the ablation process; (c) the ablated slots; (d) the measurement diagram. 211

Figure 7.3 Influence of duty cycle changes under different laser power on the ablation law. (a) Influence on ablation depth and (b) influence on ablation width.212

Figure 7.4 Influence of feed rate changes under different laser power on the ablation law. (a) Influence on ablation depth and (b) influence on ablation width.213

Figure 7.5 Influence of laser power changes under different duty cycles on the ablation law. (a) Influence on ablation depth and (b) influence on ablation width.215

Figure 7.6 Influence of laser power changes under different feed rates on the ablation law. (a) Influence on ablation depth and (b) influence on ablation width.216

Figure 7.7 Diagram for melt pool geometry and energy flows in a quasi-stationary situation [202].....218

Figure 7.8 The calculation results of the theoretical model. The ablated profile for laser powers of (a) 200 W, (b) 400 W and (c) 800 W under a feed rate of

25.0 mm/s. The ablated profile for feed rate of (d) 25.0 mm/s, (e) 50.0 mm/s and (f) 75.0 mm/s under laser power of 200 W.....	220
Figure 7.9 Ablation depth changes with duty cycle under different laser power. (a) The overview of the prediction result; (b) the influence of laser power on ablation depth; (c) the influence of duty cycle on ablation depth.....	223
Figure 7.10 Ablation width changes with duty cycle under different laser power. (a) The overview of the prediction result; (b) the influence of laser power on ablation width; (c) the influence of duty cycle on ablation width.....	224
Figure 7.11 Ablation depth changes with feed rate under different laser power. (a) The overview of the prediction result; (b) the influence of laser power on ablation depth; (c) the influence of feed rate on ablation depth.	226
Figure 7.12 Ablation width changes with feed rate under different laser power. (a) The overview of the prediction result; (b) the influence of laser power on ablation width; (c) the influence of feed rate on ablation width.....	227
Figure 7.13 Validated results under the laser power of 2,000 W. (a) Ablation depth and (b) width changed with duty cycle. (c) Ablation depth and (d) width changed with feed rate.....	228
Figure 7.14 The validation of ablation results changed with laser power changes under the duty cycle of 100%. (a) Ablation depth and (b) ablation width.	229
Figure 7.15 The validation of ablation results changed with laser power changes under the feed rate of 100 mm/s. (a) Ablation depth and (b) ablation width.	230
Figure 7.16 The errors for prediction. (a) Ablation depth and (b) ablation width.	231
Figure 7.17 An application example. (a) The ablation scheme; (b) the ablated curved grinding wheel; (c) the cross-section of the curved grinding wheel and the comparison between the measured and designed profile.....	233

Figure 8.1 Section view of the ablated slots under the same output fluence but different conditions. (a) 400 W, 30 mm/s, 1 pass and (b) 400 W, 60 mm/s, 2 passes.237

Figure 8.2 Experimental strategy. (a) The experimental setup consists of a fibre laser machine process centre, a customized positioning system and a control PC; (b) a detailed view of the ablation process; (c) a detailed view of the laser nozzle and grinding wheel; (d) parameters for the trail; (e) definition of pass number; (f) measurement strategy for ablated grooves.238

Figure 8.3 Ablation width affected by laser pass number and feed speed. (a) Optical micrographs from the side view of the ablated grooves with the pass number of 1, 3, 5, 7, 9, 11, 13, 15 at the laser power of 400 W and the feed speed of 30 mm/s; (b) top width and bottom width from 1 pass to 16 passes at a feed speed of 30 mm/s, 36 mm/s and 60 mm/s.240

Figure 8.4 Effect of laser pass number and feed speed on the depth of the ablated structure. (a), (b) and (c) the optical micrographs from one side of the ablated grooves with the pass number of 1, 4, 7, 10, 13, 16 at the same laser power of 400 W and various feed speeds of 30 mm/s, 36 mm/s, 60 mm/s. (d) the effects of laser pass number, feed speed and energy fluence (right) on the ablation depth (left) when the feed rate was 30 mm/s (blue), 36 mm/s (green), 60 mm/s (red).242

Figure 8.5 Bottom morphology affected by laser pass number and feed rate. (a) Definition of morphology characters; (b) bottom morphology with four passes under the feed speed of 30 mm/s, 36 mm/s and 60 mm/s; (c) bottom morphology with the feed rate of 30 mm/s under the pass numbers of 1, 8 and 15.244

Figure 8.6 Diagram for laser ablation parameter selection for different ablation depths.245

Figure 8.7 An application example. (a) The ablation scheme; (b) the ablated curved grinding wheel; (c) the cross-section of the curved grinding wheel and

the comparison between the measured (red) and designed (blue) profile. 246

Figure 9.1 The ablation process. (a) Ablation process diagram and the character of the ablated slot (View A); (b) general shape of a focused laser beam; (c) energy distribution at a certain cross-section along the laser propagation direction [276]. 251

Figure 9.2 Definition of overlap ablation. (a) The overlap ratio definition in single pass ablation; (b), (c) and (d) in multi-pass parallel overlap ablation; (e) the diagram of ablation depths change tends with ORs change (see Figure 9.3 and Figure 9.4)..... 252

Figure 9.3 Ablation results after multiple passes. (a) and (b) the physical model of the ablated samples; (c) and (d) The ablation width and depth changes with feed rate and pass number under laser power 60 W. 253

Figure 9.4 Diagram of parallel overlap ablation. (a) No overlap (OR 00%); (b) less than half overlap (OR 20%); (c) less than half overlap (40%); (d) over than half overlap (60%); (e) over than half overlap (80%); (f) total overlap (100%). 255

Figure 9.5 Experiment methodology. (a) Experimental setup including the laser machine (left) and the specially-designed positioning system (right); (b) the ablation strategy where the wheel was equally divided into six segments (A-F) and in each segment there were six ablated tracks along the wheel axis direction (OR 00 % - OR 100% with an interval of 20%, where OR refers to Overlap Rate). The laser feed rate was incrementally increased from segment A (5 mm/s) to F (10 mm/s), while the tracks OR was incrementally increased from the OR 00% to OR 100% and there are five parallel passes for each OR; (c) the measurement system for the ablated slots, and the nine key points that the ablated width (W), depth (H) and topography are based on being recorded. 259

Figure 9.6 Influence on the ablated topography under varying feed rates and overlap rates. (a)-(f) refer to feed rate of 5.0 mm/s, 6.0 mm/s, 7.0 mm/s, 8.0

mm/s, 9.0 mm/s, 10.0 mm/s, respectively. Slot No. 1-No. 6 refer to the overlap rate from 00% to 100% with an interval of 20%, where OR 00% and OR 20% showed a flat bottom, OR 40% and OR 60% showed a transition bottom, and OR 80% and OR 100% showed a round bottom.261

Figure 9.7 Influence of overlap rate changes on the ablation law under different feed rates. (a) The effect of overlap rate on ablation width; (b) the effect of overlap rate on ablation depth.263

Figure 9.8 Influence of feed rate changes on the ablation law under different overlap rates. (a) The effect of feed rate on ablation width; (b) the effect of feed rate on ablation depth.264

Figure 9.9 Ablation width changes with overlap rate and feed rate. (a) The overview of the prediction result; (b) the influence of overlap rate on ablation width; (c) the influence of feed rate on ablation width.267

Figure 9.10 Ablation depth changes with overlap rate and feed rate. (a) The overview of the prediction result; (b) the influence of overlap rate on ablation depth; (c) the influence of feed rate on ablation depth.268

Figure 9.11 The fitted profile of the ablated topography with 95% confidence bounds. (a), (b) flat bottoms generated by overlap rates 00% and 20% (fitted by Super Gauss Formula); (c), (d) transition bottoms generated by overlap rates 40% and 60% (fitted by Super Gauss formula); (e), (f) round bottoms generated by overlap rates 80% and 100% (fitted by Polynomial). Wherein, the alphabetic subscript (a-f) and numeric subscript (1-6) in the fitting functions (f_{xx}) represent feed rates (5.0 mm/s - 10.0 mm/s, increased by 1.0 mm/s) and ORs (00% - 100%, increased by 20%), respectively.269

Figure 9.12 Goodness of the fitted profiles. (a)-(c) the Sum of Squares for Error (SSE), Root Mean Square Error (RMSE), and Coefficient of Determination (R-square) changes for each feed rate under various overlap rates, respectively.271

Figure 9.13 Planned ablation strategies for designed non-flat grinding wheels.

(a) Strategies on multi-steps wheel featured with large-span macro-steps (steps tagged with No. 1, 2 and 3), deep-narrow slot (slot tagged with No. 7) and high-resolution micro-steps (steps tagged with No. 4, 5 and 6); (b) curved-surfaces wheel featured with exponential (surfaces tagged with No. 1), parabolic (surfaces tagged with No. 2) and arcuate (surfaces tagged with No. 3) generatrix..... 272

Figure 9.14 Ablation results using proposed strategies. (a) Multi-steps profile wheel featured with large-span macro-steps (steps tagged with No. 1, 2 and 3), deep-narrow slot (slot tagged with No. 7) and high-resolution micro-steps (steps tagged with No. 4, 5 and 6); (b) curved-surfaces profile wheel featured with exponential (surfaces tagged with No. 1), parabolic (surfaces tagged with No. 2) and arcuate (surfaces tagged with No. 3) generatrix..... 274

List of Tables

Table 2.1 Indexes of refraction and extinction coefficients of iron at various conditions [135].....	48
Table 2.2 Characteristics of the utilised CO ₂ and disk laser beam [159].....	64
Table 3.1 Detailed parameters of the used CO ₂ laser.....	105
Table 3.2 Detailed parameters of the used fibre laser.	106
Table 3.3 Specifications of the used diamond grinding wheel.	116
Table 3.4 Concentration definition of diamond abrasive wheel [253].	117
Table 3.5 The ingredients' properties of the grinding wheel.....	117
Table 3.6 Comparisons between the calculated and experimental material properties.....	119
Table 3.7 Material properties of the grinding wheel.	120
Table 6.1 The employed laser processing parameters in the trials.....	190
Table 7.1 Details of the experimental parameters.....	210
Table 7.2 Goodness of fit for the prediction models.....	227
Table 8.1 Details of the experimental parameters.....	239
Table 9.1 Details of the laser distance sensor.	257
Table 9.2 Employed laser parameters in the trials.....	257
Table 9.3 Goodness of fit for the prediction models.....	268

List of Abbreviations

AI	Artificial Intelligence
ANN	Artificial Neural Network
AWJ	Abrasive Waterjet
BPP	Beam Parameter Product
CAS	Chinese Academy of Sciences
CBN	Cubic Boron Nitride
CFD	Computational Fluid Dynamics
CFRP	Carbon Fibre Reinforced Polymer
CO ₂	Dioxide Carbon
CNC	Computer Numerical Control
CNITECH	Ningbo Institute of Materials Technology & Engineer, CAS
CVD	Chemical Vapour Deposition (diamond)
CW	Continuous Wave
DAQ	Data Acquisition
DC	Direct Current
DLCs	Diamond-Like Carbons
DSP	Digital Signal Processing
EDM	Electrical Discharge Machining
EDS	Energy-Dispersive X-ray Spectroscopy
ER	Electrorheological
FEA	Finite Element Analysis
FIR	Far Infrared
FR	Feed Rate
FSMJIC	Fuzzy Sliding Mode Joint Impedance Controller
GA	Genetic Algorithm
GB	Gaussian Beam (laser)
Ge	Germanium
GFRP	Glass Fiber Reinforced Polymer ()
HAZ	Heat-Affected Zone
IDGM	Empirical Glazing Model
LASER	Light Amplification by the Stimulated Emissions of Radiation
LED	Light Emitting Diode
MFRAC	Model-Free Robust Adaptive Control

Nd:YAG	Neodymium-doped Yttrium Aluminium Garnet (laser)
NIR	Near Infrared
OR	Overlap Rate
PCD	Polycrystalline Diamond (composite)
PCBN	Polycrystalline Cubic Boron Nitride (composite)
PDMS	polydimethylsiloxane
PID	Proportion Integration Differentiation (control)
PLA	Pulsed Laser Ablation
PMMA	Polymethyl Methacrylate
PVC	Polyvinyl Chloride
Q-switched	Quality switched giant pulse formation (laser)
RMSE	Root Mean Squared Error
R-Square	Coefficient of determination
SDC	Synthetic Diamond Cubic
SEM	Scanning Electron Microscope
SGB	Super-Gaussian Beam (laser)
SMC	Sliding Mode Control
SMI	Self-Mixing Interferometry
SNR	Signal to Noise Ratio
SPR	Surface Plasmon Resonance
Std.Res.	Standard Deviation of Residues
TATs	Textured Abrasive Tools
TDATs	Textured Diamond Abrasive Tools
3D	Three-Dimensional
TGW	Textured Grinding Wheel
Ti	Titanium
UV	Ultra-Violet (rays)
XRD	X-Rays Diffraction

List of Nomenclature

A	thermal diffusivity (mm^2/s)
C_{ab}	absorption coefficient ($1/\text{m}$)
C_p	specific heat capacity ($\text{J}/(\text{kg}\cdot\text{K})$)
D_m	the depth of ablation trench (mm)
D_w	the waist diameter of the laser beam (mm)
I	laser intensity ($\text{J}/(\text{m}^2\cdot\text{s})$)
I_0	initial laser intensity ($\text{J}/(\text{m}^2\cdot\text{s})$)
L_f	latent heat of fusion (kJ/g)
M^2	beam propagation factor
P_L	laser power (W)
Q_C	energy conveyed from liquid-solid boundary to the unmelt material (J)
Q_L	laser energy (J)
Q_F	required energy beside the melt pool (J)
R_m	melt pool radius (m)
T_b	boiling point (K)
T_c	critical temperature (K)
T_f	material failure temperature (K)
T_m	melting point (K)
T_0	initial sample ambient temperature (K)
T_R	reference temperature (K)
$T_{x,y,z,t}^{in}$	the temperature of interior cells (K)
$T_{x,y,z,t}$	spatial transient temperature (K)
$T_{x,y,z,t}^w$	wall temperature (K)
T_∞	environment temperature (K)
W_m	width of melt pool (m)
c	specific heat capacity ($\text{J}/(\text{kg}\cdot\text{K})$)
d	depth of melt pool (m)
d_{RG}	Rayleigh range (m)
d_w	distance from laser waist (m)
h_n	convection-radiation coefficient ($\text{W}/(\text{m}^2\cdot\text{K})$)
n	super Gaussian order
r	radius of laser beam (m)
r_w	radius of laser beam waist (m)

v_f	axial feed rate (m/s)
v_s	grinding wheel rotational speed (m/s)
z_c	melt pool depth (m)
z_{depth}	depth of the heat-affected zone (mm)
α	material thermal diffusivity (*10 ⁻⁶ m ² /s)
β	absorptivity
ρ	density (kg/m ³)
Γ	Gamma function
Δd	mesh cell dimension (m)
Δt	increment of time (s)
δ_k	heat affect zone depth (m)
η	attenuation rate
λ	laser wavelength (m)

Chapter 1

Introduction

1.1 Research Background

Grinding is commonly used in the finish machining of critical mechanical components in the precision manufacturing process due to its high precision, effectiveness, and low cost. Especially for most superhard materials and hard-brittle materials, grinding is often considered the efficient way to the process. Therefore, the global abrasive tools market size has continued to increase. According to the report of *Industry Research*, the global abrasive tools market will still maintain rapid growth with the development of construction and manufacturing, and the global market size will reach 84.84 billion USD in 2030 (see **Figure 1.1a**) [1].

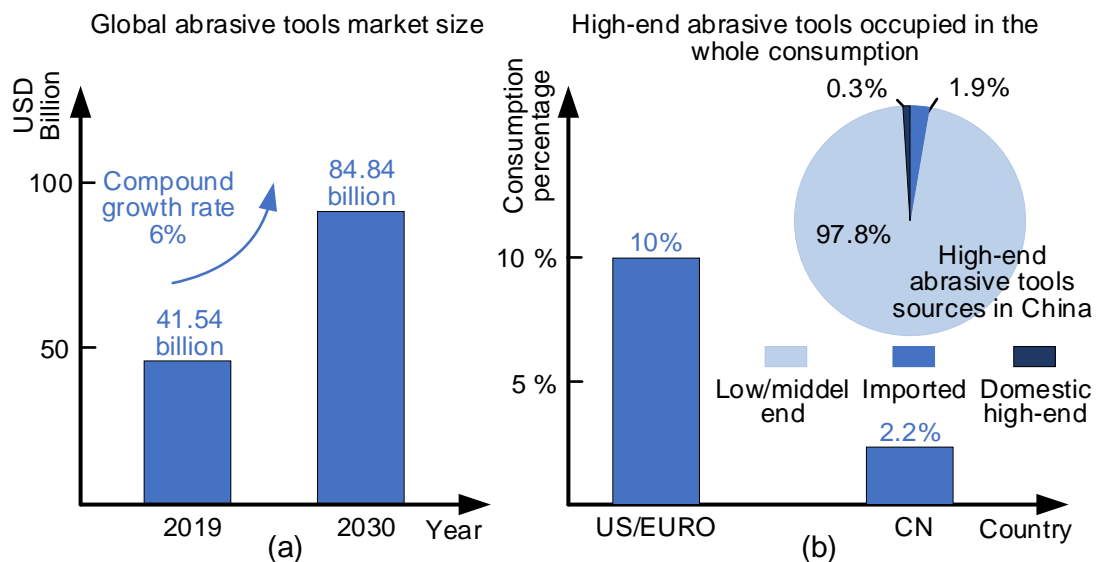


Figure 1.1 Present situation of abrasive tools. (a) Global abrasive tools market size prediction and (b) current consumption condition of high-end abrasive tools [1].

Meanwhile, With the increasingly demanding requirements for nowadays ultra-high-precision processes, the need for high-performance abrasive tools has

been highly emphasised. It has been reported that the consumption of high-end abrasive tools in the developed countries (e.g., in Europe and America) has increased to 10%, while this figure in China has only accounted for 2.2% (see **Figure 1.1b**) [1].

High-performance abrasive tools usually refer to those with specially designed purposes featuring a high grinding ratio, ultra-high grinding precision, good ground surface integrity, or functional surfaces. To achieve the goals, these abrasive tools either improve the tool performance by exploring the high-performance abrasives, bond agency, coating, or tool structures. Generally, diamond and CBN grits are the two kinds of the most widely used high-performance abrasive tools, which are often used to hard-brittle materials with high grinding precision. Furthermore, to achieve a high shape-keeping ability, coated abrasive tools, metal and ceramic bond based abrasive tools have been studied in recent years, and outstanding achievements have been used in automotive & transportation products, heavy machinery, and electrical & electronics equipment (see details in **Figure 1.2**) [1].

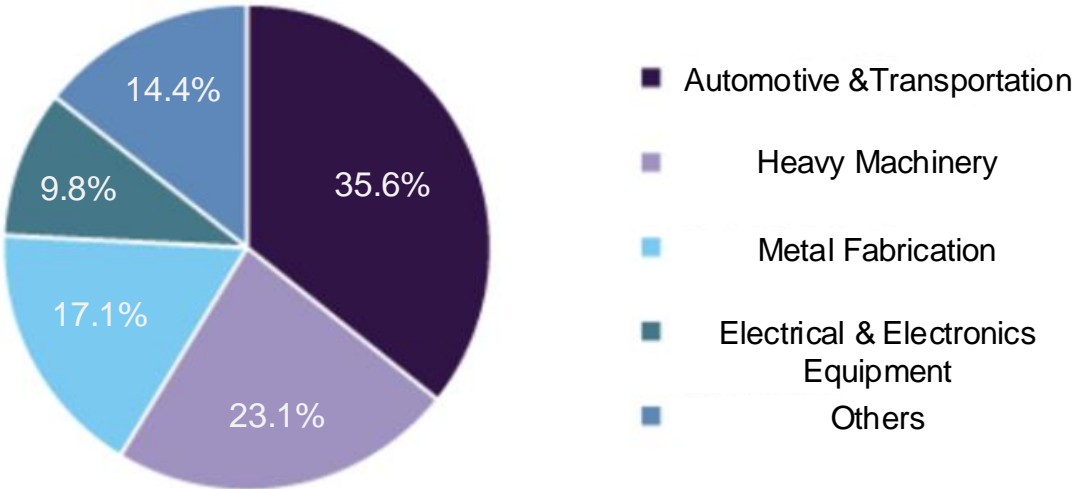


Figure 1.2 Downstream application of abrasive tools worldwide in 2020 [1].

Nevertheless, diamond abrasive tools with resin bond agency are especially popular in the industrial application for their super performance of the high wear-resistance, high elasticity, and good thermal conductivity. **Figure 1.3** shows the proportions of resin bond diamond abrasive tools used in the different regions [2].

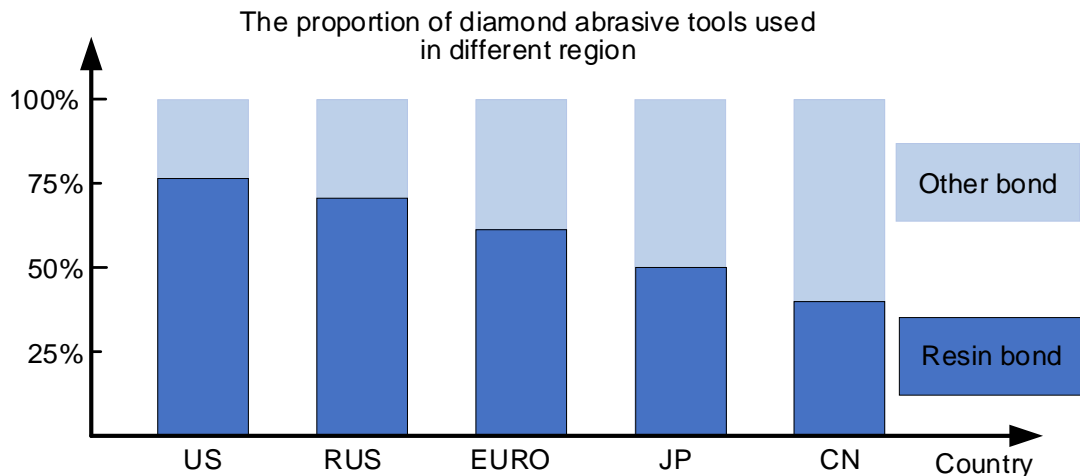


Figure 1.3 Proportions of resin bond diamond abrasive tools used in the different regions [2].

Structured grinding wheels are the newly proposed, most used, high-performance abrasive tools, mainly containing textured grinding wheels and profiled grinding wheels. Textured grinding wheels, where the abrasives within specific areas on the tool surface have been artificially removed [3], have been proposed and have already attracted multitudes of attention from academic scholars and industrial engineers [3, 4]. The superior performances of textured grinding wheels have been extensively found in experimental trials, including good coolant transportation ability [5], effectiveness to lower the grinding temperature [6], and achievable ultra-smooth surfaces [3]. They are currently designed for the increasingly severe working conditions in the modern ultra-high-precision processes featured by intensive load and high temperature.

Profiled grinding wheels, where the profile is purposely dressed to make the generatrix consistent with the designed product. They are aimed to solve the current strenuous industrial requirements characterised by high precision for assembling, high efficiency for production, high profile accuracy keeping ability and lower cost for large batch orders. Typically, the textured and profiled grinding wheels are expected to be the two most capable strategies to be selected for these demanding modern manufacturing tasks in many cases. Therefore, the need to find appropriate methods to develop these high-performance structured grinding tools has been highly emphasized.

Since the structured grinding wheels need to be precisely dressed, the state-of-the-art structuring strategies on abrasive tools have been intensively investigated worldwide. From dressing by mechanical shaped tool, via the chemical method (e.g., electroplating and brazing), to applying energy beam (e.g., laser/plasma/ion beam and waterjet). Among the various dressing strategies, laser ablation is considered a promising method due to its superior advantages such as high efficiency, low vibration, environmental friendliness, and no tool wear [7-9]. Therefore, many researchers take advantage of the process and use it to carry out machining work for material removal or cutting [10-12]. Up to now, many efforts have been paid so far to try to properly produce macro/microscale structures on the abrasive tool surfaces by laser ablation.

To this end, a systematic research scheme including theoretical analysis, model simulation and experimental study is formulated based on the previous studies. The research in the thesis is anticipated to solve the precision fabrication-related issues in machining high-performance abrasive tools, which

has great value in academic research and industrial application.

1.2 Problem Definition

As the most widely-reported issue has been closely related to various kinds of thermal damage [3], including residual stress [13], phase transformation [3], grinding hardening layer [6], and heat-induced surface [14, 15] or subsurface [16] microcracks. It has been widely believed that the successful application of structured grinding wheels could solve some of the most pressing issues in production [17]. Nevertheless, dressing a grinding wheel is not easy because the ultra-high hardness of abrasives embedded in various bond agents makes it challenging to remove material in a controllable way [3, 4]. Therefore, the fabrication technologies for structured abrasive tools can still be considered an open question.

Up-to-date studies show that controllable ablation depth and width are the first challenges researchers constantly face. Currently, the most popular patterns used on the grinding wheels are straight/tilt/zigzag grooves, or shapes formed by straight and tilt lines, like a parallelogram, hexagon, triangle, and rectangle. However, no research has studied the grinding wheels with smooth curved grooves or the non-uniform changing ablated width and depth. In particular, no attention has been given to the ablated heat-affected zone, topography and morphology under different processing parameters, including feed rate, laser power and overlap rate. Besides, no specialised independent experimental system for the research has been made for the manufacturing/ investigation of structured grinding wheels. However, this is the key to generating complex functional textures or grinding wheel profiles with high precision.

Secondly, to the best of the author's knowledge, although significant signs of progress by using laser ablation have been made (like micro-arrayed spatial structures) via intensive research on the machining, they mainly worked with homogeneous materials, e.g., polymer, metal, diamond [18-23]. So far, little attention has been paid to studying the laser ablation process on inhomogeneous non-metallic compound materials. Incredibly, no research or dramatic achievement has been made on the effect of laser beam ablation on the compound materials with obviously different deterioration thresholds due to the complex interaction of laser beam with multi-materials. These issues are essential when dressing a structured abrasive tool via the thermal method.

Thirdly, applicability is also a crucial factor that affects the application of the structured grinding wheel. By using a pulsed laser, the surface geometrical accuracy and multi-scaled structural integrity can be controlled in both time and spatial domains. Therefore, structures with feature sizes in the order of a few micrometres on the workpiece surface are successfully produced. Some prior research has been done on non-uniform matrix ablation (including the dressing process on diamond grinding wheels). However, despite the efforts that have been made, it is hard to apply the results to the machining process due to (i) the high equipment maintenance costs, especially for the laser generators and modulation magnifiers, (ii) the limited ablation penetration depth, especially for abrasive tools having multi-material nature, and (iii) the relatively low machining efficiency due to the small average laser power. Some research attempted to perform the work using the continuous-wave CO₂ laser generator with high average power, but the unwanted heat-affected zone and unpredictable ablation topography would be the critical bottlenecks for the

application.

1.3 Objectives of this Study

Based on the understanding of the previous research and application prospects, this research work aims at developing a specialised manufacturing system for the precise generation of structured diamond grinding wheels via laser ablation. Firstly, a controllable electromechanical laser ablation system with a stable CO₂ laser beam generator and a precise positioning platform is established, and the ablation performance is evaluated. Secondly, a model regarding the heat-affected zone involved in the ablation process is calculated and experimentally validated. The strategies for removing target materials from the grinding wheel in a controllable and optimal manner are investigated using the model and the laser ablation system. Then, the flat grinding wheels with regular patterns (e.g., tilt slots, parallelogram, triangle, hexagon, and rectangle) and irregular patterns (e.g., sine slots and variable depth zigzag groove) are generated after the experimental work regarding the ablation law of laser feed rate and laser power on ablation depth and width is carried out. Finally, the topographies of the ablated slots changing with feed rate and track overlap rate are studied, and the possibilities to generate precise profiled grinding wheels (including stepped wheels and curved surface wheels) by controlling feed rate and overlap rate is addressed. In particular, the main objectives of the present work are:

Objective 1: Modelling of the laser ablation process. The objective includes: (i) establishing the analytical model to understand the ablation process and developing the predictive model for the ablated topography; (ii) understanding the material removal mechanism and the ablation behaviours of the laser

beam on workpiece materials; (iii) investigating the ablation parameters on the ablated topography; (iv) studying the leading causes, identification, and active control of the heat-affected zone.

Objective 2: Establishment of the specialised experimental platform. The specialised experimental platform is crucial for conducting the planned trial and validation entirely. When manipulating lasers, consider focal plane adjustment, laser power control, and laser occlusion. Therefore, this objective covers: (i) establishing the grinding wheel motion-control positioning system, including position, speed, acceleration, response time, and precision; (ii) exploring the existing measurement technology to detect ablated grooves and understand the robustness of the ablation system; (iii) developing a specialised experimental platform for the ablation of abrasive grinding wheels with a high-power continuous-wave laser beam.

Objective 3: Experimental investigation of the textured grinding wheel generation. This objective covers: (i) studying the ablated topography and morphology changed with laser feed rate and laser power; (ii) understanding the laser ablation law on multiple non-metallic inhomogeneous materials; (iii) exploring the optimum processing parameters for the single-pass ablation; (iv) studying the path planning and motion control strategies for the textured grinding wheels; (v) generating regular and irregular textures on flat grinding wheels.

Objective 4: Experimental investigation of the profiled grinding wheel generation. This objective includes: (i) studying the ablation strategies for generating non-flat diamond grinding wheels, and understanding the optimum

way to remove composite materials; (ii) revealing the law of laser ablation strategies' effect on the ablated topography under various processing parameters; (iii) exploring the optimum ablation strategies for profiled grinding wheels; (iv) generating profiled grinding wheels with multi-step surfaces and freeform surfaces.

1.4 Outline of this Thesis

The overall structure of this study is presented in this section, where each chapter and its content are briefly outlined, and the correlation between each chapter is revealed. The plan of this thesis is presented below:

1) *Chapter 1* serves as a general introduction to the background of the study, which aims to understand the significance of this research, evaluate the research gaps, and define the research scopes that would be beneficial to exploit to achieve the final goal of this research.

2) *Chapter 2* covers a detailed literature review related to the field of study by including the introduction to abrasive tools, the dressing strategies on abrasive tools, the heat-affected zone associated with the thermal-based dressing strategies, and the electromechanical system for laser manipulation.

3) *Chapter 3* includes the strategies, procedures, equipment, and techniques used to achieve the objectives and aims throughout the study. The modelling simulation, experimental design and validation, and results analysis are successfully performed.

4) *Chapter 4* contains detailed simulation work on composite materials regarding the laser ablation process. The actual heat effects zone in the ablated area is proposed in this work. In addition, a correlation between the

ablation parameters (laser powers and feed rates) and the ablated topographies is revealed.

5) *Chapter 5* contains a detailed study on establishing and evaluating the electromechanical ablation system. In particular, a complete set of design ideas to develop and evaluate the system (laser beam manipulating system and grinding wheels precise positioning system) is presented.

6) Based on results included in chapter 4 and Chapter 5, *Chapter 6* contains the ablated topography and morphology of diamond grinding wheels in response to the thermal effects of CO₂ laser parameters. In particular, a generic diagram for finding optimal laser ablation parameters is proposed. By using the selection diagram, the application to generate regular (tilt grooves, parallelogram, triangle, and hexagon) and irregular (sine-shaped grooves and polyline with variable-depth) patterns are demonstrated.

7) Combined with the results included in chapter 4 and Chapter 5, *Chapter 7* refers to the strategies to generate profiled diamond grinding wheels by a single pass of a high-power fibre laser. Notably, this chapter aims to present a generic methodology applicable to the ablation process. In addition, this chapter includes the law of fibre laser single pass processing parameters on the target composite materials and the establishment of predictive model results. An application of the predictive model to generate a profile grinding wheel is also included in this chapter.

8) Parallel to Chapter 7, *Chapter 8* refers to the strategies to generate profiled diamond grinding wheels by multiple passes. It aims at understanding the topography and morphology of diamond grinding wheels in response to laser beam pass number and feed rate. A diagram for the ablation depth

selection strategies is presented. A profile grinding wheel is produced in this chapter based on this diagram.

9) Parallel to *Chapter 7* and *Chapter 8*, *Chapter 9* refers to the strategies to generate profiled diamond grinding wheels by combining multiple parameters (focal planes, feed rates, and line overlap rates). Based on the results included in *chapter 7* and *Chapter 8*, a further investigation to a deep understanding of ablated topography in response to laser spot overlap rate and feed rate is performed. Furthermore, a comparison among the ablation strategies is included, which offers scientific evidence of the importance of this study in terms of future perspectives of a reliable generation of precise profiled grinding wheels.

10) *Chapter 10* includes a summary of the discussion of the research work, particularly outlining the project's outcomes and how those could be beneficial for cutting-edge industrial applications. It also includes a conclusion and a future work section.

Figure 1.4 is a flow chart representing the relationship between each chapter. As mentioned above, the research contents are determined to be performed based on the understanding of the research topics in Chapter 1, the summarising the literature review in Chapter 2 and the research methodologies in Chapter 3. In addition, a methodology that covers theoretical analysis, model simulation and experimental work are scheduled for this research. Specifically, simulation work is first performed in Chapter 4 to understand the laser ablation process better and to explore the strategies to have the heat-affected zone under control. Meanwhile, an electromechanical

laser ablation system is established in Chapter 5 to support further experimental study and validation. With the results included in Chapter 4 and Chapter 5, the thermal response of composite materials to laser processing parameters is studied. Based on understanding the laser parameter effects and optimisation on composite materials, the work that generates special textures on flat grinding wheels is performed in Chapter 6. The ablation strategies based on a single pass, multiple passes and combining multi-parameters to generate profiled grinding wheels are respectively presented in Chapter 7, Chapter 8, and Chapter 9. Finally, a separate section regarding the research outcomes and further work is presented in Chapter 10.

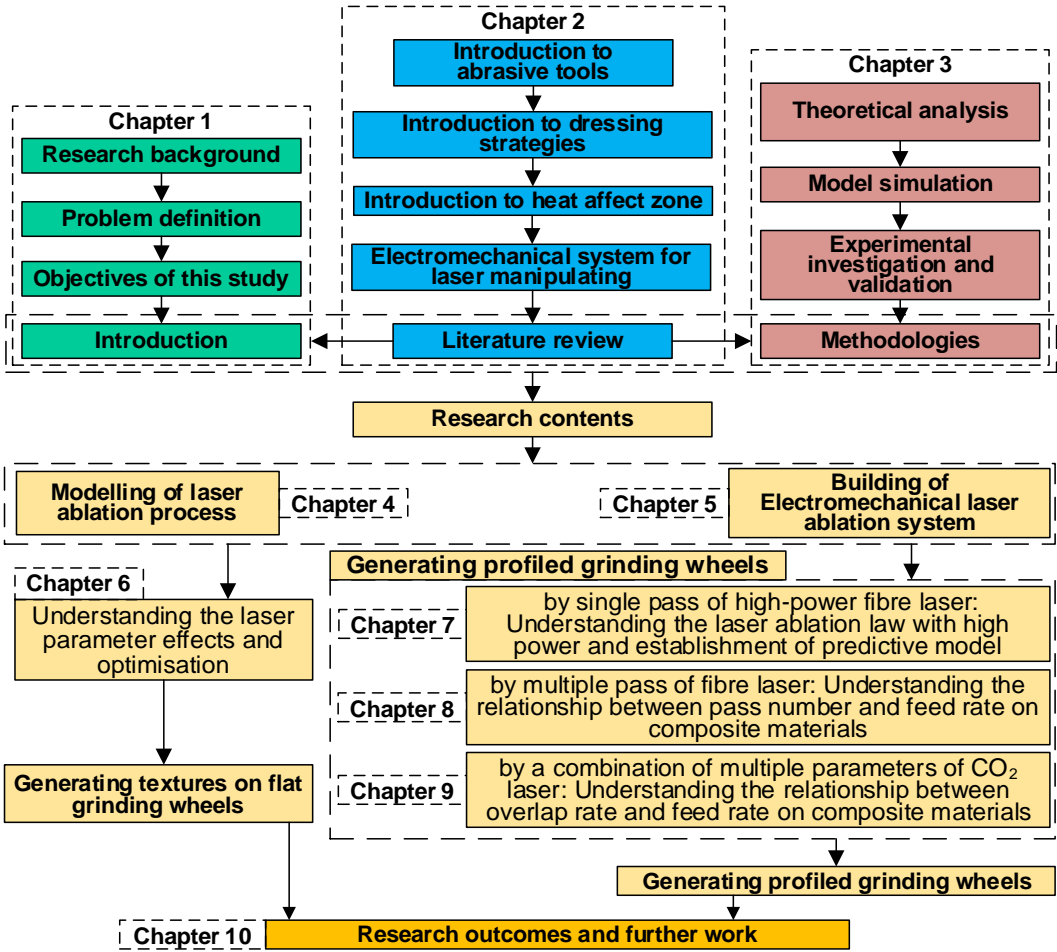


Figure 1.4 Flow chart representing the outline of the thesis and each chapter.

Chapter 2

Literature Review

2.1 Introduction to Abrasive Tools

The use of abrasive tools can be traced back to the Stone Age. Abrasive tools were first used for grinding and polishing tools, weapons, and armour during the Middle Ages and early industrial revolution. Until the early 19th century, grinding wheels made of solidly bonded abrasives were manufactured in India for manual grinding of gemstones. The abrasives in this period were mainly diamond sand and natural corundum, and the bond agency was resin glue. At the end of the 19th century, silicon carbide and alumina artificial abrasives appeared. At the beginning of the 20th century, the grinding wheels made of artificial alumina and silicon carbide, with ceramic, rubber, resin and oxychloride bond agency were used. In the same period, special attention had been paid to the emergence of ultrahard abrasives of diamond and CBN. The resin bond grinding wheel with nature diamond abrasive was firstly produced in 1930. Ten years later, diamond grinding wheels with the ceramic and metal bond agency were also turned up. However, the diamond grinding wheel was unsuitable for grinding ferrous metals because it can guide the graphitization tendency of excessive wear. Hence, General Motors used a similar method to the synthetic diamond to develop the CBN grinding wheel to meet the demand, and it was first used in commercial products in 1969 [24].

Abrasive tools served in the grinding process were key factors determining the qualities of the ground workpiece surfaces. Generally, it could be categorised

into three groups (as shown in **Figure 2.1**): (i) conventional abrasive tools [25, 26], (ii) super-abrasive tools [27, 28], and (iii) structured abrasive tools [29, 30]. Most materials (e.g., stone, steel, and its alloy) and processes (a relatively lower requirement for ground surfaces) can be finished using standard abrasive tools. However, some super-hard materials (e.g., super-hard alloy, gemstone, crystal) and special occasions with high requirements for manufacturing precision (e.g., profile grinding, workpieces with delicate structures.) must be performed with super abrasive or/and structured abrasive tools.

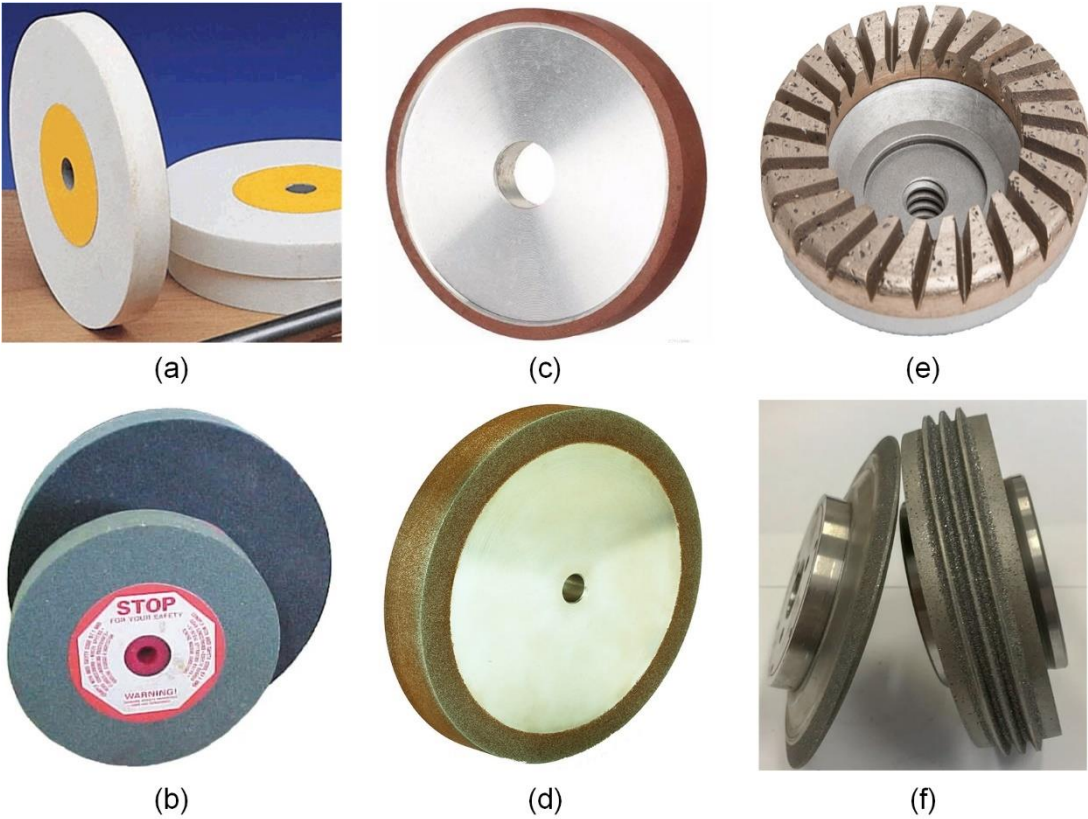


Figure 2.1 Typical abrasive tools. Conventional abrasive tools, including (a) aluminium oxide [25] and (b) silicon carbide [26] abrasive tools. Super-abrasive tools, including (c) diamond [27] and (d) Cubic Boron Nitride (CBN) [28] abrasive tools. Structured abrasive tools, including (e) textured [29] and (f) profiled [30] abrasive tools.

2.1.1 Conventional Abrasive Tools

Conventional abrasive tools are widely used in our daily lives, with no uniqueness in both abrasive materials and structures. Typically, these abrasive tools contain either aluminium oxide (see **Figure 2.2a**) or silicon carbide (see **Figure 2.2b**) abrasives with vitrified or resinoid bonds[31]. Some natural abrasives such as sandstone, flint, iron oxide, emery, and garnet are examples that are rarely utilised in grinding wheels.

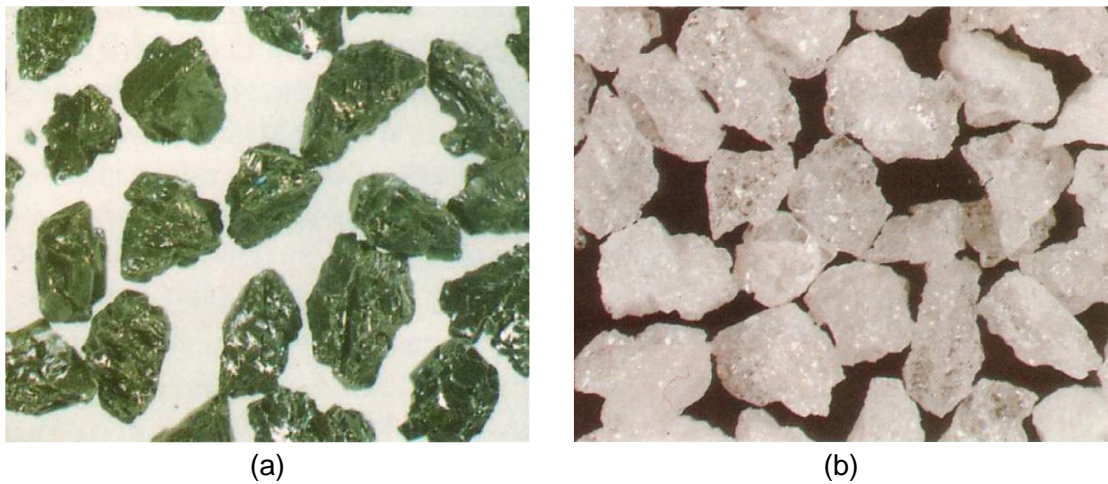


Figure 2.2 Conventional abrasives [31]. (a) Green silicon carbide and (b) white aluminium oxide.

Aluminium oxide (or corundum) is utilised in various ferrous materials, including steel. This category includes well-known abrasives such as white alumina, pink or ruby alumina, zirconia alumina, and brown alumina. In recent decades, significant progress has been achieved for aluminium oxide abrasives with the development of chemical precipitation and sintering processes. Webster and Tricard [32] report that when crystallite size decreases, grinding forces decrease. The crystallite size of the grains is around $0.2\ \mu\text{m}$. The high porosity wheels have a substantially better retention

strength than conventionally shaped grains [33]. Wheels with high wheel speeds and removal rates have been produced thanks to the novel constructions [34].

Silicon carbide, including green and black silicon carbides, is the hardest conventional abrasive. However, it shows a higher wear rate when grinding metals with an affinity for carbon (such as iron and nickel steels) than aluminium oxide due to its lower impact resistance. As a result, it is mostly utilised for non-ferrous materials. Green silicon carbide is a purer form of silicon carbide than black silicon carbide. Green silicon carbide is a great abrasive since it is sharp and friable. It is the hardest of the standard abrasives, and it is used to grind less ductile, lower-tensile-strength materials like carbides and ceramics. Black silicon carbide is somewhat less hard than white silicon carbide and is utilised for abrasive workpiece materials like ceramics and ductile nonferrous metals. It is also used for irons that have a more significant carbon content, namely grey cast iron.

The standard marking system used in North America for conventional abrasive tools containing aluminium oxide and silicon carbide abrasive is presented in **Figure 2.3**. The same or comparable systems may be found all around the world. The following parameters are defined in the wheel specification for designating ordinary grinding wheels in standard marking methods: (i) the type of abrasive in the wheel; (ii) the abrasive grain size; (iii) the wheel's hardness; (iv) the wheel's structure; (v) the bond type and (vi) any other maker's identification codes.

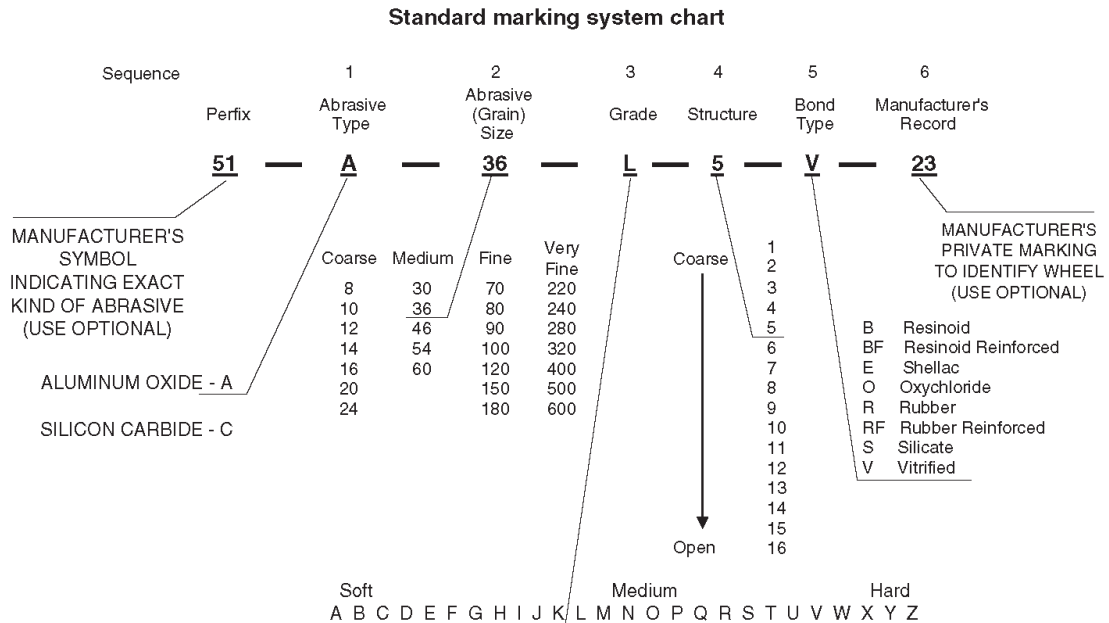


Figure 2.3 Standard marking system for aluminium oxide and silicon carbide wheels [35].

The letter A or C denotes whether the abrasive substance is aluminium oxide or silicon carbide. To the left of the abrasive letter, a manufacturer's prefix (a letter or number) appears typically to denote the kind of alumina or silicon carbide used. The letter after the grit number denotes the wheel grade or hardness. The structural number on the wheel marking represents the volumetric concentration of abrasive grain in the wheel, with a higher number suggesting a less abrasive or more open-wheel. The bond material is denoted by a letter, which an additional notation may follow to indicate a specific formulation.

2.1.2 Superhard Abrasive Tools

Tools containing diamond (see **Figure 2.4a**) or cubic boron nitride (CBN) (see **Figure 2.4b**) abrasives are usually termed superhard abrasive tools, as they are much harder than conventional abrasive tools. Although much more expensive than conventional abrasive tools, superhard abrasive tools are

economical in many cases. For example, in the cases that the process is only possible by using superhard abrasive tools or the overall cycle time is reduced with the increased service life.

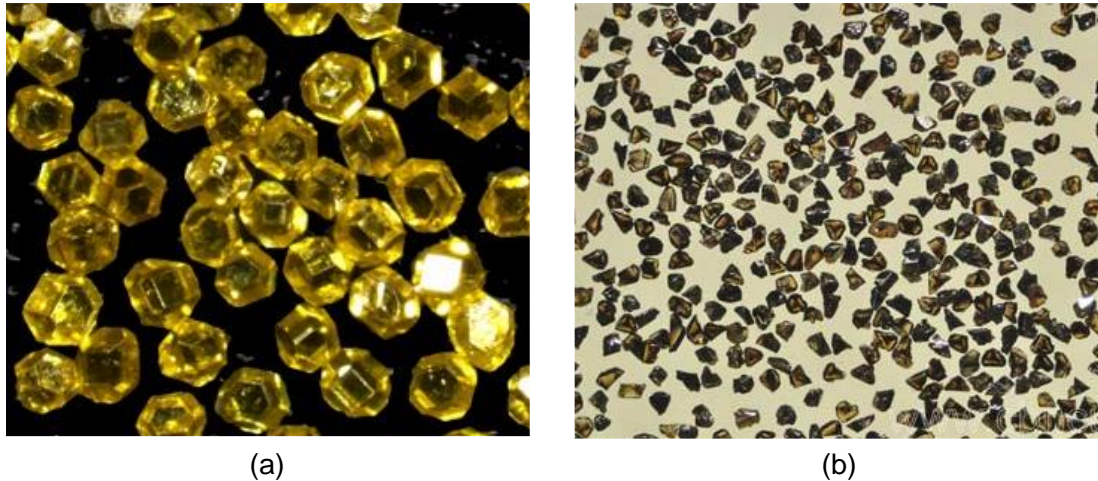


Figure 2.4 Superhard abrasives. (a) Synthetic diamond [36] and (b) CBN [37].

Diamond is the hardest known material that makes it possible to be used to deal with hard-brittle materials, even the hardest ceramics. Meanwhile, the diamond abrasive tools have various thermal advantages (e.g., high thermal stability and conductivity), making them high retention ability for hardness at high temperatures. Typically, the thermally stable of the diamond is up to 760 °C in the air before oxidising and is over 1,400 °C in a vacuum. However, the diamond abrasive tools are not suitable for grinding low-carbon iron and steel. As a form of carbon, the solubility of carbon in these materials makes the abrasive tool rapid wear. Besides, the potential chemical-thermal degradation also makes it unsuitable for nickel-based alloys [38].

CBN is the second hardest material (only second to diamond), widely used for machining steels. CBN tools also have superior ability for thermal stability. As the CBN forms a stable passivation layer of boron oxide that can be prevented

further oxidation up to 1,300 °C in air. In an inert atmosphere, CBN is thermally stable up to 1,500 °C. However, since this layer dissolves in water, CBN wears faster in water-based fluids than in pure oil fluids. Meanwhile, due to chemical-thermal degradation, CBN abrasive tools are not suitable for grinding aerospace titanium alloys. The hardness of CBN decreases quite quickly at high temperatures due to its transformation to a hexagonal structure. Despite the disadvantages, the hardness keeps higher than that of regular abrasives even at relatively high temperatures. In addition, the sharp nature of grain protrusions offers advantages for cool grinding and high removal rates. As a result of its low rate of wear and ability to retain close size tolerance on the products produced, CBN is rapidly replacing traditional abrasives for precision grinding of hardened steels.

The specification system for superhard abrasive tools is somewhat different from conventional ones (see **Figure 2.5**) [35]. A symbol designating a specific abrasive material is usually preceded by the letter denoting the abrasive type like the diamond (D) or cubic boron nitride (B). The bond material, such as the resin (B), vitrified (V) or metal (M), is also indicated by a letter, often followed by an additional manufacturer's notation to identify a particular formulation. Due to the high cost of abrasive grain, only a tiny portion of the active area of the wheel surface is made up of bonded abrasive that is connected to a metal or plastic hub. Therefore, the depth of the abrasive portion is shown in the wheel markings. As with conventional abrasives, the letter grade in the tool marking provides a relative indicator of the strength or hardness of the bond. The concentration number follows after the grade and reflects the quantity of

abrasive in the wheel.

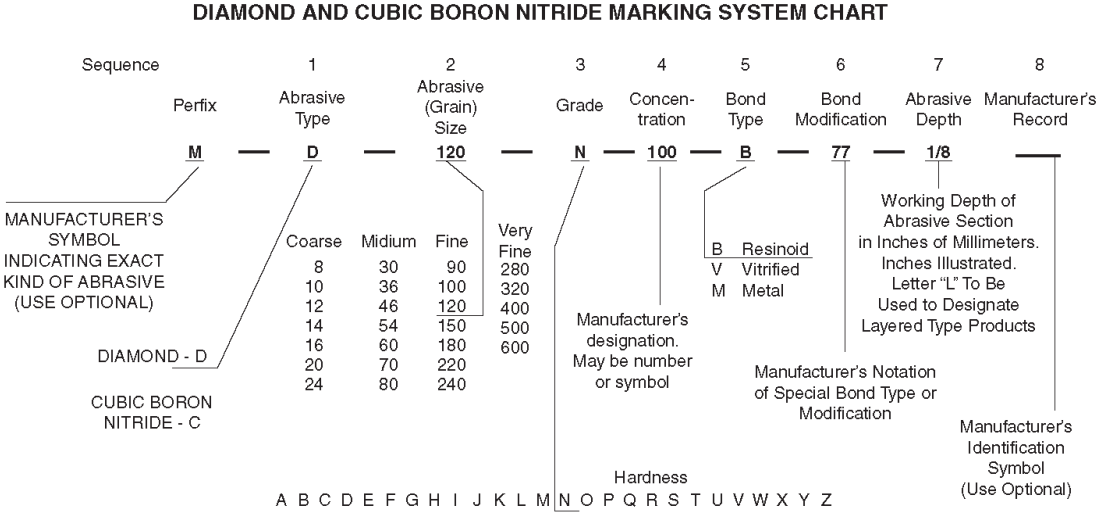


Figure 2.5 Standard marking system for diamond and cubic boron nitride grinding wheels and other bonded abrasives [35].

2.1.3 Structured Abrasive Tools

1) Textured Abrasive Tools (TATs)

Textured Abrasive Tools (TATs), where the abrasives within a specific area on the tool surface are artificially removed, have both specially-designed active and passive grinding areas on their geometrically active surfaces [17]. Hence, the abrasive tools discontinuously contact the workpiece surface, facilitating grinding conditions, such as coolant transportation, heat dissipation, and lower grinding force. Therefore, since the first Textured Grinding Wheel (TGW) was proposed in the 1920s [39], it immediately attracted the attentions of researchers and various structured abrasive tools have been proposed, as shown in **Figure 2.6**.

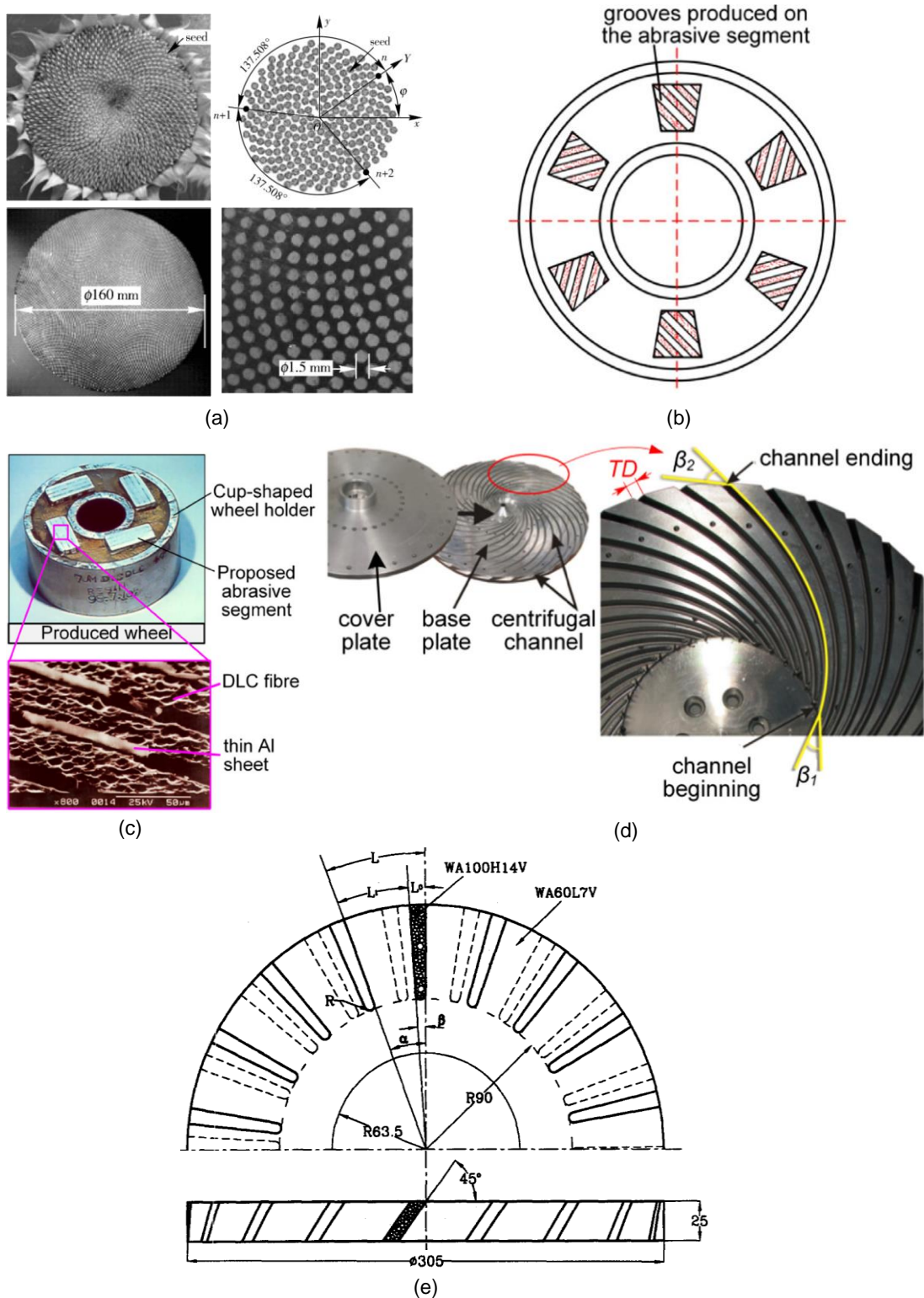


Figure 2.6 Structures on pad abrasive tools. (a) Phyllotactic pattern [40]; (b) tilt slot pattern [41]; (c) straight slot pattern [42]; (d) centrifugal channel pattern [43]; (e) cone slot pattern [44].

First and foremost, Malshe et al. [45] proposed bio-inspired functional surfaces

for advanced applications. Lv et al. [40] investigated a polishing pad with a phyllotactic pattern (see **Figure 2.6a**) based on the phyllotaxis theory, finding the surface roughness and flatness profile of polished wafer can be improved when the diameter D of tin alloy block and the phyllotactic coefficient is appropriately selected. Yamaguchi et al. [41] proposed to add grooves on abrasive segment surfaces (see **Figure 2.6b**) to facilitate chip removal. Similarly, Yamaguchi et al. [42] proposed a segmented GW with abrasive segments made of diamond-like carbons (DLCs), thin aluminium sheets and binders (see **Figure 2.6c**), and the nanometre surface finish with the roughness value of Ra 2.5 nm was achieved. Aurich et al. [43] created internal channels in the base plate of the wheel (see **Figure 2.6d**), accelerating the coolants to a higher speed and pressure at the exits than the previous. Kim et al. [44] studied the slots structures (see **Figure 2.6e**) on the grinding pad, finding that with the increase of intermittent ratio λ , the workpiece surface roughness and wheel wear were significantly increased when using TGWs with the λ values larger than 50%.

Regarding the research on flat abrasive tools, Pacella et al. [46] developed non-abrasive and binderless grinding tools with defined cutting edges (see **Figure 2.7a**). Similarly, Butler-Smith et al. [23] designed the precision diamond micro-arrays (see **Figure 2.7b**), with each abrasive element in the arrays having a specific cutting shape, experimentally showed a 3.5 times improvement to surface finish and a 21.5 times improvement to the flatness of the workpieces when ground with the proposed innovative diamond micro-arrays.

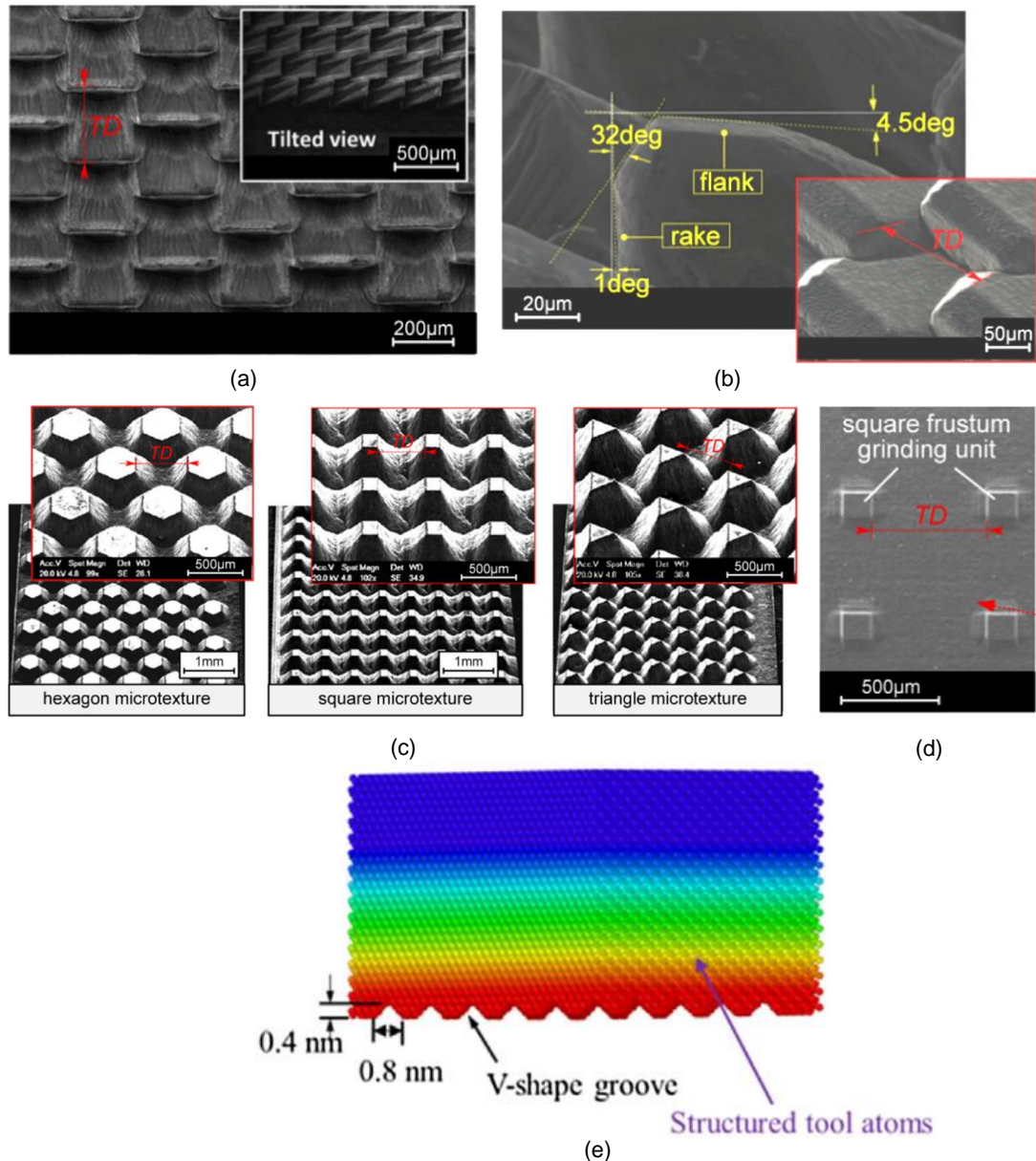


Figure 2.7 Structures on flat abrasive tools. (a) Wedge angle pattern [46]; (b) cutting edge pattern [23]; (c) hexagon, square and triangle pattern [47]; (d) square frustum pattern [48]; (e) V-shape groove pattern [49].

Butler-Smith et al. [47] generated hexagon, square, and triangle patterns (see **Figure 2.7c**) on the thick-film chemical vapour deposition (CVD) diamond. Zhou et al. [48] used the same methods to investigate the grinding pad with square frustums and saw tooth grinding units (see **Figure 2.7d**). Finally, Dai et al. [49] investigated the subsurface damage mechanism through the

theoretical method, finding that the friction coefficient for a tool with V-shape grooves (see **Figure 2.7e**) is smaller than those for non-structured tools and other structured nanoscale tools, and the tool with V-shapes groove can reduce the resistance to cutting during the nanoscale machining process.

Regarding the research on abrasive wheel tools, Zhang and Fu [50] textured straight slots (see **Figure 2.8a**) on the Ni-Cr alloy bond matrix wheels, performing high-speed grinding of ceramics. Islam et al. [51] used a grinding wheel with a single helical groove shape (see **Figure 2.8b**) on its circumference to lower the grinding force. Walter et al. [52] generated zigzag slots and parallelogram patterns (see **Figure 2.8c**) by employing ultrashort picosecond pulsed lasers, evidentially showing that the structured tools generally reduce ground forces by up to 54%. Aurich and Kirsch [53] produced slots with inclination inside the grinding wheels (see **Figure 2.8d**) by milling to improve the cooling efficiency and reduce the tool wear. Rabiey [54] made blind holes (the depth of 5 mm and the spot diameter of 500 μm , see **Figure 2.8e**) by Nd: YAG laser on the wheel surface to reduce the contact layer. Finally, Aurich et al. [55] improved process stability, minimised heat generation and achieved a high surface quality while preserving a high material removal rate by electroplating protrude grains with defined location requirements (see **Figure 2.8f**).

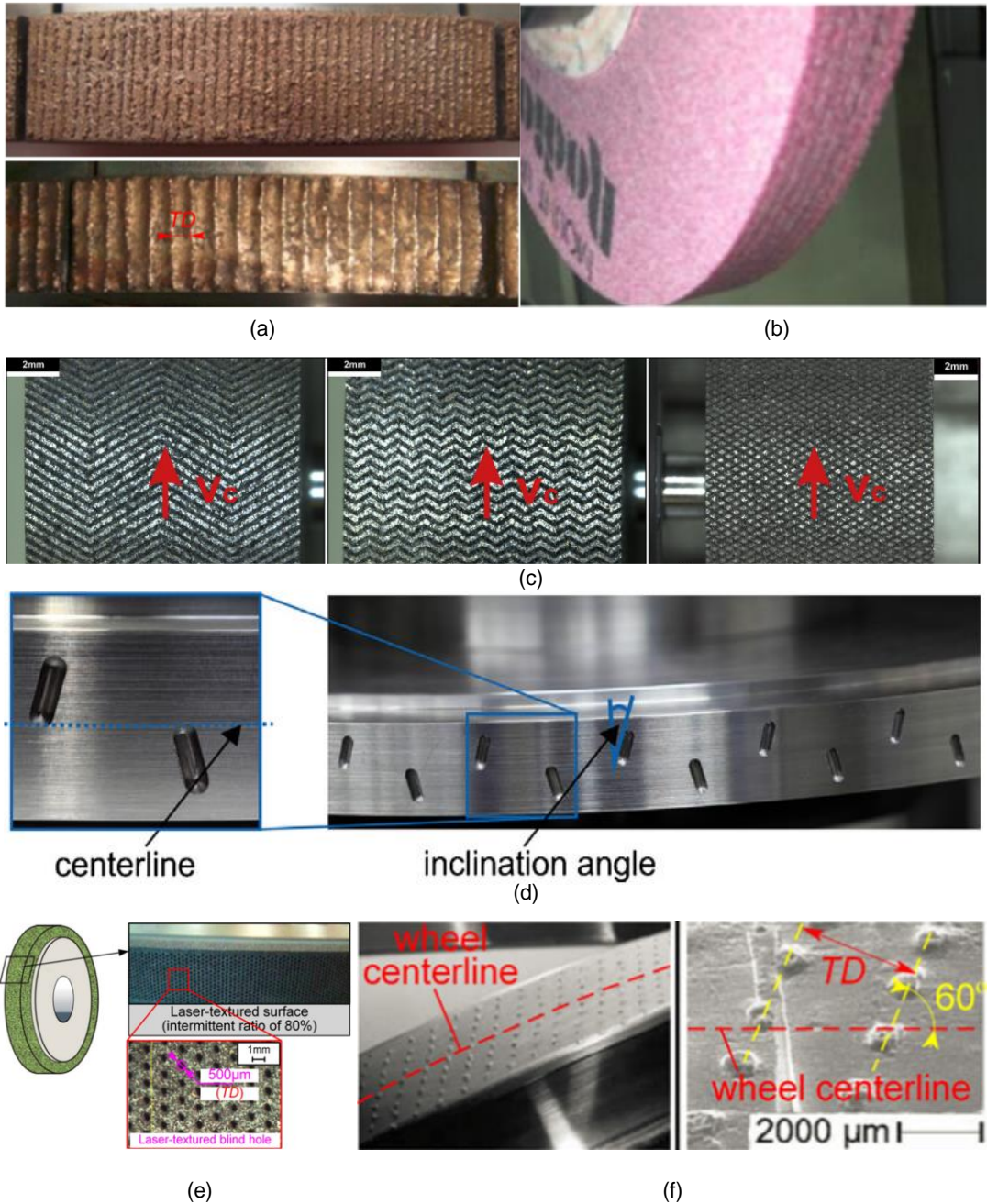


Figure 2.8 Structures on abrasive wheel tools. (a) Straight slots; (b) helical slots; (c) zigzag slots and parallelogram patterns; (d) milled slots; (e) blind micro-hole; (f) protruding grains with defined requirement.

From the review mentioned above, the existing structures have been explored, including slots, blind holes, and micro-arrayed patterns, evidentially showed that the specially designed structured grinding wheels did have functions, like lower grinding force and temperature, enhanced coolant transport, and chip-

holding capacity. However, these structures are uniform arranged depth, meaning that the depth is the same along one direction (see **Figure 2.9**), which will highly restrain the potential complex design of the structures.

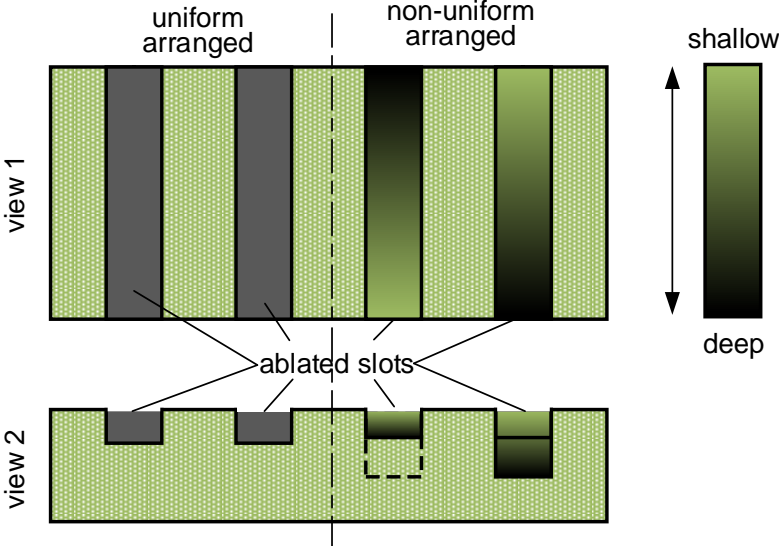


Figure 2.9 The definition of uniform and non-uniform arranged ablation slots

Meanwhile, Li and Axinte predicted in a review that reducing texture dimensions might also be a possible way to improve further the grinding performances, which has been the research trend and still seems to continue [56]. However, the functions in small scale structures have kept being explored, indicating that the controllable precise micro-fabrication techniques are highly expected to be developed.

2) Profiled Abrasive Tools

Profiled abrasive tools (see **Figure 2.10**) that the generatrix of the tools has the same profile as the workpieces'; they can be directly used for the finishing process of the hard-to-machine material with high efficiency and precision [57]. Previously, non-flat grinding wheels have been studied for use in various scenarios (e.g. ultra-high-strength gears [58, 59], screw tools [60, 61], aero-

space engine blade tenons [57, 62], optical components [63-66], and other machine components, like dry vacuum pump rotor [67] and the groove of the ball bearing's inner ring [68]) and significant progress has been achieved.



Figure 2.10 Applications of profiled abrasive tools [57].

For the manufacturing of high-performance gears, form grinding has remained one of the most important finishing methods. By changing the gear setting errors, Fang et al. [58] proposed an error compensation method to improve the form grinding accuracy for gears (see **Figure 2.11a**). By creating modification forms based on a predesigned adjustable fourth-order Transmission Error (TE) function and error sensitivity evaluation, Li et al. [69] developed a function-oriented form-grinding approach to produce outstanding and stable contact performance of cylindrical gears (see **Figure 2.11b**). Jin et al. [70] developed a comprehensive thermal model to analyse the heat transfer mechanism in the grinding of involute gears (see **Figure 2.11c**). Yi et al. [71-73] studied the temperature field distribution, grinding force, heat flux, and residual stress in gear form-grinding by theoretical calculation and experiments. It demonstrated

that the calculated temperature distribution along the tooth profile has a rather good agreement with the measured result (see **Figure 2.11d**).

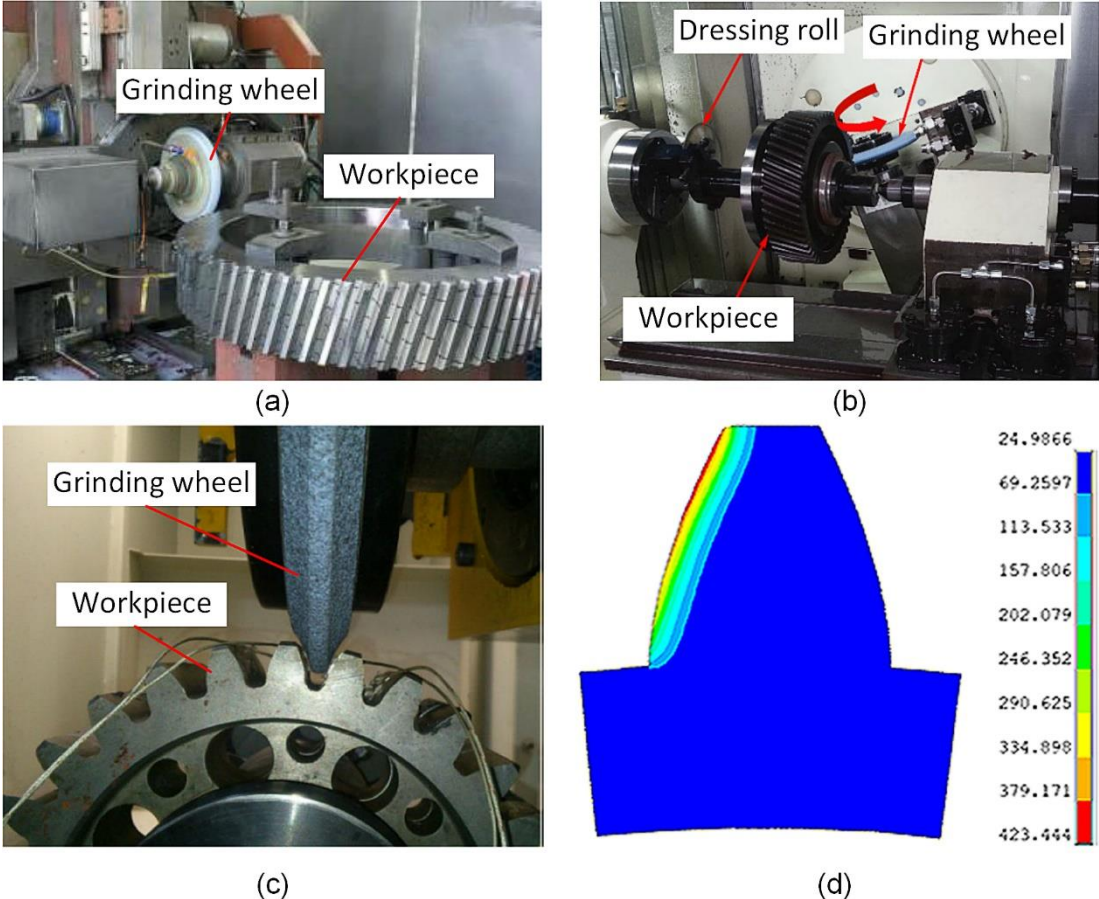


Figure 2.11 Form grinding of gear. (a) Error compensation method to improve the form grinding accuracy [58], (b) function-oriented form-grinding approach to producing outstanding cylindrical gears [69], (c) heat conduction mechanism analyses in grinding of involute gears [70], and (d) simulation study of temperature field distribution in gear form-grinding [71].

To optimize the gear grinding process parameters and prevent tooth surface burn, Su et al. [74] studied the temperature field of the grinding zone by using both the theoretical calculation and finite element software and verified the validity and feasibility of the model by metallographic analysis. By using self-developed, new micro-crystal corundum grinding wheels, Wang et al. [75] conducted experimental and theoretical work studied the form grinding

processes of 20CrMnTi steel involute gears tooth surfaces, providing an essential reference for the prediction of grinding temperature and minimising tooth burning through on-line monitoring of the tangential grinding forces.

For the free-form profile manufacturing, Li et al. [76] employed electroplated cubic boron nitride (CBN) profiled grinding wheels, carrying out profile grinding experiments on FGH96 turbine disk slots, high precision slot error with ± 0.012 mm and low surface roughness of $0.8 \mu\text{m}$ are obtained (see **Figure 2.12a**). To enhance the wheel shape retention, suppress thermal damage, and increase the material removal rate, Zhao et al. [77] investigated the directional solidified nickel-based superalloy DZ125 with an electroplated CBN wheel that the high shape accuracy and good surface integrity were achieved. Meanwhile, the specific material removal rate improved to $50 \text{ mm}^3/\text{mm}$ with only a tiny change in the grinding temperature detected in the grinding zone between different places along with the profile when utilising a profile-adapted needle nozzle (see **Figure 2.12b**). Wang et al. [64] studied the ultra-precision grinding of the non-rotational asymmetric biconical free-form optics with a raster grinding route using a unique feeding-compensation truing approach. As a result, two types of grinding wheels with high profile accuracy and desired surface topography were successfully trued: a larger monocrystalline silicon biconical free-form optics with profile accuracy of $6.0 \mu\text{m}$ and nanometre surface roughness was successfully manufactured (see **Figure 2.12c**). Liao et al. [78] proposed a 2D wheel-profile errors model to directly compensate for 3D curved wheel errors in automatic grinding, which avoided any on-machine measurement and improved freeform grinding accuracy and efficiency (see

Figure 2.12d).

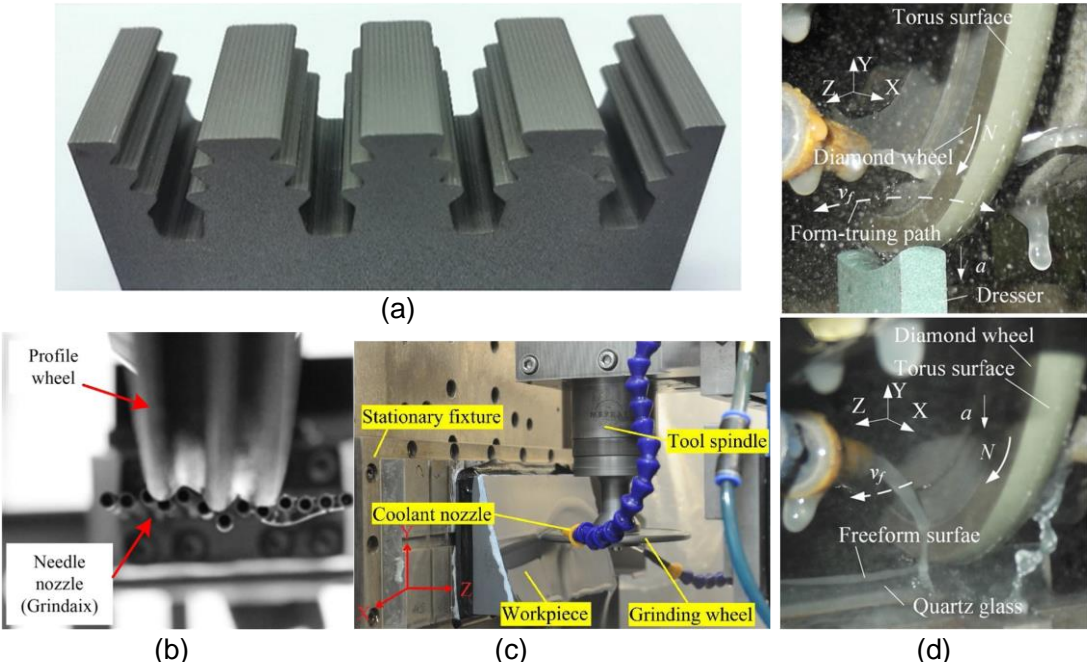


Figure 2.12 Grinding of free form profile. (a) Turbine disk slots [76], (b) profile-adapted needle nozzle for good grinding performance [77], (c) ultra-precision grinding of the biconical free-form optics [64], and (d) errors compensation to directly used for 3D curved wheel [78].

Zhang et al. [79] investigated the wear detection of the wheel, which provides the basis for the precision NC curve point grinding strategy. Wang et al. [65] studied the envelope grinding of micro-cylinder array lenses using a near arc-profile wheel without on-machine precision truing. Starkov et al. [80] comparatively analysed the performance of Cubic Boron Nitride (CBN) and Microcrystalline alumina tools in profile grinding of form cutter under production conditions, finding the vitrified cubic boron nitride wheel has demonstrated an essentially better performance in terms of removal rate, the minimum time for dressing cycles, and overall labour input in shaping a working profile of the broach. Miao et al. [62] used microcrystalline alumina abrasive wheels to investigate the grinding force and surface quality in creep feed profile grinding

of turbine blade roots of nickel-based superalloys, which provided industry guidance to optimize the machining process for the high-valued parts with complex profiles. Xie et al. explored the strategies to improve the accuracy of the freeform surfaces from the aspect of form-truing error compensation [81], dispersing grinding wheel profiles [82], and adjusting tool posture angle without on-machine wheel-profile truing [83]. Some researchers manage to improve the surface accuracy by path planning method, e.g., for error region grinding of aero-engine blades with the free-form surface [84] and Elastic-contact-based tool-path planning for the free-form surface in belt grinding [85].

In addition to the applications mentioned above, Bogutsky et al. [86] calculated the intermittent grinding wheel's profile for the broach's sharpening teeth. Chen et al. [63] investigated the influence of curvature on surface topography and uniform scallop height management in normal grinding of optically curved surfaces while taking wheel vibration into consideration. Ichida [87] used creep-feed grinding to produce V-shaped grooves on a flat surface in one pass to study the performance of ultrafine-crystalline CBN abrasive wheels, it showed a 5%-15% drop in grinding force and four times increase in grinding ratio, and high dimensional accuracy and better form retention are achieved when compared to conventional ones. Liu et al. [88] proposed a unique optimisation design approach for form grinding wheels for screw rotors, and the effectiveness of the way is proved by the evidence that it made the screw profile significantly improved compared with the empirical method.

2.2 Introduction to Dressing Strategies on Abrasive Tools

The dressing is the process of shaping the grinding wheel with a dressing tool

or removing the dull surface layer to restore the grinding performance and correct geometry of the working surface. The timely and correct dressing of the grinding wheel is an indispensable part of improving grinding efficiency and ensuring grinding quality. Based on the basic material removal principles, most of the previous TATs fabrication methods can be mainly divided into three groups: (i) mechanical, (ii) chemical, and (iii) thermal methods.

2.2.1 Dressing by Mechanical Methods

By introducing geometrical interference between standard diamond wheel surfaces and texturing tools (e.g., milling cutters, rollers), mechanical methods removed both diamond abrasives and bond agents to create textures by consuming the mechanical energy of either texturing tools and/or rotating diamond wheels. Due to low cost, the most widely studied ways were based on single-diamond grinding wheel dressing tools. By translationally moving the single-point diamond dressing tool (see **Figure 2.13a**), Mohamed et al. [89] successfully generated the spiral-shaped grooves on the wheel surface, based on which both the improved achievable depth of cut up to 120% and reduced power of 64% was found in the comparison of conventional wheels. Mohamed et al. [90] further upgraded this system by synchronising the grinding wheel angular position with the dressing tool translational work, enabling the diamond dressing tip repeatedly engage the grinding wheel at the same angular position. Similarly, Oliveira et al. [91] introduced a controlled external excitation in the grinding wheel dressing tool (see **Figure 2.13b**) to dynamically change the dressing depth during the dressing operation, allowing micro-patterning inscriptions on the wheel surface. Silva et al. [92] further improved the hardware (e.g. the new grinding head with direct drive) installed in the system

to get a more stable angular speed, and the produced textures on the wheel surface were expected to be promising as the lubrication pocket. Denkena et al. [93] proposed the fly-cutting technique (see **Figure 2.13c**) to texture grinding wheels to overcome the issues of the single-diamond methods, including the limited achievable patterns due to the continuous tool-wheel contact and the cost- and time-intensive feature of the texturing process. The grinding force was reduced by up to 30%, and the coolant flow rate increased by up to 25% was measured in the experiments for the wheels produced by the proposed texturing method. Tawakoli and Daneshi [94] proposed a “T-Dress” approach to dressing and structuring grinding wheels, making the wheel almost no difference in the ground surface roughness values compared to the case of dressing with conventional profile rollers.

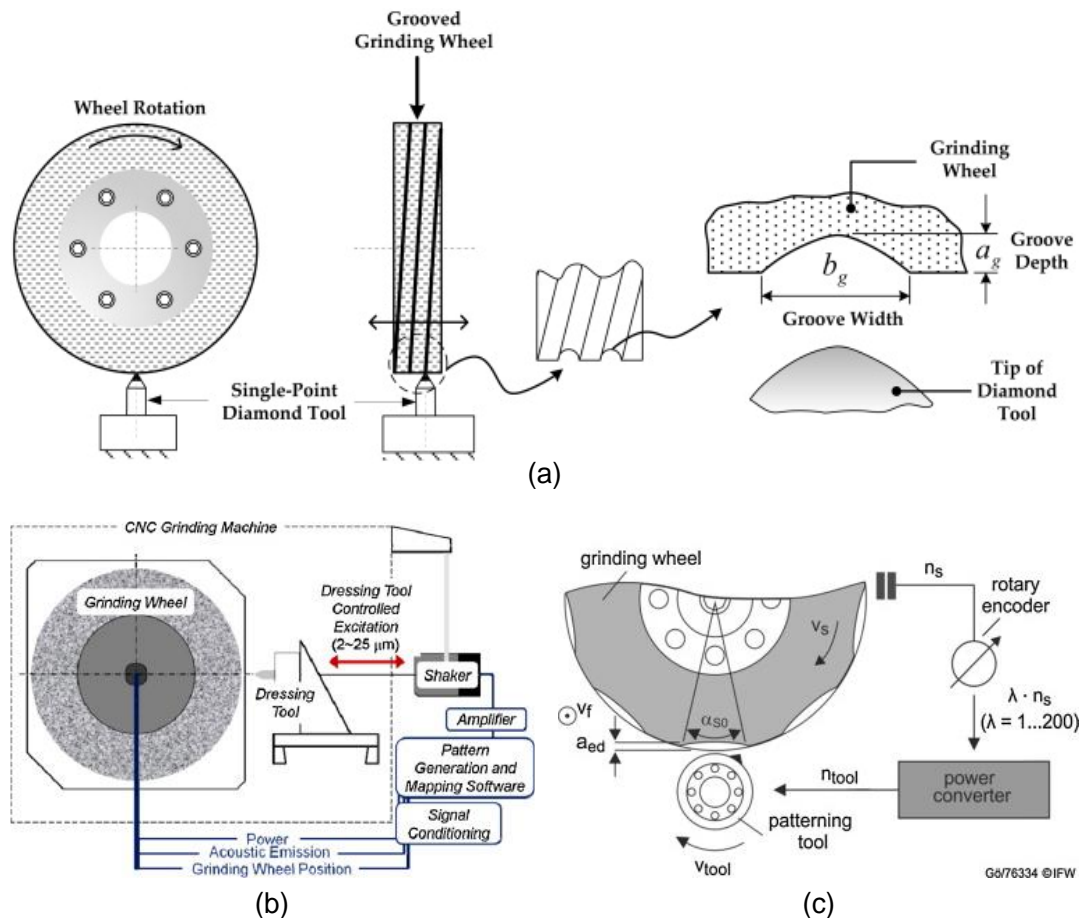


Figure 2.13 Dressing by mechanical method. (a) Single point tool [89], (b) dressing

tool controlled excitation [91], and (c) fly-cutting [93].

Unlike any studies above based on the single cutting edge, the milling process relying on multiple cutting edges was used to produce structures on the wheel surface as well, where both the CFD simulation [95] and the analytical model [53] proved the coolant transportation ability of the produced wheel was increased at least five times in comparison with conventional wheels. However, substantial drawbacks have been considered as the key barriers to mechanical methods, including intensive texturing tool wear [96], significant chatter induced by the fluctuation of texturing forces [97], and unsatisfied machinability to achieve either micro-scaled textures (limited by tool size) or complex texture geometries (constrained by complicated tool path generation and multi-axis controllability) [3].

2.2.2 Dressing by Electrochemical Methods

Unlike mechanical methods based on material removal, electrochemical methods, on the contrary, create structured abrasive tool surfaces by adding materials (including both abrasives and sometimes bond agents) in a controllable way and can mainly include (i) electroplating (see **Figure 2.14 a, b&c**) and (ii) brazing (see **Figure 2.14 d&e**) methods. In the abrasive electroplating process, the wheel body was firstly placed in a tank where the diamond grits were tacked to the exposed surface, and then nickel was electroplated to strengthen the hold of the diamond abrasive to the body by hydrolysis. Aurich et al. [98] applied the masking technology for the preliminary adhesion of the grains on the wheel hub so that the uniformly-distributed grain pattern was achieved. The better performances of the produced wheels,

including lower grinding force and power of up to 40%, were obtained in both wet and dry grinding trials in comparison with conventional abrasive tools. The interesting study here can be bio-inspired electroplating grinding tools generated by Iyu et al. [99] and Yu et al. [100], where the phyllotactic pattern of the abrasives was allocated on the abrasive tool surfaces by using light-sensitive PVC together with UV exposure technology. Although the additional electroplating process to thicken the coating layer was emphasized in most previous studies, the failures, including whole abrasive dislodgement, grain fracture, and attrition, were still widely reported due to the weak grain-holding ability of the electroplated textured wheels [101].

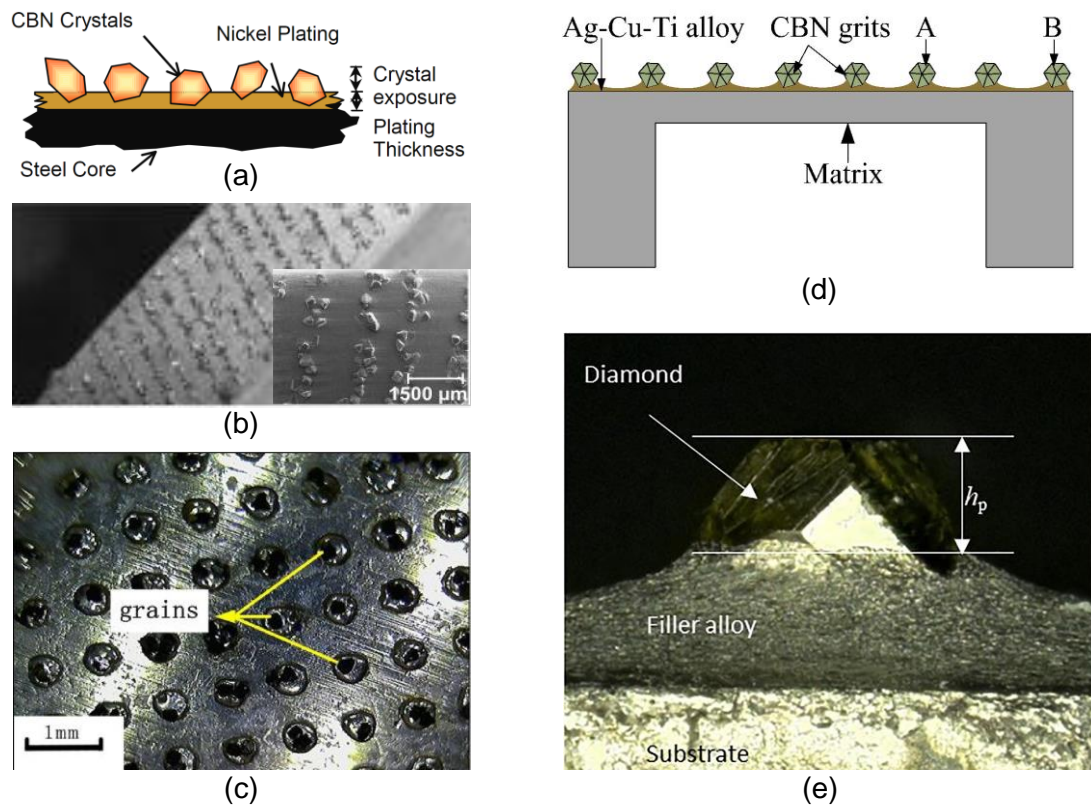


Figure 2.14 Dressing by electrochemical method. (a) Schematic diagram [101], (b) and (c) microscopes of electroplating method [98, 100]; (d) Schematic diagram [102] and (e) digital microscope [103] of brazing method.

Brazing methods can be considered an alternative to overcome this issue,

during which grinding wheel hubs and abrasives can be joined together by melting a filler metal as the junction. Both Chattopadhyay et al. [104] and Chen et al. [105] performed wide and deep research where the Ni-Cr alloy was employed as the filler due to its high strength and resistance to heat, wear, and corrosion. Ding et al. [106] and Chen et al. [102] found the mismatch of the thermal expansion between abrasives, filler alloys, and the substrate can result in substantial residual stress, and therefore both the Cu-Sn-Ti and the Ag-Cu-Ti filler systems were separately employed to achieve a lower filler melting point. To release residual stress after brazing, Huang et al. [103] introduced ultrasonic vibration into the diamond brazing process and successfully obtained the textured grinding wheel with a high bonding strength between filler alloy and diamond grits and the high bonding strength between filler alloy and diamond grits grain protrusion and therefore large chip storage were achieved. However, the inevitable issues, containing poor time efficiency and process controllability, huge environmental hazards thanks to the various chemical reagents, and complex fabrication procedures, should be properly solved to make this method more applicable and feasible [3].

2.2.3 Dressing by Energy Beam Methods

Parallel to mechanical and chemical methods, energy beam mainly refers to waterjet (see **Figure 2.15a**) and thermal (see **Figure 2.15b**) methods. By employing a high-pressure water beam, the waterjet violently impacts the workpiece surfaces to force the target materials to break away from the matrix. Thermal methods (mainly laser beam) employed high power laser or plasma/ion to remove or degrade the bond agents and the abrasives by

gasification, oxidation, melt, and decomposition. Both of the dressing strategies have been intensively studied because most of the hard-to-machine materials can be machined by the methods. Since the waterjet method has little thermal effect on the workpiece, it provides a promising way for most thermal-sensitive materials. While laser method has a unique advantage when machining the fine structures on the hard-brittle materials as it has little impact force on the workpiece. Nevertheless, a similar weakness of both methods can be the nonlinear issues for depth-controlled etching, which has been addressed by Bilbao-Guillerna et al. [107].

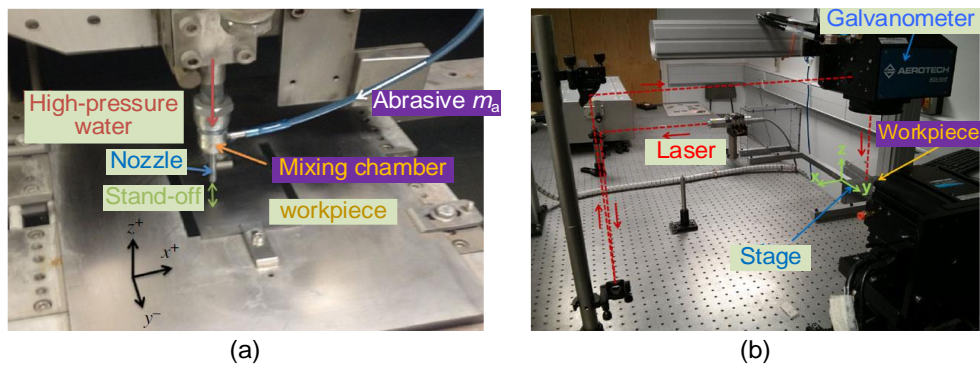


Figure 2.15 Diagrams of two leading energy beam methods [107]. (a) Abrasive waterjet and (b) laser beam.

So far, waterjet technology has been studied to machine various materials, including aluminium alloy [108], Titanium Alloy [109], nickel-based superalloy [110], C/SiC composites [111], carbon fibre reinforced polymers [112], ceramics [113], rocks [114], and even double-layered structure [115]. However, the studies regarding dressing an abrasive wheel are seldom presented. The most relevant studies can be the work of Axinte et al., who use abrasive waterjet turning for profiling and dressing Al_2O_3 type bonded with rubenite™ grinding wheels and successfully generate serial profiled grinding wheels (see **Figure 2.16**) [116]. Another crucial related work can be Morczinek and Putz

[117], who use abrasive waterjet machining metal bonded cubic boron nitride (CBN) with a softer abrasive material.

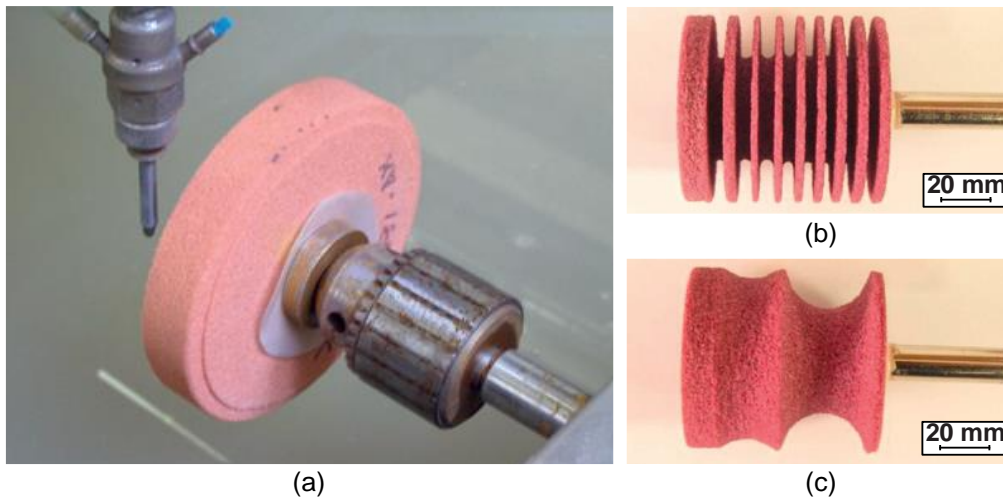


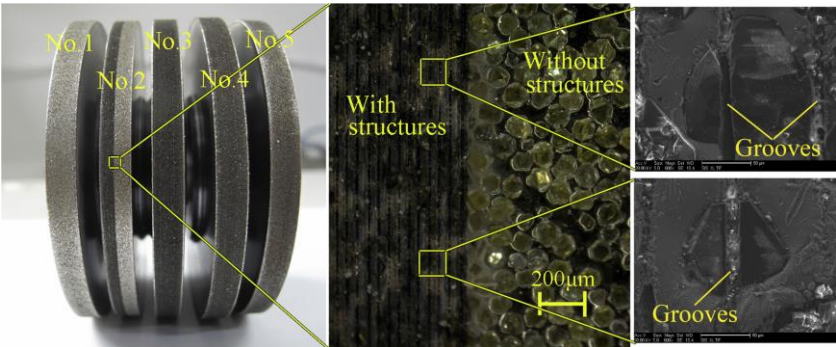
Figure 2.16 (a) Schematic diagram of AWJ turning; (b) grooved and scalloped grinding wheel [116].

Laser stands for Light Amplification by Stimulated Emission of Radiation (LASER) and has numerous distinguishing characteristics such as being monochromatic, coherent and having a very low divergence. Previously, various types of lasers have been employed to investigate the controllable non-uniform matrix ablation. Among the researches, Walter et al. [52] emphasized the unique advantages of thermal methods, including the high possibility to fabricate macro, meso, and micro simple/complex structures in theory on nearly all the materials literally without any tool wear. The structures having the feature size in the order of a few micrometres on the abrasive tool surface were successfully produced using the picosecond pulse laser, and the grinding force was reduced by 25~45% compared to conventional tools. To be specific, Li et al. [118] investigated the ablation law of a continuous laser by employing a continuous CO₂ laser, and based on their derived ablation law, generated complex textures on diamond resin bond grinding wheels, with a minimum of about 800 μm width and 250 μm depth slots. Rabiey [54] made

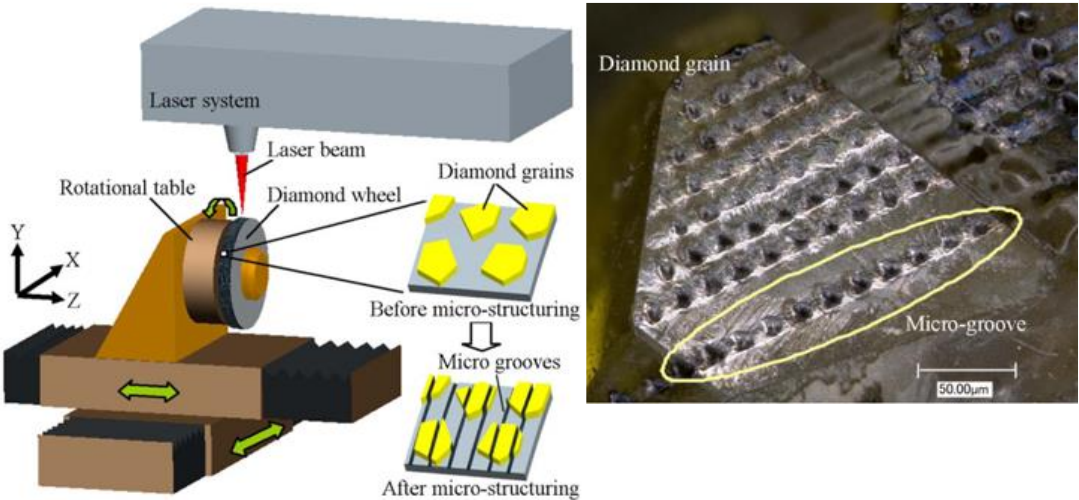
blind holes on a CBN grinding wheel surface using Nd: YAG laser to reduce the contact area between the grinding wheel and the workpiece. It shows roughly 5 mm ablation depth and a 500 μm spot diameter is obtained.

In terms of the work carried out by pulsed lasers, Guo et al. [119] employed a UV nanosecond laser to generate micrometre-scaled textures with various intervals from 30 μm to 150 μm on diamond grinding wheels (see **Figure 2.17a**), finding that the surface roughness and subsurface damage depth were both reduced with the decreasing interval. The falling off of the broken diamond was not widely observed, implying the improved wheel cutting ability due to the increased number of cutting edges. However, a careful selection of process parameters is required; otherwise, the discontinuous textures might be damaged if the pulse parameters (pulse frequency and width) cannot match the laser feed rate (see **Figure 2.17b**) [120]. Beausoleil et al. [7] carried out experiments on alumina ceramics using a picosecond laser, explored the process parameters, such as focal position, linear speed, and wobble amplitude to control the cut depth and optimize cut quality in terms of kerf width, kerf taper, and surface cleanliness while avoiding crack formation, and a maximum material removal rate of 10 mm^3/min was achieved. Walter et al. [8] generated zigzag slots and parallelogram patterns by employing ultrashort picosecond pulsed lasers, a minimum 120 μm slot width and 50 μm slot depth are achieved in their research. Zhang et al. [121] studied the femtosecond laser ablation mechanisms at the molecular dynamics level for the effective processing of film-cooling holes in Ni_3Al -based single crystal superalloy turbine blades. Zhang et al. [122] studied the evolution of micro/nano-structural arrays on crystalline silicon carbide, finding the irradiated surface evolves from a near-damage-free zone to one with a recast layer and thermal-induced micro-

cracks. Cai et al. [123] carried out experiments with a femtosecond laser (where the power employed is at a hundred mW level) and studied the diamond ablation depth changes law with laser power and processing time. Another avenue on thermal texturing of abrasive tools can be a series of studies performed by Butler-Smith et al. [47], where the pulse laser was used to ablate thick-film CVD diamond so that preferential micro grinding arrays in rectangular, triangular, and hexagonal shapes can be generated. A more superior grinding array element with well-designed rake and flake angles was generated, later on, allowing the smooth chip to flow during the grinding process [124].



(a)



(b)

Figure 2.17 (a) Photo of micro-structured wheels and its morphology [119]; (b) experimental setup for micro-structuring grinding wheel and the grain morphology

processed by 300 mm/s laser scanning [120].

It can be seen that little progress regarding controllable material removal has been made by using continuous lasers. By using a pulsed laser, the surface geometrical accuracy and multi-scaled structural integrity can be properly controlled in both time and spatial domains. However, high equipment maintenance costs especially for the pulse laser generators and modulation magnifiers, limited ablation penetration depth, especially for abrasive tools having multi-material nature, and relatively low machining efficiency due to the small average laser power would be the critical bottlenecks of the current laser-based texturing methods. Besides, few articles regarding ablated depth prediction and control have been published. Although some researchers manage to establish prediction models, the model is either only valid for lower laser power with a limited prediction range or established based on a femtosecond laser, for which it is hard to achieve a relatively higher average laser power, limiting its application in texturing structured abrasive wheels with high efficiency and precision.

By comparison, despite the disadvantages in the texturing strategies of the thermal method, it is still considered a promising way to manufacture the structured abrasive tools in general due to the advantages such as high efficiency and low noise and no tool wear happens. However, thermal methods will inevitably produce a Heat-Affected Zone (HAZ), which is quite undesirable in the fabrication process. Besides, the issues related to the heat-affected zone are also one of the major obstacles in the application [125], as the precise measurement of heat-affected zone thickness and the temperature field

distribution within the processes area are not only challenging but also expensive [126]. Therefore, removing material effectively, at low cost, and accurately has remained a problem. Hence, lower HAZ in the thermal method manufacturing process has been critical in generating high-quality structures.

2.3 Introduction to Laser Processing Technology

Laser ablation is typical for most hard materials with various advantages, such as high efficiency, low vibration, and low environmental impact. As such, numerous researchers take advantage of this technique in carrying out the dressing process on grinding wheels containing super-hard abrasives. The general process for laser ablation is by either gasification, melt, oxidation, deterioration, or decomposition to make the target materials separate or removed from the matrix. This technology has been familiar with advantages such as high efficiency, low vibration, environmentally friendly, and no tool wear [7-9]. Therefore, many researchers take advantage of this process and use it to carry out machining work for material removal or cutting [10-12]. Correspondingly, significant progress has been made in machining standard materials, e.g., wood, polymer, metal, and diamond [18-22]. In addition, some prior research on non-uniform matrix ablation includes the dressing process for grinding wheels with super-hard abrasives by laser ablation. However, due to the complex interaction of laser beams with multiple materials, removing materials from the non-uniform matrix in a controllable way has remained an open question. No significant progress has been made on the controllable removal of materials from grinding wheels, which is the key when manufacturing a structured abrasive wheel.

The following review covers the investigation results on laser classification, generation of a laser beam, the interaction of laser beam with target materials and the critical factors that affect laser ablation.

2.3.1 Laser Classification

Although there are a variety of lasers, however, based on the type of medium involved, they can be categorised into four groups (as shown in **Figure 2.18**):

(i) solid, (ii) gas, (iii) liquid, and (iv) semiconductor.

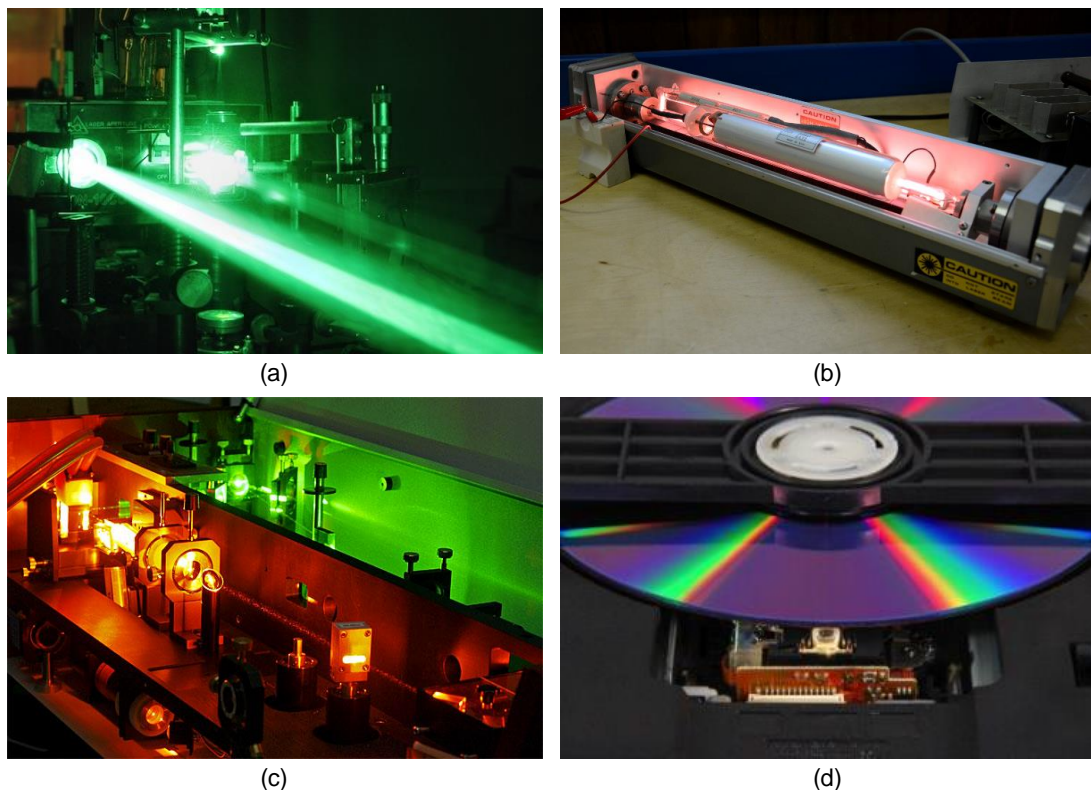


Figure 2.18 Different types of laser. (a) Solid [127], (b) gas [128], (c) liquid [129], and (d) semiconductor [130].

1) Solid-state lasers

These lasers are made of solid material, such as ruby or crystalline and have a flash tube wrapped around them to excite electrons. Solid-state laser media, like semiconductors, must be doped with impurities to generate light of a given

frequency and wavelength. These lasers are generally employed for target destination systems in boring holes in metals or military applications.

2) Gas lasers

These lasers often employ helium or helium-neon as the gain medium and emit distinctive red laser light. In addition, there are also CO₂ lasers that emit infrared radiation. These powerful and efficient lasers are commonly utilized in industrial cutting and welding applications.

3) Liquid dye lasers

These lasers use liquid dyes like rhodamine in a liquid solution as a gain medium by using an arc lamp, a flash lamp, or a similar laser to stimulate electrons. Liquid dye lasers, unlike solid-state or gas lasers, can create a larger spectrum of light frequencies and, as a result, may be used in a variety of applications.

4) Semiconductor lasers

These lasers are inexpensive to manufacture and may be used in various electronic equipment, ranging from laser printers to barcode scanners. Commonly, these lasers are sometimes called diode lasers since they use an LED to create light in a monochromatic pattern.

2.3.2 Laser Beam

Laser is a typical two-step description of atomic excitation (see **Figure 2.19a**): (i) the atom absorbs energy (heat, light, and electricity) and (ii) moves from an orbit with lower energy to a higher one. Naturally, an excited electron relaxes

and releases photonic energy by returning to the ground state (see **Figure 2.19b**). These photons are not yet laser light, and however, when they hit with additional excited atoms, they can create laser light via stimulated emission (see **Figure 2.19c**). The incidence photon triggers the excited atom to emit a photon with equal energy as the original photon and in phase with it. As a result, one stimulated atom and one photon led to one released atom and two photons are produced. Photons are reflected continuously in the laser medium to increase the likelihood of this scenario.

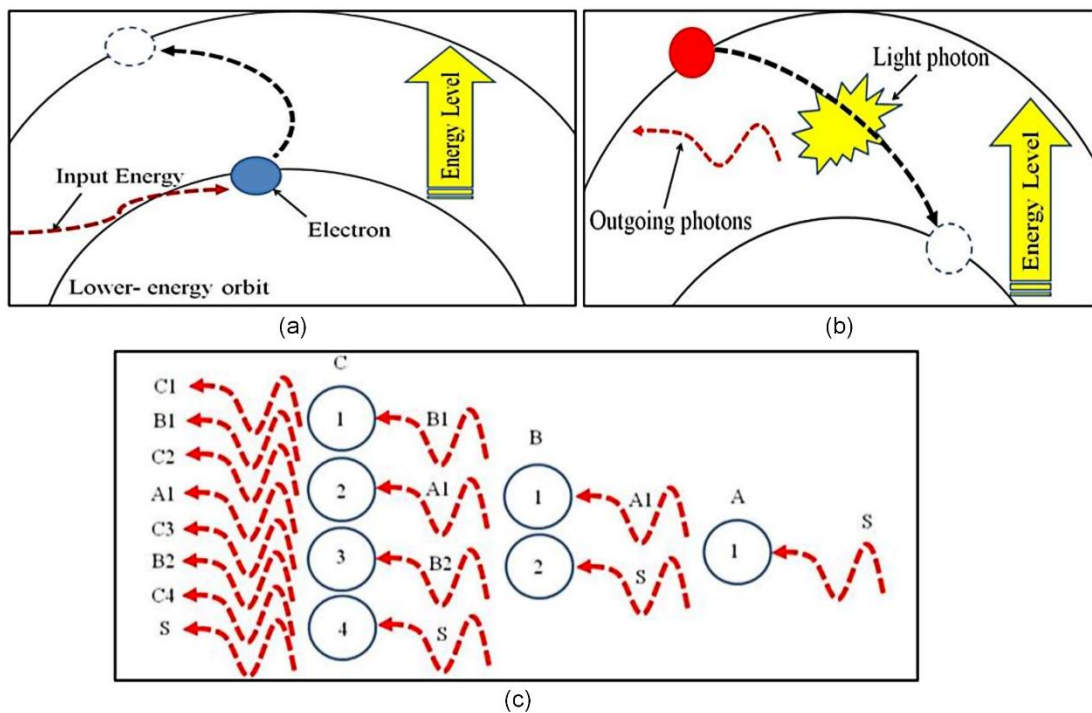


Figure 2.19 Interpretation of the atomic excitation [131]. (a) An electron absorbs input energy and moves from an orbit with lower energy to a higher one; (b) an excited electron decays, it emits a light photon; (c) photons clash with other energised atoms in stimulated emission.

A flash tube excites existing atoms in the medium (see **Figure 2.20a**), making the photons be reflected among two mirrors, and the emission of further photons is promoted, resulting in the formation of the laser beam (see **Figure 2.20b**), which leaves via the partially reflected mirror [132].

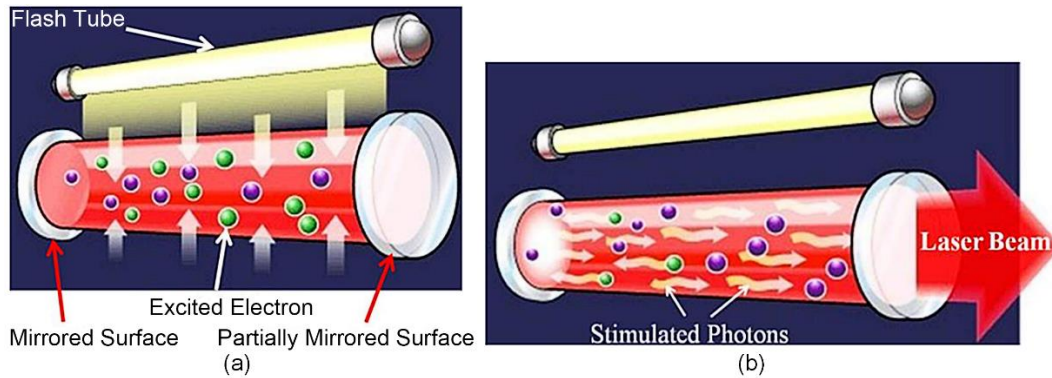


Figure 2.20 Generation of laser beam [132]. (a) The fundamental design of a laser device lies in its excited state; (b) a laser beam is formed when the stimulated photons travel through the mirror.

The typical structure and detailed working mechanism for a laser generator can be explained in **Figure 2.21**. The high-intensity flash lamp will first be switched on and off by an electric current, which will excite the electrons in the ruby crystal. Then, by the mechanism of spontaneous emission, these excited electrons return to their ground state and emit a photon of light. These photons fly across the medium, reflecting off mirrors and causing additional electrons to get excited. The process of stimulated emission causes additional photons to be emitted. As a result, the reflective cylinder soon has more excited electrons than grounded electrons, resulting in a population inversion. Photons bounce back and forth in the crystal medium between the two mirrors. Notably, one is less reflective than the other, allowing some photons to pass through.

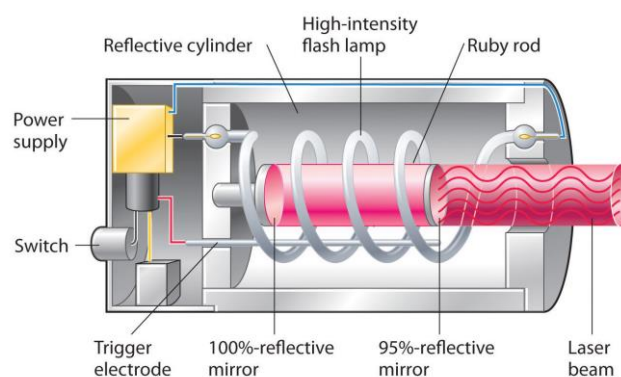


Figure 2.21 A ruby laser in action with a set of simple components [127].

2.3.3 Interaction of Laser Beam with Target Materials

It has been proved that some lasers have trouble cutting or engraving on specific materials, such as metals, glass, and plexiglass. The rationale is that straightforward materials absorb and reflect different wavelengths. As a result, cutting and engraving get easier when more power is absorbed and vice versa.

1) From a macro-level view

When a laser beam collides with the workpiece surface at an incidence angle, a part of the light is reflected back, while the remaining light is refracted and/or absorbed by the material [133]. It has been noted that the Brewster angle is a specific angle of incidence that, around it, the unpolarised beam is completely polarised (perpendicularly) reflected off a partially polarised surface while the absorbed light is partially polarised. **Figure 2.22** depicts an incident laser beam's reflection and absorption schematic representation.

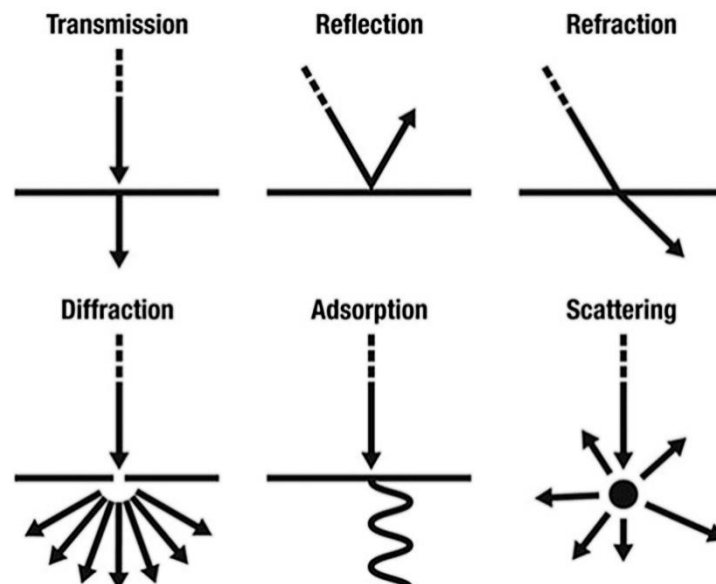


Figure 2.22 Interaction of laser beam with materials in macro-level view [134].

The values of absorption and reflection have a substantial impact on the

process quality in laser applications, such as cutting and welding. According to Mahrle and Beyer [135], the reflection value for a polarised laser beam may be computed using Fresnel formulas in the fibre laser cutting process, as demonstrated by **Equation (2.1)** and **(2.2)**:

$$R_P = \frac{(n \cdot \cos \varphi_{in} - 1)^2 + k \cdot \cos \varphi_{in}^2}{(n \cdot \cos \varphi_{in} + 1)^2 + k \cdot \cos \varphi_{in}^2} \quad (2.1)$$

and

$$R_S = \frac{(n - \cos \varphi_{in})^2 + k^2}{(n + \cos \varphi_{in})^2 + k^2} \quad (2.2)$$

where R_P represents the reflection of parallel polarised laser radiations and R_S represents the reflection of perpendicular polarised laser radiations, φ_{in} is the inclination angle, n represents the refractive index, and k represents the extinction coefficient. The average of R_P and R_S utilised for circularly polarised or unpolarised radiation is demonstrated by **Equation (2.3)** [135]:

$$R_{Ave} = \frac{R_P + R_S}{2} \quad (2.3)$$

The indexes of reflection (n) and absorption (k) fluctuate modestly with temperature, but they are greatly influenced by wavelength. **Table 2.1** shows the indexes of refraction and extinction coefficients of molten iron at various conditions.

Table 2.1 Indexes of refraction and extinction coefficients of iron at various conditions [135]

Temperature (K)	Wavelength = 1.07 μm		Wavelength = 10.6 μm	
	k	n	n	k
1800	5.46	3.96	15.5	15.1
3000	5.14	3.68	14.6	14.1
2400	5.30	3.82	15.0	14.6

Figure 2.23 depicts the predicted absorptivity as a function of incident angle for two different unpolarised CO₂ (10.6 μm) and fibre/disk (1.06 μm) laser beams. The absorptivity reaches its peak at a certain angle of incidence, known as the Brewster angle. With increasing values of the inclination angle after reaching this degree, the absorptivity dramatically decreases. At the Brewster angle, the fibre/disk laser has a maximum absorptivity at 79.6°, while CO₂ has an absorptivity at 87.3°. The absorptivity of both wavelengths is the same in theory at an angle of 85.9°.

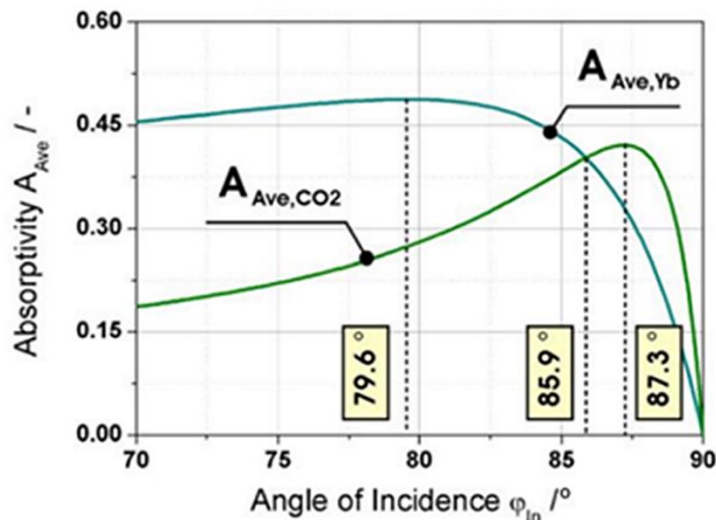


Figure 2.23 Absorption of two different unpolarised beams from CO₂ and solid-state laser light measured as a function of the incident angle from a molten iron surface [135].

Some published work [136-138] uses glancing angle (complementary angle of incidence angle, see details in **Figure 2.24**) as a function for the absorption study, which is similar to that in **Figure 2.23**. Due to higher absorptance in metal at glancing angles, Petring et al. [139] discovered that thick plates profit more from a higher Brewster angle at the 10.6 μm CO₂ wavelength.

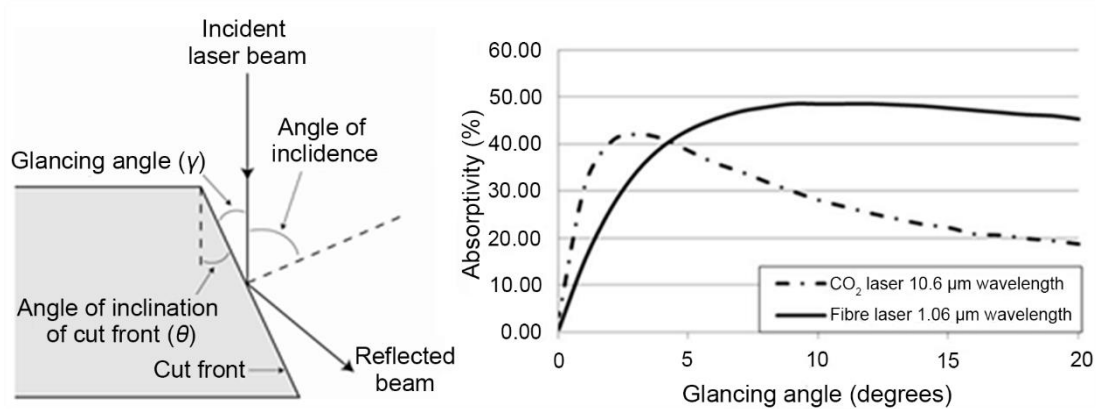


Figure 2.24 Definition of glancing angle (left) and absorptivity as a function of glancing angle (right) [136]

Bergstrom et al. [140] investigated the absorption of Nd: YAG laser light by steels, finding that laser absorption is enhanced by surface conditions, such as oxides, contamination, roughness, and the presence of alloying elements. For example, when the surface roughness values were greater than 1.5 μm , a tendency of increased absorptance was seen in stainless steel samples, while there is no evident roughness-absorptance correlation for mild steel below the roughness value of 6 μm .

When utilising fibre/disk lasers for operations like welding, drilling, or cutting, Kaplan [137] discovered that ripples on the melt surface generate a complicated absorptivity distribution. He highlighted that the absorptivity for a relatively smooth melt surface keeps relatively constant. However, a complex and nonlinear absorptivity modulation (on average 33%) occurs across the surface when the roughness levels are high, proportionally reduced by local absorptivity due to the shadow domains.

According to Fomin et al. [141, 142], the absorbance coefficient in the process rises with sheet thickness in CO₂ laser cutting of steel utilising oxygen (see

Figure 2.25.) However, unlike CO₂ lasers, the absorptivity of fibre/disk lasers diminishes as the material thickness increases [135].

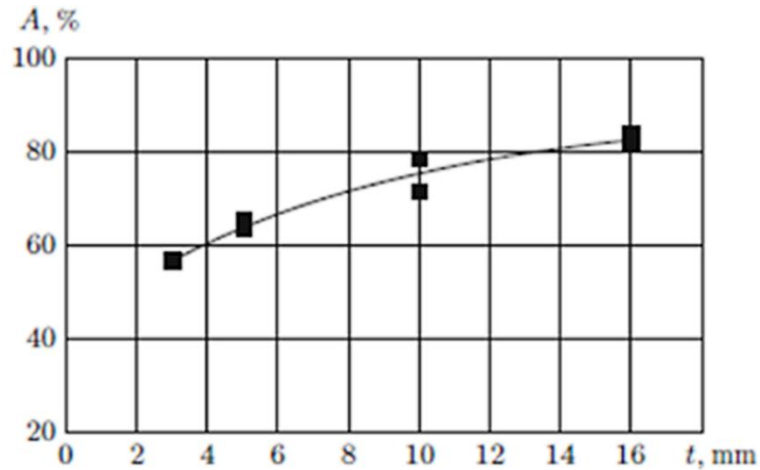


Figure 2.25 CO₂ laser absorption coefficient of steel utilising oxygen as a function of material thickness [141].

2) From a micro-level view

As various physical phenomena are coupled with each other in the laser ablation process, it is kept challenging to understand the complexity of the micro-behaviours. Therefore, Otto and Schmidt [143] studied the state of the art models, gave an overview of potential micro-behaviours in the ablation, and simulated the laser process based on the analysis.

As described in **Figure 2.26**, when the laser pulse strikes on the worksheet, five general micro-behaviours may be involved: (i) absorption, (ii) vapour dynamics, (iii) melt dynamics, (iv) heat conduction and (v) phase transitions. Firstly, the worksheet absorbs a portion of the energy involved in the laser beam, while others are either reflected by the worksheet or escape from the ablation zone with vapour and plasma. On the one hand, the worksheet absorbed the energy making the material within the ablation zone melt and

expulsed from the basic structures. On the other hand, the heat in the ablation zone is dissipated either by heat conduction, heat convection, or phase transitions. Meanwhile, the pressure wave can be generated by the vapour and plasma. As a result, the strong impact of the pressure wave will further damage the basic structures.

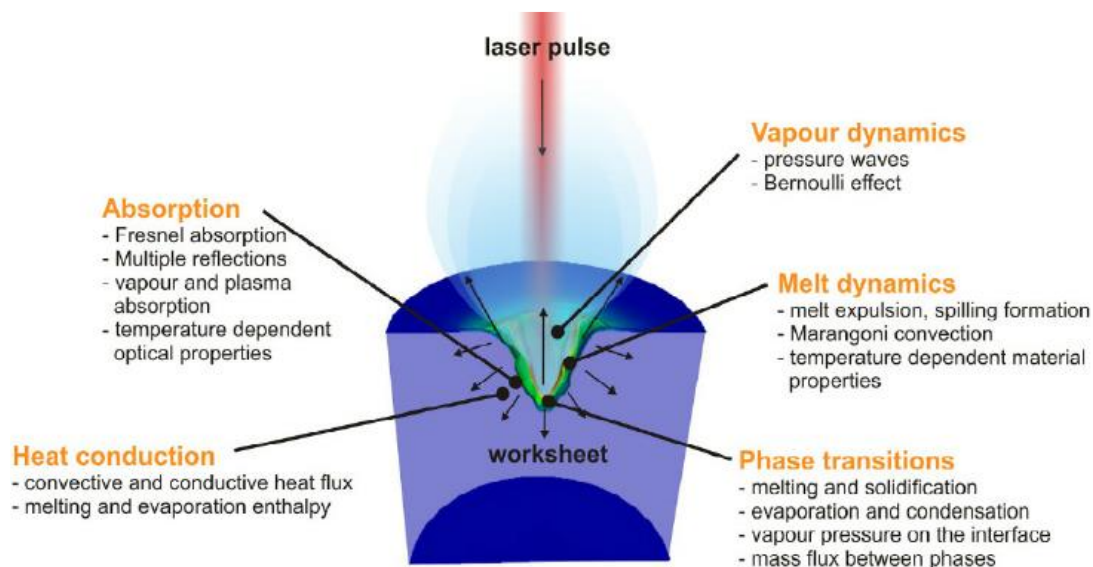


Figure 2.26 Micro-behaviours in the laser processing zone [143]

2.3.4 Key Factors Affect Laser Processing

1) Wavelength

The wavelength of a laser is determined by the energy levels of atoms in the laser medium as well as transitions in the stimulated emission process [144]. As various materials absorb light at different wavelengths, the first criteria for considering a laser source for material machining is to determine the wave range of the laser beam. Commonly, a laser beam with the 1,064 nm wavelength of an Nd:YAG laser can be well absorbed by aluminium and steel, while the wavelength of a 10,600 nm from the CO₂ laser beam can be well absorbed by organic materials such as paper, wood, leather, plastic, and fabric.

The two most common laser sources nowadays are fibre and CO₂ lasers. Fibre lasers have a wavelength of 1,064 nm, while CO₂ lasers have 10,600 nm if there are no specific comments. It is worth noting that, depending on the trace elements included in the fibre, fibre lasers can produce wavelengths of 1,060, 1,500, 2,000, 3,000, or 5,000 nm. On the other hand, depending on the specific gas combination (mainly the CO₂ ratio), a CO₂ laser can produce a 10,600, 10,300, or 930 nm laser beam.

Generally, the naming of laser in the industry may refer to a laser source by its wavelength rather than its gain medium. For example, an NIR (Near Infrared) laser with a wavelength of 1,064 nm is known as a NIR (Near Infrared) laser, whereas an FIR (Far Infrared) laser with a wavelength of 10,600 nm is known as an FIR (Far Infrared) laser. The wavelength of the laser source must be matched to the substance to be treated for laser operations to be successful [145].

A laser beam should penetrate the workpiece's surface to melt the material in laser material processing [146]. In terms of the physical process of laser contact with a material's surface, the wavelength of the laser has a significant impact on the material's surface absorptivity (see **Figure 2.27**) [147]. Therefore, a given wavelength can achieve optimum laser energy absorption with the least amount of reflection for a specific material type. CO₂ lasers with a wavelength of 10,600 nm and Nd:YAG lasers with a wavelength of 1,060 nm are the two most prevalent commercial lasers utilized in cutting and welding operations. Fibre/disk/Nd:YAG offers several benefits over CO₂ due to the shorter wavelength.

Figure 2.27 shows that the absorption of fibre lasers in metallic materials is greater than that of CO₂ lasers [145]. However, the causes for the disparities in performance between fibre/disk and CO₂ laser cutting have yet to be fully understood, and there are ongoing debates in the literature.

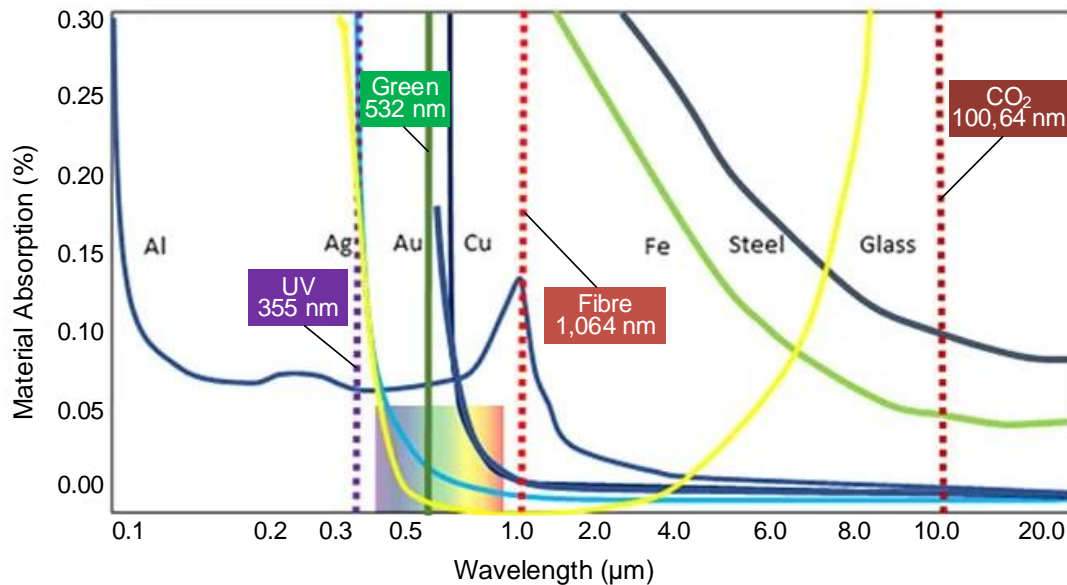


Figure 2.27 Absorption wavelength spectrum for different materials [145].

Because photon energy is inversely related to wavelength, most intense photons with short wavelengths can penetrate the bonded electrons of material surface atoms, reducing reflection and increasing absorption [140, 147, 148]. Meanwhile, due to their low wavelengths and lack of interaction with silica glass, fibre, Nd:YAG, and disk lasers are able to be delivered through optical fibres for flexible applications.

2) Wave mode

Laser sources can be categorised into Continuous Wave (CW) and Pulsed Wave (PW) by the beam output mode. **Figure 2.28** illustrates the mechanism of how a CW or pulsed beam output is created.

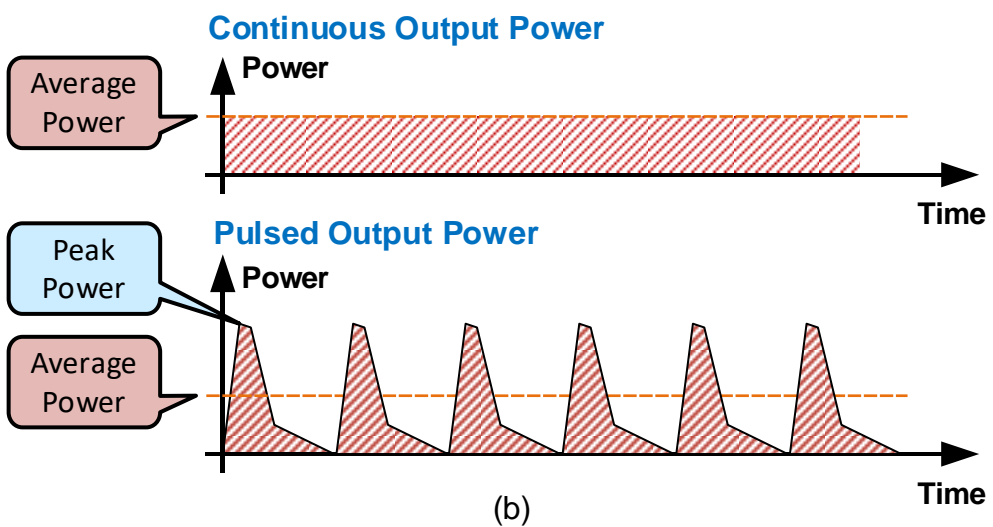
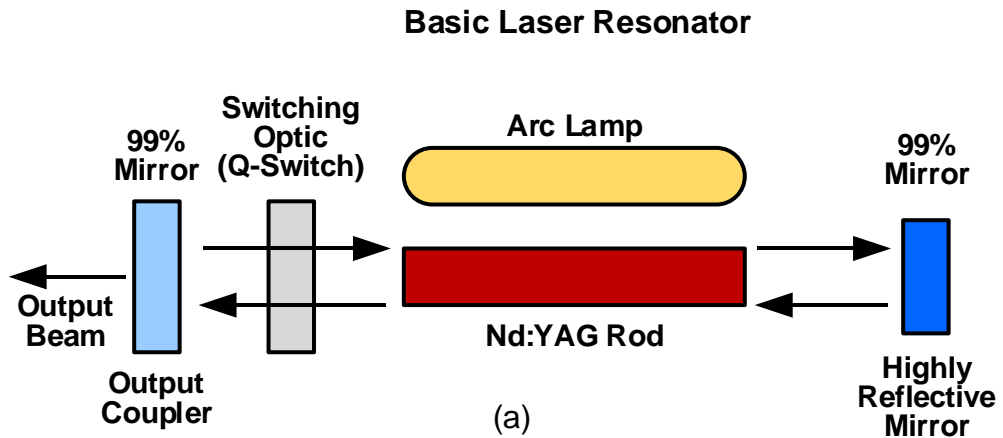


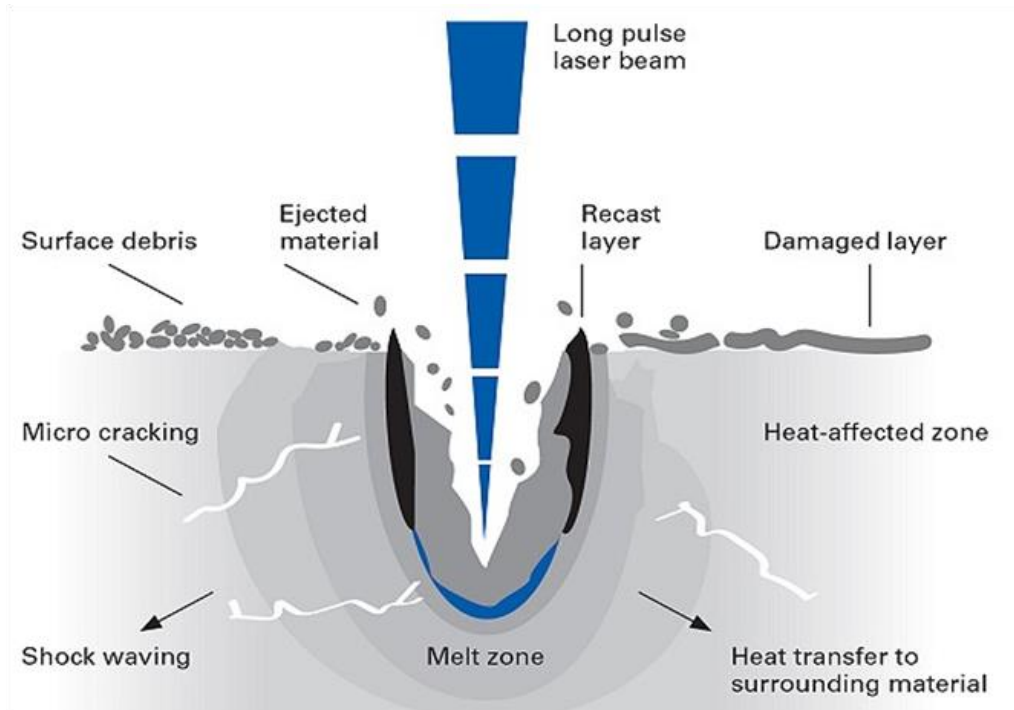
Figure 2.28 Mechanism of CW or PW beam creation. (a) The basic mechanism of the laser resonator and (b) CW vs Pulsed laser [145].

As shown in **Figure 2.28a**, assuming that one end of the light-pumped laser cavity has a 90% reflecting mirror, and the other end has a highly reflective mirror. When the arc lamp shines a light on the Nd:YAG rod, it emits light with a wavelength of 1,064 nm from both ends, which is directed towards the mirrors. These light photons reflect back and forth between the two mirrors, attracting more photons each time as they travel through the Nd:YAG rod. Due to one mirror being only 90% reflecting, a fraction of photons can travel through it, resulting in laser energy that can be used for marking [145].

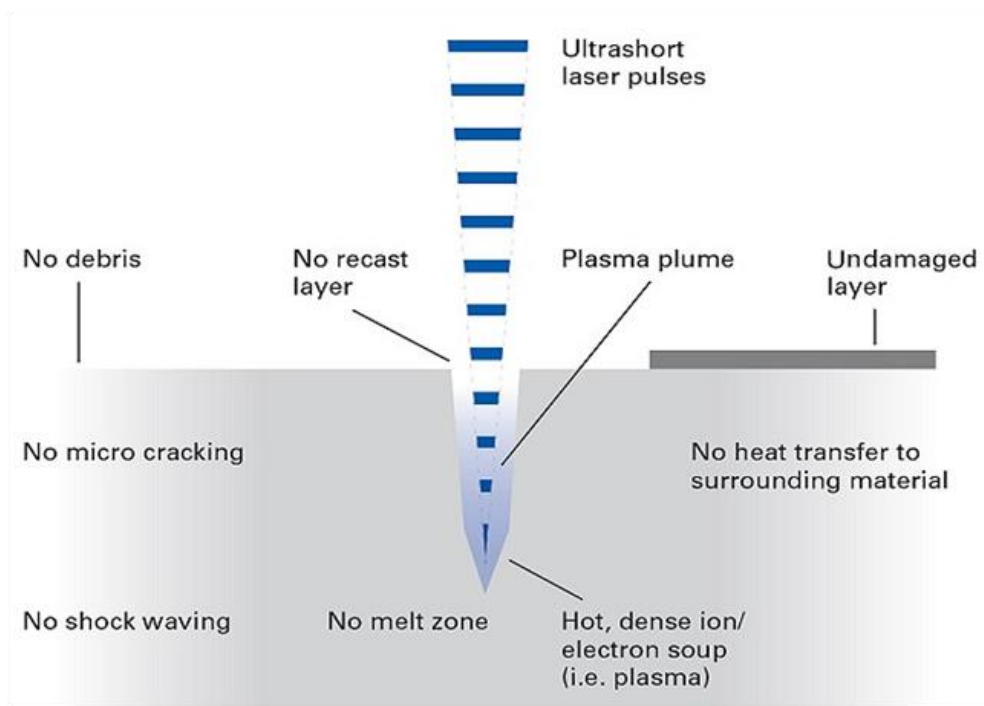
As the energy within the laser rod will be a build-up if a switch between the Nd:YAG rod and one of the two mirrors is installed (usually an Acusto-Optic Modulator, or “Q-Switch”) and then “shut” to prevent photons escape from the mirror cavity. When the switch is “opened”, allowing photons to flow freely again, this energy is removed from the rod, resulting in a high-energy pulse.

Figure 2.28b shows the impact of CW and pulsed laser. The energy-over-time (average power) is the same in both modes. However, a significant power spike is built up when the laser is pulsed, followed by a similarly reduced power portion. The peak intensity of a pulsed laser can be thousands or millions of times higher than the average output power when the pulse duration is modulated in nanoseconds, picoseconds, femtoseconds, or even attoseconds. As a result, even a low-power beam can be used to evaporate or ablate the workpiece material rather than just melting it.

As CW (or long pulse laser beam) laser has continuous output power, more heat will be rapidly generated in the ablation zone, causing the materials to melt and eject from the molten zone, and the thermal shock wave is likely to cause the generation of micro-cracks. In addition, other issues such as the recast layer, larger heat-affected zone and surface damage are all like to happen in this mode (see **Figure 2.29a**) [149].



(a)



(b)

Figure 2.29 Damage effects of different wave modes [149]. (a) Damaging effects of a long pulse laser beam on the surface and surrounding material; (b) ultrashort laser pulses do not affect the surface, minimize heat transfer to surrounding material and avoid micro-cracks and a melt zone.

In contrast, a pulsed laser (or ultrashort laser beam) has an extremely short

duty cycle but a considerable peak laser power, making the target materials evaporate in no time before the heat is transferred to surrounding materials. As a result, most thermal-related problems will not happen in this mode (see **Figure 2.29b**). However, due to the higher peak laser power and the discontinuous nature of the pulsed laser, it is hard to achieve to higher average power. Therefore, CW lasers often are used for cutting and welding applications, while pulsed lasers often are used for micro-scale machining, labelling (or marking), and engraving applications.

3) Power intensity

The laser power intensity can be changed apart by pulsing the beam at varying intervals of lengths, and it can also be changed by sending the laser beam through a focusing optic. The former compresses the laser energy, while the latter reduces the focal size of the beam. The reduced focal size concentrates a tremendous quantity of energy into a tiny area, amplifying its influence.

However, a laser's output cannot be shrunk smaller than its wavelength, regardless of how good a focusing optic is employed, and a laser with a low-quality output cannot form a high-quality spot at its focal point. This fact imposes a strict limitation on the size of each laser point (e.g., a CO₂ laser cannot shrink down smaller than roughly 0.01 mm, even performed by a perfect beam and perfect optics). However, a smaller spot size is not appropriate for every purpose. Laser welding, sintering, surface cleaning, surface hardening, and other surface treatment applications, for example, all require a somewhat big spot size to assure performance. Meanwhile, laser

annealing is also easier with larger spot size. On the other hand, a smaller spot size is advantageous for laser micromachining, marking, and engraving, while a medium spot size is advantageous for laser cutting applications.

Figure 2.30 shows that the power range corresponds to the application scope. Generally, laser micromachining applications require less than 50 W of mean power but greater peak power and energy density to allow extremely precise HAZ control [145].

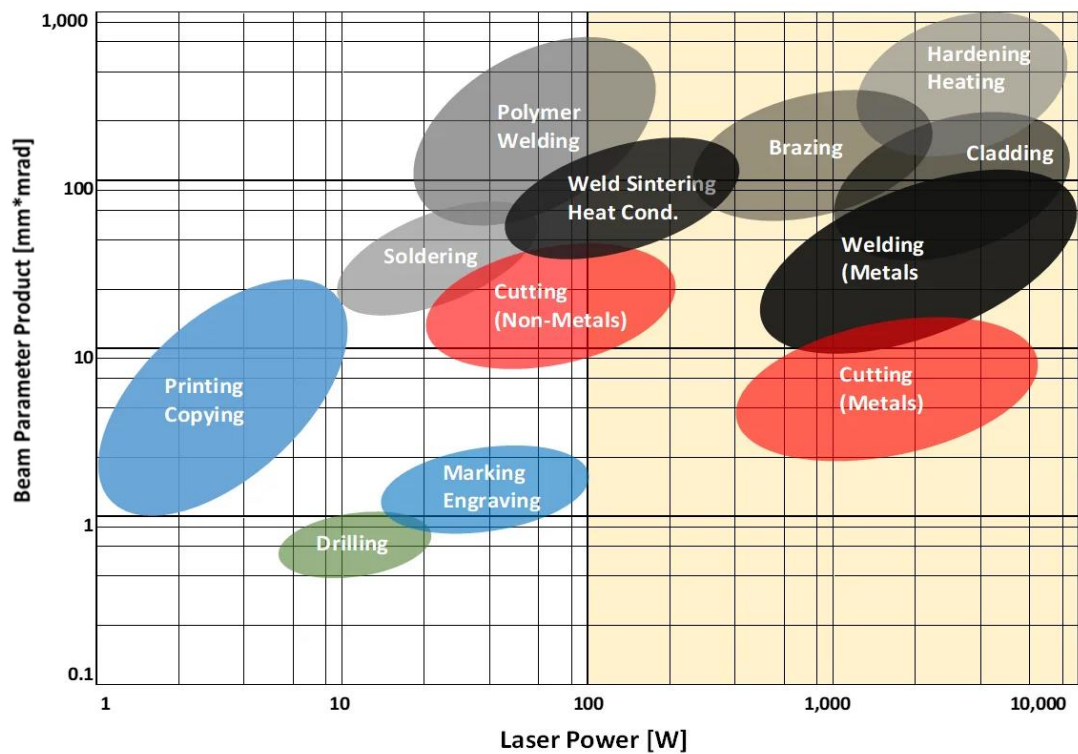


Figure 2.30 Laser power range fits the application scopes [145].

The typical power range for laser marking and engraving will be 20 to 100 W. When undertaking deep engraving, higher average power can increase cycle time. The usual power range for laser cutting applications for most organic will be 30 to 400 W. For optimum beam absorption, this is usually done with a CO₂ laser. The power range for laser-cutting metal workpieces will be anywhere

between 700 and 10,000 W, determined by the thickness of the workpiece. In most cutting applications, an assist-gas is used to blast away melted material while the laser is working. For the applications of laser surface treatment and welding, they require 500 to 10,000 W for metal workpieces and 10 to 500 W for common non-metal materials [145].

4) Polarisation

Any laser beam contains electrical and magnetic fields, which are created by an electromagnetic oscillation, and one beam's polarisation might be linear, circular, or random. Polarization in fibre lasers, for example, is unpredictable. The claim that the polarisation of a laser beam might alter laser processing is noteworthy [150-152]. According to Weber et al. [151], polarised CO₂ laser beams exhibit unusual absorbed intensity behaviour, which is critical in industrial and research applications. The perpendicular polarised beam has a lower absorptivity than others (see **Figure 2.31**). Niziev et al. [150] found that laser polarisation affects cutting efficiency, depth of cut, and cutting edge quality using 3D modelling.

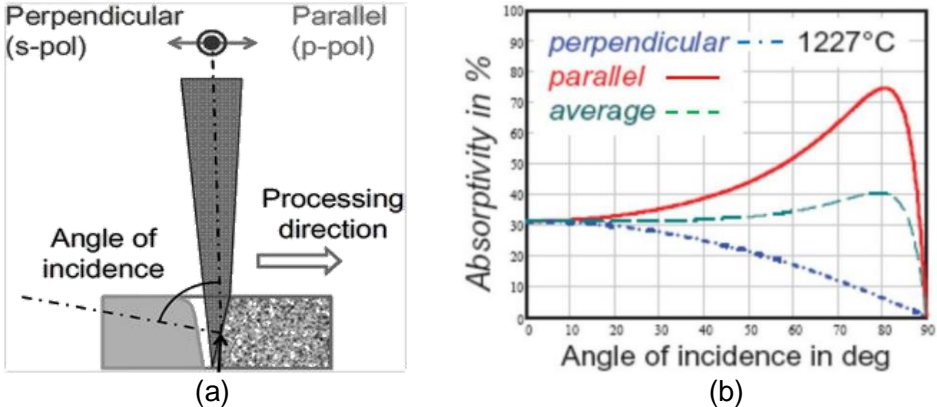


Figure 2.31 (a) Diagram of a typical laser-material interaction geometry; (b) the absorptivity of CO₂ laser affected by perpendicular and parallel [151].

Weber et al. [151] found that both the cutting efficiency and the maximum cutting speed could be boosted by up to above 35% when cutting a 2 mm stainless steel plate using a radially polarised CO₂ laser beam (see **Figure 2.32**).

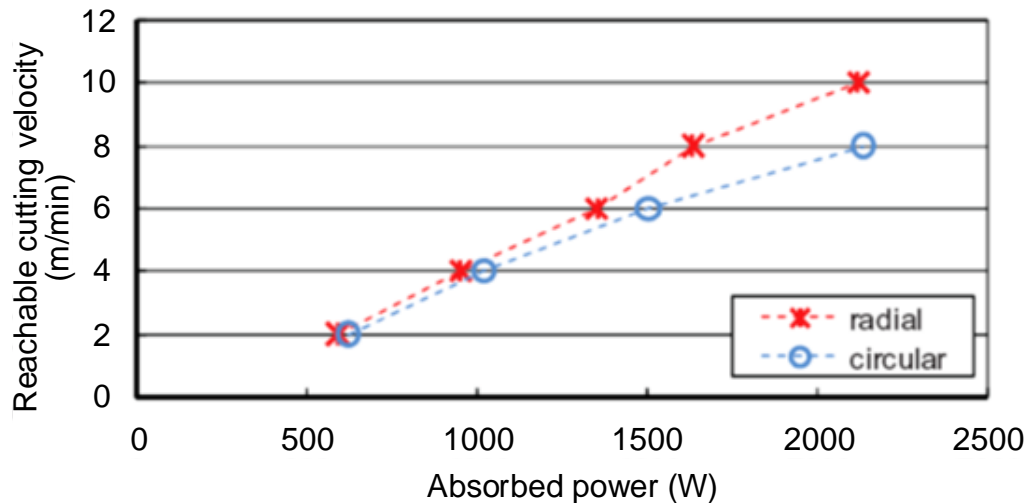


Figure 2.32 Radial and circular polarizations affect the cutting speed of CO₂ laser for 2 mm stainless steel [151].

They also discovered that when a tangentially polarised laser beam was used in deep welds at a low welding velocity, the spatter was reduced by more than 80% compared to a random polarised beam. Besides, radial polarisation improves drilling efficiency in shallow holes, but tangential polarisation improves drilling efficiency in deep holes [151].

5) Beam quality

Based on the divergence angle, the two commonly used beam quality indexes are M^2 and BPP (Beam Parameter Product).

The M^2 is a beam quality metric frequently used to compare lasers of various wavelengths, which is expressed as **Equation (2.4)**:

$$M^2 = \frac{\pi W_0 \theta}{4\lambda} \quad (2.4)$$

where W_0 is the focused diameter of a laser beam (mm), λ is the wavelength (μm), and θ is the divergence angle ($^\circ$).

As a diffraction limit factor, M^2 refers to the quality of a given laser beam compared to a perfect beam. According to **Equation (2.4)**, a laser with $M^2=1.2$ will produce a 20% wider beam diameter than a perfect one with $M^2=1$ [153].

When evaluating beam quality, *BPP* considers the ability of a certain beam to focus. Although a diffraction-limited Gaussian beam produces the least amount of *BPP*, a real laser beam has a larger *BPP*, as described by **Equation (2.5)**.

$$BPP = \theta_0 W_0 = \frac{\lambda}{\pi} M^2 \quad (2.5)$$

The definition of parameters for beam propagation and beam characterization formulas is shown in **Figure 2.33**.

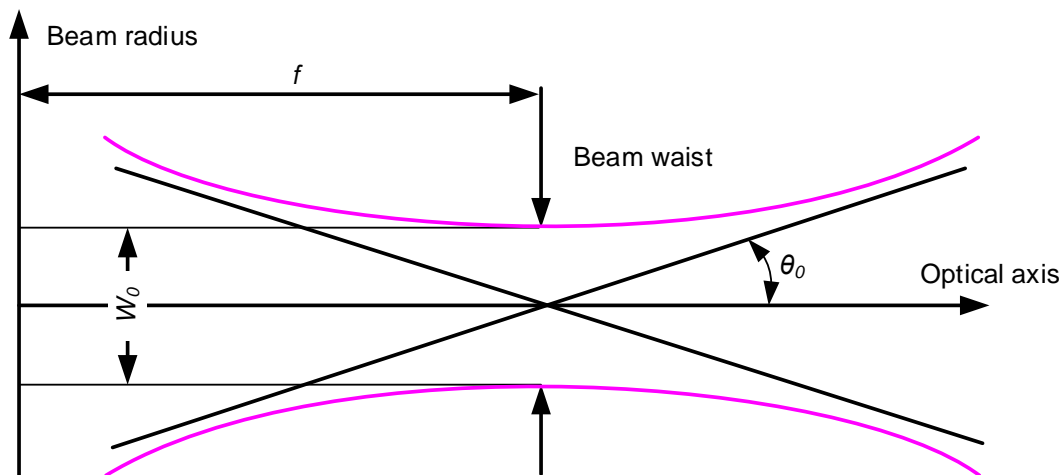


Figure 2.33 Definition of parameters for beam propagation and beam characterization formulas [154].

M^2 indicates how much the *BPP* of the actual laser exceeds the *BPP* of an

ideal Gaussian beam ($M^2 = 1$). Many laser beam parameters, such as beam diameter, wavefront radius, Rayleigh radius, depth of focus, and focused spot size, may be estimated using M^2 [155]. **Figure 2.34** depicts the influence of M^2 on the beam diameter.

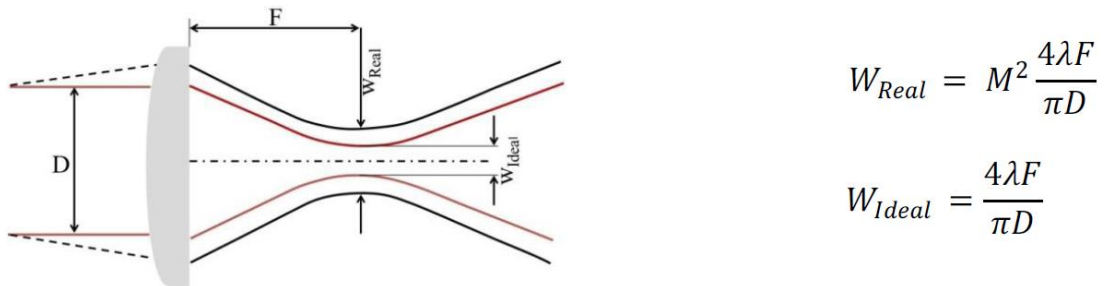


Figure 2.34 Diagram for the definition of M^2 and its influence on the beam diameter. The functions are generated from Equation (2.4).

O'Neill [156] demonstrated the practical use of the *BPP*, as shown in **Figure 2.35**). The deeper the laser focus depth, the smaller its *BPP*. The smaller *BPP*, the greater the beam quality (smaller spot size). According to Hugel [157], *BPP* is used to evaluate the quality of lasers with diverse wavelengths (fibres and diodes) while M^2 is more commonly employed for lasers with the same wavelength.

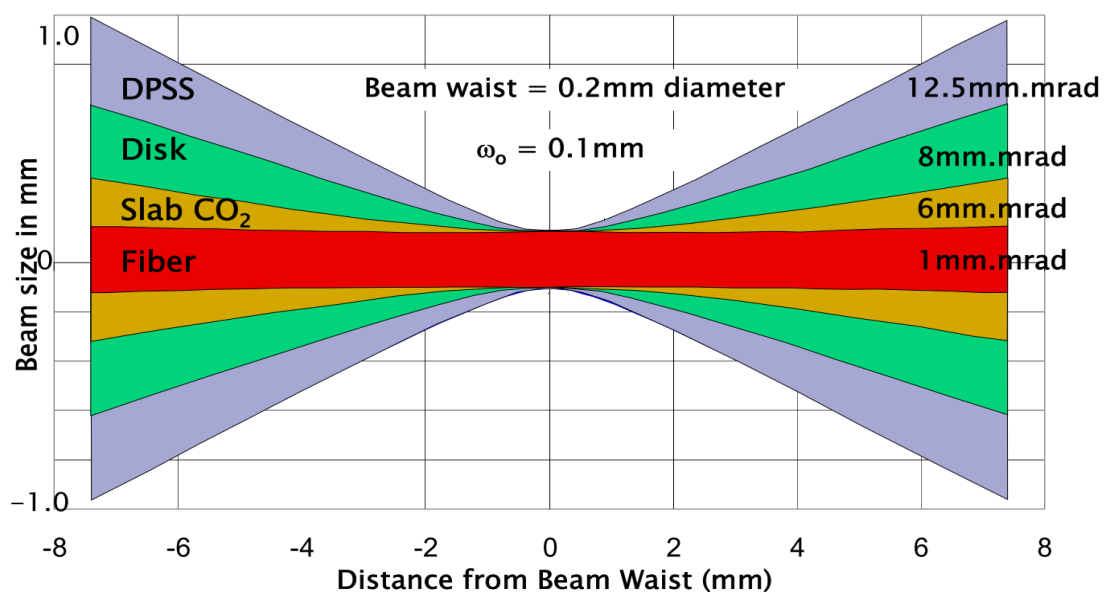


Figure 2.35 Focused beam profile affected by beam parameter product [156].

A comparison between CO₂ and a disk laser revealed that the energy intensity distribution of the two lasers varies as the M^2 for these laser types differs.

Table 2.2 shows typical values of beam output characteristics after the laser beam goes through the laser head (obtained at 3,000 W) [158, 159].

Table 2.2 Characteristics of the utilised CO₂ and disk laser beam [159].

Laser source	Cutting head	M^2	Focus radius	Rayleigh length
CO ₂	Precitec HP 1.5"	1.36	76.123 μm	1.27 μm
Disk	High YAG BIMO FSC	14.30	76.171 μm	1.20 μm

The intensity profile of the CO₂ laser is roughly a Gaussian distribution (seen in **Figure 2.36**). The highest power intensity of CO₂ is 42.99 MW/cm², almost double the value observed for disk laser (about 24.67 MW/cm²) [158, 159].

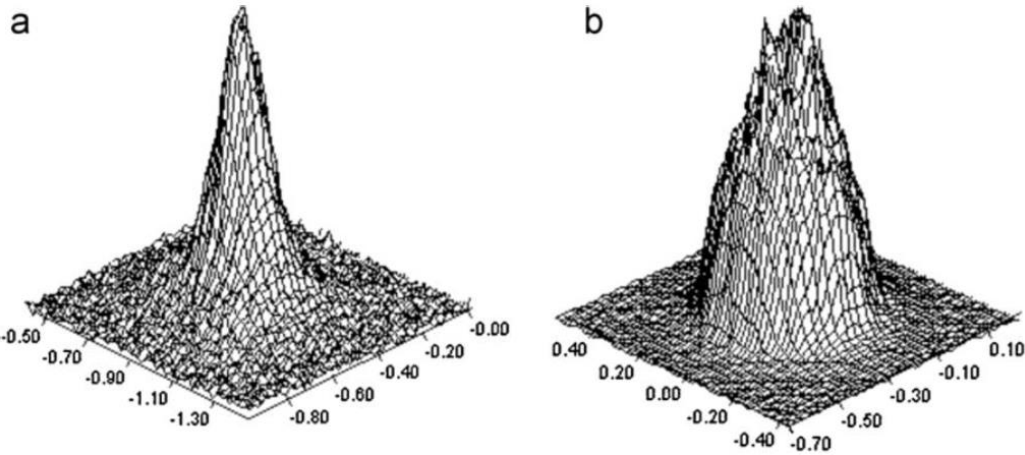


Figure 2.36 Intensity distribution of two different laser types. (a) CO₂ and (b) disk laser beam [158].

Figure 2.37 depicts the relationship between the laser beam width and the power density with BPP . With the same optical setup, increased BPP causes a decrease in power density and an increase in the beam diameter. As a result, smaller BPP lasers can be operated at lower powers to attain the same power density [160].

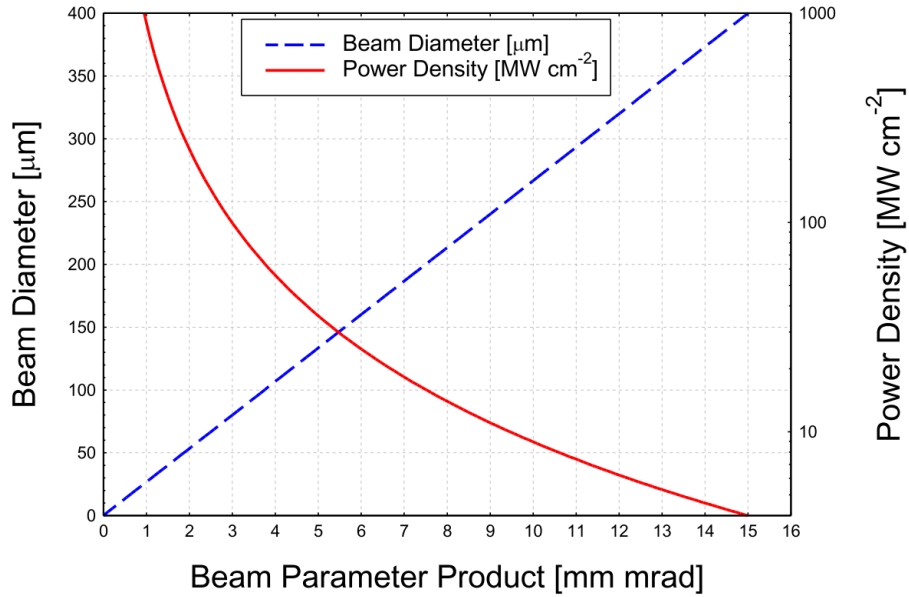


Figure 2.37 Effect of *BPP* on beam diameter and power density [160].

2.4 Introduction to Ablation Results Evaluation and Control

The most concerning issues of the ablation results evaluation in this study are the ablation topography, morphology, and the heat-affected zone. Therefore, the general scopes in this section cover the measurement technologies, the observation strategies, and the heat-affected zone identification and control.

2.4.1 Topography Measurement Technologies

In this project, as the topography can be sketched by measuring the ablation depth along the cross-section of the ablated trench, a comprehensive investigation and study on depth measurement technologies are highly needed.

Generally, the measurement technologies can be divided into contact-based and non-contact-based technologies. Based on the principle of mechanical movement, the contact-based technologies can be further sub-classified into probe-triggered levers and probe-triggered springs. Meanwhile, the non-contact technologies based on their principle can be further subdivided into (i)

laser (like structured light, laser reflection time and laser triangle refraction), (ii) light (such as structured light and photoelectric encoder), (iii) ultrasonic (ultrasonic reflection time), (iv) stereo cameral (pixel), (v) magnet (magnetic induction). The overview of the overall distance measurement technologies is shown in **Figure 2.38**.

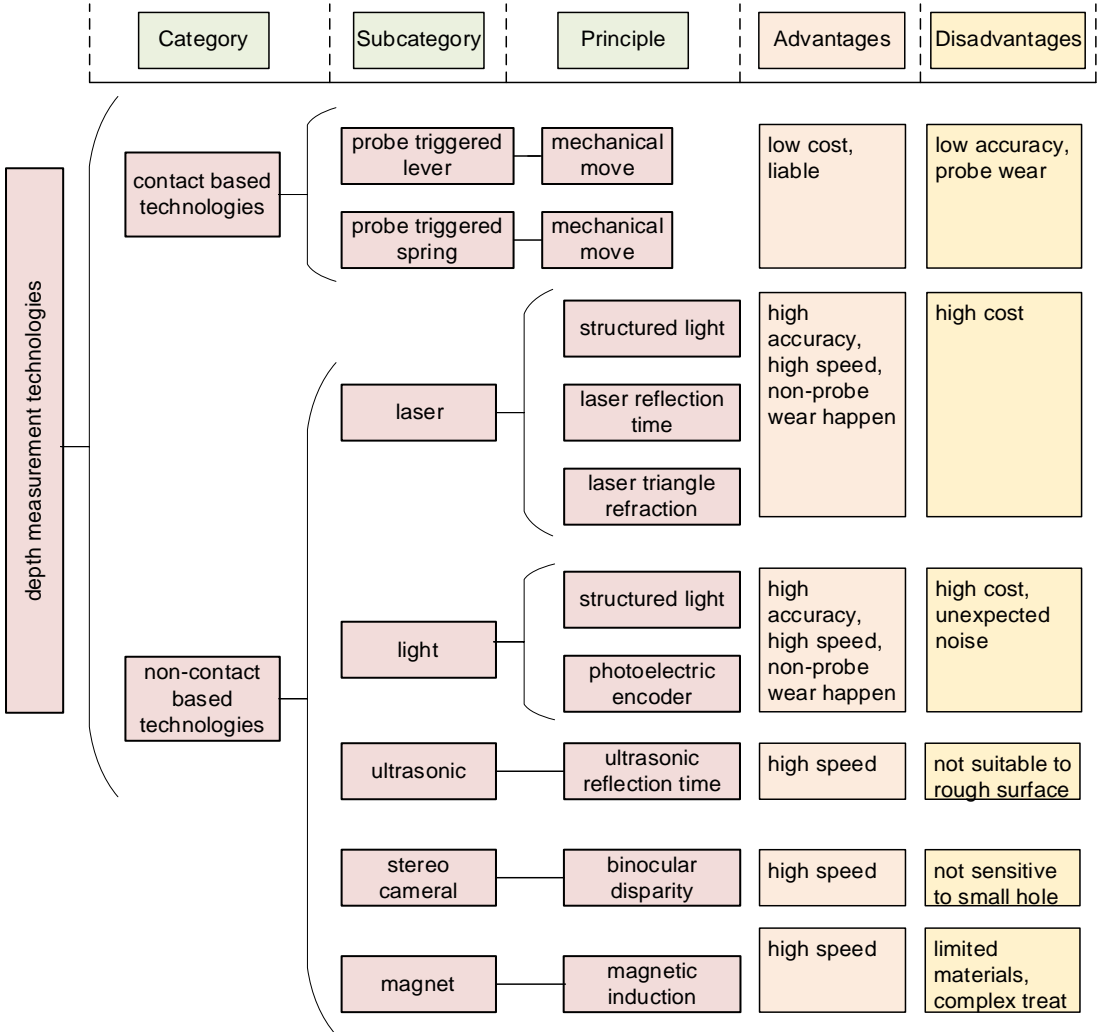


Figure 2.38 Depth measurement technologies.

Contact-based technologies are widely used because of their low cost and high reliability, but most of the probes will be worn when measuring the moving parts, especially for the part with bonded abrasives. Therefore, an intensive investigation of non-contact-based technologies has been performed.

Li et al. [161] introduced an algorithm for depth acquisition of multi-state targets based on structured light, making the technique available to detect the depth of static, slow motion or fast motion objects. Hu et al. [162] proposed a new binary defocusing technique to address the problem in three-dimensional (3D) structured light measurement regarding the type of binary fringe and the degree of defocus. However, the accuracy and speed of 3D measurement may not be satisfactory for certain industrial applications. The verified experiment showed a measurement error reduced by 16.9% or more for a standard block with a depth of 1 mm. Kytö et al. [163] presented a method to evaluate stereo camera depth accuracy based on the binocular disparity, it was found that the maximum error was within ± 1 mm at all trialled distances ranging from 0.7 m to 5.8 m, and the error could be further reduced when improving the pixel quality.

Chiu et al. [164], based on geometrical optics and the use of a Surface Plasmon Resonance (SPR) sensor, developed a real-time small absolute distance measurement method (the measurement principle is shown in **Figure 2.39**) with nanometer resolution.

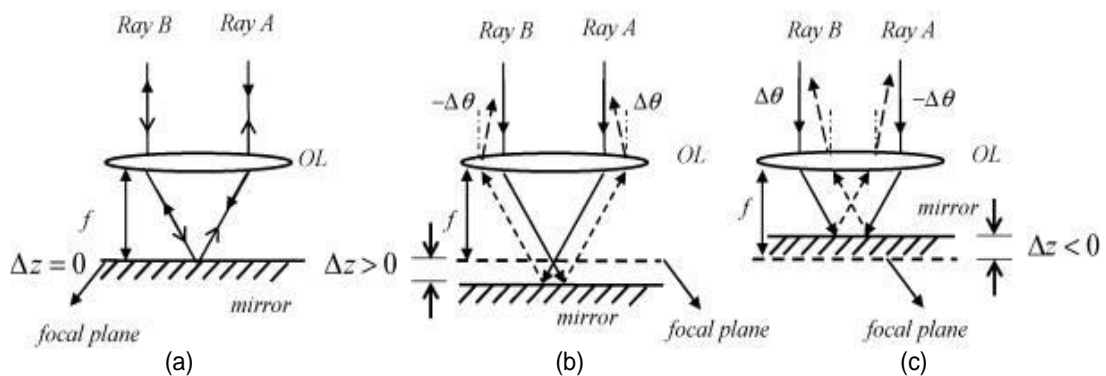


Figure 2.39 Diagram of optics principles of an SPR angular sensor [164]. Rays

back from an objective lens and a mirror are (a) parallel, (b) converging, and (c) diverging.

Norgia et al. [165] proposed an instrument to simultaneously measure absolute distance and velocity with a high measurement speed (equal to 25 μ s) based on self-mixing interferometry. The simultaneous measurement achieved a relative standard deviation of approximately 4×10^{-4} in the absolute distance and 5×10^{-3} in velocity measurement. The instrument also shows good performance in harsh environments, such as detecting the movement of an opaque iron tube rotating under a running water flow. To improve distance measurement precision using laser Self-Mixing Interferometry (SMI) and compute short distances, Duan et al. [166] proposed a method of Multiple Self-Mixing Interferometry (MSMI) that is modulated with a triangular wave based on easily operated, low-priced experimental devices (as shown in **Figure 2.40**). Experiments showed a resolution of 2.7 mm for absolute distances ranging from 2.2 to 23 cm.

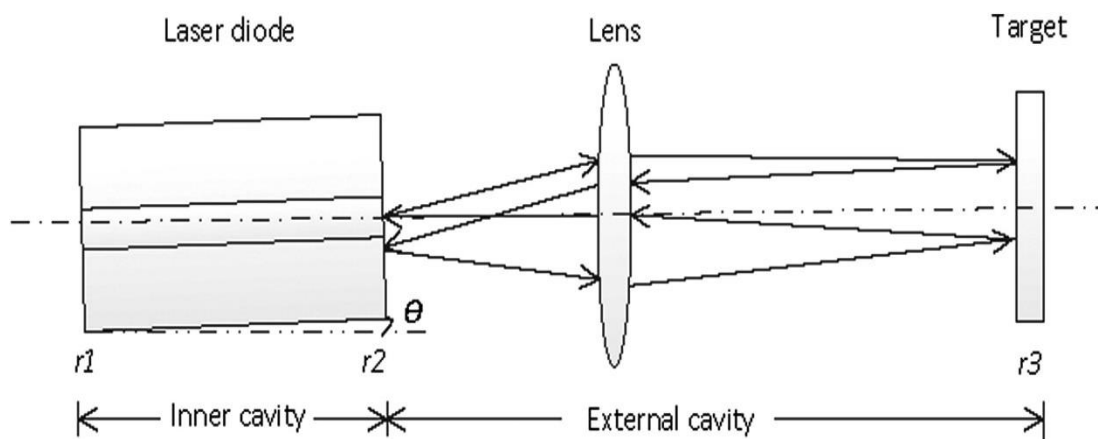


Figure 2.40 Principle of MSMI [166].

Wang et al. [167] proposed a machine vision measurement technology (see **Figure 2.41a**) by using a closed-loop kinematic calibration method (based on

mechanical principle as shown in **Figure 2.41b)** to improve absolute position accuracy. After calibration, the average distance error of robot motion is decreased from 2.05 mm to 0.24 mm.

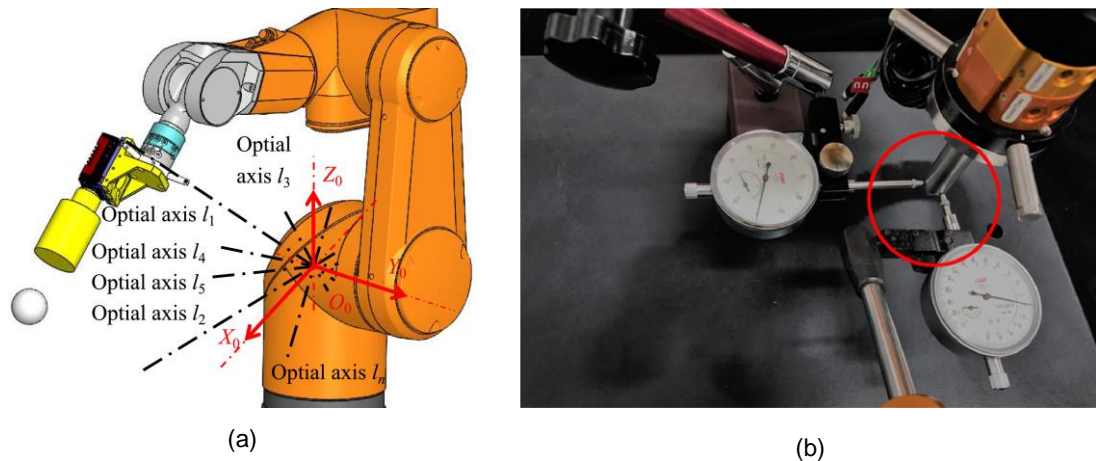


Figure 2.41 The robot calibration system [167]. (a) Machine vision measurement, (b) mechanical measurement.

Fu et al. [168] proposed a distance measurement technique using a triangular-wave amplitude modulation laser based on the least squares (see **Figure 2.42**). According to experimental results, the proposed method has a high Signal to Noise Ratio (SNR), and the average measuring error is maintained within 2.8 mm with a detection distance of 10 m.

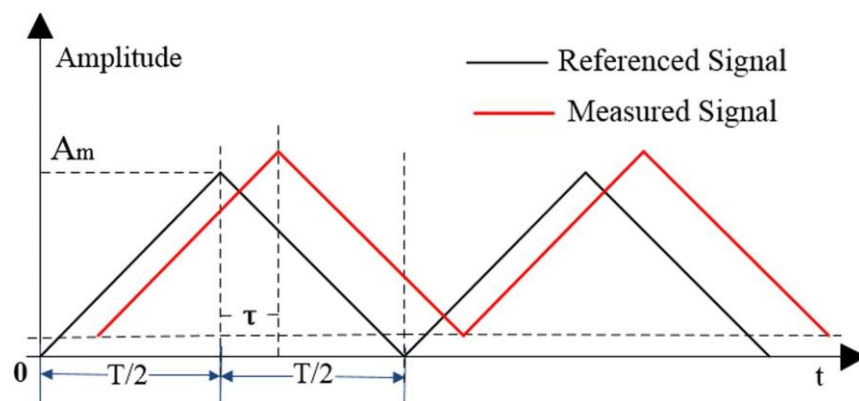


Figure 2.42 Schematic of the measurement principle [168].

Medhat et al. [169] used frequency scanning interferometry to measure

absolute distances up to 5 m. The measuring system works by simultaneously acquiring fringes from measuring and a reference interferometer and then counting both fringes to find the ratio between them by a software algorithm. The system showed a ± 0.3 mm measurement uncertainty for the short distance calibration of a laser distance meter.

Kim et al. [170] used the ultrasonic measurement approach to calculate the absolute parameter from a measured relative parameter and a proportionality constant between the normalized absolute and relative parameters (see **Figure 2.43**). The method was experimentally validated for Al6061-T6 alloy specimens heat-treated for different ageing times. The results showed that the absolute and measured parameters were close to each other within the measurement errors.

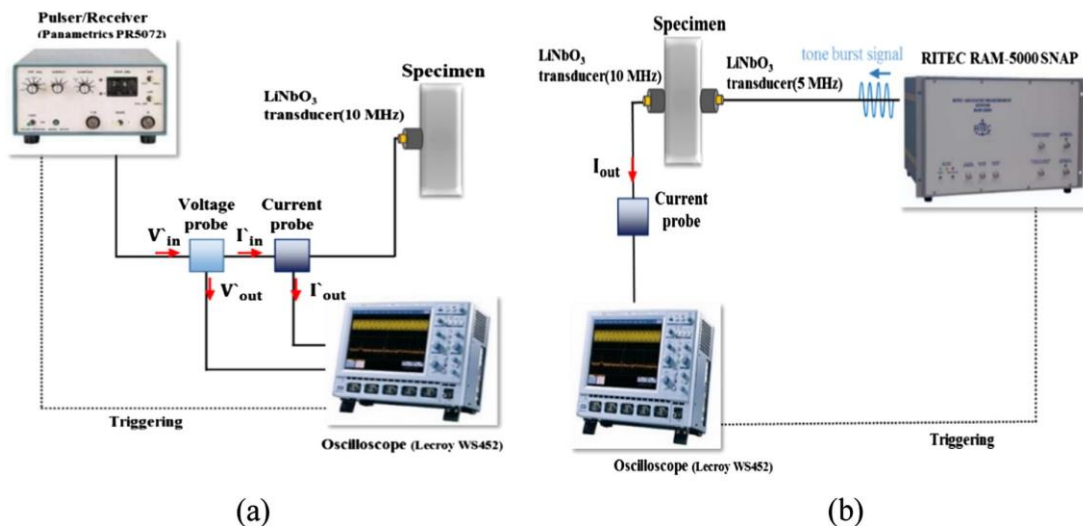


Figure 2.43 Experimental setups for absolute measurements: (a) calibration, (b) nonlinearity measurement.

Shi et al. [171] designed a linear encoder system (see **Figure 2.44**) that is able to be used for commercial absolute precision positioning applications. The prototype showed an accuracy for the measured incremental displacement of

at least 1 μm and the positioning accuracy within 0.22 μm according to their statistical analysis of 12 groups of repeated trials.

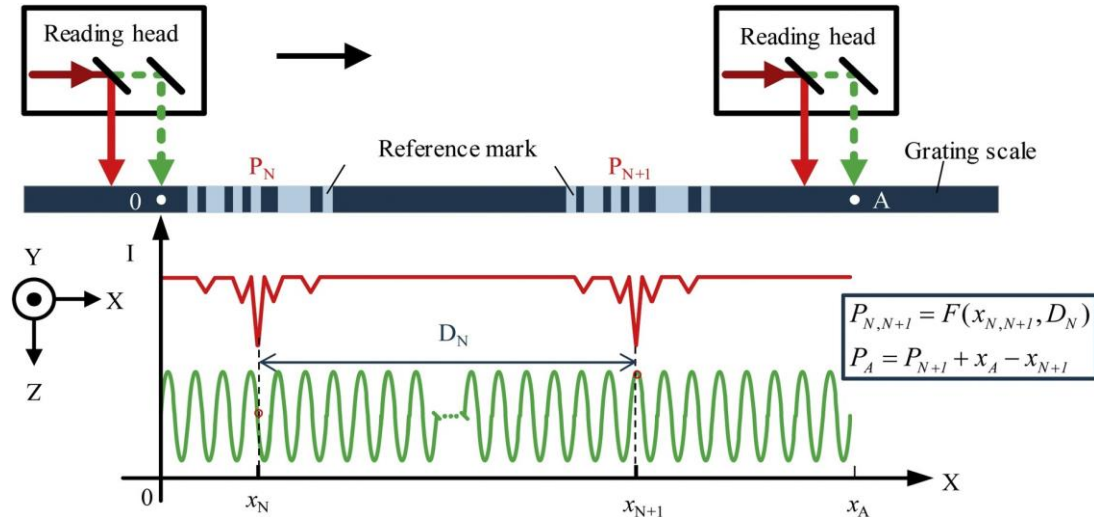


Figure 2.44 Diagram for locating process of reading head [171].

From the overview regarding depth measurement technologies, the contact-based technologies may have abrasion problems that are quite undesirable for the measurement in this project. Therefore, non-contact-based technologies would be preferred in the application of this project. Furthermore, among the non-contact-based technologies, the light, ultrasonic, stereo camera, and magnet-based technologies either have low precision or large volume problems. In contrast, laser-based measurement technologies can have precision, focus point, response, measurement speed, volume, and anti-interference advantages. Therefore, we can draw the conclusion that laser-based measurement methods could be a promising way in special applications, like this project that needs a small point, rapid response, high measurement speed, and accuracy.

2.4.2 Morphology Observation Strategies

Ablation morphology and topography are two important indexes to evaluate the ablation results. The ablated morphology may affect little on the final profile, but its effect on the performance of the workpiece can not be underestimated. Currently, SEM and optical images are still the two most used methods for morphology observation. Because both the microstructures and metallography can be studied using SEM, the colour changes can be well studied using optical images.

Feng et al. [172] studied the morphology of a hybrid laser-waterjet machining on single-crystal silicon carbide by carrying out SEM method, finding that the morphology (as shown in **Figure 2.45a**) around the path is different from the base materials. Leone et al. [173] experimented on Carbon Fibre Reinforced Polymer (CFRP) by using a Q-switched 30W Yb: YAG fibre laser and studied the morphology structure and HAZ formation mechanisms using the SEM method (see **Figure 2.45b**).

As the SEM method had a shortage in colour resolution, Fazli and Mahdavinejad [126] validated an integrated Artificial Neural Network (ANN) and genetic algorithm (GA) model by using an optical method (see **Figure 2.45c**), which was built to predict the HAZ and temperature distribution of the specimens. Finally, Leone and Genna [174] studied the relation between the HAZ extension and the process parameters by studying the HAZ extension (see **Figure 2.45d**) in pulsed Nd:YAG laser cutting of CFRP, illustrating that the maximum cutting speed and a narrow HAZ can be obtained by accurately

selecting the process parameters.

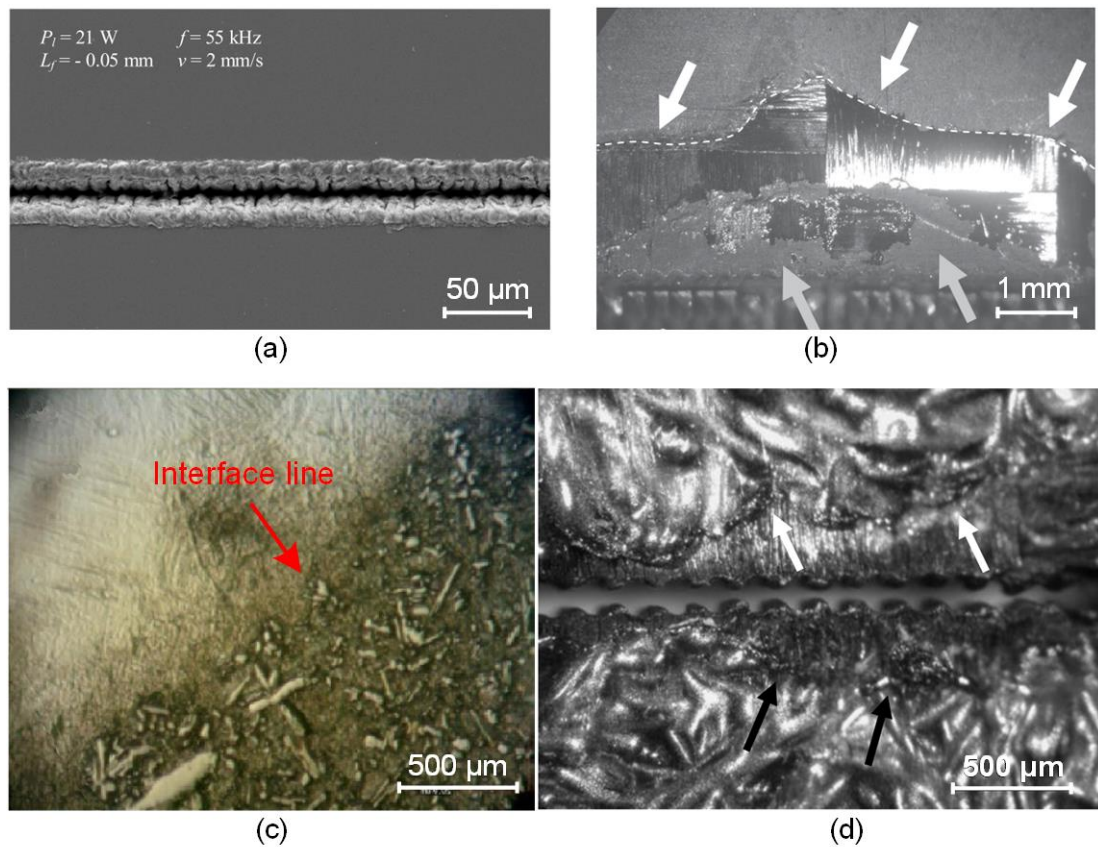


Figure 2.45 Morphologies observed by SEM and optical images. (a) Single-crystal silicon carbide [172] and (b) CFRP [173]; (c) Ti-6Al-4V [126] and (d) CFRP [174].

To be a little different, Belhadj et al. [175] studied the metallography changes of non-oriental electrical steels (see **Figure 2.46**) cut by a CO₂ CILAS™ 2,000 laser with oxygen assist gas using a PHILIPS ESEM XL-30 electron microscope. It shows that the microstructures near the cut edge changed with temperatures can be observed. However, due to the complex sample preparation process and fuzzy interface line, the method is usually used for the metallography of metal materials.

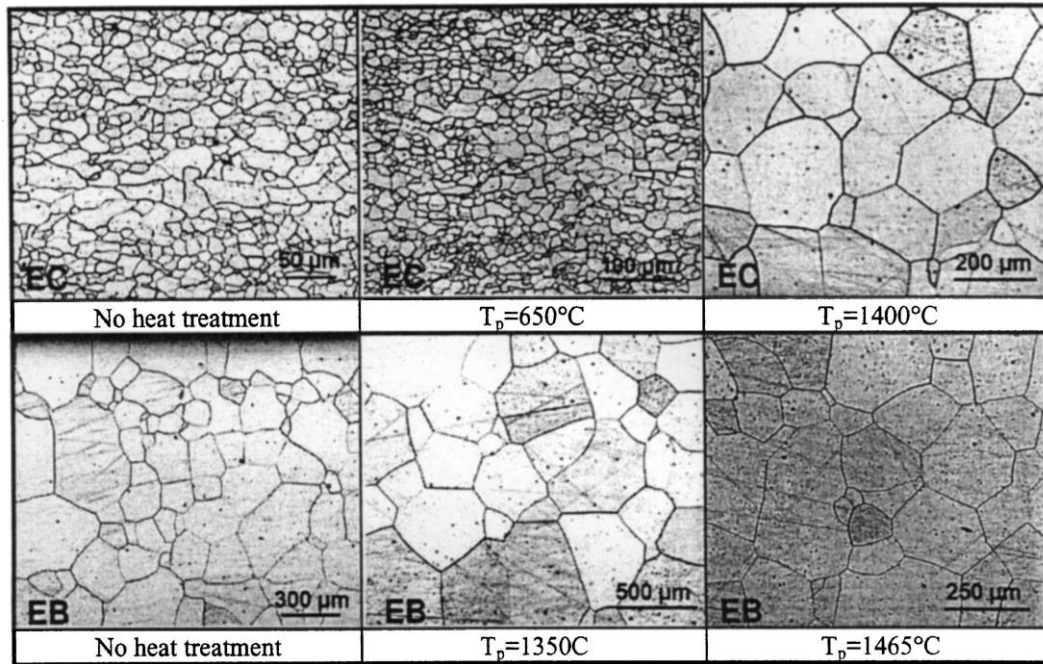


Figure 2.46 Metallography changes with temperature observed by ESEM [175].

2.4.3 Heat Affected Zone Identification and Control

Heat-Affected Zone (HAZ) is defined (or formed) as the area that underwent thermal-induced effects that caused the remained materials within this zone to suffer from unwanted changes. The heat-affected materials are different from the matrix in the aspects such as functional performance, metallography, appearance, and substance composition.

1) Heat Affected Zone Identification

Generally, the present ways to detect HAZ are quite limited. To some extent, SEM and Optical images have remained the two main essential methods for detecting the heat-affected zone. As the HAZ is usually visible by a microscope, these methods can identify the HAZ by judging the interface line (colour changes) because its colour will be changed compared with the base material [176].

Using the SEM method, Solati et al. [177] identified the HAZ extension and proposed a combined GA-ANN approach to predict HAZ and bearing strength in laser drilling GFRP composite by the SEM micrographs. Kumar and Gururaja [178] studied the HAZ (see **Figure 2.47a**) of titanium (Ti) and carbon fibre reinforced plastic (Ti/CFRP/Ti) laminates machined by a CO₂ laser. The SEM view revealed that the HAZ varies among the different materials and experimentally showed that using a higher frequency and lower line energy can significantly improve the hole quality.

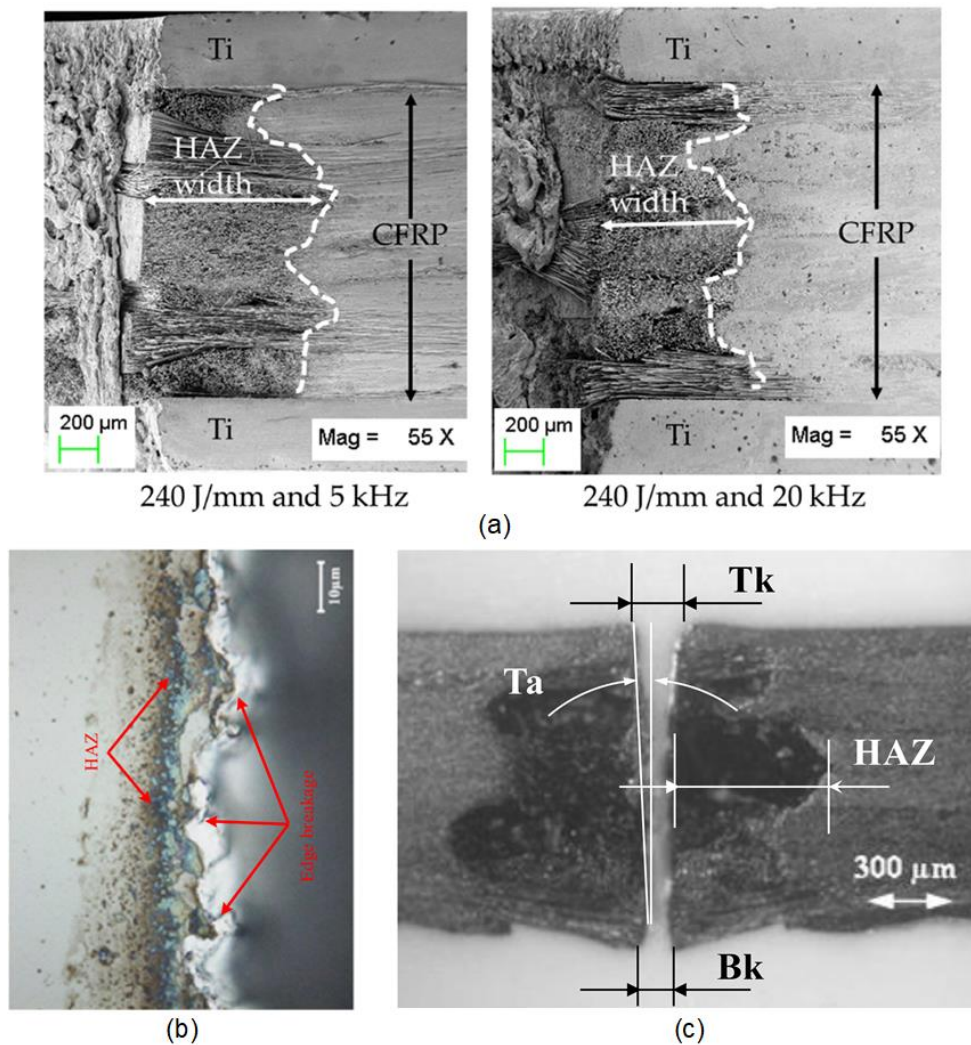


Figure 2.47 HAZ detection by (a) SEM and (b, c) optical image. (a) Titanium (Ti) and carbon fibre reinforced plastic [178], (b) single crystal 4H-SiC wafer [172], and

CFRP [174].

Feng et al. [172], using the optical method, studied the surface quality evaluation of a single crystal 4H-SiC wafer machined by hybrid laser-waterjet to compensate for the shortage of colour resolution in SEM, finding that though it is blurred, the HAZ boundary still could be identified (see **Figure 2.47b**). Besides, Leone and Genna [174] studied the heat-affected zone extension when cutting CFRP plate by Nd:YAG pulsed laser and the boundary of HAZ can be clearly distinguished by the optical image (see **Figure 2.47c**).

Although both of the mentioned methods can detect the HAZ, they are hard to quantify the HAZ as the boundary usually fluctuates accurately. The colour differences for different materials also made it too subjective to identify. Additionally, both methods cannot precisely reflect the temperature field distribution. Using a thermal infrared camera, Shang et al. [179] investigated the temperature field distribution and changing with time (see **Figure 2.48a**), carried out laser-assisted milling by developing inverse heating models by performing extensive temperature experiments and obtained good machining performance.

Zhu et al. [180] developed a numerical model describing the heat transfer and material ablation in a hybrid laser-waterjet micro grooving process for single-crystalline germanium (Ge), showing that the respective calculated and the thermal infrared camera measured quantities are in reasonably good agreement (see **Figure 2.48b**). Fazli Shahri and Mahdavinejad [126] used an Infrared camera to check the HAZ and temperature distribution on the

specimen (see **Figure 2.48c**). The measurement results showed a good agreement with the ablated area. Based on the results demonstrated, they developed a combinatory model (ANN-GA) that is more effective than a trial-and-error ANN model in predicting the HAZ and temperature.

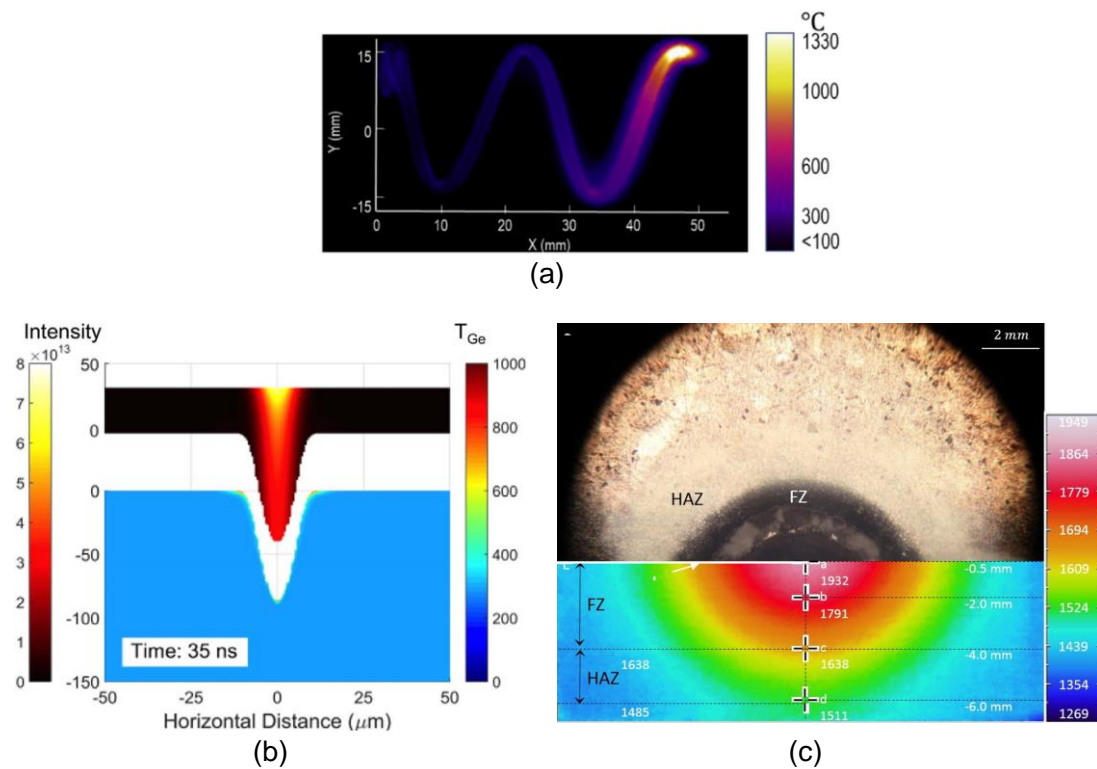


Figure 2.48 HAZ detected by the thermal infrared camera. (a) Temperature field distribution with time [173], (b) calculated and the thermal infrared camera measured results comparison [180], and (c) prediction of temperature distribution [126].

2) Heat Affected Zone Control

In previous studies, researchers control heat-affected zones either by hybrid machining or adjusting parameters. Bharatish et al. [181], studying CO₂ laser drilling on Alumina ceramics, found that both entrance and exit circularities were significantly influenced by hole diameter and laser power, HAZ was influenced by frequency, and taper was significantly influenced by laser power. Popescu et al. [182] carried out studies on the energy intensity distribution

within the laser beam spot, revealing that it obeys the Super-Gaussian distribution, which is consistent with previous studies. As nonmetallic materials have a strong absorption capability at CO₂ laser wavelength (a wavelength of 10.6 μm), Wu et al. [183] investigated producing microchannels on polymethyl methacrylate (PMMA) using a CO₂ laser. It revealed the degree of defocusing phenomenon of the beam increased with the microchannel ablation depth increases, and larger bottom HAZ will be produced.

Currently, the ways to lower the HAZ may include (i) by using ultrashort pulse laser [184] (e.g. nanosecond, picosecond, and femtosecond, etc.) and (ii) hybrid manufacturing (e.g. under-water laser [185-187], waterjet-assisted laser [125, 180, 188, 189]). Salama et al. [184] revealed that the availability of ultra-short laser pulse sources, such as picosecond lasers makes it possible to improve the quality (e.g. heat affected zone less than 10 μm) in laser machining engineering materials. Sun et al. [125] experimentally showed that the HAZ of waterjet-guided laser is smaller than conventional laser beam machining. Feng et al. [172] carried out a hybrid laser-waterjet machining (as shown in **Figure 2.49**) on single-crystal silicon carbide, finding no recast layer and HAZ on the cut side of the hybrid laser-waterjet micromachining. However, a short pulse is at the expense of average power, as the narrower the pulse width, the more difficult it is to obtain high average power. The existing hybrid manufacturing would, on the one hand, add the cost as more accessories (e.g. high-pressure pump, protection cover, etc.) are needed to assist the system and on the other hand low the efficient as the waterjet would also take away the thermal energy [125].

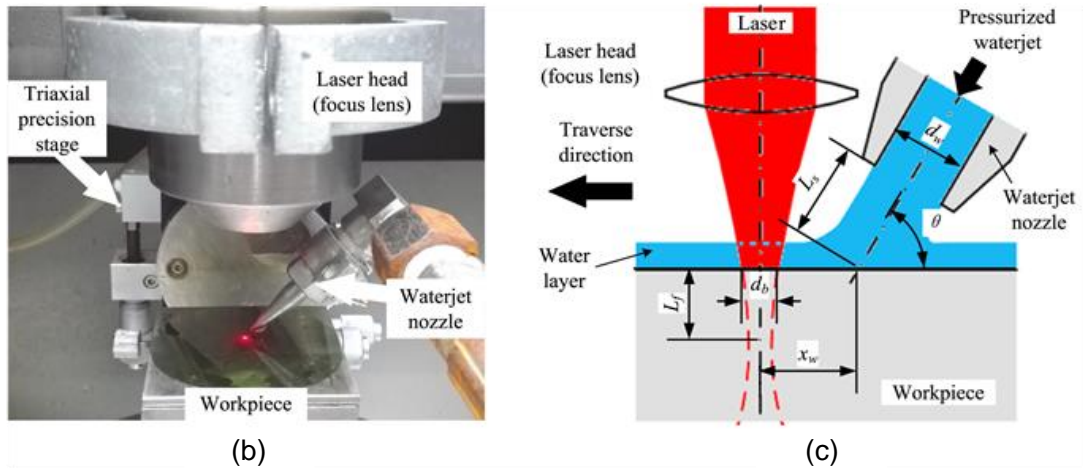


Figure 2.49 The hybrid cutting head. (a) Experimental platform and (b) working diagram [172].

In general, the current methods to lower the HAZ would either be at the expense of average power or at the cost of adding necessary peripheral facilities. Meanwhile, the objective and effective way to accurately detect and quantify the HAZ still keeps an open question. Based on this, it is necessary to develop appropriate methods to detect and control the HAZ exactly. Furthermore, the high-level positioning system and the electromechanical control strategies are highly required to fill the needs. They are indispensable parts to make it available as they are crucial factors to guarantee the proper process parameters to generate a uniform depth, which is an essential obstacle to obtaining accurate ablation.

2.5 Introduction to Simulation Models for Laser Processing

Simulation models are crucial for studying laser processing before machining. With the proper simulation model, the ablation results can be precisely predicted, which is helpful to manufacturing. Li and Guan [190] explored the state-of-the-art methods for the theoretical simulation of the laser ablation of metals and presented the theoretical fundamentals of short pulse laser–metal

interaction. Parandoush and Hossain [19] presented a review of the various methods used for modelling and simulation as well as key research in this field so far and figured out they are indispensable for optimization purposes. It shows that empirical, numerical and analytical models are the most used among various models.

2.5.1 Empirical Model

The empirical model is frequently utilised when there is no evident association between a large number of experimental factors. Therefore, the indirect parameters must be measured by detailed experimental design, then the function based on the empirical formula must be fitted and finally substituted the function relationship into the model. Therefore, the reliability and accuracy of this kind of model seriously depend on the reasonable experimental design, the accuracy and the scale of the data.

Thanks to the least complex of this model type, a pleasant prediction result can be easily achieved with the proper design of the experiment. Therefore, many essential works have been done using the model to study the key machining factors affecting the experimental results. For example, Parthiban et al. [191] used the response surface method to model the CO₂ laser cutting process. It shows that the finish product quality mainly depends on the input parameters such as laser beam power, cutting speed and assist gas pressure (see **Figure 2.50**).

Despite the usefulness of the model, it lacks an understanding of the machining process from the scientific level. Therefore, few works regarding the

laser ablation process were published based on the empirical model.

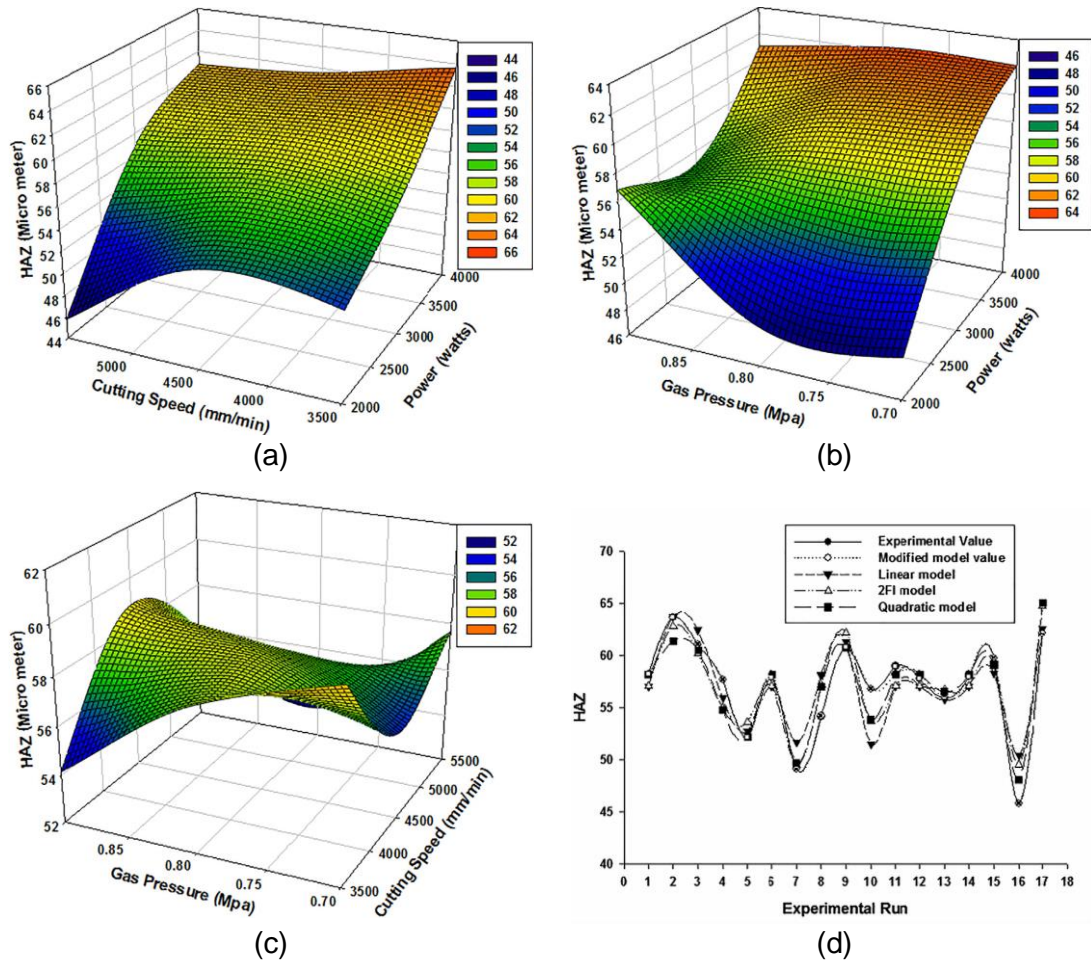


Figure 2.50 Prediction results of the empirical model. Results for HAZ (a) cutting speed vs power, laser power vs gas pressure, and (c) cutting speed vs gas pressure; (d) validation of response surface models with experimental results [191].

2.5.2 Numerical Model

The numerical model is built strictly according to the mathematical-physical relationship, which is time-consuming and computationally expensive and is usually accomplished with the use of finite element multiphysics software such as Ansys, Abaqus, and COMSOL [192, 193]. This is commonly a computer-based numerical analysis that is currently widely used in all fields, including titanium-matrix composites [194] and vivo bio-tissues [195, 196].

Orimi et al. [197] used the COMSOL software to build a model considering the laser parameters like laser power, sampling rate, and optomechanical parameters to predict the machined path's roughness, depth, and thickness. The simulation results are in good agreement with experimental outcomes, which can be used to estimate the effect of the process parameters before the machining. Ma et al. [198] proposed a Finite Element Analysis (FEA) simulation model (see **Figure 2.51**) for Pulsed Laser Ablation (PLA). This model accurately described the energy distribution on component surfaces, which is crucial for further study of the ablation topography.

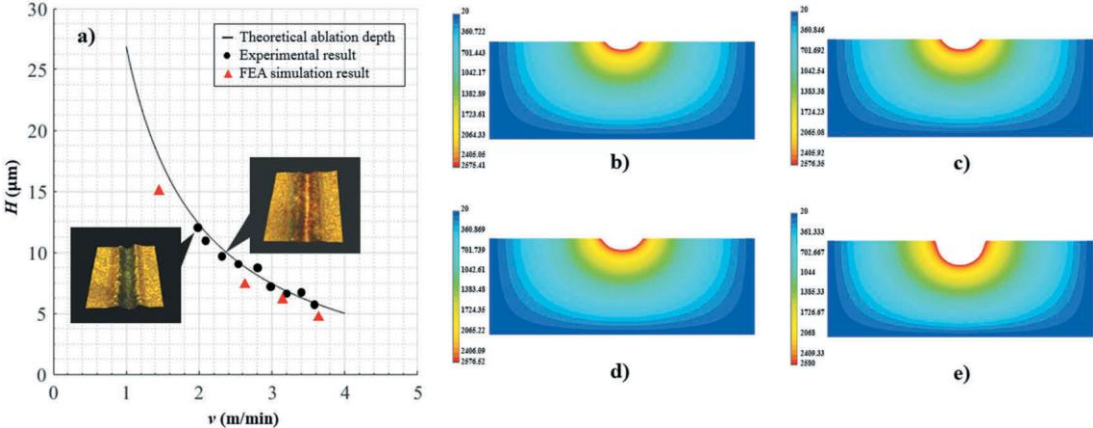


Figure 2.51 (a) Ablation depth (H) against feed rate (v) in FEA simulation and experimental validation (F_0 set as $5.0 \text{ kJ}/\text{m}^2$ and f set as 30 kHz). Simulation time (b) 298.34 ns , (c) 342.86 ns , (d) 407.54 ns , and (e) 744.83 ns [198].

By considering the energy distribution of the laser beam model and element birth and death technique, Moradi et al. [10] developed a numerical simulation of the CO_2 laser cutting process of polycarbonate sheets by a finite element method (see **Figure 2.52**). The results showed the effectiveness of the model when the death of the element was used.

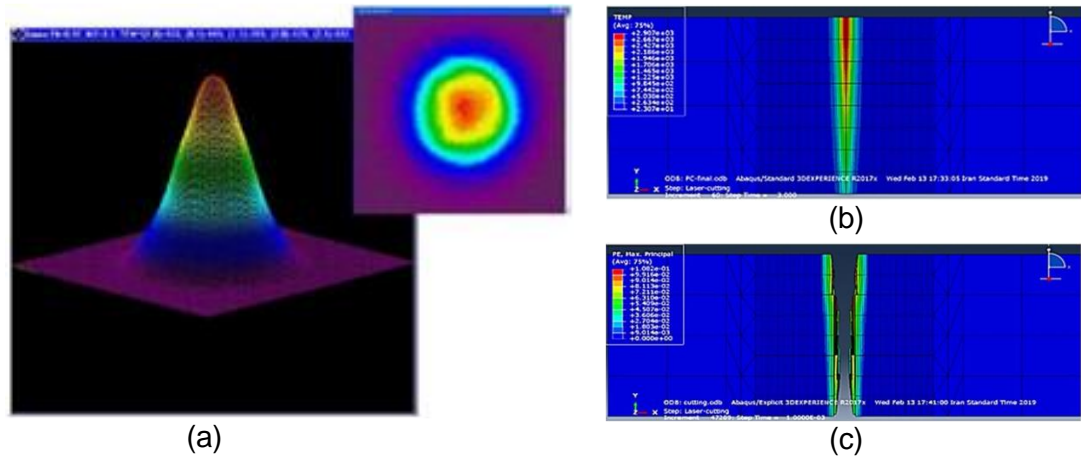


Figure 2.52 (a) Gaussian distribution of the laser beam. The bottom of the thermal simulation model (b) before and (c) after the death of the elements [10].

Otto and Schmidt [143] presented a new but still quite universal numerical simulation model for laser material processing. Simulation results on several processes like laser beam deep penetration welding, drilling or cutting are presented. Finally, an outlook on planned further developments is given, and possible model applications are discussed.

Notably, the numerical model is the most commonly used, and significant progress has been made thanks to the many reliable commercial application software that have been developed making it friendly to be used. With the application of the model, the micro-behaviours within the laser-material interaction area can be observed and studied. Nevertheless, the accuracy and floatability are relatively large based on the conditions such as the modelling level of the researcher and the treatment of the boundary conditions and load cases.

2.5.3 Analytical Model

The analytical model is built with several simplifications and assumptions. It is

a function based on the theoretical relationship calculated by analysing the physical mechanism and establishing the appropriate physical model of the object. As it does not require a lot of processing power, it can be processed by Digital Signal Processing (DSP) and used for online monitoring. However, this model type is challenging as there is no experience or fitting constant in this relationship, and each parameter has a distinct physical meaning.

Criales et al. [199] closely investigated the effects of varying process parameters on the ablated topographies and the resultant microchannel dimensional quality in the polymethyl methacrylate (PMMA) and polydimethylsiloxane (PDMS) polymers by analytical modelling and experiment ($\lambda = 355$ nm UV wavelength). The result showed that the predicted depth and profile are reasonably acceptable (see **Figure 2.53a**). Cha and Axinte [200] developed a transient thermal model of nanosecond pulsed laser ablation to study the effect of heat accumulation during the processing of semi-transparent ceramics. It showed that the non-linear absorption mechanism allows absorption of laser energy for photon energy below the material's bandgap (see **Figure 2.53b**). Furthermore, the ablation threshold investigation experiments reveal a stark difference between the behaviour observed during the ablation of single pulses and multiple pulses. Similarly, Li et al. [201] developed a transient thermal analytical model of a complete single-track profile in wire-fed laser cladding by considering the laser beam energy distribution along with propagation, the heat transfer within the matrix and the heat convection with the environment. Based on this model, the entire shape of the material deposition was analytically modelled, and sensitivity analysis

response to determinations of cell size Δd and time step Δt was also analysed (see Figure 2.53c).

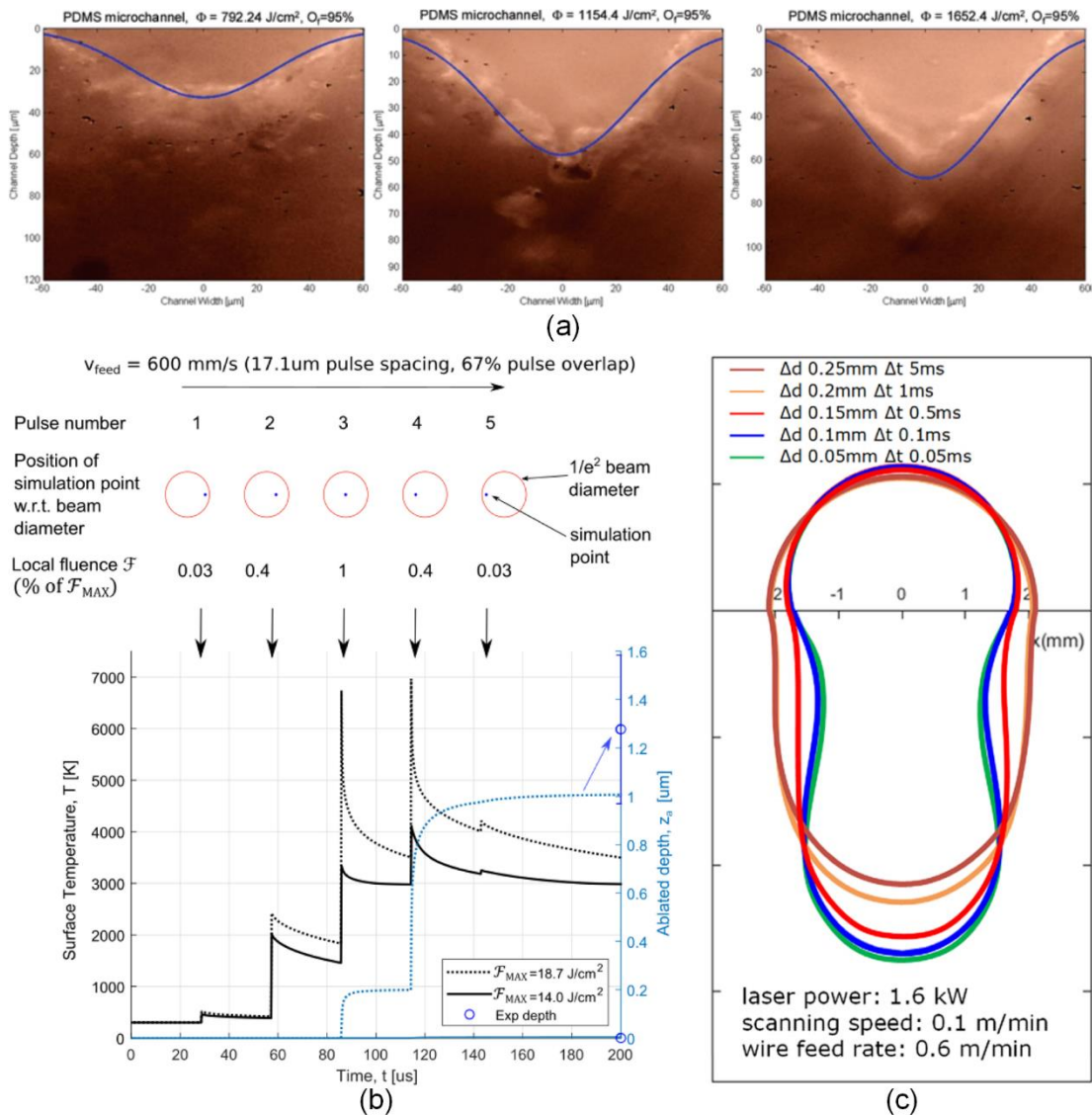


Figure 2.53 (a) Comparison of experimental and predicted microchannel profiles with 95% pulse overlapping under different conditions [199]; (b) surface temperature and ablation depth during trench ablation for heat buildup and temperature-dependent absorption [200]; (c) sensitivity analysis with various determinations of cell size Δd and time step Δt [201].

Two most relevant research works regarding non-metallic inhomogeneous materials analytical modelling have also been found. Peligrad et al. [202] built an analytical model for the CO₂ laser glazing of inhomogeneous workpieces

(clay tiles) based on parabolic melt pool geometry. The theoretical results showed a close correlation with the experimental when the parameter $P_L/\sqrt{d\nu}$ is less than 15 W/mm/s. Salim et al. [203] further developed the analytical model by combining the empirical element to the model and carried out experiments on concrete surface ablation with a continuous CO₂ laser. As a result, a new empirical glazing model (IDGM) for glazing depth measurement is established, which showed a high agreement (96%) with the experiments. Although the results of the improved model are pleasing for non-metallic inhomogeneous materials, they are validated available under limited conditions that they are validated under the maximum laser power of 65 W and the maximum ablation depth of 1.6 mm. Meanwhile, due to the idealised assumptions of the model, it can not be generally applicable.

2.6 Electromechanical Systems for Laser Manipulation

2.6.1 Positioning System and Electromechanical Control

1) Positioning system

Overall, these positioning systems can be divided into two groups, (i) the motor-based conventional group and (ii) the piezoelectric-based group.

(a) Motor-based conventional group

The motor-based conventional group is widely used in the industrial field as it has the advantages of low cost, long-range, simple mechanism, high precision, easy to be controlled, and highly robust, which usually contains components like position and speed controllable motor, screw rod, and slide stage. For example, Chen et al. [204], based on the integral type sliding mode control (SMC) law, designed a conventional ball-screw-driven x-y stage. Experimental

results demonstrate that the single-axis stage system achieves high-precision (10 nm) and long-range (10 cm) positioning performance with repeatability and robustness by the proposed control approaches (see **Figure 2.54**).

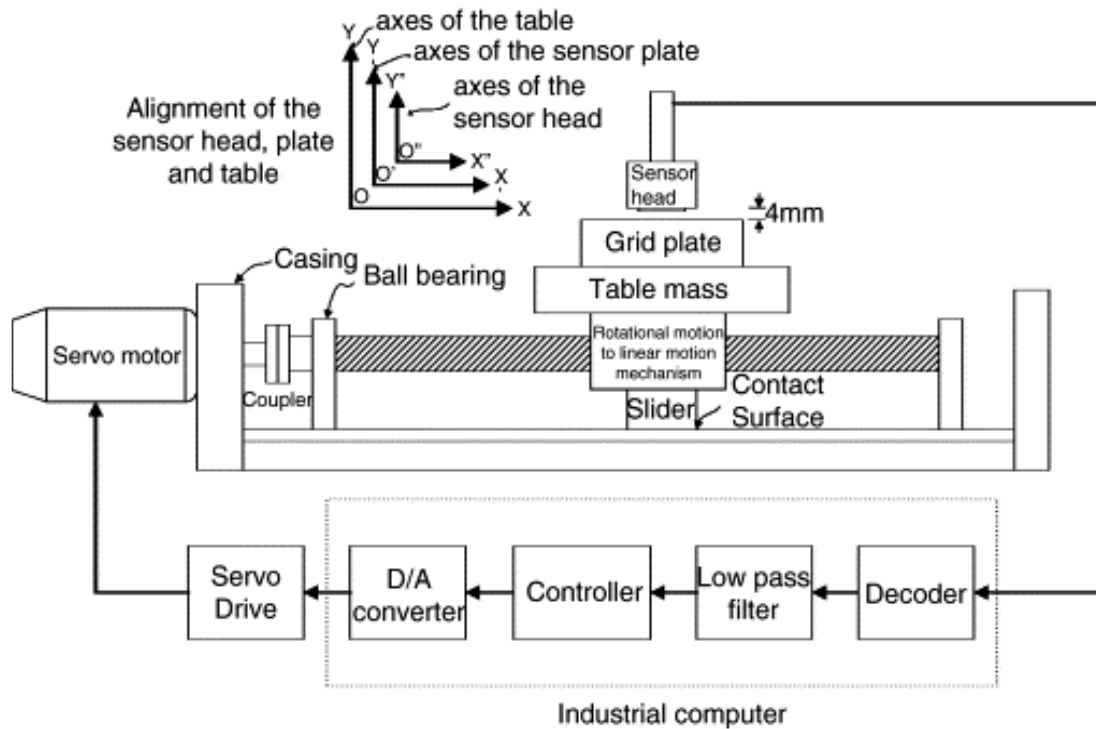


Figure 2.54 The schematic diagram of the single-axis stage [204].

Wu et al. [205] studied the case that a low-stiffness beam driven by a ball-screw slide stage, cooperating with an adaptation algorithm and accelerating sensor, developed a stable movement control system.

Campbell and Jones [206] based motors and screw stages created a fully open-source, versatile, and low-cost 3-D positioning system (**Figure 2.55a**) using 3D printer components. Zhou et al. [207] experimentally studied the wear coefficient of linear stage ball screws and proposed a model for calculating the wear coefficient by considering the wear mechanism at the ball–raceway contact in ball screws (**Figure 2.55b**). It is found that the turning point of the two wear stages corresponds to the wear depth reaching about 20% of the

initial deformation, which is essential for the design to improve the service life.

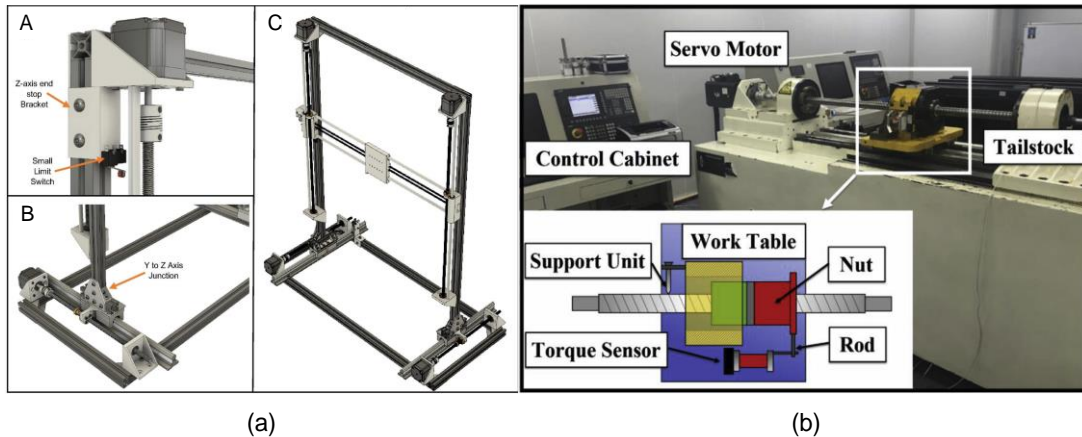


Figure 2.55 The screw based position system. (a) 3D positioning system [206]; (b) running bench for ball screws [207].

(b) Piezoelectric based group

Usually, piezoelectric-based positioning actors have the advantages of rapid response, low energy consumption, low vibration, and miniaturization that are highly emphasized in certain applications. Since Fujimoto [208] first proposed the inchworm-type piezoelectric actuator with flexure hinges (see Figure 2.51a) in 1988, various piezoelectric actuators have been springing up. However, the demerit of the limited working stroke has kept an obstacle in the application. As precision positioning systems with large working stroke (a millimetre or more) and micro/nano-scale positioning resolution are widely required in both scientific research and industries [209], Huang et al. [210] presented a parasitic motion principle linear actuator (see **Figure 2.56b**), which can realise the large displacement range and high speed easily through the parasitic motion of the microgripper. To further overcome the demerit for a single piezoelectric element, Li et al. [211] utilized the electrorheological (ER) clampers to design a linear stepper piezoelectric actuator (see **Figure 2.56c**),

which largely enlarged the working stroke.

Some research has also been carried out on developing a rotary piezoelectric actuator. For instance, Kim et al. [212] developed a novel inchworm-type rotary piezoelectric actuator (as shown in **Figure 2.56d**) based on the combination of flexible belts and flexure hinges. Song et al. [213] designed a piezo-driven rotary actuator (see **Figure 2.56e**) with a simple and compact structure based on the inchworm principle to realize long-range rotary motion. Similarly, Li et al. [214] presented a piezoelectric-driven stepping rotary actuator based on the inchworm motion (see **Figure 2.56f**). With the help of nine piezoelectric stacks and the flexure hinges, the designed actuator can realize large rotary ranges and high rotary speed with high accuracy.

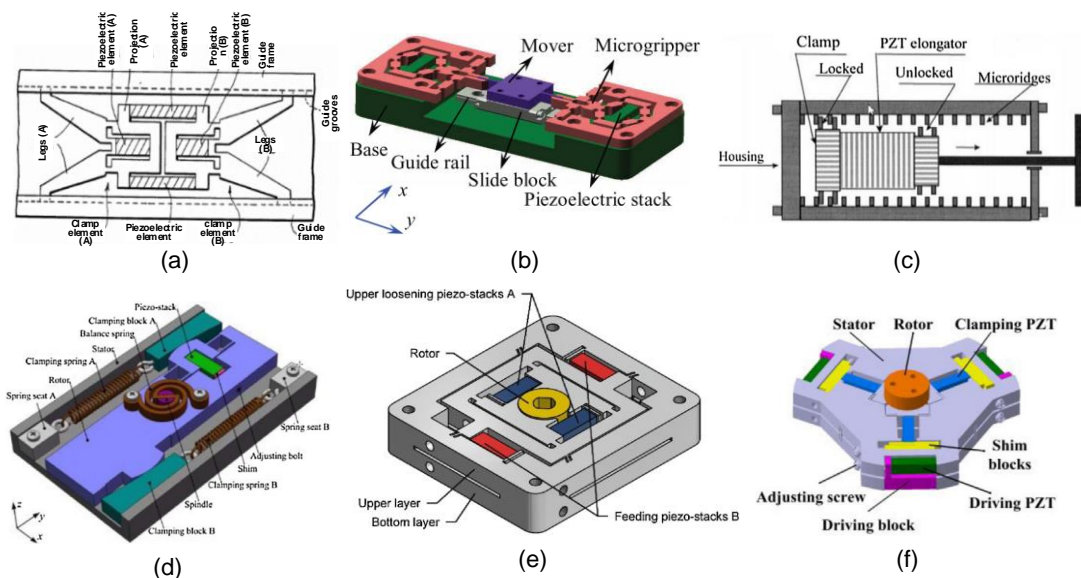


Figure 2.56 Piezoelectric actuator. (a), (b) and (c) linear movement types [208] [210] [211]; (d), (e) and (f) rotary movement types [212] [213] [214].

2) Electromechanical Control

By employing a novel adaptation algorithm to tune the centre frequencies of the notch filters in real-time, Wu et al. [205] developed a control system (**Figure**

2.57) elaborate progressively with the root-locus and bode-plot analyses and a physical interpretation. Moreover, the effectiveness of the control method is verified by extensive experimental tests.

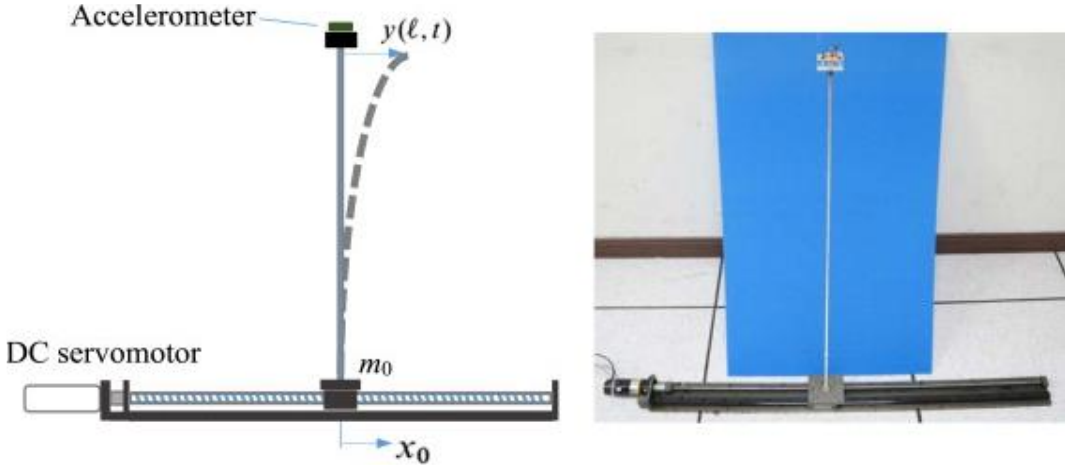


Figure 2.57 Schematic diagram and photo of the flexible beam driven by a ball-screw stage [205].

Saravanakumar et al. [215] gave a review of recent research trends in servo pneumatic positioning systems (the typical structure of the control system is shown in Figure 2.58), pointing out the high nonlinear nature (which affects the system dynamics) of pneumatic drives is the main drawback that limited the replacing of electromechanical and hydraulic drives in many applications.

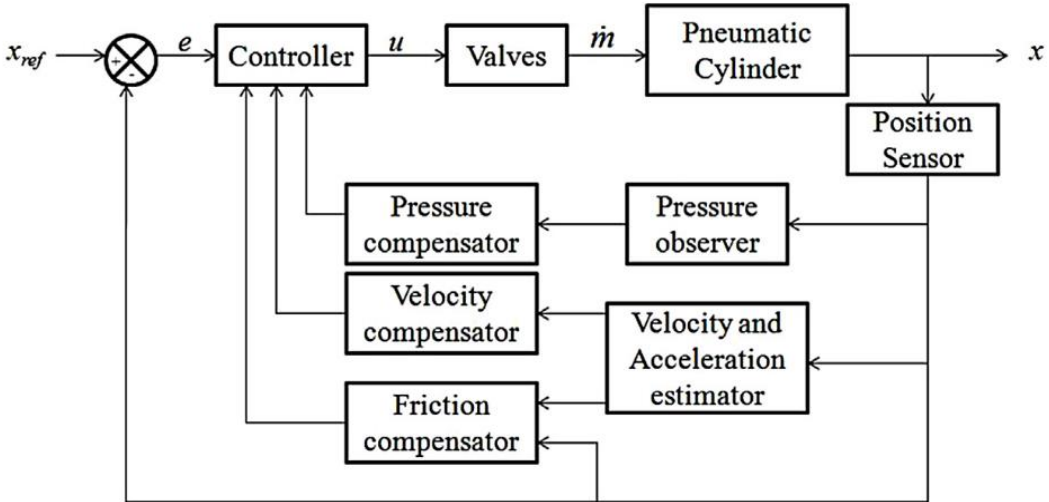


Figure 2.58 The structure of the position control system with observers and

compensators [215].

Beerens et al. [216] presented a reset control approach to improve the transient performance of a PID-controlled nano-positioning motion stage (see details in **Figure 2.59**). The settling time for system overshoots, robustness, and stability improved when the formulated closed-loop system was used. Bisoffi et al. [217] proposed a reset-enhanced PID control theory to deal with nonlinear frictional effects in PID-controlled positioning systems, and extensive simulations and experimental validation on an industrial nano-positioning system were conducted. The result enables transforming the discontinuous function into smooth or at least Lipschitz ones that are very important for stability control.

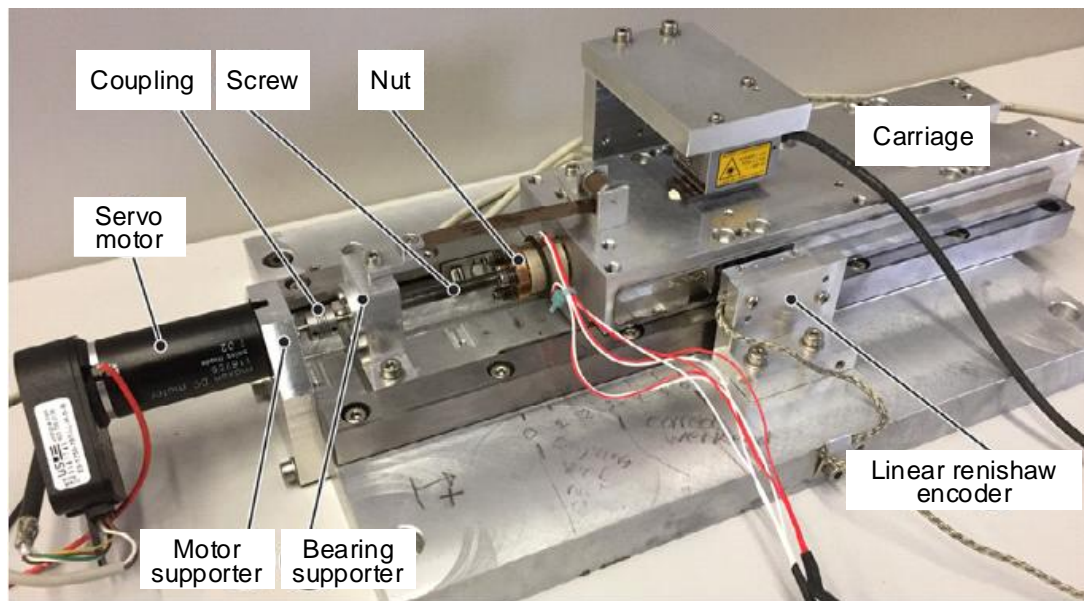


Figure 2.59 Nano-positioning motion stage [217].

As position-controlled tasks have been widely applied for industrial robots, Jiang et al. [218] investigated the state-of-the-art robotic assembly technologies, which provided an overlook regarding the cutting-edge robotic

control technologies. According to the review, the main three control strategies used in this field are passive compliance control [219-222], active compliance control [223-225], and hybrid force/position control. In a passive compliant mechanism, the robot relies on a supplemental mechanism to generate natural compliance with external forces when the end-effector tool contacts an object in the environment [219-221]. The compliance device is not adaptable and has no self-learning capability. However, Artificial Intelligence (AI) algorithms can be used together with passive compliance devices to enhance the adaptability of the assembly robot [222]. Superior to passive compliant, active compliant control [223] measured the contact force/torque and fed back it to the controller to generate the desired trajectory of the robot end effector (as shown in **Figure 2.60**).

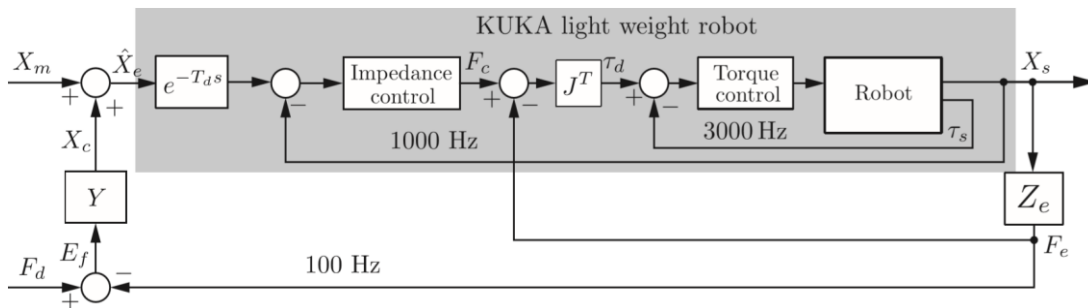


Figure 2.60 Impedance control design with a delay in the outer admittance control loop [223].

Therefore, active compliant control has a broad application prospect [224]. Based on the adaptive fuzzy system, sliding mode control, and standard Lyapunov functions, Jasim et al. [225] proposed an integrated method called the model-free robust adaptive control (MFRAC) strategy to deal with flexible rubber objects. The results showed that the MFRAC strategy was effective for assembly even with uncertainty. Wen et al. [226] used an Elman fuzzy adaptive

controller to adjust the exact distance between the robot and the obstacles [227]. To simultaneously deal with force and position, Wang et al. proposed a hybrid force/position control strategy, a fuzzy sliding mode joint impedance controller (FSMJIC) was applied to merge the vision and force feedback to improve robotic control.

Nascimento and Saska [228] presented a comprehensive review of state-of-the-art works regarding the position and attitude control of multi-rotor aerial vehicles, which helped form a starting point for researchers to initiate their endeavours in linear/nonlinear position, altitude or attitude control. Using Arduino and Python, Campbell and Jones [206] designed and constructed a programmable adaptable XYZ positioning system (see **Figure 2.61**) with high-resolution montages, open-source, free to access or available at low cost.

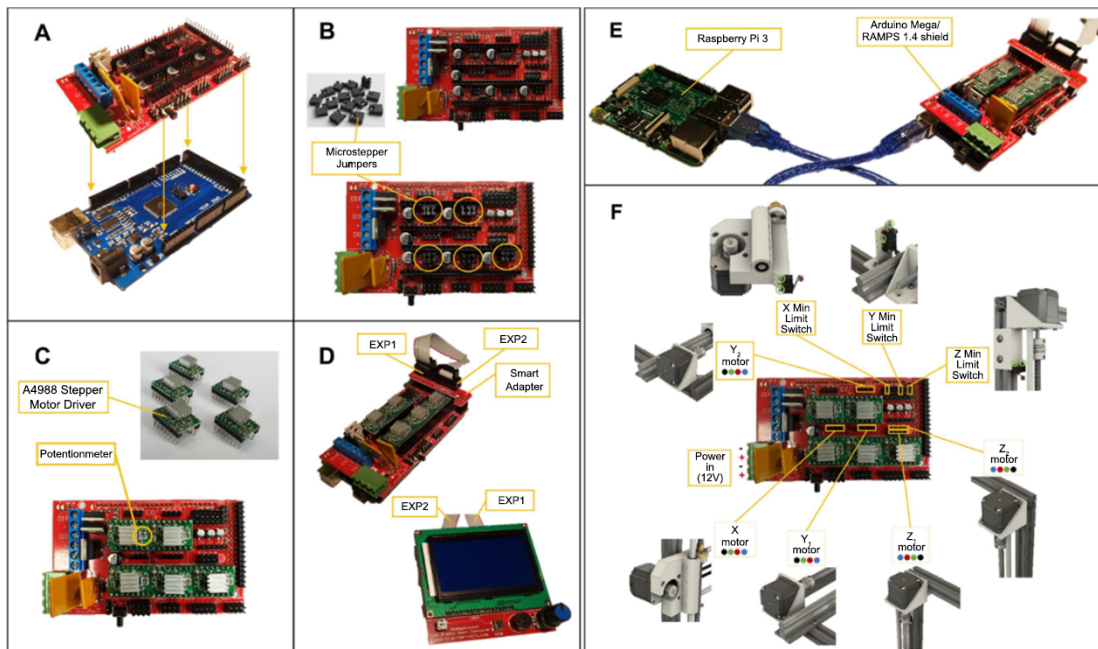


Figure 2.61 Stepper motor wiring of XYZ System [206].

According to the findings, the motor-based conventional group is better suited for long-range movement with high robustness due to its low cost, large motion

range, simple mechanism, high precision, ease of control, and strong robustness. In contrast, the piezoelectric-based group is better suited for miniaturization and rapid response due to its quick response, low energy consumption, low vibration, and usually small size.

For the application in this project, the positioning stage should be featured with a large motion range, high response speed, high robustness, and be easy to be maintained. Therefore, the motor-based conventional group would be the best choice. As for the control strategies, it can be generally concluded that closed-loop-based controls are almost an essential part of a precision positioning system. For instance, the PID control strategy showed outstanding transient performance in the application of the nano-positioning motion stage.

2.6.2 Laser Beam Manipulation

Aside from the positioning system and electromechanical control, the laser shutter is another component that influences precise ablation, particularly fine pattern ablation. Due to the discontinuous nature of complex patterns, laser shutters are essential components to prevent the laser beam from damaging the machined surface.

The laser shutter is a device that controls whether a laser beam passes through or not and is used in many laser-based physics experiments. It is also used in modern optics laboratories to provide time-dependent laser light extinction. However, due to the most used commercially available shutters (like

Thorlabs SH05, Newport 71445, SRS 475, Uniblitz LS2, Edmund NT59596, EOPC CH-40 or EOPC SH-10) are expensive and generally suffer from some combination of high vibration, low pulse rate, or large size, experimenters frequently construct their own shutters. Martínez et al. [229] presented three novel mechanical laser shutter designs that are ideally suited to a specific shuttering application based on a stepper motor (**Figure 2.62a**, for applications requiring low vibrations), a relay (**Figure 2.62b**, for compact and capable of rapid bursts), and a piezoelectric actuator (**Figure 2.62c**, for faster response), respectively.

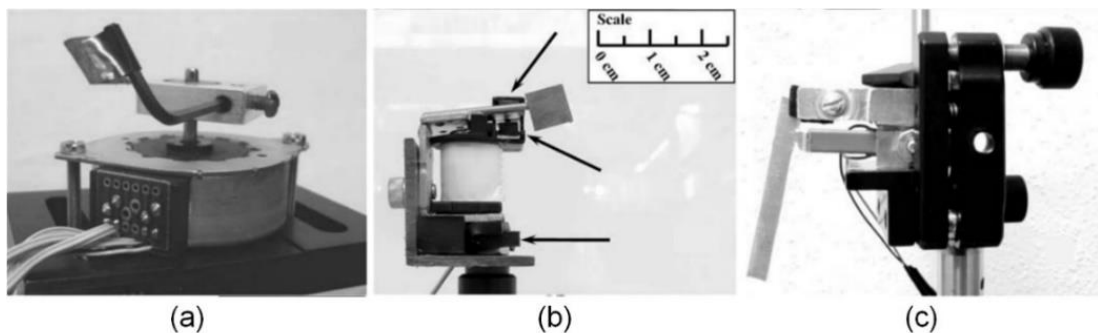


Figure 2.62 Shutters. (a) Stepper motor, (b) relay and (c) piezoelectric actuator [229].

In recent years, Zhang et al. [230] presented a DC electric motor-based mechanical laser shutter design (as shown in **Figure 2.63a**) that by rotating a blade to block and unblock a light beam, achieving a switching speed of above 1.0 m/s with 1 ms activation delay and 10 μ s jitter in its timing performance. The shutter design is simple, easy to replicate, and highly reliable, showing no failure or degradation in performance over more than 10^8 cycles. Given that the short activation delay (short light pulses can be obtained), fast switching

time (pulses with well-defined edges can be obtained), and small timing jitter (precise pulse timing control and synchronization with other parts of the experimental apparatus can be allowed) are the basic and necessary indexes for the most applications. Colquhoun et al. [231] presented a design of an inexpensive and reliable mechanical laser shutter and its electronic driver (as shown in **Figure 2.63b**), enabling the opening and closing durations of less than 800 μs , timing jitter less than 25 μs , and no shutter performance degradation happens after a 5×10^4 cycles test. Besides, the protective shielding of the shutter mechanism up to a laser beam power of 1 W. Bowden et al. [232] reported a piezoelectric cantilever-based shutter to developing the shutter performance further (as shown in **Figure 2.63c**). Compared to conventional electromagnetic shutters, the device is intrinsically low power, acoustically quiet, and has a minimum pulse duration of 250 μs .

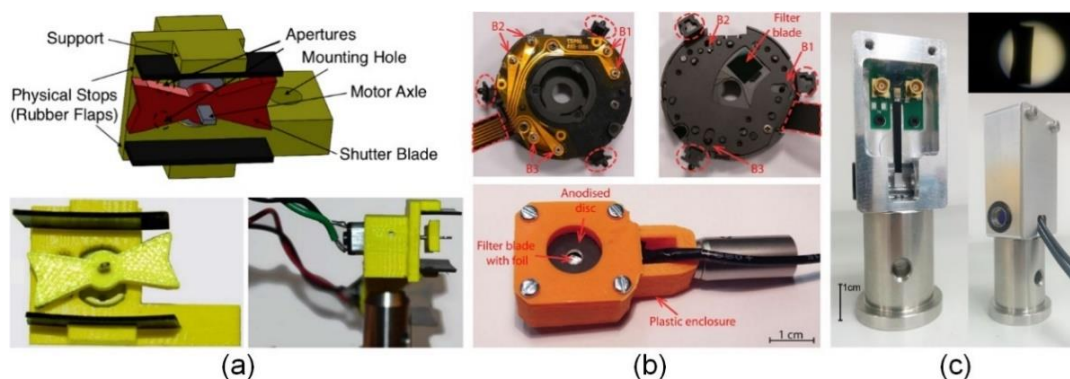


Figure 2.63 Shutters. (a) DC motor shutter [230]; (b) motor-shield shutter [231]; (c) piezoelectric cantilever shutter [232].

According to the review, shutters require excellent timing performance, short activation delays, fast switching times, and low timing jitters to be useful for

precise laser experiments. To be more specific, the general requirements for a laser shutter could be short switching time, slight activation delay, high timing precision or low jitter, low vibration and heat dissipation, an aperture size capable of accommodating the appropriate beam sizes, high extinction ratio, laser power handling sufficient for the blocked beam, and a long operation lifetime. The application in this project basically needs the shutter to be strong enough to tolerate the high temperature and have low vibration. As the relay-based shutters have the disadvantages of shock and vibration, and the piezoelectric cantilever-based shutters are hard to tolerate high laser power shock, which is quite unfavourable for the precision ablation in this application, motor-based shutters show significant advantages in the flexible design that can be fixed to various of applications. Therefore, the motor-based shutters will be an apt selection for the manufacturing system.

2.7 Summary and Research Gaps

Abrasive tools are widely used in our daily life, and it becomes indispensable in the finishing process of modern industries. Moreover, with the development of society, the requirement for high-performance abrasive tools keeps increasing, especially for high-performance grinding wheels. Hence, numerous studies on grinding wheels have been conducted, ranging from abrasive grits, via bonds, to structures to meet the needs. An extensive literature review has shown the massive applications and the superior performance of diamond grinding wheels with resin bond agency in high-

efficiency and high-precision machining due to their high wear resistance and good thermal conductivity. However, although progress has been achieved, various issues (e.g., heat and profile precision-induced problems) have been intensively reported until the successful implementation of structured grinding wheels allows researchers to construct high-performance abrasive tools in a novel approach. Typically, textured and profiled grinding wheels are two widely used structured abrasive tools that are believed to solve most concerning issues in production.

Since both the textured and profiled grinding wheels need to be precisely dressed, various dressing techniques have been intensively studied by scholars. The studies cover dressing by mechanical, electrochemical, and energy beam methods. Among the studies, dressing by energy beam (in particular referring to the laser beam) appears promising thanks to the nature of the laser, such as no tool wear, no vibration, high precision, high efficiency and environment-friendly. Nevertheless, the precise removal of target materials in a controllable way has kept the challenge due to the complex ablation threshold of composites. As a result, the use of this technology is severely constrained.

Therefore, a comprehensive review of laser processing technology has been studied to understand the technical constraints. The review covers the studies on laser classification, laser beam, and the interaction of laser beam with the

target material. Most importantly, the key factors that affect laser processing are reviewed as well. Besides, the research on ablation result evaluation and control is also reviewed (including topography and morphology evaluation, and heat-affected zone identification and control), which helps the experimental studies. Moreover, the work on laser processing simulation models is also presented in the review, which is helpful further to study the temperature distribution in the heat-affected zone and the ablation law regarding ablated profiles change with ablation parameters. Finally, the electromechanical systems for laser beam manipulation are also viewed to guarantee that the research can be experimentally studied and validated.

Despite the fact that previous studies have made progress, no research systematically studied the generation of the textured and profiled grinding wheels in a precise and efficient way, which largely limited the application of the special high-performance grinding wheels. From the intensive investigation of the literature review and the deep understanding of the research topic, the following key gaps may account for the obstacles, and it is believed that with the filling of the gaps, most of the concerned scientific and technical issues are sure to be solved.

1) Controllable laser ablation strategy. Although many patterns on the grinding have been successfully textured, no one reveals the strategies regarding how to select the proper processing parameters. Particularly, no research is carried out using a continuous-wave high-power laser. Therefore,

the texture types for the current grinding wheels are quite limited and it is difficult to precisely profile a grinding wheel in an efficient and low-cost way.

2) Reliable modelling for the time-dependent ablation simulation.

Time-dependent modelling is a key to understanding the temperature field distribution in the heat-affected zone, a series of analyses can be made based on the model to predict the material deterioration and the ablation topography. However, little research has been performed to study the time-dependent modelling simulation.

3) Specialised equipment for the performing of the experiments.

Specialised equipment is highly needed for the validation of the modelling results and to precisely control the experimental variables, but most of the equipment used in the literature review is a standard platform they are hard to be available for all the needs of the experiments, especially for the custom validation of the simulation model and to conduct the relevant experiments to precisely study the ablation law.

Chapter 3

Methodology

This chapter will introduce the platform establishment, modelling process, experimental procedures and research approaches utilised to conduct the research and achieve the objectives, which is the crucial chapter to understanding the research.

3.1 Methodology Background

Studying the material removal mechanism, exploring the materials removal model, and establishing the corresponding predictive models for the ablation result are the overall clues for this study. Finally, based on the study's findings, a specialised laser ablation platform was developed to generate textured and profiled grinding wheels. To be specific, four main parts have been included in accomplishing the aim and objective: (i) development of the specialised manufacturing system; (ii) establishment of the analytical model; (iii) generation of textured flat grinding wheels and (iv) profiled grinding wheels based on the understanding of the laser ablation law on resin-band diamond grinding wheel.

The material's thermal response to laser ablation parameters will be investigated using the analytical model first. It is helpful to develop an analytical model for understanding the ablation process and developing a predictive model for the ablated topography. The material removal mechanism and the ablation behaviours of laser beams on workpiece materials can be understood. The ablation parameters on the ablated topography can be investigated. The

primary causes, identification, and active control of the heat effects zone can be investigated.

With the understanding of the ablation law, a systemically experimental plan and platform will be set. Then a further study regarding the material removal strategies can be developed with the predictive models and experiment platforms. The ultimate goal of precise generation of textured and profiled grinding wheels can be achieved using the developed material removal strategies. The flow chart represented the methodology for the research programme was shown in **Figure 3.1**.

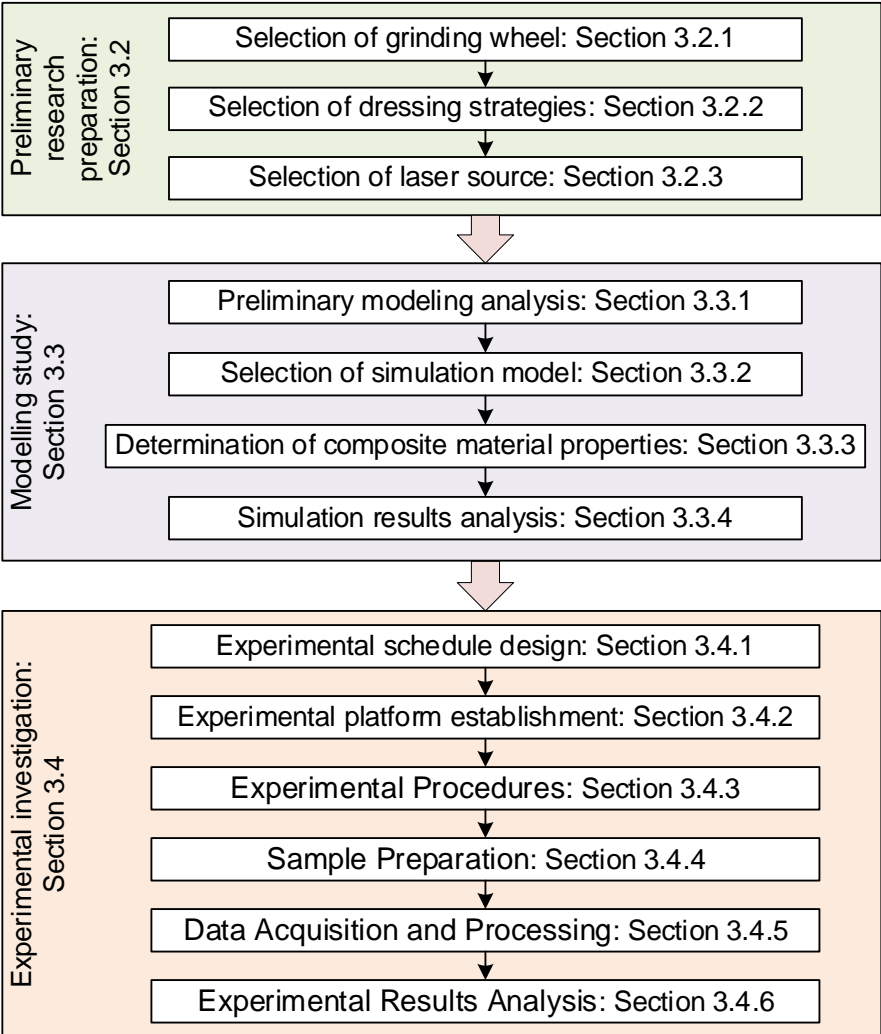


Figure 3.1 Flow chart of the methodology for the research programme.

3.2 Preliminary Research Preparation

3.2.1 Selection of Grinding Wheels

The diamond grinding wheels (D125N75B771/8, 3M, Ltd) with a resin bond agency (see details in **Figure 3.2**) are selected for the studies. An extensive literature review in Chapter 2 has shown the massive applications and the superior performance of diamond grinding wheels with resin bond agency in high-efficiency and high-precision machining due to their high wear-resistance and good thermal conductivity. Meanwhile, as diamond abrasive tools are top-rated in industrial applications for their superb performance, they are widely used in different industrial developed regions [2]. Therefore, the studies on the resin-bond diamond grinding wheel have a significant sense and application prospect.

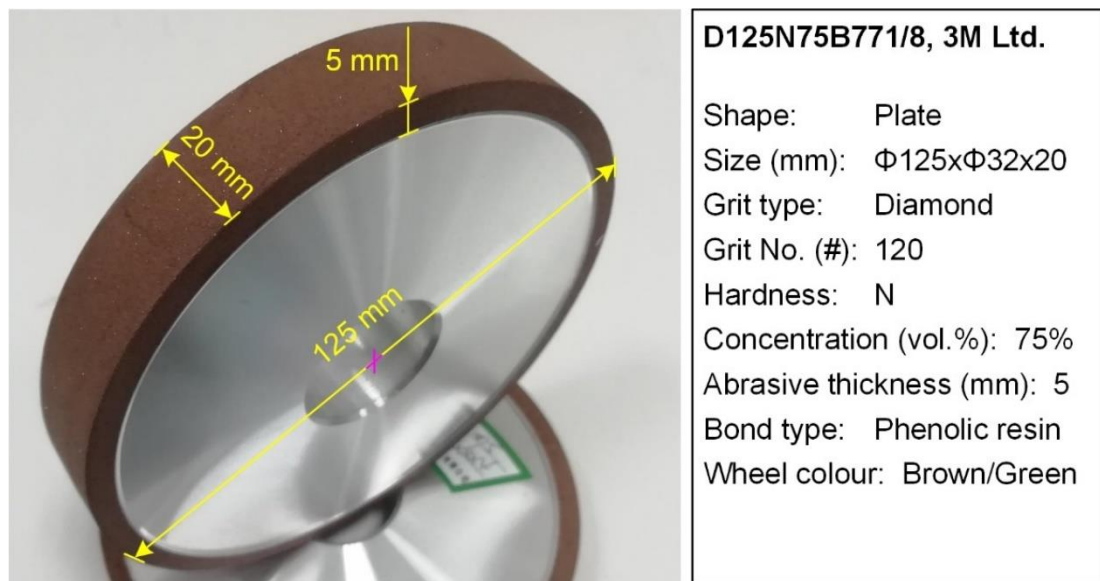


Figure 3.2 Selected resin bond diamond grinding wheels.

3.2.2 Selection of Dressing Strategy

As reviewed in the literature, despite the disadvantages in the dressing strategies of the laser method, it is still considered a promising way to

manufacture structured abrasive tools in general due to the advantages such as high efficiency and low noise and no tool wear happens. Therefore, laser dressing technology is employed in this study.

The laser dressing technique cyclically scans the whole surface of a grinding wheel. It removes material selectively to allow the grinding wheel to achieve the requisite size and profile as well as suitable surface topography. There are two types of laser beam incidence [233]: (i) tangential (see **Figure 3.3a**) and radial (see **Figure 3.3b**).

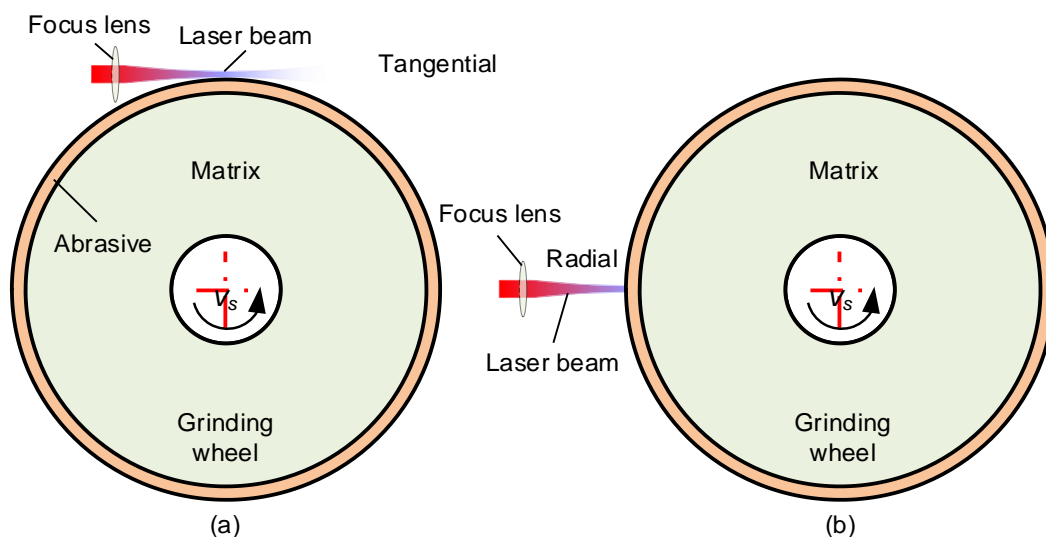


Figure 3.3 Schematics of incidence of laser beams in the (a) tangential and (b) radial directions.

Apart from Deng et al. [234, 235] using tangential ablation for precision profile and Zhou et al. [236] utilising a combination of tangential and radial laser shaping of concave rectangular profile diamond wheels, most of the research are conducted by radial incidence [237-239]. Although tangential ablation has the advantages of the precise profile, it comes at the expense of efficiency as the laser beam spot can not be wholly located on the grinding wheel.

3.2.3 Selection of Laser Source

This project aims to make the laser dressing technology for resin-bond diamond grinding wheels industrial available. Therefore, the reliability and efficiency of the laser generator are the most two concerning issues. As having learned from the review, CO₂ and fibre lasers are the two most widespread industrial used laser generators. Both of them can achieve a higher average laser power with high reliability. However, the fibre laser has a higher beam quality than the CO₂ laser, enabling deeper ablation. In comparison, CO₂ has the advantage of better absorptivity for non-metallic materials than fibre lasers, which removes the target materials in lower laser power and benefits energy conservation.

To achieve the goal, both two kinds of lasers are employed in this study. The texturing process on the flat grinding wheel and the profiling process on the grinding wheels with a relatively shallow profile will be conducted by the CO₂ laser (the work presented in Chapter 4, Chapter 5, Chapter 6 and Chapter 9). The details of the CO₂ laser machine (LE900, Hongfan Tech. Company) parameters are shown in **Table 3.1**.

Table 3.1 Detailed parameters of the used CO₂ laser.

Maximum power (W)	Wavelength (μm)	Repeat frequency (Hz)	Focal spot (mm)	Focal length (mm)
60	10.6	5000	0.3	12.5

Meanwhile, the other works aimed at a deeper ablation depth will be performed by fibre laser (the work presented in Chapter 7 and Chapter 8). The details of the fibre laser machine (YLS-2000, Han's machine, IPG Photonics) are shown

in **Table 3.2**.

Table 3.2 Detailed parameters of the used fibre laser.

Maximum power	Wavelength	Minimum focus	Repeat frequency	Duty cycle	Off-focus distance
2,000 W	1.06 μm	0.15 mm	3,000 Hz	1% - 100%	\pm 5 mm

3.3 Modelling Study

3.3.1 Preliminary Modelling Analysis

The diamond grinding wheel surface is irradiated with a high-intensity laser beam during the ablation process. Therefore, changes in processing parameters such as feed rate, laser power, duty cycle, and laser type can potentially control the ablation width and depth.

The target materials on the grinding wheel absorb the laser energy and either melt, burn, vaporise away, or are blown away by a gas jet. Thus, the following aspects should be considered in the modelling:

1) The first thing to consider when texturing diamond abrasive tools is the ablation threshold, determined by both the laser parameters (discussed later) and the target material [240]. Therefore, a novel consideration here is the non-uniform, multi-material, and non-metallic nature of diamond abrasive tools (made of diamond and polymer resin) when performing laser ablation texturing of grinding wheels because nearly all the previous studies focused on the ablation of either homogenous materials [241, 242] or metallic materials [243, 244].

The ablation threshold refers to the minimum laser fluence for which the target

material undergoes permanent damage, and at least one layer (component) of material is removed [245]. Based on the classic laser ablation theory [246, 247], the threshold of a homogenous material can be described as **Equation (3.1)**:

$$I_{th} = \frac{\lambda}{A} \left(\frac{\pi}{4\alpha t_0} \right)^{\frac{1}{2}} (T_c - T_0) \quad (3.1)$$

where λ is the thermally conductive rate of the material, A is the material absorption rate of laser radiation, α is the thermal diffusivity of the material, t_0 is the laser dwelling time, T_c is the crucial temperature, and T_0 is the room temperature.

The equivalent laser fluence, F , corresponding to this set of parameters can be obtained by **Equation (3.2)** based on the schematic in **Figure 3.4** [118]:

$$F = \frac{P_m}{2S_{o1} + S_{ABCD}} = \frac{P_m}{\pi r^2 + 2rvt} \quad (3.2)$$

where P_m is the average power (W), t is the ablation duration (s), r is the laser spot radius (mm), and v is the laser feed rate (mm/s).

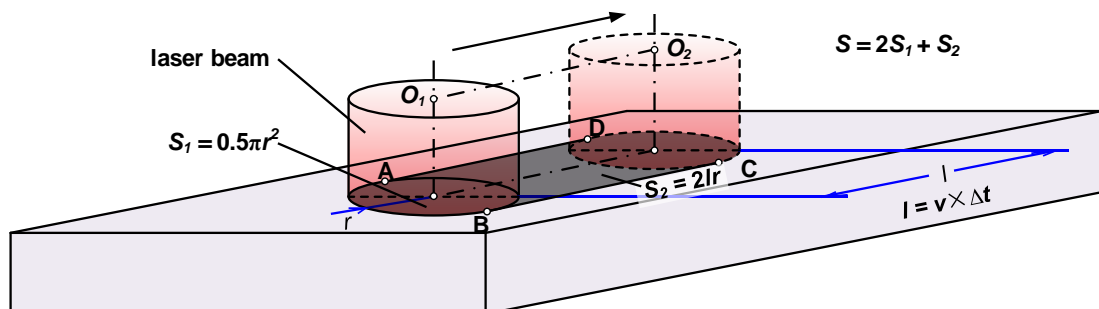


Figure 3.4 The calculation diagram of laser fluence.

2) Then the second factor would be the modelling approach, which can be determined by its relevance, applicability, and reliability. Unfortunately, although there are plenty of available models, most of them are only validated

in low laser power or short-pulsed laser, and no model has been verified applicable in high laser power yet.

3.3.2 Simulation Model Selection

Based on the understanding of the literature review, three modelling methodologies could be chosen for this project: (i) empirical modelling, (ii) numerical modelling and (iii) analytical modelling.

(1) Empirical Modelling

It can be seen from the review that this model is often employed to solve practical problems because the response estimation results can approach the actual response surface and achieve a satisfactory prediction [248]. A pleasing prediction result can be achieved with the proper design of the experiment, thanks to the least complex of this model type.

As the ablated result is affected independently by laser power, duty cycle, and feed rate in the experiment, a second-order estimation regression equation is employed to establish the prediction model for the ablation result.

The second-order regression prediction model of the laser power and the duty cycle/feed rate interaction of the two factors is given by **Equation (3.3)**:

$$f(x_1, x_2) = \varepsilon + \beta_1 x_1 + \beta_2 x_2 + \beta_{12} x_1 x_2 + \beta_{11} x_1^2 + \beta_{22} x_2^2 \quad (3.3)$$

where x_1 is the laser power (W), and x_2 is the duty cycle D_c (%) / feed rate f (mm/s), ε , β_1 and β_2 , β_{12} , β_{11} and β_{22} are the algebraic factors.

(2) Numerical Modelling

This model enables the simulation to combine the laser beam profile model with heat dynamic transfer theory, investigating the time-dependent temperature field distribution in the ablation area.

The power density distribution at the beam cross-section has a significant impact on physical phenomena in the laser-induced melt pool that is largely determined by the laser beam profile (as shown in **Figure 3.5**).

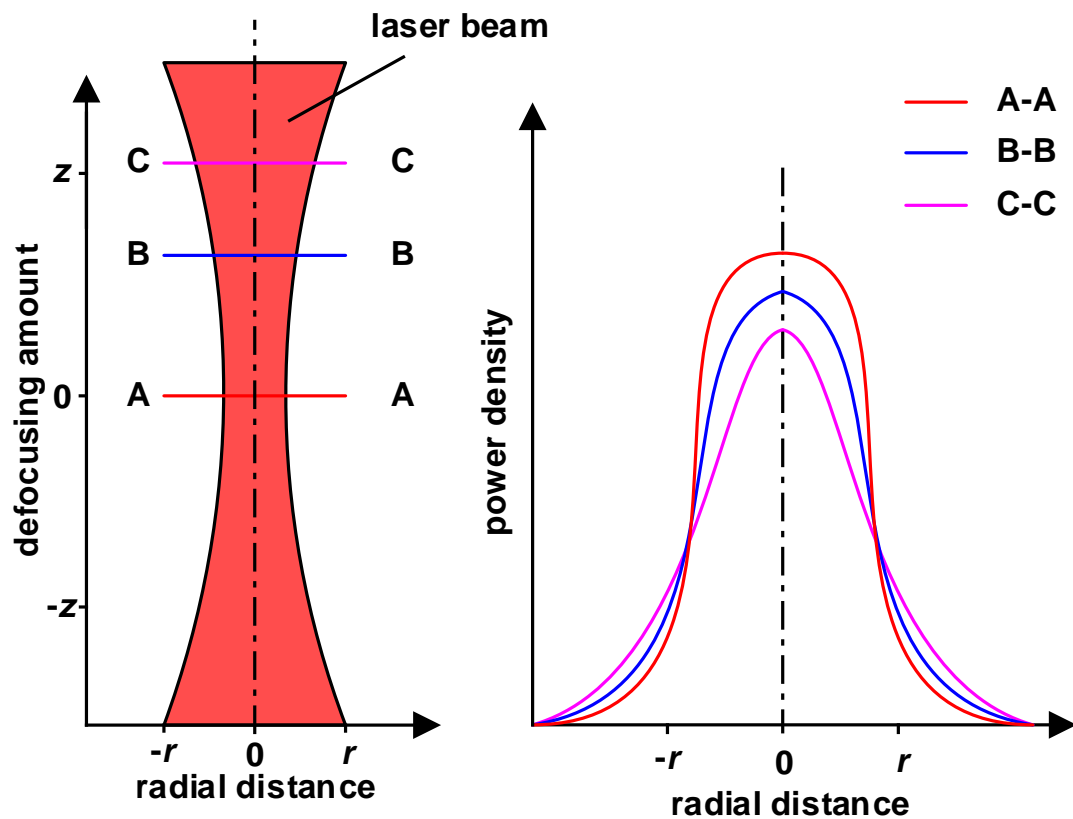


Figure 3.5 The laser beam profile model.

Wu et al. studied the laser beam profile model and illustrated that the super-Gaussian beam model (SGB) has attractive features in certain laser applications [249], e.g. in laser material processing, in the machining of sharp edges and flat bottoms, in the drilling of a hole with low wall taper, small

eccentricity, and minimal heat-affected zone. Shealy and Hoffnagle represented the SGB model according to the following form as **Equation (3.4)** [250]:

$$I_s(x, y) = \frac{2^{1/k} k P_0}{\pi r_s^2 \Gamma\left(\frac{1}{k}\right)} \exp \left[-2 \left(\frac{x^2 + y^2}{r_s^2} \right)^k \right] \quad (3.4)$$

where r_s is the SGB radius defined by the $1/e^2$ method; k is the super-Gaussian order; and Γ represents the Gamma function.

Reference [250] showed that when the defocusing amount was $|z| \leq 3.21 \text{ mm}$, the section power density distribution in the near field obeys the SG distribution and the goodness-of-fit index exceeds 0.98 when the k value is approximately 7.7. **Figure 3.6** shows the energy density distribution results of a typical CO₂ laser beam under Gaussian and Super-Gaussian models. It showed that the figure for GB had a tapered top (see **Figure 3.6a**) while that for SGB had a hat-top (see **Figure 3.6b**), indicating that steep edges can be simulated by using the SGB model.

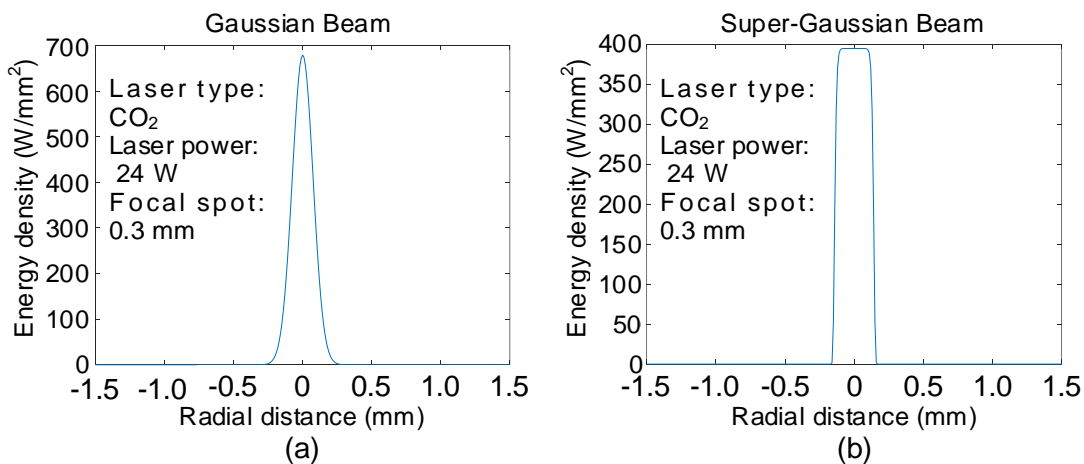


Figure 3.6 The GB and SGB laser beam model. (a) GB model and (b) SGB model.

The diagram illustrating heat transfer from the laser beam to the workpiece is shown in **Figure 3.7**. It is clear that the laser focus covers a certain area in the workpiece, and the focused area will radiate the amount of heat to the ambient area (the nodes around), which causes the temperature to rise.

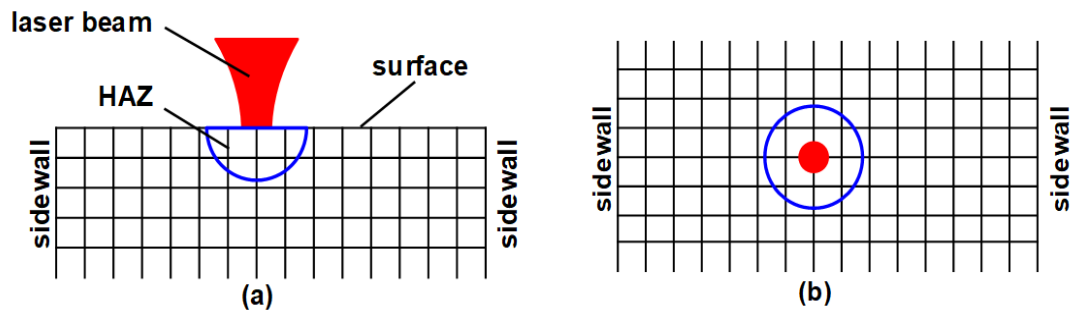


Figure 3.7 The diagram illustrating heat transfer from the laser beam to the workpiece. (a) The front and (b) top view.

The basic physical situations for the nodes are shown in **Figure 3.8**, wherein the dashed lines indicate a volume element. For the Interior node, the temperature value will be the average value of four nodes around (see **Figure 3.8a**). For the convection boundary node, the temperature value will equal the average values of the three nodes around and the boundary temperature (see **Figure 3.8b**). The value for the exterior corner with convection boundary equals the average values of two boundary nodes and two boundary temperatures (see **Figure 3.8c**). Finally, the temperature value for the interior corner with convection boundary equals the average values of four nodes around and the two boundary temperatures (see **Figure 3.8d**).

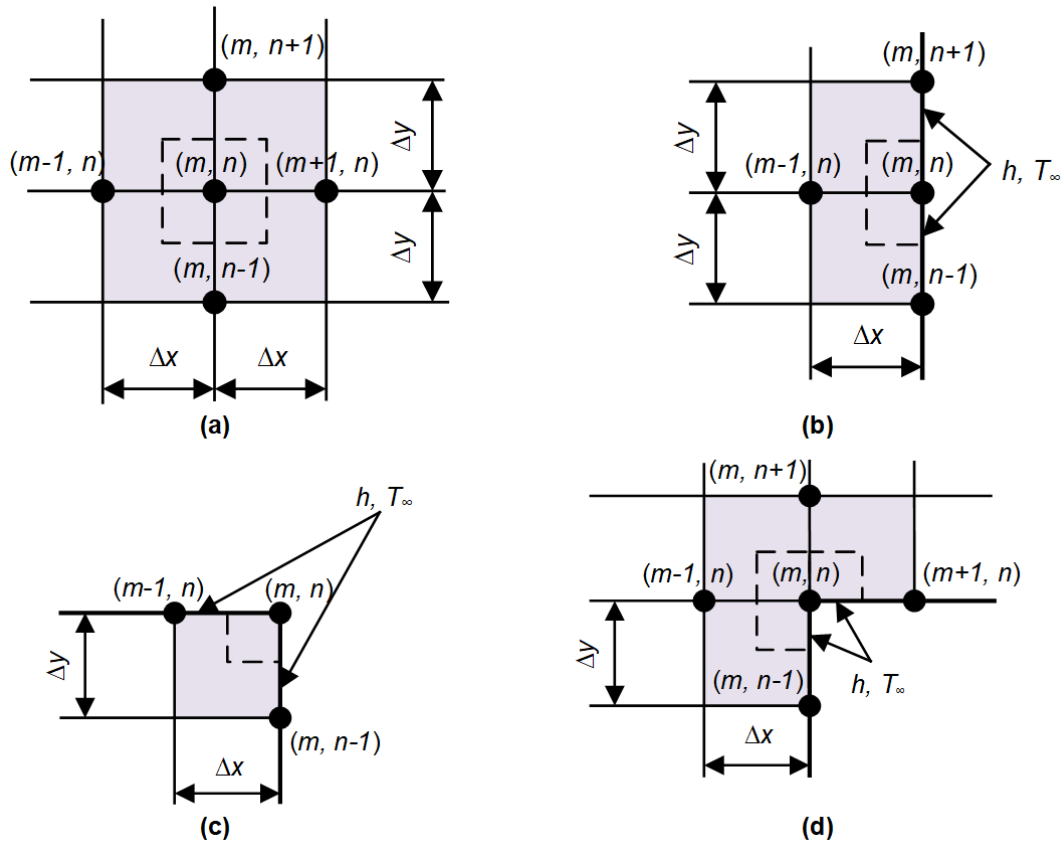


Figure 3.8 Nodes physical situations (Dashed lines indicate volume element).
 (a) Interior node; (b) convection boundary node; (c) exterior corner with convection boundary; (d) interior corner with convection boundary.

Implicit nodal equations for each physical situation (Dashed lines indicate volume element) are shown below:

For the situation described in **Figure 3.8 (a)**:

$$T_{m,n}^{p+1} = \text{Fo}(T_{m-1,n}^p + T_{m,n+1}^p + T_{m+1,n}^p + T_{m,n-1}^p - 4T_{m,n}^p) + T_{m,n}^p, \quad \text{Fo} \leq \frac{1}{4} \quad (3.5)$$

For the situation described in **Figure 3.8 (b)**:

$$T_{m,n}^{p+1} = \text{Fo}[2\text{Bi}(T_{\infty}^p - T_{m,n}^p) + 2T_{m-1,n}^p + T_{m,n+1}^p + T_{m,n-1}^p - 4T_{m,n}^p] + T_{m,n}^p, \quad \text{Fo}(2 + \text{Bi}) \leq \frac{1}{2} \quad (3.6)$$

For the situation described in **Figure 3.8 (c)**:

$$T_{m,n}^{p+1} = 2Fo[T_{m-1,n}^p + T_{m,n-1}^p - 2T_{m,n}^p + 2Bi(T_{\infty}^p - T_{m,n}^p)] + T_{m,n}^p, \quad Fo(1 + Bi) \leq \frac{1}{4} \quad (3.7)$$

For the situation described in **Figure 3.8** (d):

$$T_{m,n}^{p+1} = (4/3)Fo[T_{m,n+1}^p + T_{m+1,n}^p + T_{m-1,n}^p - 3T_{m,n}^p + Bi(T_{\infty}^p - T_{m,n}^p)] + T_{m,n}^p, \quad Fo(3 + Bi) \leq \frac{3}{4} \quad (3.8)$$

(3) Analytical Modelling

For the background mentioned above, the model established based on melt pool geometry is presented. In this laser ablation process, the temperature distribution in the workpiece can be described by the heat conduction of **Equation (3.9)** [251]:

$$\rho c_{\rho} \frac{\partial T}{\partial t} - \nabla \cdot (K \nabla T) + \nabla \cdot (U \rho c_{\rho} T) = Q \quad (3.9)$$

where the temperature at (x, y, z, t) is T (K), and t is the time (s), K is the thermal conductivity ($\text{W} \cdot \text{m}^{-1} \text{K}^{-1}$) of material, ρ is the density of the material ($\text{Kg} \cdot \text{m}^{-3}$), c_{ρ} is the thermal capacity of material (J/kg/m), U is the velocity of the heat-fluid flows as a reference to (x, y, z) system coordinating stationary with respect to the beam of laser, while the heat source and sinks in the workpiece are denoted by Q (W/m^3).

In the process, radiation, conduction and convection heat transfer are involved. Energy may be reflected back to the environment when the laser beam reaches the workpiece surface, representing radiation heat transfer. The energy could be absorbed and cause the workpiece to fail or deteriorate, standing for conduction heat transfer. The rest of the energy may be dissipated

from the interaction zone of the laser beam and material with the effect of fluid flow, referring to convection heat transfer. Given its boundary and initial condition, a well-known approach to solving heat conduction, as shown in **Equation (3.9)**, is to use Green's functions [251].

A simple analytical model can be derived by considering the heat flow down the centreline of the melt pool as approximately one-dimensional. This assumption implies that the melt pool is extensive and flat, though nearly parabolic in practice (see **Figure 3.9**) [252].

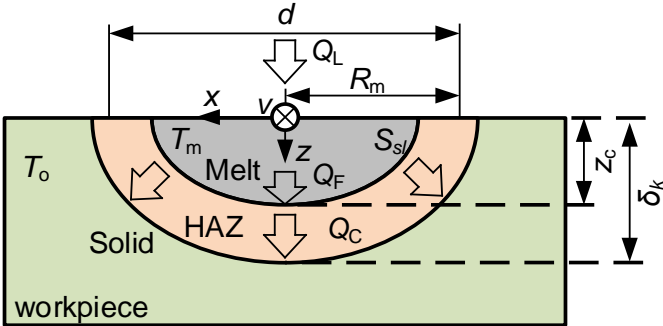


Figure 3.9 Melt pool geometry and energy flows in a quasi-stationary case [202].

In the figure, d is the laser beam diameter, v is laser beam move speed, Q_L is the absorbed laser energy, R_m is the melt pool radius, Q_F is beside the melt pool required energy, Q_C is the heat conduction energy conveyed from the liquid-solid boundary of the melt pool into the unmelt material, z_c is the melt pool depth, δ_k is the heat affect zone depth, T_o is the initial sample ambient temperature, T_m is the melting temperature.

The solid-liquid interface parabolic form is defined by **Equation (3.10)** [202]:

$$z = z_c \left(\frac{x^2 + y^2}{R_m^2} - 1 \right) \text{ for } x^2 + y^2 \leq R_m^2 \quad (3.10)$$

By assumption of a matched diameter of the melt pool and the laser beam, the total energy required for processing is higher than the latent heat of fusion and neglecting T_0 , z_c can be expressed as **Equation (3.11)** [202]:

$$z_c = \left(\frac{2A}{\rho c_p C_1 T_m \sqrt{\alpha}} \right) \frac{P_L}{\sqrt{d v}} \quad (3.11)$$

where A is the absorptivity of the material under process to Nd: YAG fibre laser (%), α is the material thermal diffusivity ($*10^{-6}m^2/s$), ρ is the material density (kg/m^3), c_p is the specific heat capacity ($J/kg/K$), C_1 is a constant, T_m is the material melting temperature (K), d is the laser spot diameter (m), v is the traverse speed (m/s), and P_L is laser power (W).

By comparison, each model has its scope of optimum application. For example, the transient numerical method for the unsteady-state conduction has a superior understanding of the ablation process and the dynamic temperature field changes within the ablation zone. As it considers the laser focus size and the laser beam energy propagation, the time-dependent temperature field can be generated for the calculation of ablation depth changes. The empirical model can be used to predict the ablation results with higher reliability when it is hard to build a comprehensive physical model, while the analytical model is well to be used to compare the ablation results with the other two models.

3.3.3 Determination of Composite Material Properties

The resin bond diamond abrasive wheel is employed in this paper, for it has the advantages of good self-sharpening ability and low risk of grinding burn, the details of the wheel are shown in **Table 3.3**. As the grinding wheel is a multi-material-based tool, to study the whole grinding wheel material properties, each of the main ingredients should be investigated first, including the exact content and properties.

Table 3.3 Specifications of the used diamond grinding wheel.

shape	size (mm)	type	grit No. (#)	Har.	Con. (vol.%)	Thick. (mm)	bond
plate	Φ125×Φ32×20	Diamond	120	N	75%	5	resin

The main ingredients for this kind of wheel include grit, resin bond, and pore (as shown in **Figure 3.10a**).

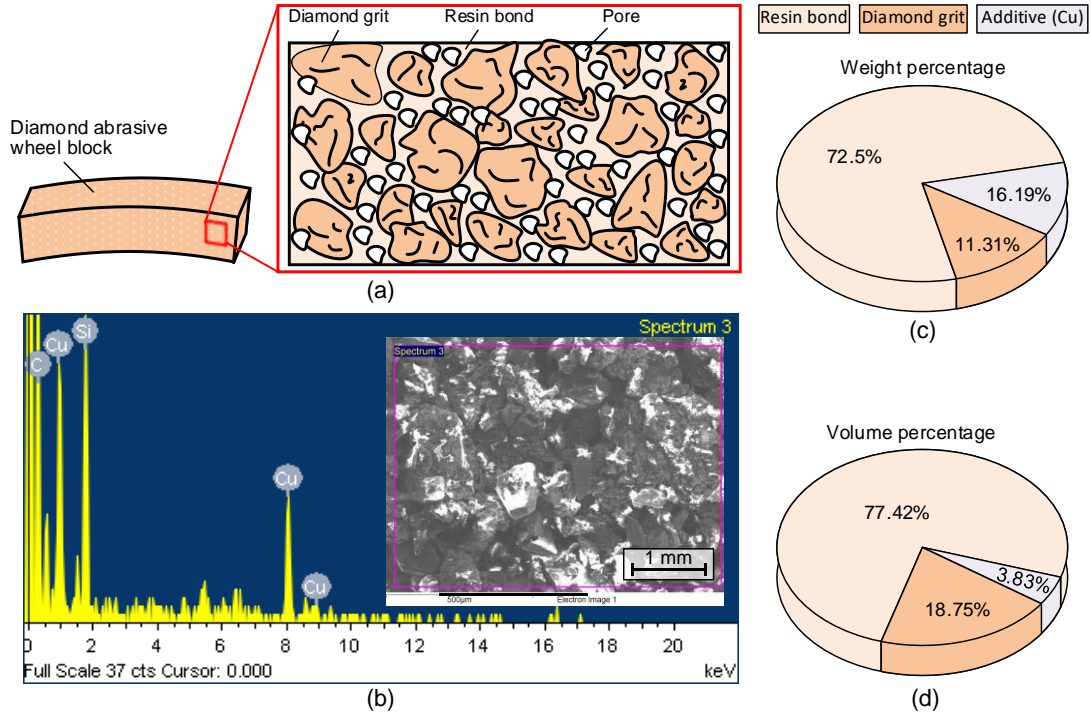


Figure 3.10 The ingredients and percentages of the diamond abrasive wheel. (a) The grinding wheel block and ingredients; (b) ingredients elements detecting EDS; (c)

the weight percentage and (d) volume percentage determination in the grinding wheel. However, pores are not practically achievable for the resin bond grinding wheel, and additives instead of pores are often added to the bond [253].

Usually, the manufacturers provide the grit contents concentration for a specific diamond abrasive wheel (see details in **Table 3.4**). The other two or more ingredients' contents are confidential for commercial purposes.

Table 3.4 Concentration definition of diamond abrasive wheel [253].

concentration (%)	50	75	100	125	150	175	200
volume (%)	12.5	18.75	25	31.25	37.5	43.75	50
Density (g/cm ³)	0.44	0.66	0.88	1.1	1.32	1.54	1.76
carat	2.2	3.3	4.4	5.5	6.6	7.7	8.8

The EDS detecting technology has been employed to determine the ingredients contents of the grinding wheel (**Figure 3.10b**). The detected results indicate that the main additive is copper, which accounts for 16.19% ± 2% of the whole material in weight percentage (**Figure 3.10c**) and around 3.83% in volume percentage (**Figure 3.10d**).

By studying the former research, the physical properties representing each ingredient are shown in **Table 3.3**, which provides a basis for calculating the composite properties.

Table 3.5 The ingredients' properties of the grinding wheel.

materials	specific heat capacity (c)	density (ρ)	thermal conductivity rate (λ)
	J/(kg·°C)	kg/m ³	W/(m·°C)
Diamond	510 [254]	3500 [255]	1000 [256]
Resin	1000 [257]	1117 [258]	0.32 [256]
Additive (Cu)	376 [259]	8960 [260]	413 [261]

Based on the percentages and properties of each ingredient, the properties of the mixed materials can be calculated from **Equation (3.12)** to **Equation (3.14)**.

As the specific heat capacity is related to mass, according to the weight percentage from **Figure 3.10c**, the formula can be expressed as

$$c_{mix} = 11.31\% \times c_d + 72.50\% \times c_r + 16.19\% \times c_a \quad (3.12)$$

where c_{mix} is the mixed specific heat capacity; c_d , c_r and c_a are the specific heat capacity of diamond, resin bond and additive, respectively.

The density is related to both mass and volume. According to the volume and weight percentage from **Figure 3.10c** and **Figure 3.10d**, the calculating formula can be written as

$$\rho_{mix} = 11.31\% \times \rho_d + 72.50\% \times \rho_r + 16.19\% \times \rho_a \quad (3.13)$$

where ρ_{mix} is the mixed density; ρ_d , ρ_r and ρ_a are the density of diamond, resin bond and additive, respectively.

As the thermal conductivity rate is related to volume size, according to the volume percentage from **Figure 3.10d**, the formula can be written as

$$\lambda_{mix} = 18.31\% \times \lambda_d + 77.42\% \times \lambda_r + 3.83\% \times \lambda_a \quad (3.14)$$

where λ_{mix} is the mixed density; λ_d , λ_r and λ_a are the thermal conductivity rate of diamond, resin bond and additive, respectively.

Due to the complexity of composite properties, especially the mixed thermal properties are hard to predict, both the calculated and experimental wheel

material properties are presented for comparison (as shown in **Table 3.6**).

The details of the material properties for the employed diamond grinding wheel are shown in **Figure 3.2**. The basic physical properties are tested by a laser thermal conductivity meter (LFA467, HyperFlash, NETZSCH Ltd.) from the Ningbo Institute of Materials Technology & Engineer, Chinese Academy of Sciences (CNITECH).

Table 3.6 Comparisons between the calculated and experimental material properties.

	specific heat capacity (c)	density (ρ)	thermal conductivity rate (λ)
	J/(g·K)	g/m ³	W/(m·K)
Calculated	0.843	2.656	199.17
Experimental	0.839	2.783	3.717

Note: $\alpha = \frac{\lambda}{\rho c}$, which denotes the heat diffusion.

Surprisingly, although the specific heat capacity and density for the calculated and experimental results are almost the same (a maximum error of 4.56%), the calculated result for thermal conductivity rate is more than 50 times the experimental data. It indicates that the thermal conductivity rate of mixed material is more complex than pure materials and it is not the simple mix of each ingredient by its weight. Therefore, detailed experimental data should be employed in the simulation process. **Table 3.7** shows the details of the material properties of the grinding wheel, which were tested by the Ningbo Institute of Materials Technology & Engineer, Chinese Academy of Sciences (CNITECH).

Table 3.7 Material properties of the grinding wheel.

Properties (Symbol)	Value	Units
Absorptivity (A_b)	0.85	N/A
Latent heat of fusion(L_f)	260	kJ/g
Material failure temperature (T_f)	650	K
Specific heat capacity (c)	0.839	J/(g·K)
Density (ρ)	2.783	g/cm ³
Thermal conductivity rate (λ)	3.717	W/(m·K)
Thermal diffusivity (α)	1.592	mm ² /s

3.3.4 Simulation Results Analysis

The most concerning simulation results in this project will be the ablation topography (mainly ablation depth and width) and the heat-affected zone. Based on this, the simulation results analysis will plan the temperature field distribution changes with time for the cross-section and the lateral section view of the ablated slot and the maximum heat-affected zone depth changes along with laser pass.

Specifically, **Figure 3.11** a&b show the left view and the front view of the relative position of the grinding wheel and laser beam under the O-XYZ coordinate system. **Figure 3.11c** represents the top view of the ablated block. Therefore, the lateral section view of the slot can be observed from view A (see **Figure 3.11d**), and the section view of the slot can be studied from view B (see **Figure 3.11e**).

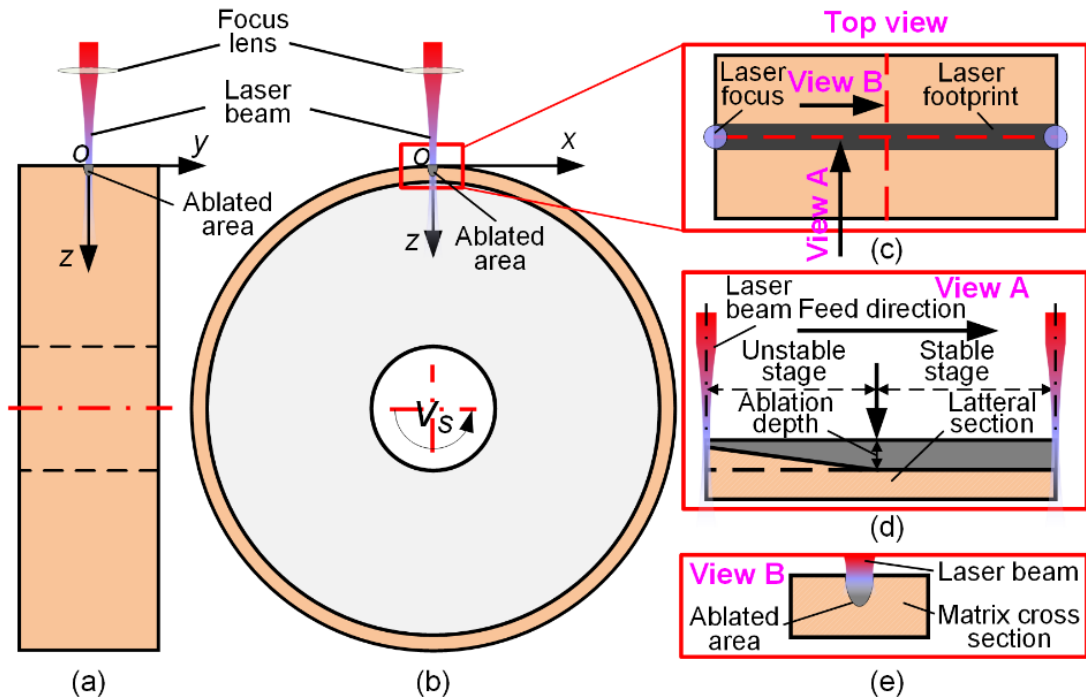


Figure 3.11 Ablation process. (a) The left view and (b) the front view of the grinding wheel; (c) the top view of the sample; (d) the lateral section, and (e) the cross-section of the slot on the sample.

The temperature field distribution changes with time can be analysed by studying the simulation result from each time step, which is essential to designing the low-level ablation depth control. Meanwhile, with the understanding of the temperature field distribution and the material properties, the ablation depth can also be calculated. However, the failure temperature for composite and organic compounds is kept to be investigated by further experiments.

3.4 Experimental Investigation

Experiments are planned to validate the theoretical analysis, the modelling simulation, and most importantly, to investigate the optimum strategies to achieve the final goal of the study. Two stages are planned in the experimental investigation.

In the first stage, preliminary results will be investigated regarding the laser ablation law response to the grinding wheel movement. The work in this stage involves the preparation of initial plans, the determination of the available experimental equipment, the establishment of the specialised platform, the performing of the preliminary experiments, and the preliminary evaluation of experimental results.

Based on the results achieved in the first stage, further experiments may be conducted in the second stage, including making detailed experimental validation plans, establishing the improved experimental platform, evaluating the experimental results and using the optimum way for the final generation of textured and profiled grinding wheels.

The equipment that used in the experiments is shown in **Figure 3.12**. Some essential parts (fixture, locator, et al.) of the experiment equipment will be machined by the 5-axis manufacturing centre (VMX42SRTi, HURCO Ltd.). The laser tool of Nd: YAG laser machine centre (YLS-2000, Han's machine, IPG Photonics) and the CO₂ laser machine (LE900, Hongfan Tech. Company) will be used to provide a stable energy beam (intensive heat) to achieve material removal on the grinding wheels. With the machine tools, the resin-bond diamond grinding wheels can be appropriately textured or profiled. Besides, the ablation result from the two different laser machines can be compared. The EDM (MV2400S, MITSUBISHI Ltd.), grinder (M250, Delta Ltd.), and handsaw can be used to cut the ablated wheels into small pieces, which will be further explored by other equipment. The ablated topography and morphology can be carefully studied by the 3D coordinate measurement machine (CLASSIC SR,

HEXCON Ltd.), optical microscope (NSZ-810, NOVEL OPTICS), SEM (SEM, 174C CZ, ZEISS Company), and XRD (D8 Advance, Bruker Company). The roughness of the ablated surface can be measured by the roughness meter (PS10, MarSurf Ltd). The topography of the ablated trenches can be detected by the depth measurement scanner. The movement control and the motion performance of the equipment can be designed and evaluated by the Data Acquisition Card (DAQ) (MyRio, 1900, NI Ltd.).



Figure 3.12 Experimental equipment. (a) 5-axis manufacturing centre; (b) Han's Nd: YAG laser machine; (c) Hongfan CO2 laser machine; (d) EDM; (e) grinder; (f) handsaw; (g) 3D coordinate measurement machine; (h) optical microscope; (i) SEM.

The software may be used in this research, including MATLAB, LabVIEW, Solidworks, and Autodesk CAD. The MATLAB software will be used for the theoretical and mathematical modelling and the visualisation of simulation

results. The LabVIEW will be installed on the computer, with which the complex movement and the data signal from the Data Acquisition Card (DAQ) (MyRio, 1900, NI Ltd.) will be appropriately handled. Meanwhile, Solidworks and CAD will be used to design the platform concretely, and the engineering drawing can also be completed based on it.

3.4.1 Experimental Scheme Design

1) Scheme for generating textured flat grinding wheel

The laser ablation law regarding feed rate and laser power on the ablation result will be investigated first. With the understanding of the ablation law, the path for generating different patterns can be planned. **Figure 3.13** shows the path plan for some typical textures, such as straight lines, tilt lines, zigzag lines and square blocks.

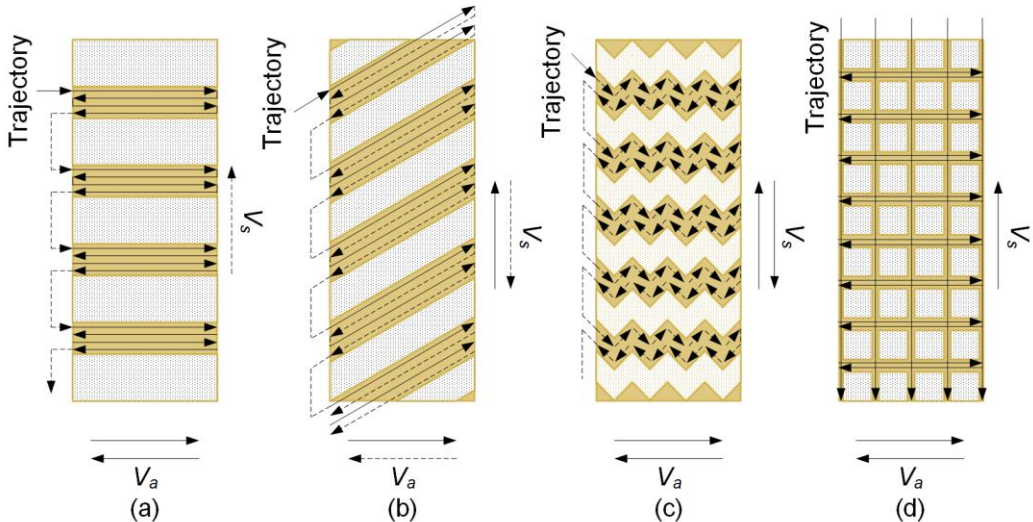


Figure 3.13 Path plan for some typical textures. (a) Straight line, (b) tilt line, (c) zigzag line and (d) square block.

2) Scheme for generating profiled grinding wheel

The laser ablation law regarding single-pass, multiple passes and a combination of multi-parameters ablation is scheduled in the experiment.

Figure 3.14 shows the definition of different ablation laws:

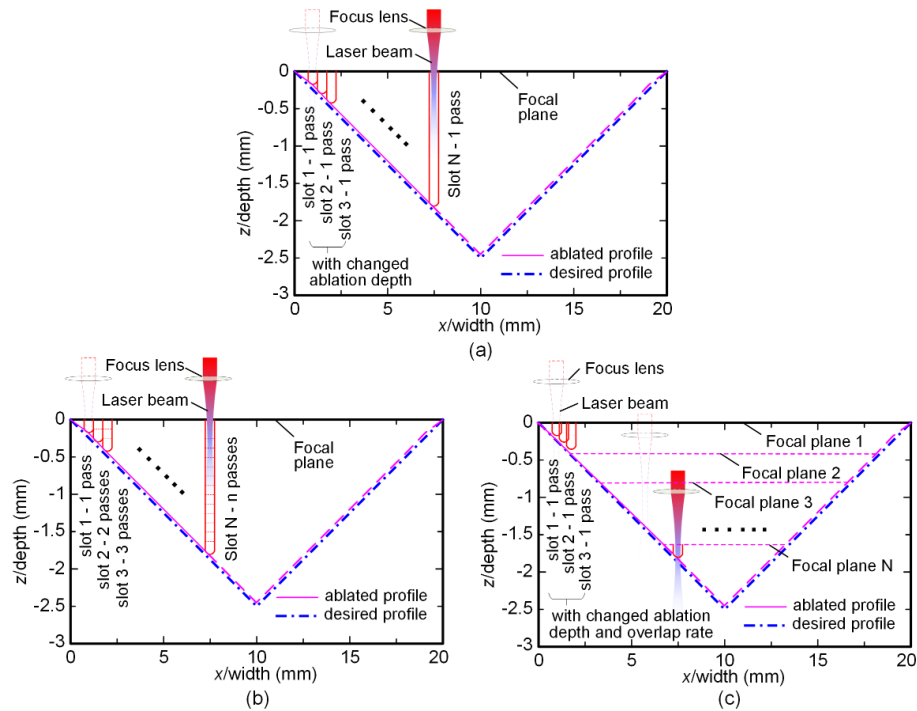


Figure 3.14 Ablation scheme for the profiled grinding wheels. Remove target materials by (a) single pass, (b) multiple passes and (c) a combination of ablation strategies.

(i) For removing target materials by multiple passes, the laser beam removes materials in a small amount at each time, and the laser beam will multiply past the single slot until it reaches the desired depth. After then, the laser beam moves to the next slot and repeats the previous step to obtain the final desired profile.

(ii) For removing target materials by a single pass, the desired ablation depth and the current one will be compared firstly to calculate the relative error. The system will determine the due fluence (determined by laser power and feed rate) according to the error to one-step obtain the desired depth.

(iii) For removing target materials by a combination of ablation strategies, the profile is achieved by a combination of laser power focal plane, feed rate

and overlap rate change. The initial shape in the former layer is achieved by controlling the laser energy fluence and overlap rate. Then, the following ablation parameters will be set by comparing the ablated and desired profile.

3.4.2 Experimental Platform Establishment

1) Overall System Functions and Layout Design

The experimental platform will be established based on the requirement of the testing scheme. The following factors have been considered in this section: (i) specialised experimental platform design for the high-power continuous laser beam ablation on abrasive grinding wheels, (ii) laser manipulation strategies determination for focal plane adjustment, laser power control, and laser occlusion, (iii) positioning system establishment for the grinding wheel motion control, including position, speed, acceleration, response time, and precision, and (iv) available measurement technology selection for the detecting of ablated grooves and understanding the robustness of the ablation system. The skeleton for the overall structural design and the system layout is shown in

Figure 3.15.

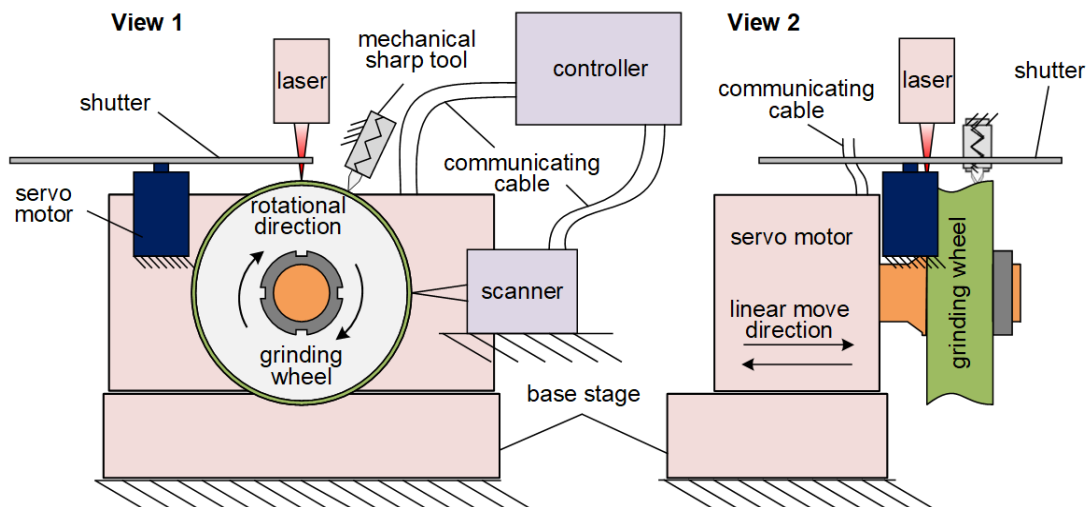


Figure 3.15 The overall scheme design of the manufacturing system.

It includes a laser system for providing a stable laser beam, a shutter for laser beam manipulating, an automated sharpened tool for cleaning the ablation slot, a laser distance measurement sensor for detecting the ablation depth, a moving stage with the ability to drive a grinding wheel horizontally move and rotates. And a PID controller with the mission to adjust the grinding wheel's cruising speed and position to be ablated according to the detected ablation depth of the laser distance measurement sensor.

2) System Performance Evaluation

The critical indexes involved in this system performance evaluation are motion control, laser beam manipulating, ablation depth detection, and robustness. However, the design principle is based on the commercial product priority to make the system reliable. The performance of the key components has been approved by the harsh industrial application. The most concerning issues for this project would be the precision movement of the custom positioning system and the functional integrity of the whole system.

Therefore, a systematic test is planned to evaluate the movement of the custom positioning system, including the positioning accuracy, speed accuracy, acceleration performance and adjusting time. In addition, the functional integrity of the whole system will be studied by the application of texturing on the diamond grinding wheels.

3.4.3 Experimental Procedures

The experimental procedure follows the technological process, including (i) sample preparation, (ii) data acquisition and processing and (iii) result analysis.

1) Sample Preparation

As the sample needs to be used for physical performance, topography and morphology study in the project, it is expected to be tested by some special equipment, such as the optical microscope, SEM, XRD, and roughness meter. Therefore, sample preparation is required based on the tested items.

Figure 3.16 shows the basic process for the sample preparation. After laser texturing on a resin-bond diamond grinding wheel, a specific serial number is first assigned to each sample, and then the sample will be cut from the grinding wheel using a hand saw and EDM. Finally, both sides of the sample will be polished and dry at room temperature.

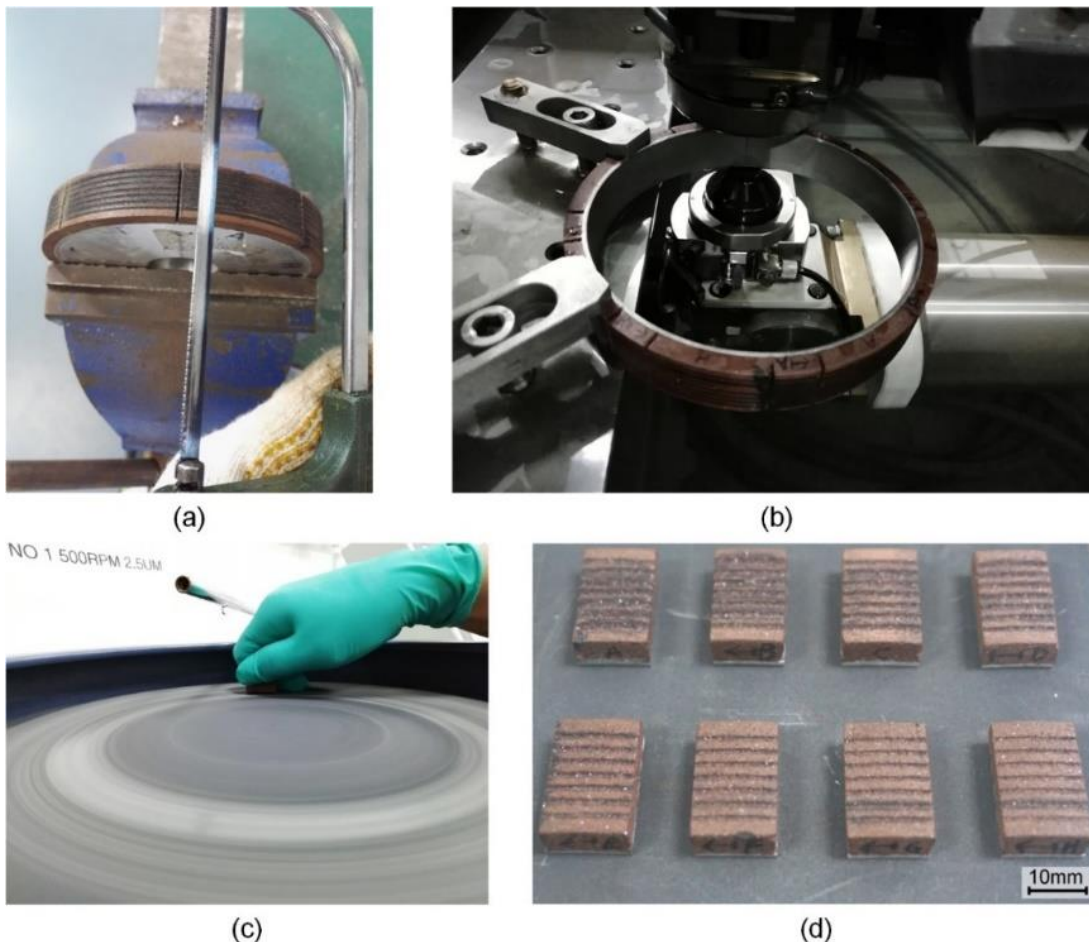


Figure 3.16 Sample Preparation. (a) Cutting through the abrasive layer by hand saw, (b) cutting the samples from the grinding wheel by EDM, (c) polishing both sides of

the samples, and (d) drying the samples.

2) Data Acquisition and Processing

Data acquisition and processing are crucial steps in the experimental study, which have an essential effect on the result analysis. The data in this project cover the image data and numerical data.

The image data for the experiment can be taken by a digital camera or by professional equipment (like the optical microscope, SEM) and processed by Matlab and/or Visio software. Likewise, the numerical data can be acquired by professional equipment (like the XRD, roughness meter, 3D coordinate meter and laser distance measurement sensor) or by small devices (like DAQ, MyRio, and PC) and processed by software like Matlab, Excel, Origin.

3) Experimental Result Analysis

The most concerning experimental data can be categorised into two groups: (i) the electromechanical system performance tests and (ii) ablation results. The electromechanical system performances will be evaluated from positioning accuracy, speed accuracy, acceleration performance, adjusting time and system functional validation, while the ablation results will be evaluated from the ablated topography, morphology, and the accuracy of pattern shape and profile.

Based on the understanding of the most concerning items in the project, the study of the performances of the electromechanical system and the ablation results evaluation items are planned as:

(1) Positioning accuracy will be tested at different moving distances under various speeds, the stable errors and maximum overshoot will be

obtained, which is crucial for guaranteeing ablated shape accuracy.

(2) Speeds varying with time under different feed rates will be checked, and the stable error and the stable error percentage will be acquired. It is crucial to achieving a desired uniform ablation depth.

(3) Acceleration performance under different feed rates will be tested as well to understand the maximum fluctuations and the fluctuations changes with time. The test results are essential for studying the vibration and impact of the system motion.

(4) The adjusting time for the positioning system to move a certain distance, to achieve a stable speed and acceleration will be presented, as they are helpful in formulating the ablation strategies of textured and profiled grinding wheels.

(5) The topography under various processing parameters will be investigated by SEM and optical microscope, including the ablation depth, width and shape. Because it directly determines the formulation ablation strategy and ablation accuracy.

(6) The morphology including the microstructures and the material composition changes under different processing parameters will be explored by SEM, EDS and XRD, as it decides the grinding performances of the grinding wheel.

(7) The pattern shape and profile accuracy should be examined by SEM, optical microscope, and profile meter. They are the key points in this project, for the ultimate goal of the study is to generate the textured and profiled resin-bond diamond grinding wheel precisely.

3.5 Conclusions and Discussions

This section aims to summarise the methodologies used to conduct the research and achieve the objectives of this thesis. Each section explains the objects, the motivation for completing them, and a plan on how to achieve them. According to sections 3.2 - 3.4, the key points can be summarized as follows:

(1) The preliminary research preparation (presented in section 3.2), including the selection of the grinding wheel, dressing strategy and laser source, is based on practical industrial applications. The resin-bond diamond grinding wheel (as described in subsection 3.2.1) is selected for the study due to its massive applications and superior performance. The laser tangential dressing method (as described in subsection 3.2.2) is chosen for the research as it has low noise, no tool wear and high efficiency. Both CO₂ and fibre laser sources (as described in subsection 3.2.3) are selected as they are the most widespread industrial lasers with higher average laser power and higher reliability than others but with different ablation characteristics. Therefore, they can be used for different application purposes and make comparisons.

(2) The modelling study (presented in section 3.3) covers the content from preliminary modelling analysis, simulation model selection, composite material properties determination, and the simulation results analysis. The preliminary modelling analysis (as shown in subsection 3.3.1) explains the factors that should be considered in the model and the limitation of the current modelling study. Three different types of modelling strategies (as shown in subsection 3.3.2) are selected in this project for diverse simulation purposes. To better understand composite properties, both the theoretical calculation and

experimental tests are used to determine the properties of the material (as shown in subsection 3.3.3). At last, the strategy for simulation results analysis is presented (as shown in subsection 3.3.4).

(3) The experimental investigation (presented in section 3.4) covers the experimental scheme design, platform establishment and experimental procedures. The instruments and the software available to be used to complete the project are summarised. Based on the summarised instruments and softwares, the experimental schemes for generating textured and profiled grinding wheels are designed (as shown in subsection 3.4.1). According to the needs of the experiments, a specialised experimental platform is established, and a systematic evaluation plan is formulated (as shown in subsection 3.4.2). Finally, a subsection covers the detailed experimental procedures, including sample preparation, data acquisition and processing, and experimental results analysis, illustrating how the trial work is conducted (as shown in subsection 3.4.3).

On the whole, the methodologies cover theoretical analysis, modelling simulation, and experimental investigation, which are closely connected to each part of the research content that will ensure the smooth progress of the research work.

Chapter 4

Ablation Process Modelling Based on Finite Difference

Method: Understanding the Ablation Parameters Effect on the Temperature Field

4.1 Introduction

To better understand the laser ablation process and further applications of laser processing technology, the time-dependent temperature distribution in the heat-affected zone and the ablation depth prediction during laser processing are planned in this study. The aim is to establish an analytical model regarding dynamic unsteady-state heat conduction. The modelling considers the laser focus size and laser beam energy intensity distribution along the propagation direction, as well as heat conduction and convection. An analytical model based on the finite difference method is used to calculate the ablation depth variation and the time-dependent temperature field distribution. Based on the simulation results, the ablation law regarding temperature field distribution and ablation depth changes with the laser power and feed rate are revealed. It shows that laser power affects little on the range of the temperature field distribution, but it increases the core temperature of the heat-affected zone as laser power increases from 24 W to 60 W. The feed rate affects the heat-affected zone that the temperature field narrows with the feed rate. It reveals that a higher laser power (e.g., 60 W) with a higher feed rate (e.g., 8.0 mm/s) is highly expected to optimise the ablation. A potential application is demonstrated to prove the usefulness of the study, which provide

help for the further understanding of the laser ablation process.

4.2 Theoretical Analysis

The general process for laser ablation is to separate or remove the target materials from the matrix through gasification, melt, oxidation, deterioration, or decomposition.

Generally, it can be categorised into three possible ablation characteristics when a laser beam passes the workpiece: (i) exposure/loosening, (ii) breakage and (iii) deterioration. The first circumstance can be considered laser focus is falling onto the resin, while the last two are on both the resin agency and grits. The mechanism of abrasive exposure/loosening (as seen in **Figure 4.1a**) can be explained as the resin bond dispersed due to the high temperature of the laser beam, bringing the abrasive initially under the bond exposed to their cutting edge. However, the massive disappearance of the resin bond could also contribute to the abrasive loosening, especially for the grits initially uncovered in the air (as seen in **Figure 4.1a**). The grit breakage (as seen in **Figure 4.1b**) can be regarded as the instantaneous heat expansion of grit or heat impact wave caused by the high energy of the laser beam. Once the heat stress exceeds the yield stress of the diamond (about 30 GPa), breakages are believed to happen. At the same time, the circumstance of grits deterioration maybe (as seen in **Figure 4.1c**) due to their chemical and physical properties under high temperature (referring to the diamond's and also the resin bond's), when it can be reacted with the oxygen in the air ambient environment and converted to graphite or other deteriorated materials, such as CO, CO₂.

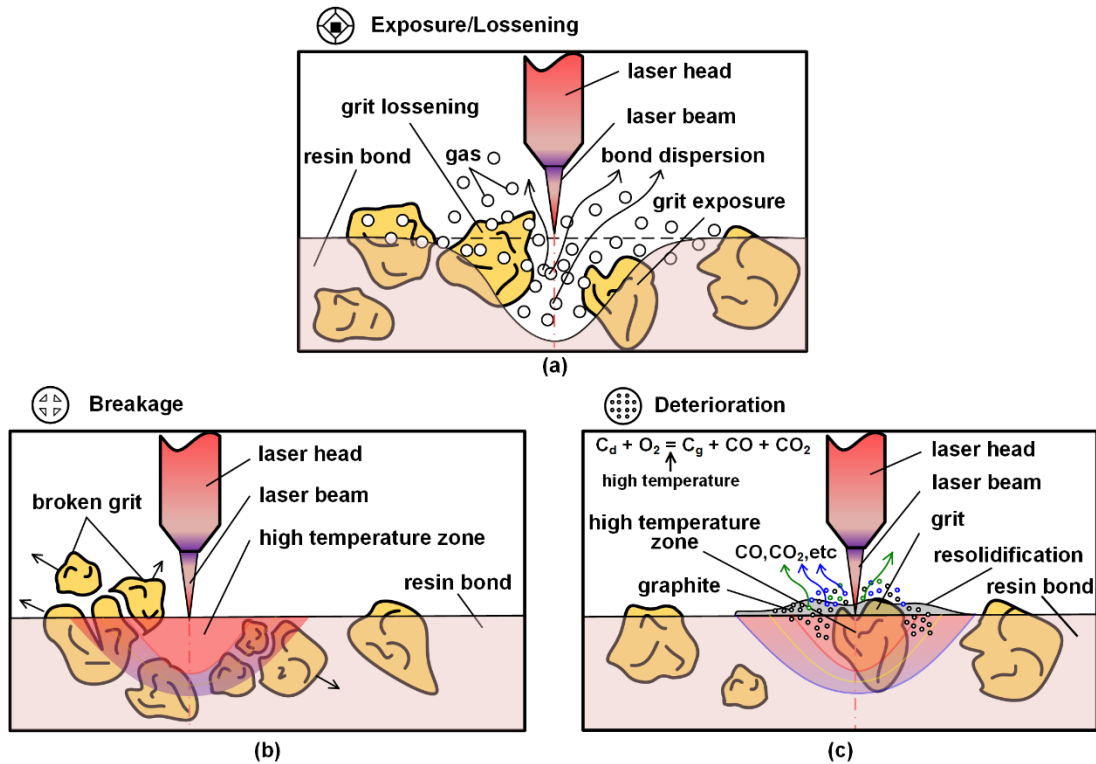


Figure 4.1 The surface characteristics generation mechanism. (a) Exposure (most of the diamond part is still under the resin)/loosening (most of the diamond part was in the air), (b) breakage and (c) deterioration.

The interaction process between diamond and laser in the ablation of the ambient air condition can be described as follows: the laser energy was first absorbed by the diamond, resulting in an increase in the diamond's surface temperature and the production of amorphous carbon. With the continuously increasing heat accumulation, carbon reacts with oxygen in the air (about 1,300 K), the ablation effect started to occur, and the material was removed gradually. With the temperature increasing to 1,600 K, the diamond content graphitises gradually. As the absorbing efficiency of graphite is higher than diamond, the temperature of graphite rises quickly. Theoretically, graphite would be melted (about 3,550 K) and sublimated (about 3,652 K), which can be considered evaporation. However, due to the facts, such as internal defects

and thermal stress, the materials would be shattered and splashed out below the temperature of 3,500 K. Besides, as other contents within the ablation zone of the resin-bond diamond grinding wheel may have a lower deterioration temperature, which would further low the crucial ablation temperature (T_c) of the grinding wheel.

Furthermore, as the phenolic resin bond contained in the employed grinding wheel is an organic substance, it has no fixed failure temperature. However, according to up-to-date research, most of the phenolic resin bond usually starts to fail during 400 K - 500 K, depending on the heat time [262]. Besides, the case would be more complex if considered the properties of additives. Therefore, to simplify the study, the crucial temperature for material failure is set based on the average results of the allowable grinding temperature in the practical application (an average failure temperature of 650 K) [263].

4.3 Modelling Process

4.3.1 Model description

In the ablation process, a laser beam with intensive energy radiated on a grinding wheel's surface and moved along with the wheel rotation (see **Figure 4.2a**). As a result of absorbing the energy, the target materials deteriorated and formed a slot. Therefore, the following factors should be included in the modelling:

(1) The laser intensity accorded with an axisymmetric super-Gaussian model. Therefore, the laser beam energy distribution exerted a significant influence on the calculation, which finally affected the prediction of the

temperature field distribution. In line with the facilities employed in this study, the laser beam intensity followed the axisymmetric super-Gaussian distribution model that a flat-top function located in the beam waist (as shown in **Figure 4.2 b&c A-A**) and evolved into a standard Gaussian function along with the beam propagation (as shown in **Figure 4.2 b&c B-B** and **C-C**). Besides, after the laser beam penetrated into the workpiece surface, the intensity attenuated due to the material absorbing energy and reflecting some of the energy to the surroundings.

(2) The relationship between the laser processing parameters and the output temperature field should be considered because a control strategy of selecting the processing parameters is feasible to control the heat-affected zone online for industrial application. Among these processing parameters, feed rate and laser power were the two most important and convenient ways to be controlled online by an electromechanical system.

(3) It is assumed here that the material is an isotropic solid material of uniform mixing and heat conduction.

This model is generally based on discretising the entire domain into cubic unit cells. The calculation domain (see **Figure 4.2a View A**) contains the initial relative position information of the laser beam and the workpiece block with dimensions. For each slice (see **Figure 4.2d**), the laser beam radiates through the target materials and brings heat to the heat-affected zone. At the surface of the substrate, the heat is conducted to the ambient atmosphere through heat convection and radiation. Moreover, at the inner of the substrate, the energy is conducted to the substrate around by conduction and finally to the

surrounding ambience.

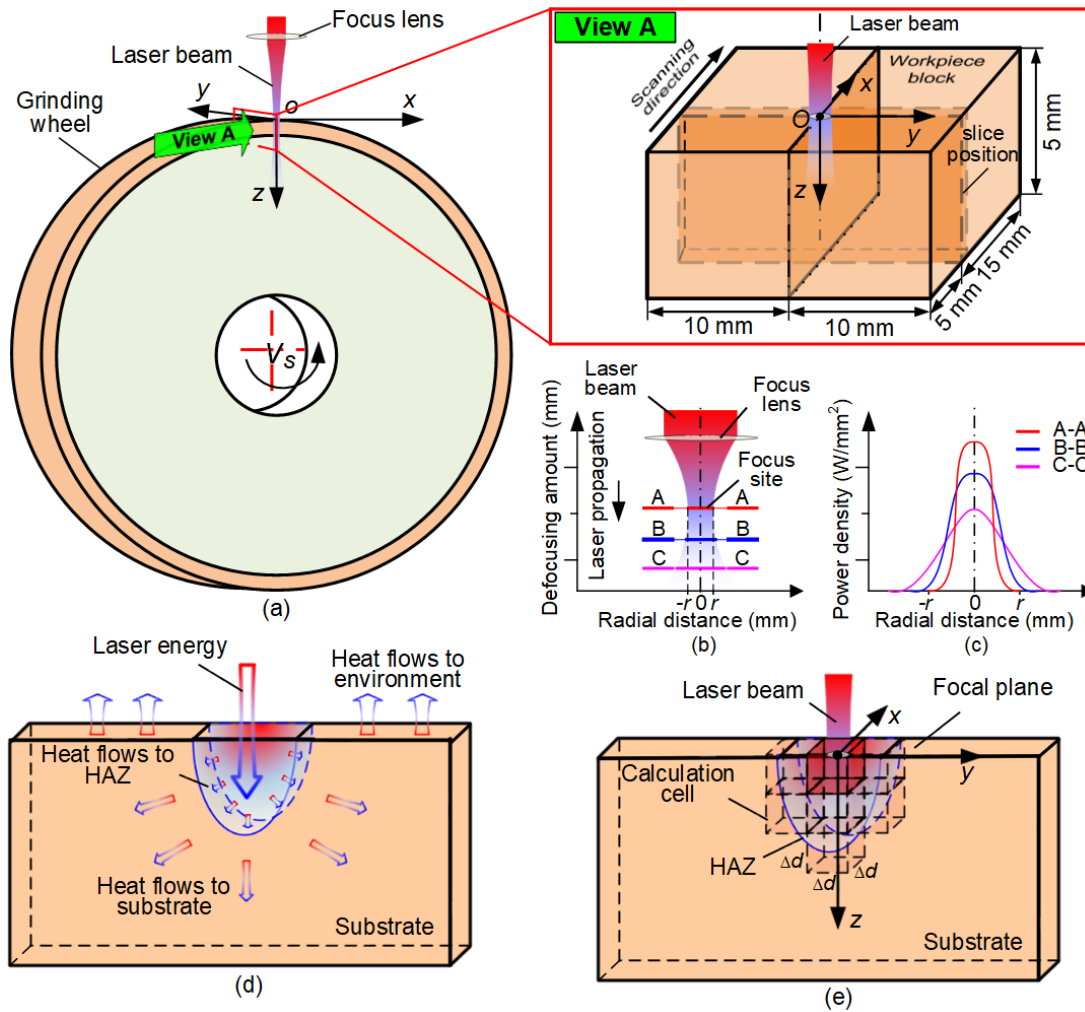


Figure 4.2 The diagram of the calculation position.

With the principle above, (a) the isotherm for the temperature field distribution dominated by laser energy is calculated firstly to reveal the region of the heating zone roughly, and (b) the ablation depth (the position of the lowest temperature point which could cause the failure of the materials for each time step) is calculated.

(a) Isotherm for temperature field distribution calculation

The temperature field is solved to predict the shape of the ablated area. To

calculate the entire temperature field in the workpiece block, the computing domain is separated into finite small cubic cells with an edge length of Δd . Each position of the cell is defined as (x, y, z) in the global coordinate system (see **Figure 4.2e**) and has a changing temperature as it absorbs the laser energy and transfers the energy to ambient cells or the atmosphere.

The cell temperature can be expressed as **Equation (4.1)** when being radiated by a laser beam.

$$T_{x,y,z,t+\Delta t} = T_{x,y,z,t} + \frac{Q_l}{\rho(\Delta d)^3 C_p^*} \quad (4.1)$$

where $T_{x,y,z,t}$ is the spatial transient temperature, ρ is the material density, C_p^* is the modified specific heat capacity of composite, and Q_l is the laser energy input. All properties of the composite are hypothesised constant.

The temperature computed through **Equation (4.1)** can be renewed by including heat conduction behaviours, containing (i) heat conduction through higher temperature to low per unit time Δt as described in **Equation (4.2)** [264]

$$\rho C_p \frac{\partial T_{x,y,z,t+\Delta t}^{in}}{\partial t} = k \left(\frac{\partial^2 T_{x,y,z,t}}{\partial^2 x} + \frac{\partial^2 T_{x,y,z,t}}{\partial^2 y} + \frac{\partial^2 T_{x,y,z,t}}{\partial^2 z} \right) \quad (4.2)$$

where k is the conductivity, and $T_{x,y,z,t+\Delta t}^{in}$ is the temperatures of the interior cubic cells, and (ii) the convection and radiation transfer from the workpiece surface to the environment expressed as **Equation (4.3)** [265]

$$h_n (T_{x,y,z,t+\Delta t}^w - T_\infty) = -k (\nabla T_{x,y,z,t} \cdot \vec{n}) \quad (4.3)$$

where $\nabla T_{x,y,z,t}$ is the temperature gradient of boundary cell and interior cell, \vec{n}

is the normal vector of the surface, h_n is the combined convection and radiation coefficient, $T_{x,y,z,t+\Delta t}^w$ is the boundary temperature of the cell, and T_∞ is the environmental temperature.

It is worth mentioning that the solutions of heat transfer in **Equation (4.2) - (4.3)** involve a numerical finite difference method proposed by Holman [264].

Equation (4.2) depicts conduction inside the material (see red cells in **Figure 4.3**) and is numerically solved by **Equation (4.4)** [201, 264]

$$T_{x,y,z,t+\Delta t}^{in} = \frac{k\Delta t}{\rho C_\rho (\Delta d)^2} (T_{x-\Delta d,y,z,t} + T_{x+\Delta d,y,z,t} + T_{x,y-\Delta d,z,t} + T_{x,y+\Delta d,z,t} + T_{x,y,z-\Delta d,t} + T_{x,y,z+\Delta d,t} - 6T_{x,y,z,t}) + T_{x,y,z,t} \quad (4.4)$$

Equation (4.3) describes convection and radiation between boundary cells and the environment, which can be solved based on the three different cases:

In Case (i), where exactly one cell face is adjacent to the environment in either x , y , or z direction (see the light red cells in **Figure 4.3**), **Equation (4.3)** is numerically solved by **Equation (4.5)** [201, 264]

$$T_{x,y,z,t+\Delta t}^w = \frac{k\Delta t}{\rho C_\rho (\Delta d)^2} \left(\frac{2h_n\Delta d}{k} (T_\infty - T_{x,y,z,t}) + 2T_{x-\Delta d,y,z,t} + T_{x,y-\Delta d,z,t} + T_{x,y+\Delta d,z,t} + T_{x,y,z-\Delta d,t} + T_{x,y,z+\Delta d,t} - 6T_{x,y,z,t} \right) + T_{x,y,z,t} \quad (4.5)$$

In Case (ii), where exactly two cell faces are adjacent to the environment in either combination of the direction (see the yellow cells in **Figure 4.3**), **Equation (4.3)** is numerically solved by **Equation (4.6)** [201, 264]

$$T_{x,y,z,t+\Delta t}^w = \frac{2k\Delta t}{\rho C_p(\Delta d)^2} \left(\frac{2h_n\Delta d}{k} (T_\infty - T_{x,y,z,t}) + T_{x-\Delta d,y,z,t} + T_{x,y-\Delta d,z,t} + T_{x,y,z-\Delta d,t} + T_{x,y,z+\Delta d,t} - 4T_{x,y,z,t} \right) + T_{x,y,z,t} \quad (4.6)$$

In Case (iii), where three faces are adjacent to the environment (see the light blue cells in **Figure 4.3**, **Equation (4.3)** is numerically solved by **Equation (4.7)** [201, 264]

$$T_{x,y,z,t+\Delta t}^w = \frac{2k\Delta t}{\rho C_p(\Delta d)^2} \left(\frac{2h_n\Delta d}{k} (T_\infty - T_{x,y,z,t}) + T_{x-\Delta d,y,z,t} + T_{x,y-\Delta d,z,t} + T_{x,y,z-\Delta d,t} - 3T_{x,y,z,t} \right) + T_{x,y,z,t} \quad (4.7)$$

The laser energy Q_l in **Equation (4.1)** is computed by the definition of laser energy absorbed by the workpiece in a specific area and time as **Equation (4.8)** [266]

$$Q_l = \beta(\Delta d)^2 \Delta t \eta I \quad (4.8)$$

where β is the absorptivity of material, Δt is the time step for computing, η is the attenuation function, and I is the laser intensity. The processing parameters affect the energy absorption by the way (i) the feed rate that determines the dwell time causing heat accumulated and (ii) the laser power that determines the laser intensity varying the energy in unit area and time.

The attenuation function η depicts the remaining laser intensity I after being absorbed by the workpiece along the penetrating direction and can be expressed as **Equation (4.9)** [267]

(b) Ablation depth calculation

As most of the previous studies have investigated the ablation depth by the empirical model, the ablation depth was calculated from the analytical solution in this study, which can be written as **Equation (4.11) - (4.13)**.

$$T_{y,z,t+\Delta t} = T_{x,y,z,t+\Delta t}(x = x_0 + xt) \quad (4.11)$$

$$T_{z,t+\Delta t} = T_{y,z,t+\Delta t}(y = 0) \quad (4.12)$$

$$z_{depth} = -P_{min}(T_{z,t+\Delta t} \geq T_F)\Delta d \quad (4.13)$$

where $T_{y,z,t+\Delta t}$ is the temperature distribution in the y-z section at the time, $T_{z,t+\Delta t}$ is temperature distribution along the centre line of the y-z section. z_{depth} is the depth of the heat-affected zone, T_F is the failed temperature, and P_{min} is the minimum position for the temperature on the centre line of the y-z section over the failed temperature.

The laser beam parameters used here are from a continuous-wave carbon dioxide generator (LE900, Hongfan Tech. Company) with a maximum power of 60 W, a wavelength of 10.6 μm , a circular focus with a diameter of 0.3 mm, and a focal length of 12.5 mm. The grinding wheel (D125N75B771/8, 3M Company) used in this study is a standard commercial resin bond diamond abrasive tool (see more details in **Table 3.3 & Table 3.7** in **Chapter 3**).

4.3.2 Flowchart

The flowchart concluding the modelling steps for the full calculation is presented in **Figure 4.4**. All the equations mentioned above are transferred

into codes in MATLAB. Wherein, the input parameters include laser power and feed rate, while the output results include temperature field distribution and ablation depth. **Equation (4.10)** was first used to calculate the laser intensity, and then **Equation (4.8)&(4.9)** were employed to compute the energy absorbed by the workpiece, the temperature field distribution and ablation depth can be finally solved by **Equation (4.1)-(4.3)** and **Equation (4.11)-(4.13)**.

The time step for the stability of this calculation was governed by the Biot and Fourier number in the following way for the problems in the numerical format [264]:

$$B_i = \frac{h_n \Delta d}{k} \quad (4.14)$$

$$F_o = \frac{k \Delta t}{\rho C_p (\Delta d)^2} \quad (4.15)$$

where the stability requirement for the interior node was $F_o \leq \frac{1}{4}$, for the convection boundary node was $F_o(2 + B_i) \leq \frac{1}{2}$, and for the exterior corner with convection boundary was $F_o(1 + B_i) \leq \frac{1}{4}$.

As it can be seen that Δt and Δd were the only two changeable parameters in the function that decided the two stability factors. The Δd (0.01 mm) were firstly selected according to the measurement precision that the experiment was able to be achieved. By fixing the cells' edge length Δd , the basic time step Δt for simulation stability requirement can be calculated. To further improve the simulation precision and understand the details in the process, the time step was kept reduced till the time step made little effect on simulation results. Therefore, a time step of 10^{-4} s was finally selected.

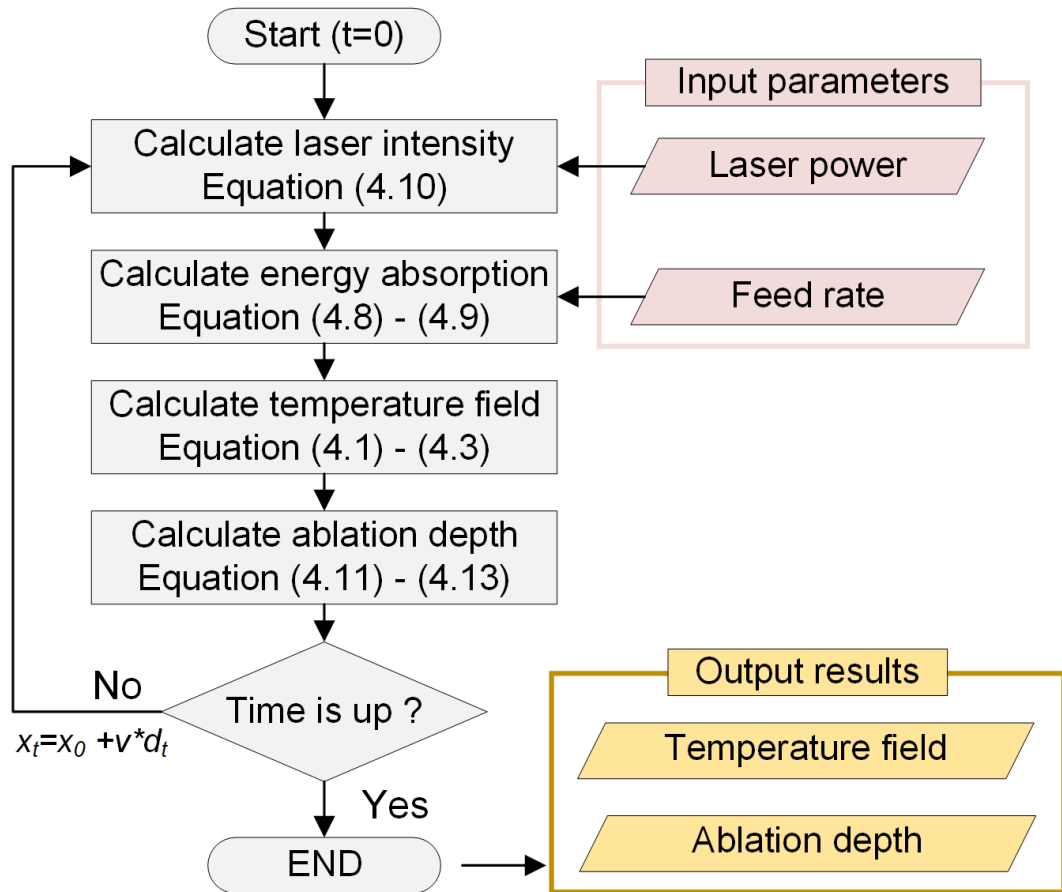


Figure 4.4 Flowchart for the theoretical model, solving the temperature field distribution and ablation depth estimation by inputting processing parameters of laser power and feed rate.

4.4 Simulation Results and Analysis

4.4.1 Temperature Field Responds to Time

Figure 4.5 shows the cross-section view of the temperature field responses to time (within the first 2 seconds) during the laser ablation process under laser power of 24 W and feed rate of 3.0 mm/s.

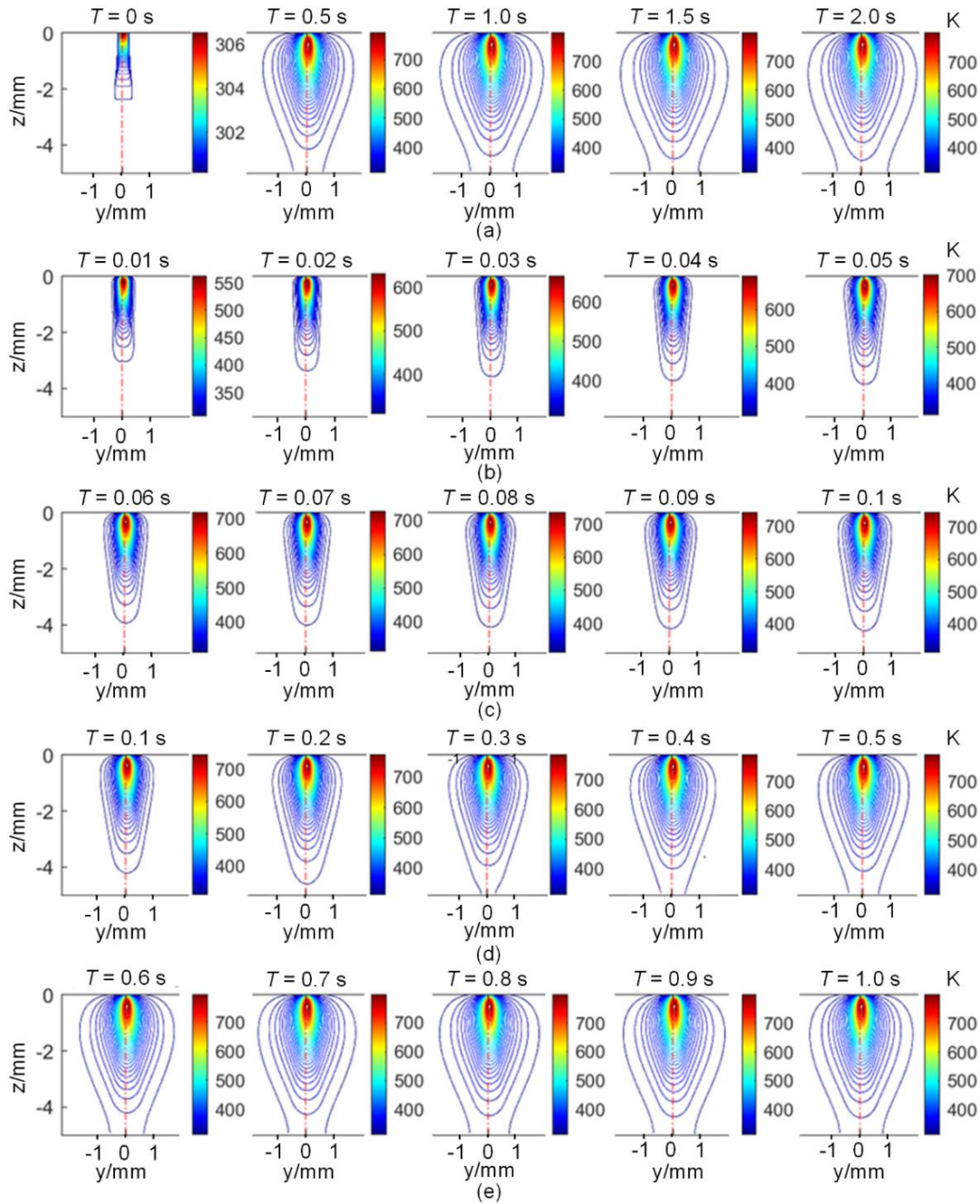


Figure 4.5 Temperature field responses to time during laser ablation under the laser power of 24 W and feed rate of 3 mm/s. The transient temperature field of the slot cross section for (a) the time at 0, 0.5, 1.0, 1.5 and 2.0 s, (b) the time at 0.01, 0.02, 0.03, 0.04 and 0.05 s, (c) the time at 0.06, 0.07, 0.08, 0.09 and 0.1 s, (d) the time at 0.1, 0.2, 0.3, 0.4 and 0.5 s, and (e) the time at 0.6, 0.7, 0.8, 0.9 and 1.0 s.

To be specific, **Figure 4.5a** shows the transient temperature distribution along the cross-section of the slot for the time at 0 s, 0.5 s, 1.0 s, 1.5 s and 2.0 s. It indicated that the most significant temperature field changes happened in the

first 0.5 s, while it nearly remained unchanged for the time from 1.0 s to 2.0 s.

As it shows that the most significant temperature field changes happened in the first 0.5 s, smaller time intervals are used to present the simulation results.

Figure 4.5b and **Figure 4.5c** show the temperature distribution along the cross-section for the time from 0.01 s to 0.1 s, with an interval of 0.01 s. It revealed that the temperature field rapidly extended in the depth direction while extending slightly along the width direction. It is likely because of the directivity of a laser beam that makes heat mainly flows along the laser beam. Although the workpiece absorbed the heat, little heat was transferred to the surroundings.

Given that the trend of the temperature field was becoming stable for the time from 0.01 s to 0.1 s, a slightly larger time interval of 0.1 s is employed to present the results from the time at 0.1 s to 1.0 s, as shown in **Figure 4.5d** and **Figure 4.5e**. It showed that the temperature field started to extend in both the width and depth directions during the time from 0.1 s to 0.5 s, as shown in **Figure 4.5d**. However, it is worth noting that the temperature field stopped extending along the depth direction and mainly extended along the width direction for the time from 0.6 s to 1.0 s, as shown in **Figure 4.5e**. Three reasons may account for this phenomenon: (i) the laser beam energy cannot flow deeper with the laser defocusing effect and the absorption of energy by surrounding materials, (ii) the moving of the laser beam makes the energy flow into different positions of the workpiece, and (iii) the heat balance in the ablation zone makes the processing enter a stable processing stage.

4.4.2 Laser Power Effects on the Temperature Field

Based on the transient heat transfer method for the unsteady-state conduction, the simulation results represent temperature field distribution for lateral section and cross-section in a stable stage under the laser powers of 24 W, 36 W, 48 W, and 60 W with different feed rates (from 3.0 mm/s to 6.0 mm/s with an interval of 1.0 mm/s) are presented (as shown in **Figure 4.6** to **Figure 4.9**). As demonstrated that the temperature field nearly remained unchanged after 1.0 s (as shown in **Figure 4.5a**), the following section considered the simulation at 2.0 s as the stable stage. Overall, it showed that the shapes of the temperature field distribution were unchanged under a specific feed rate, but the core temperature of the temperature field increased with the laser power.

Figure 4.6 shows the simulation results of temperature field distribution in the stable stage response to laser powers from 24 W to 60 W with an interval of 12 W under the feed rate of 3.0 mm/s. It revealed that the shapes of the temperature field distribution under different laser powers are almost the same. However, differently, the core temperature increased with the laser power, rising from around 800 K at 24 W to about 1,500 K at 60 W.

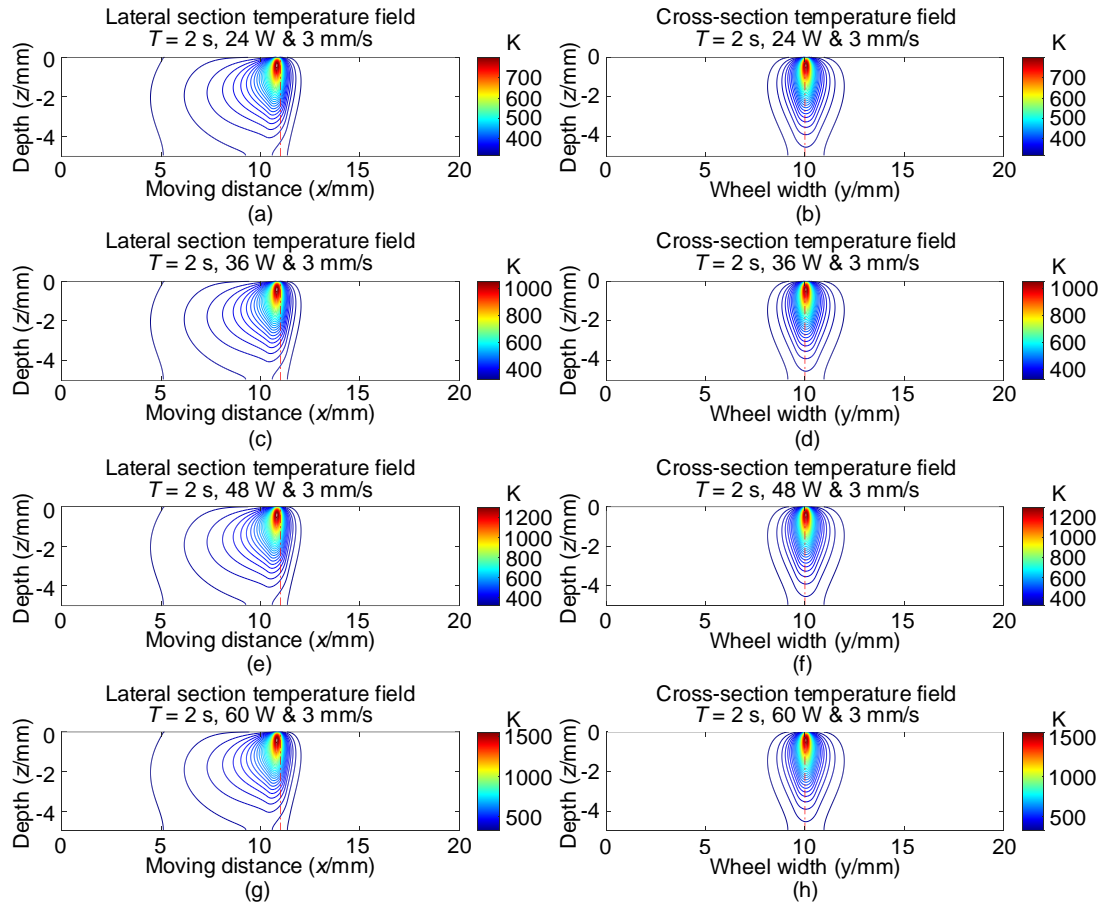


Figure 4.6 Simulation results of temperature field distribution response to laser powers from 24 to 60 W with an interval of 12 W under the feed rate of 3.0 mm/s. (a), (c), (e) and (g) are the lateral section view (from the x-z plane) and (b), (d), (f) and (h) are the cross-section view (from the y-z plane) for the laser powers of 24 W, 36 W, 48 W and 60 W, respectively.

Figure 4.7 shows the simulation results of temperature field distribution in the stable stage response to laser powers from 24 W to 60 W with an interval of 12 W under the feed rate of 4.0 mm/s. It revealed no noticeable changes when comparing the results presented in **Figure 4.6**.

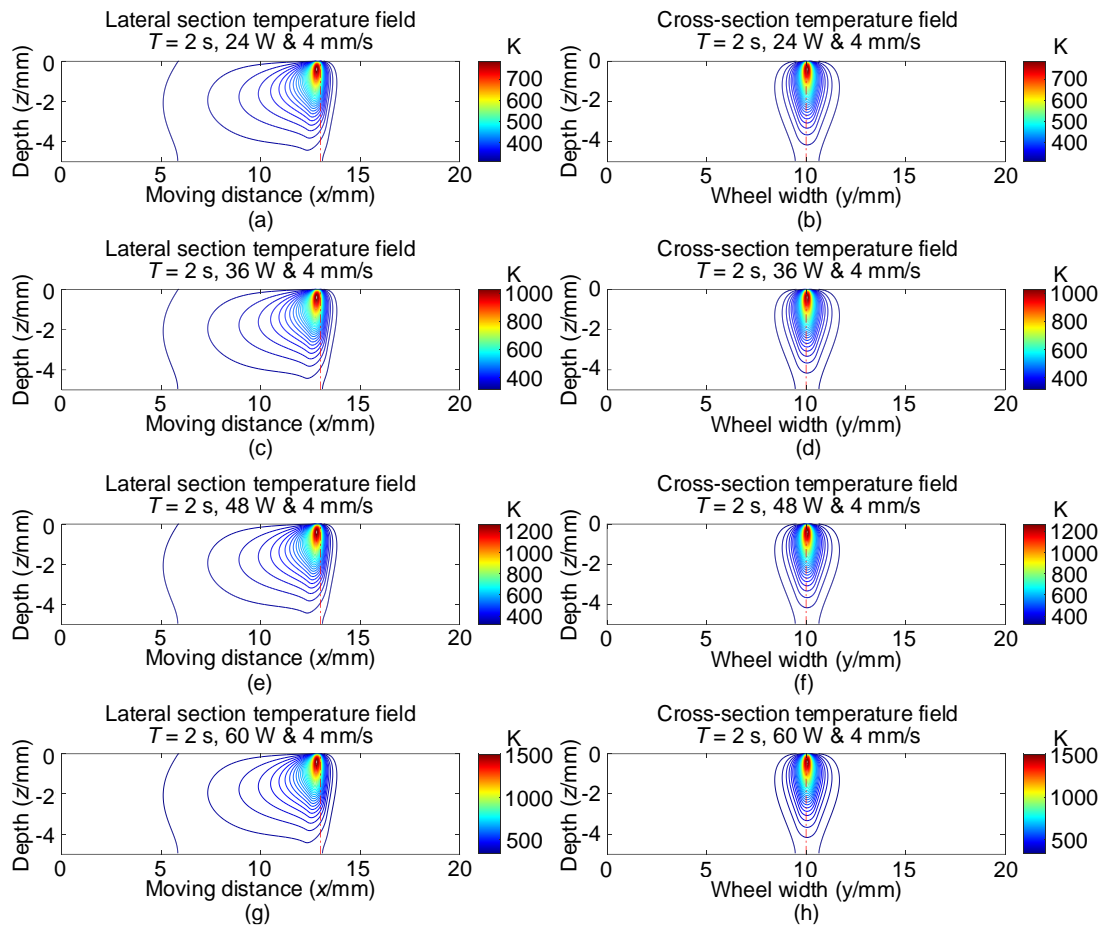


Figure 4.7 Simulation results of temperature field distribution response to laser powers from 24 to 60 W with an interval of 12 W under the feed rate of 4.0 mm/s. (a), (c), (e) and (g) are the lateral section view (from the x-z plane) and (b), (d), (f) and (h) are the cross-section view (from the y-z plane) for the laser powers of 24 W, 36 W, 48 W and 60 W, respectively.

Figure 4.8 shows the simulation results of temperature field distribution in the stable stage response to laser powers from 24 W to 60 W with an interval of 12 W under the feed rate of 5.0 mm/s. Again, no significant changes were found in the temperature distribution K shape, but the highest core temperature dropped from 1,500 K to 1,400 K compared with **Figure 4.7**.

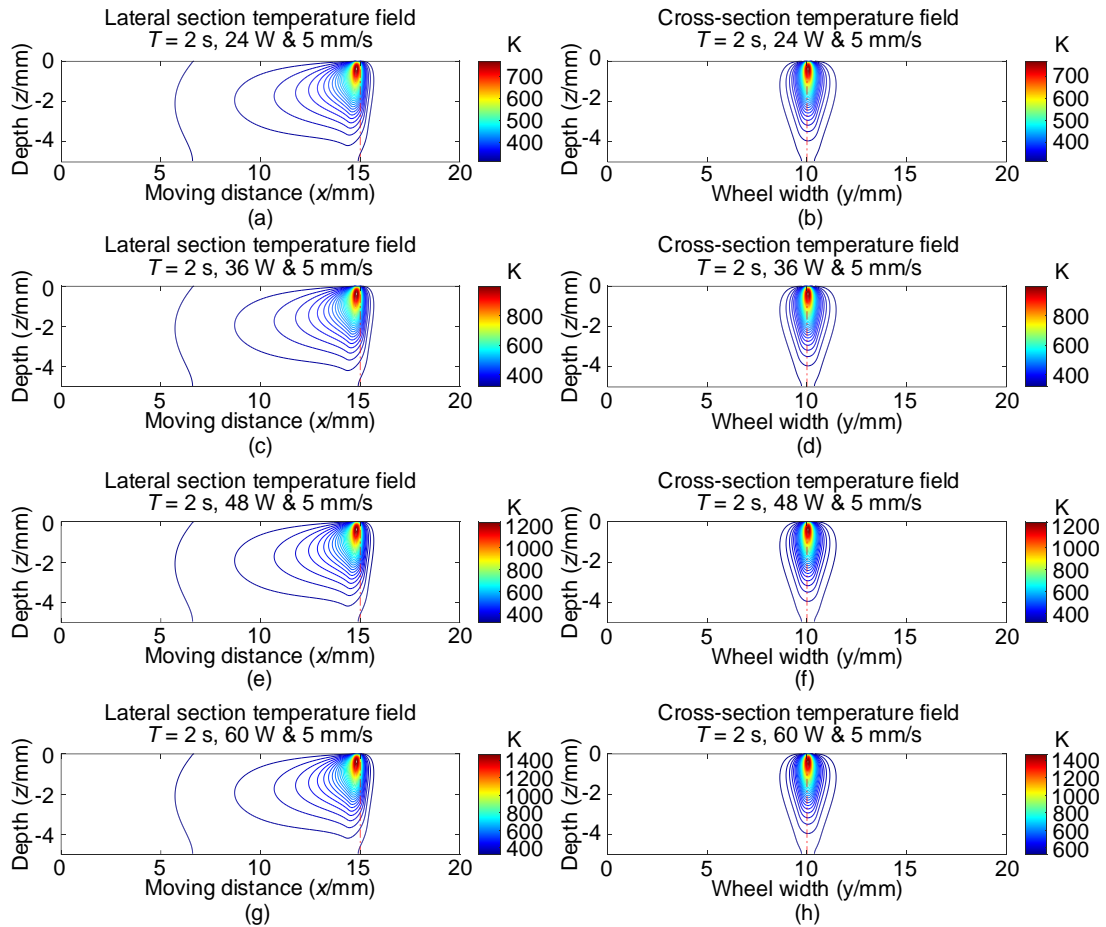


Figure 4.8 Simulation results of temperature field distribution response to laser powers from 24 to 60 W with an interval of 12 W under the feed rate of 5.0 mm/s. (a), (c), (e) and (g) are the lateral section view (from the x-z plane) and (b), (d), (f) and (h) are the cross-section view (from the y-z plane) for the laser powers of 24 W, 36 W, 48 W and 60 W, respectively.

Figure 4.9 shows the simulation results of temperature field distribution in the stable stage response to laser powers from 24 W to 60 W with an interval of 12 W under the feed rate of 6.0 mm/s. Compared with **Figure 4.8**, it showed nearly no difference in the temperature field distribution along the cross-section. Nevertheless, the distribution ranges along the lateral section were increased due to the increased feed rate.

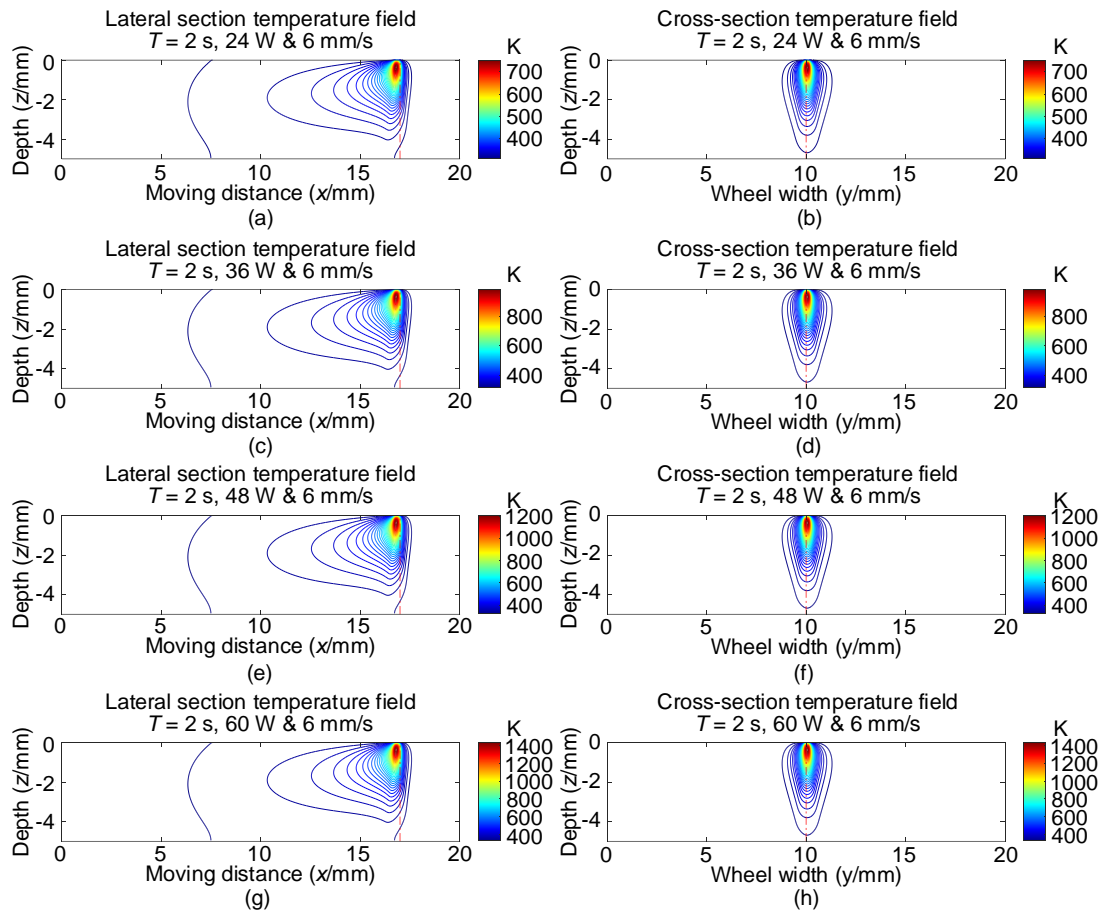


Figure 4.9 Simulation results of temperature field distribution response to laser powers from 24 to 60 W with an interval of 12 W under the feed rate of 6.0 mm/s. (a), (c), (e) and (g) are the lateral section view (from the x-z plane) and (b), (d), (f) and (h) are the cross-section view (from the y-z plane) for the laser powers of 24 W, 36 W, 48 W and 60 W, respectively.

In conclusion, the results show that the shapes of the temperature field distributions for a specific feed rate do not change a lot. However, the core temperature for the temperature field increased with the laser power. Besides, as the temperature field distributions for a specific feed rate do not change a lot, the increased laser power would not significantly enlarge the heat-affected zone. Therefore, the results indicated that a higher processing efficiency could be promised by increasing the laser power.

4.4.3 Laser Power Effects on Ablation Depth

Based on the crucial temperature of workpiece failure (650 K) as explained in section 4.2, the simulation results of ablation depth under the laser powers of 24 W, 36 W, 48 W, and 60 W with different feed rates (from 3.0 mm/s to 6.0 mm/s with an interval of 1.0 mm/s) are presented (as shown in **Figure 4.10** to **Figure 4.13**).

Figure 4.10 shows the ablation depth in the stable stage response to laser powers from 24 W to 60 W with an interval of 12 W under the feed rate of 3.0 mm/s. It revealed that the ablation depth increased with the laser power from -1.15 mm at 24 W to -2.35 mm at 60 W. Moreover, it appeared that the transition distance (x-direction) to reach a stable ablation depth is not obviously affected by the increased laser power, which indicated that a steep ablation depth could be achieved by larger laser power.

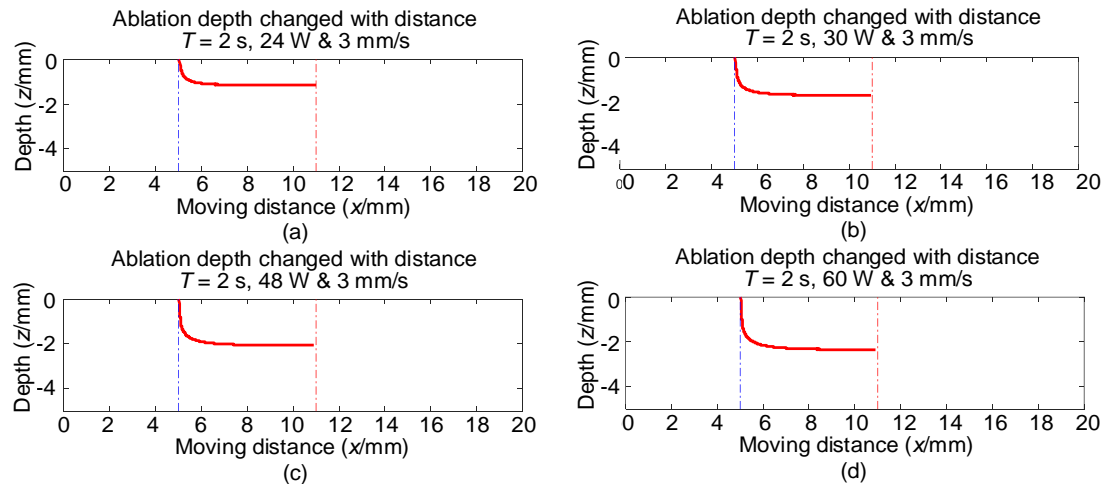


Figure 4.10 Simulation results of the ablation depth response to laser powers from 24 W to 60 W with an interval of 12 W under the feed rate of 3.0 mm/s. (a), (b), (c) and (d) are the ablation depth for the laser power of 24 W, 36 W, 48 W and 60 W, respectively.

Figure 4.11 shows the ablation depth in the stable stage response to laser

powers from 24 W to 60 W with an interval of 12 W under the feed rate of 4.0 mm/s. Overall, it showed the same trends as the results presented in **Figure 4.10**, except that the corresponding ablation depths are slightly reduced. This is likely due to the increased feed rate lowering the heat-affected zone, hindering the increase of ablation depth.

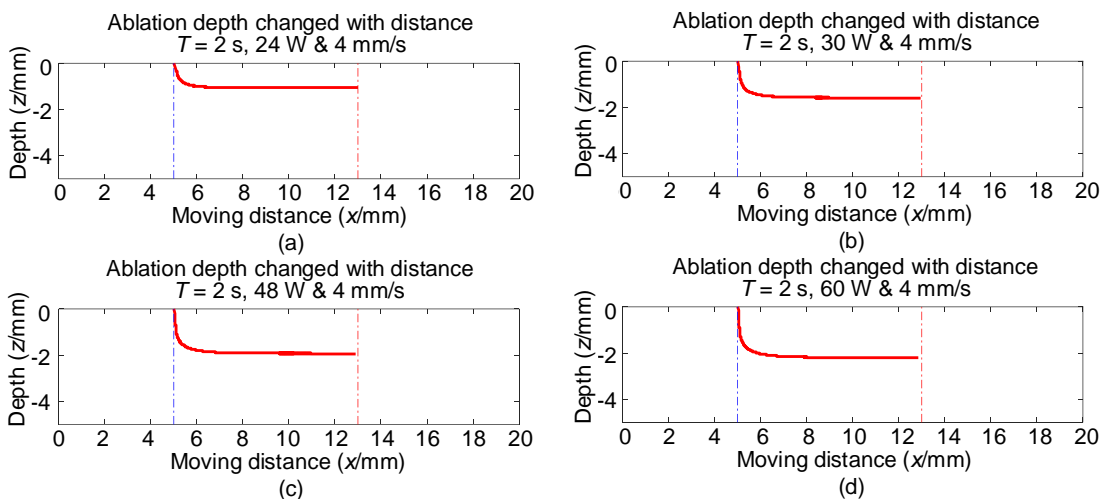


Figure 4.11 Simulation results of the ablation depth response to laser powers from 24 to 60 W with an interval of 12 W under the feed rate of 4.0 mm/s. (a), (b), (c) and (d) are the ablation depth for the laser power of 24 W, 36 W, 48 W and 60 W, respectively.

Figure 4.12 shows the ablation depth in the stable stage response to laser powers from 24 W to 60 W with an interval of 12 W under the feed rate of 5.0 mm/s. It revealed that the tendencies are consistent with results for other feed rates, but the ablation depth kept a dropping trend.

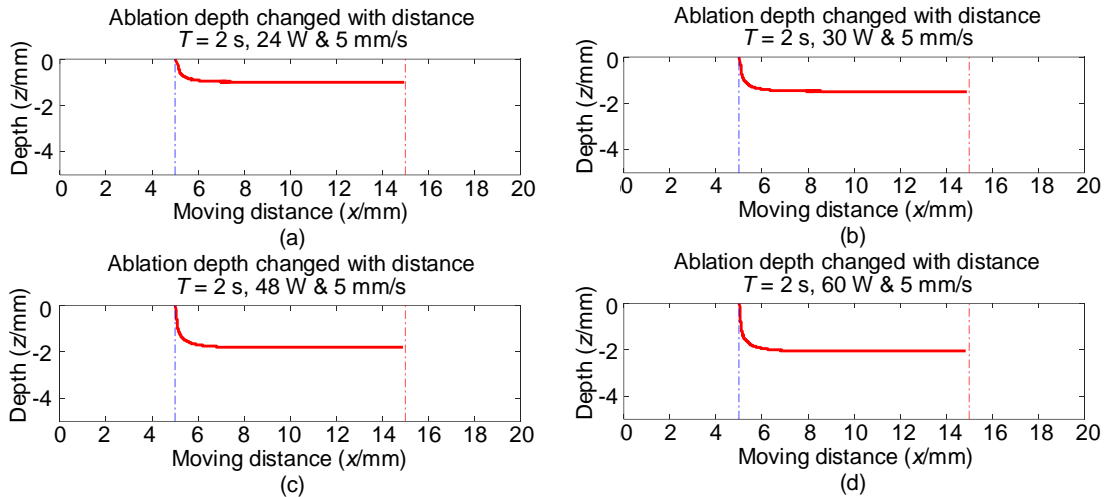


Figure 4.12 Simulation results of the ablation depth response to laser powers from 24 to 60 W with an interval of 12 W under the feed rate of 5.0 mm/s. (a), (b), (c) and (d) are the ablation depth for the laser power of 24 W, 36 W, 48 W and 60 W, respectively.

Figure 4.13 shows the ablation depth in the stable stage response to laser powers from 24 W to 60 W with an interval of 12 W under the feed rate of 6.0 mm/s. Apart from the ablation depth reduced, the most noticeable change is that the ablation depth in stable stages became smooth.

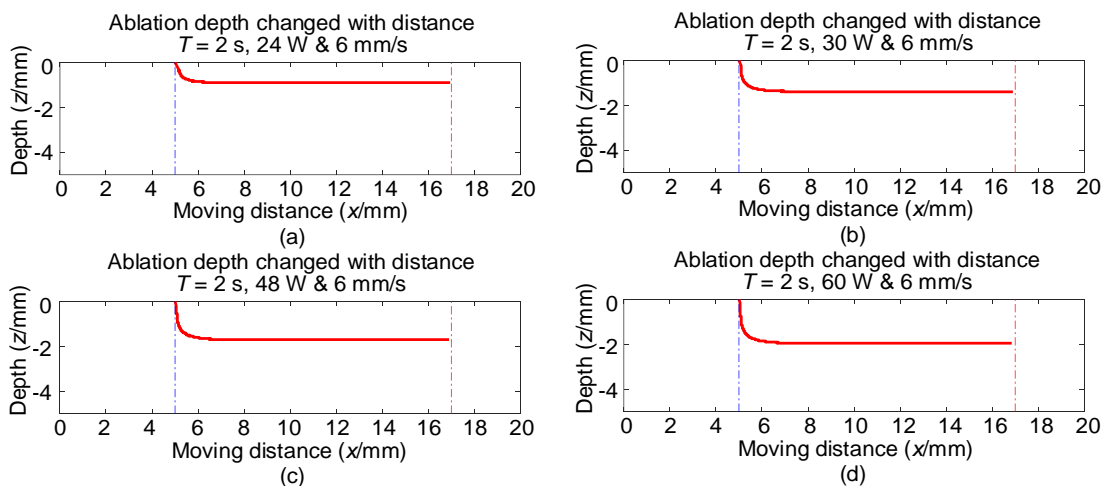


Figure 4.13 Simulation results of the ablation depth response to laser powers from 24 to 60 W with an interval of 12 W under the feed rate of 6.0 mm/s. (a), (b), (c) and (d) are the ablation depth for the laser power of 24 W, 36 W, 48 W and 60 W, respectively.

These figures show that the ablation depths change obviously with the laser powers change, and all these ablation processes can reach a stable stage within 2 s. The figures also showed that the ablation processing takes about 2 mm to change from the unstable stages (ablation beginning stages) to the stable stages. By comparison, it could also be found that the ablation depth curves obtained under higher laser powers have a steeper ablation edge, while an increase in the feed rate dominates a relative uniform ablation depth.

In general, it can be calculated from the figures that higher laser power with a higher feed rate was highly expected to achieve a steep ablation edge and uniform ablation depth.

4.4.4 Feed Rate Effects on the Temperature Field

The simulation results of temperature field distribution for lateral section and cross-section under the feed rates of 3.0 mm/s, 4.0 mm/s, 5.0 mm/s, and 6.0 mm/s with different laser powers (from 24 W to 60 W with an interval of 24 W) are shown in **Figure 4.14** to **Figure 4.17**. The temperature field variation with feed rate under a specific laser power was recorded in each chart.

Figure 4.14 shows the simulation results of temperature field distribution for the lateral section and cross-section for the feed rate of 3.0 mm/s, 4.0 mm/s, 5.0 mm/s, and 6.0 mm/s under the laser power of 24 W. It showed that the temperature field ranges for the lateral section were increased with the feed rate, while they were reduced for the cross-section. In addition, the core temperatures for the temperature field dropped slightly with the feed rate.

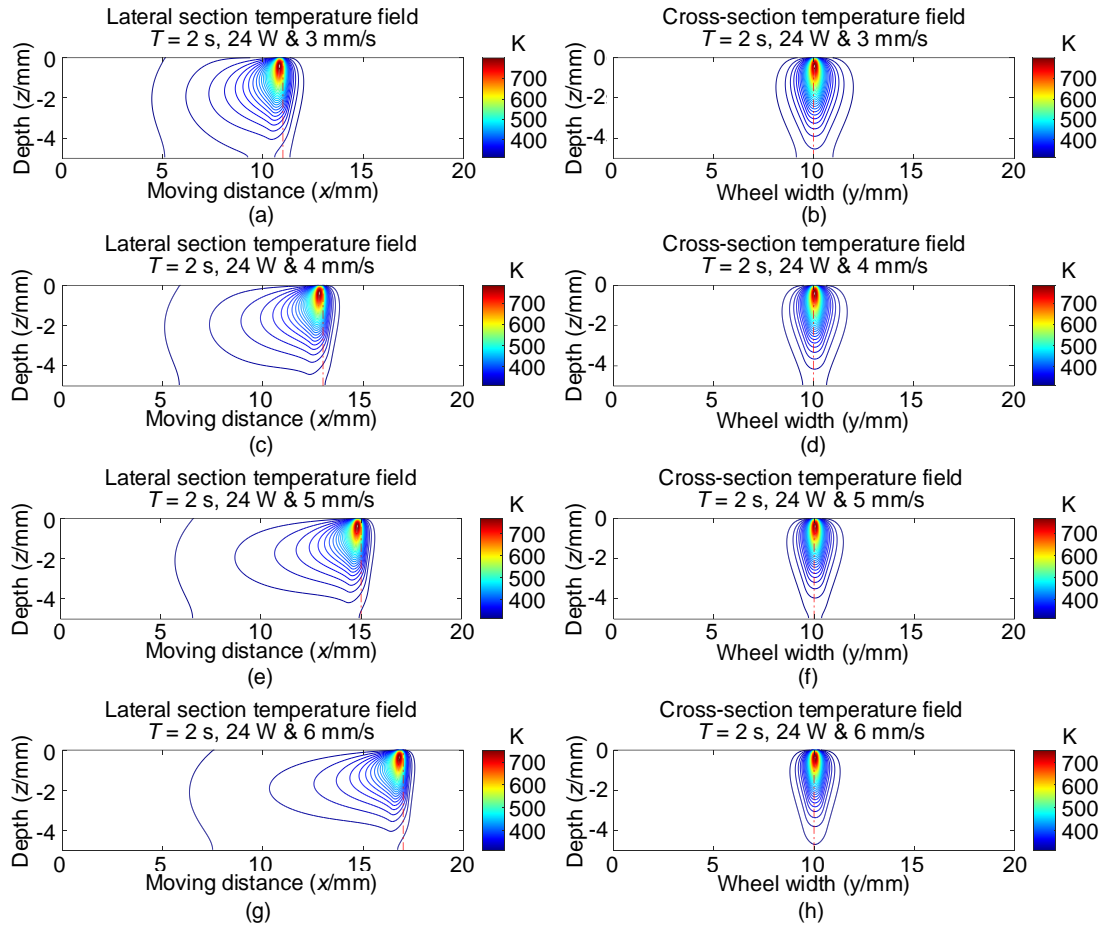


Figure 4.14 Simulation results of temperature field distribution response to feed rates from 3.0 to 6.0 mm/s with an interval of 1.0 mm/s under the laser power of 24 W. (a), (c), (e) and (g) are the lateral section view (from x-z plane) and (b), (d), (f) and (h) are the cross-section view (from y-z plane) for the feed rate of 3.0 mm/s, 4.0 mm/s, 5.0 mm/s and 6.0 mm/s, respectively.

Figure 4.15 shows the simulation results of temperature field distribution for the lateral section and cross-section for the feed rate of 3.0 mm/s, 4.0 mm/s, 5.0 mm/s, and 6.0 mm/s under the laser power of 36 W. It showed similar behaviours when the laser power increased, but a higher core temperature was observed than the results from the laser power of 24 W.

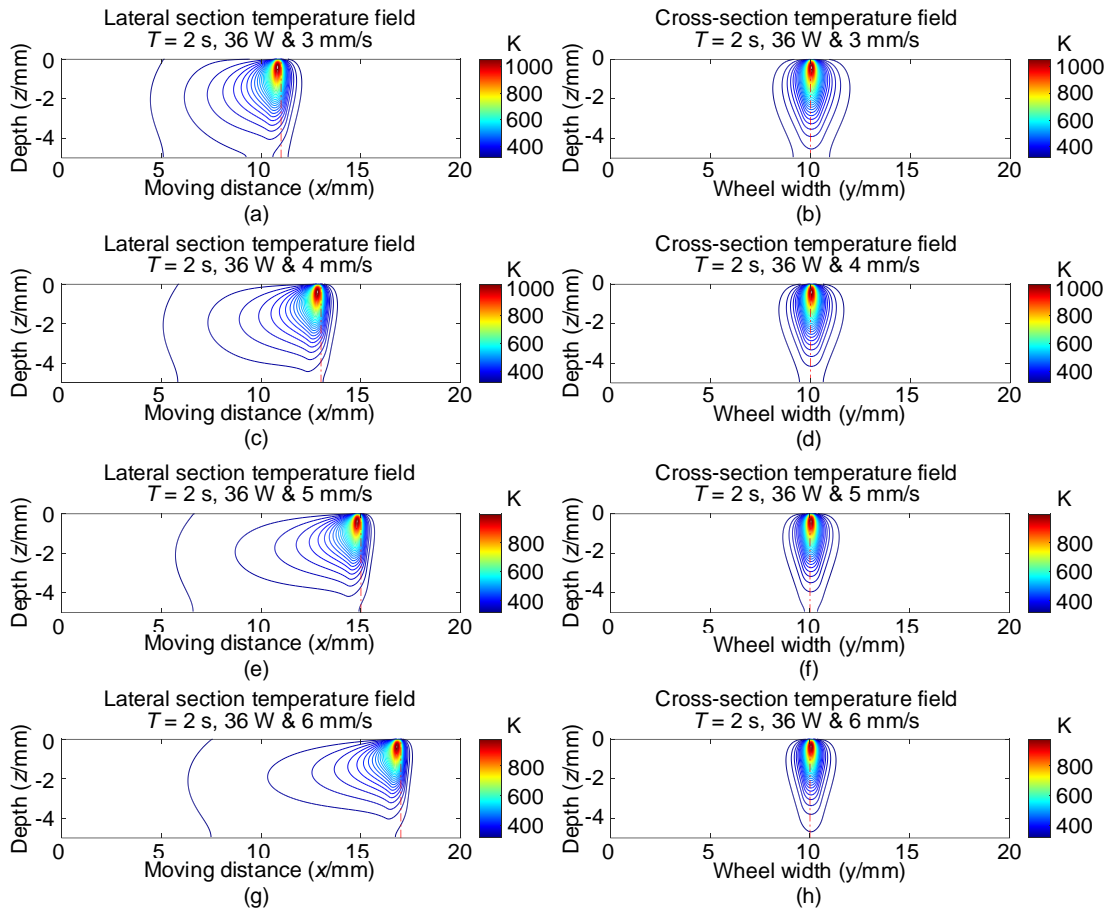


Figure 4.15 Simulation results of temperature field distribution response to feed rates from 3.0 to 6.0 mm/s with an interval of 1.0 mm/s under the laser power of 36 W. (a), (c), (e) and (g) are the lateral section view (from x-z plane) and (b), (d), (f) and (h) are the cross-section view (from y-z plane) for the feed rate of 3.0 mm/s, 4.0 mm/s, 5.0 mm/s and 6.0 mm/s, respectively.

Figure 4.16 shows the simulation results of temperature field distribution for the lateral section and cross-section for the feed rate of 3.0 mm/s, 4.0 mm/s, 5.0 mm/s, and 6.0 mm/s under the laser power of 48 W. It showed the temperature field distribution rules are consistent with the above results and the core temperature of the temperature field kept increasing as the laser power increased.

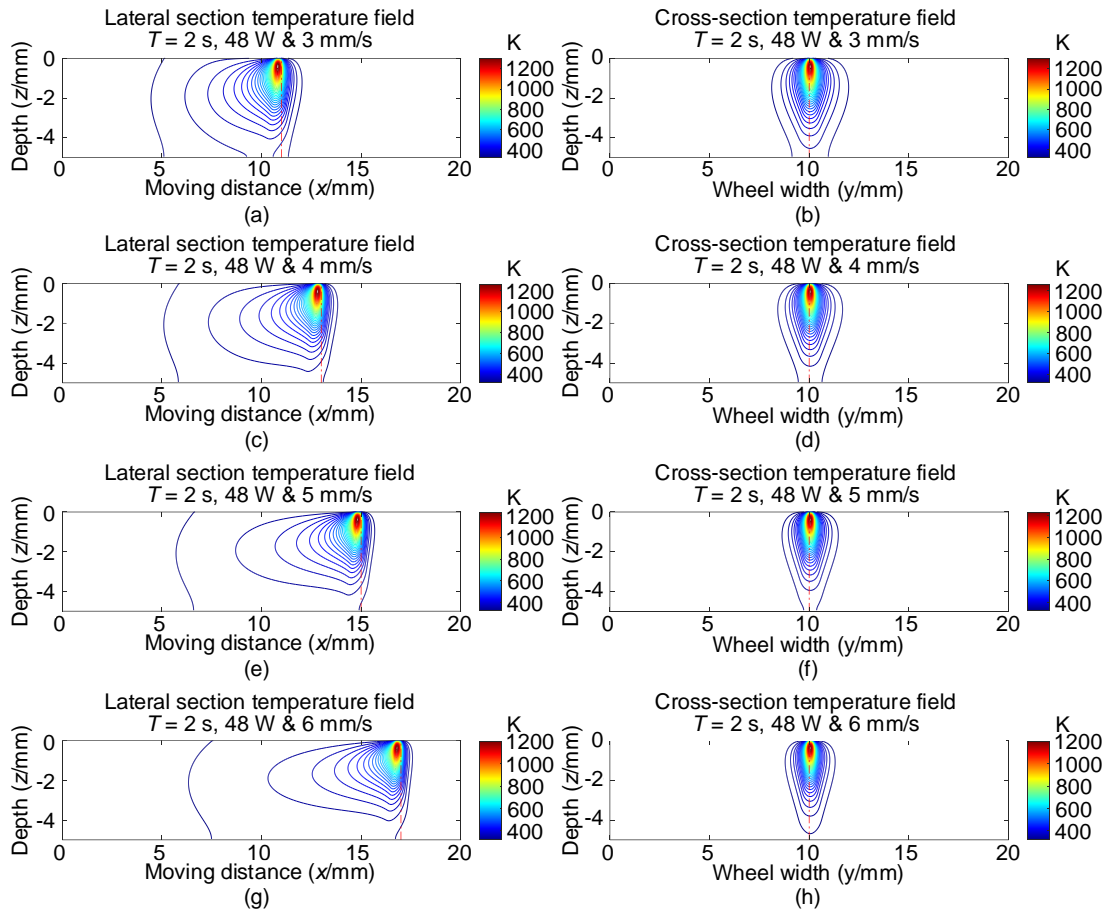


Figure 4.16 Simulation results of temperature field distribution response to feed rates from 3.0 to 6.0 mm/s with an interval of 1.0 mm/s under the laser power of 48 W. (a), (c), (e) and (g) are the lateral section view (from x-z plane) and (b), (d), (f) and (h) are the cross-section view (from y-z plane) for the feed rate of 3.0 mm/s, 4.0 mm/s, 5.0 mm/s and 6.0 mm/s, respectively.

Figure 4.17 shows the simulation results of temperature field distribution for the lateral section and cross-section for the feed rate of 3.0 mm/s, 4.0 mm/s, 5.0 mm/s, and 6.0 mm/s under the laser power of 60 W. Overall, the rules observed were kept unchanged. However, it is worth noticing that although the core temperature along the cross-section kept increasing with the laser power, the temperature field range was not dramatically increased. Besides, it showed a clear drop in the width of the temperature field with the increase in feed rate.

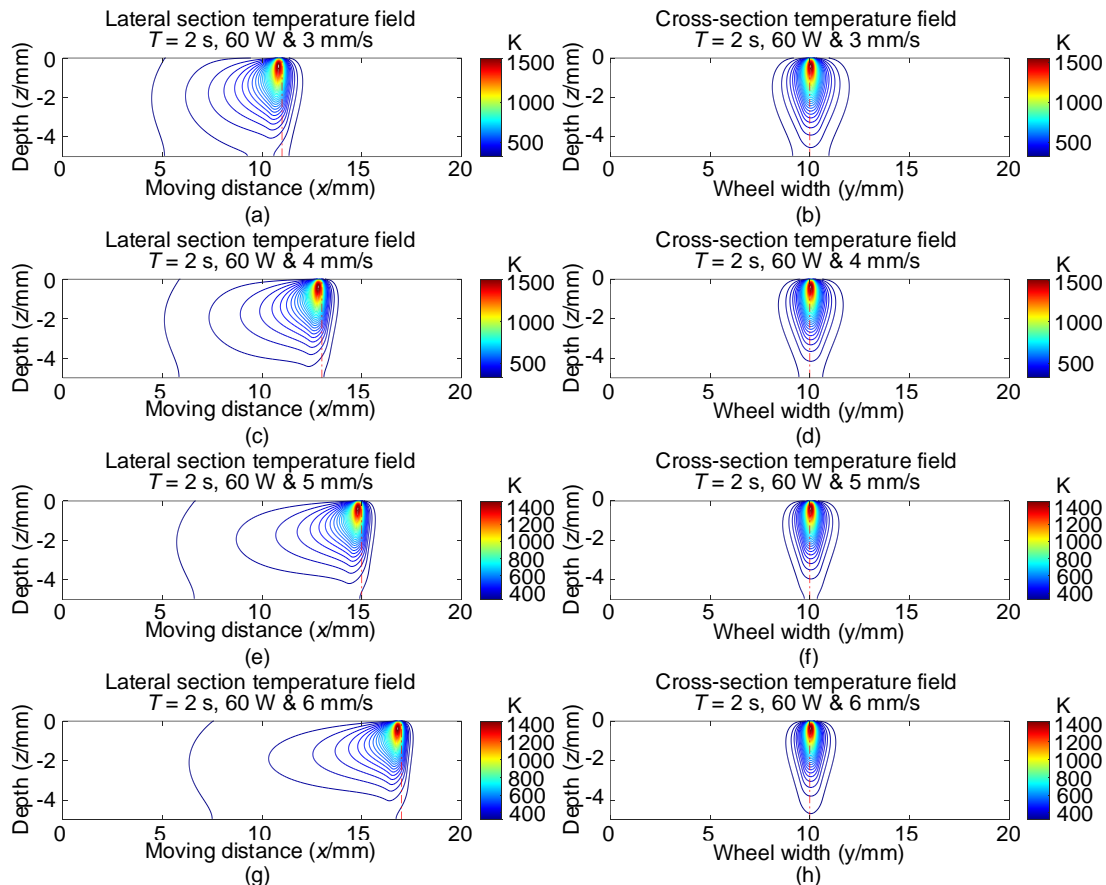


Figure 4.17 Simulation results of temperature field distribution response to feed rates from 3.0 to 6.0 mm/s with an interval of 1.0 mm/s under the laser power of 60 W. (a), (c), (e) and (g) are the lateral section view (from x-z plane) and (b), (d), (f) and (h) are the cross-section view (from y-z plane) for the feed rate of 3.0 mm/s, 4.0 mm/s, 5.0 mm/s and 6.0 mm/s, respectively.

This phenomenon indicated that the increased laser power would not dramatically broaden the heat-affected zone, but the rising feed rate would clearly narrow the heat-affected site. Meanwhile, the expanded temperature field distribution along the lateral section with feed rate indicated the ablation efficiency could be improved by the increased feed rate.

In all, the presented figures showed that the increased feed rates would benefit the increase of ablation efficiency and the decrease of the heat-affected zone. Meanwhile, the increased laser power would not largely affect the heat-

affected area, but it would be beneficial to material removal.

4.4.5 Feed Rate Effects on the Ablation Depth

The simulation results of ablation depth under the laser powers of 3.0 mm/s, 4.0 mm/s, 5.0 mm/s, and 6.0 mm/s with laser powers (from 24 W to 60 W with an interval of 12 W) were presented in **Figure 4.18** to **Figure 4.21**. Overall, it showed that the ablation depth dropped slightly with the feed rate for specific laser power and the ablation depth became more uniform with the increased feed rate. Meanwhile, the material removal rate is also increased with the feed rate as the ablation area is enlarged.

Specifically, **Figure 4.18** shows the simulation results of ablation depth under the feed rates of 3.0 mm/s, 4.0 mm/s, 5.0 mm/s, and 6.0 mm/s with a laser power of 24 W. It showed that the ablation depth dropped from -1.15 mm at 3.0 mm/s to -0.9 mm at 6.0 mm/s. With the feed rate doubling, the ablation depth decreased by 0.25 mm.

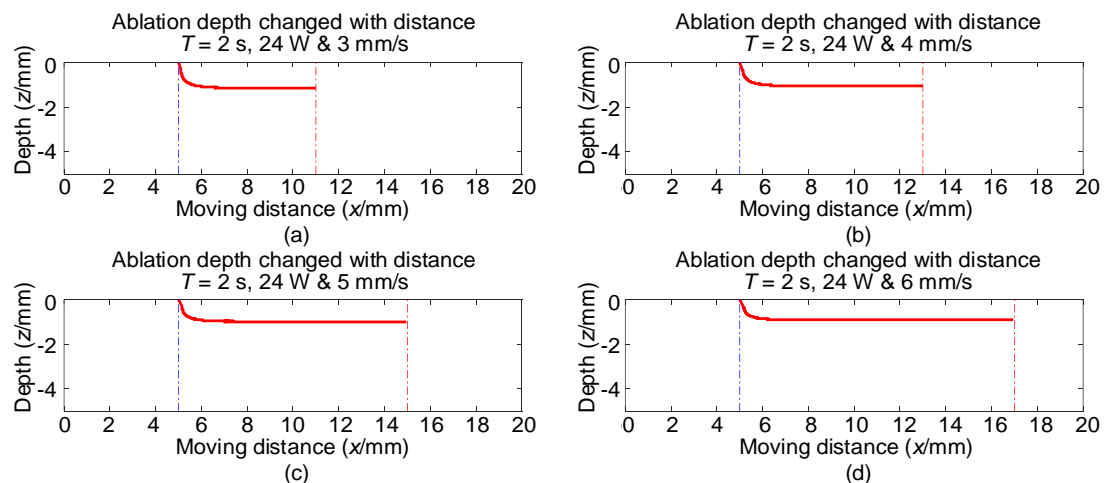


Figure 4.18 Simulation results of the ablation depth response to feed rate from 3.0 mm/s to 6.0 mm/s with an interval of 1.0 mm/s under the laser power of 24 W. (a), (b), (c) and (d) are the ablation depth for the feed rate of 3.0 mm/s, 4.0 mm/s,

5.0 mm/s and 6.0 mm/s, respectively.

Figure 4.19 shows the simulation results of ablation depth under the feed rates of 3.0 mm/s, 4.0 mm/s, 5.0 mm/s, and 6.0 mm/s with a laser power of 36 W. It showed a 0.3 mm drop for the ablation depth as the feed rate doubled from 3.0 mm/s. Besides, the ablated area was increased with the increased feed rate (the laser moved distance multiplied the ablation depth).

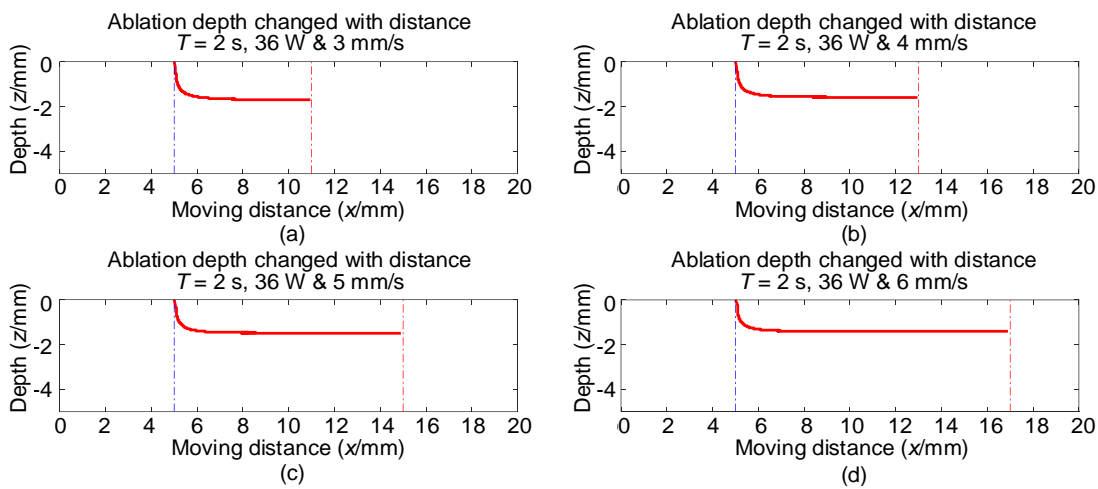


Figure 4.19 Simulation results of the ablation depth response to feed rate from 3.0 mm/s to 6.0 mm/s with an interval of 1.0 mm/s under the laser power of 36 W. (a), (b), (c) and (d) are the ablation depth for the feed rate of 3.0 mm/s, 4.0 mm/s, 5.0 mm/s and 6.0 mm/s, respectively.

Figure 4.20 shows the simulation results of ablation depth under the feed rates of 3.0 mm/s, 4.0 mm/s, 5.0 mm/s, and 6.0 mm/s with a laser power of 48 W. It showed that the ablation depth dropped from -1.95 mm at 3.0 mm/s to -1.7 mm at 6.0 mm/s, and a 0.25 mm drop was found. Meanwhile, the ablation depth under a higher feed rate was smoother than that in a lower one.

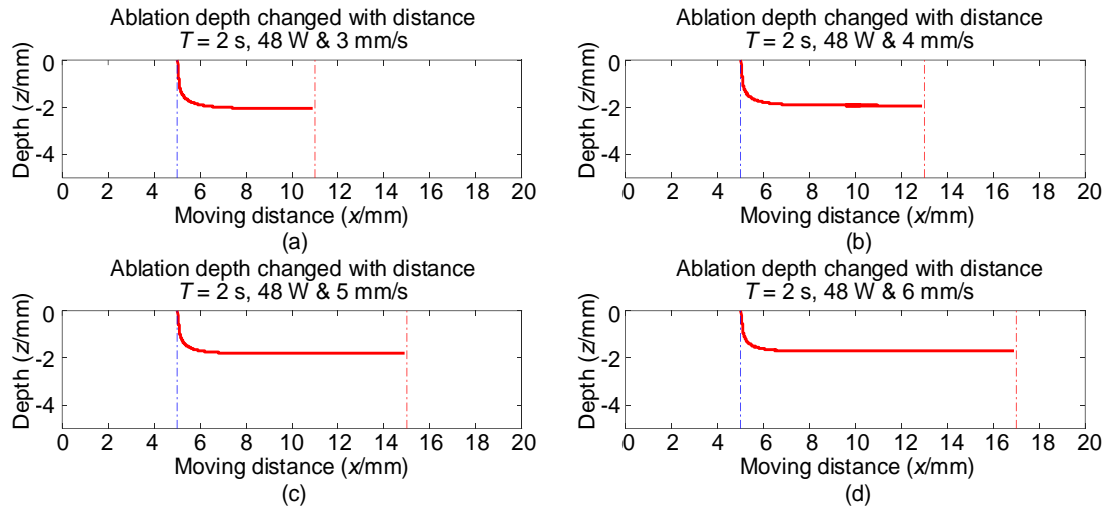


Figure 4.20 Simulation results of the ablation depth response to feed rate from 3.0 mm/s to 6.0 mm/s with an interval of 1.0 mm/s under the laser power of 48 W. (a), (b), (c) and (d) are the ablation depth for the feed rate of 3.0 mm/s, 4.0 mm/s, 5.0 mm/s and 6.0 mm/s, respectively.

Figure 4.21 shows the simulation results of ablation depth under the feed rates of 3.0 mm/s, 4.0 mm/s, 5.0 mm/s, and 6.0 mm/s with a laser power of 60 W. Unexpectedly, it showed that the ablation depth dropped by 0.4 mm with the feed rate increased from 3.0 mm/s to 6.0 mm/s. A sudden increase in the rate of decline indicated that the feed rate affected ablation depth was increased under higher laser power. However, this effect was tiny relative to the ablation depth since the drop is only 0.4 mm (dropped from -2.35 mm to -1.95 mm) when the feed rate is doubled.

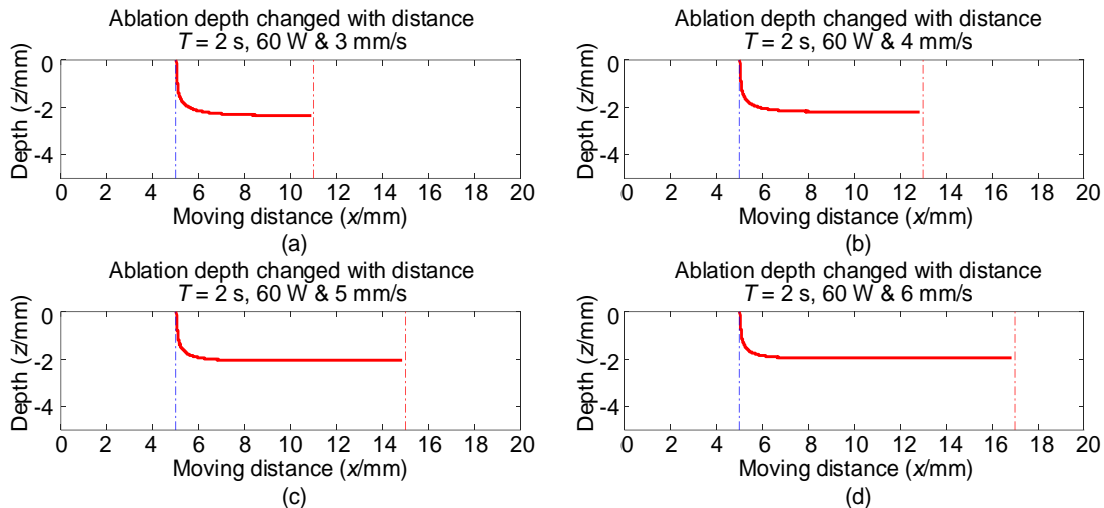


Figure 4.21 Simulation results of the ablation depth response to feed rate from 3.0 mm/s to 6.0 mm/s with an interval of 1.0 mm/s under the laser power of 60 W. (a), (b), (c) and (d) are the ablation depth for the feed rate of 3.0 mm/s, 4.0 mm/s, 5.0 mm/s and 6.0 mm/s, respectively.

In general, it shows that the ablation depth decreased with the increase in feed rate for specific laser power, but the ablation depth became uniform. Besides, figures showed that the decline rate relative to the ablation depth was tiny with the increased feed rate for specific laser power. Meanwhile, the material removal rate calculated from the measured area increased as the ablation area was enlarged with the feed rate. These phenomena indicated that the higher feed rate with higher laser power was highly expected to achieve an optimum ablation effect.

4.5 Application

Figure 4.22 shows an application for heat-affected zone control on resin-bond diamond grinding wheels, which was the usage of the modelling results analysis. This application aimed to find an optimum way to reduce the heat-affected zone. The laser machine and the grinding wheel parameters used for the trial were presented in **Subsection 4.3.1**.

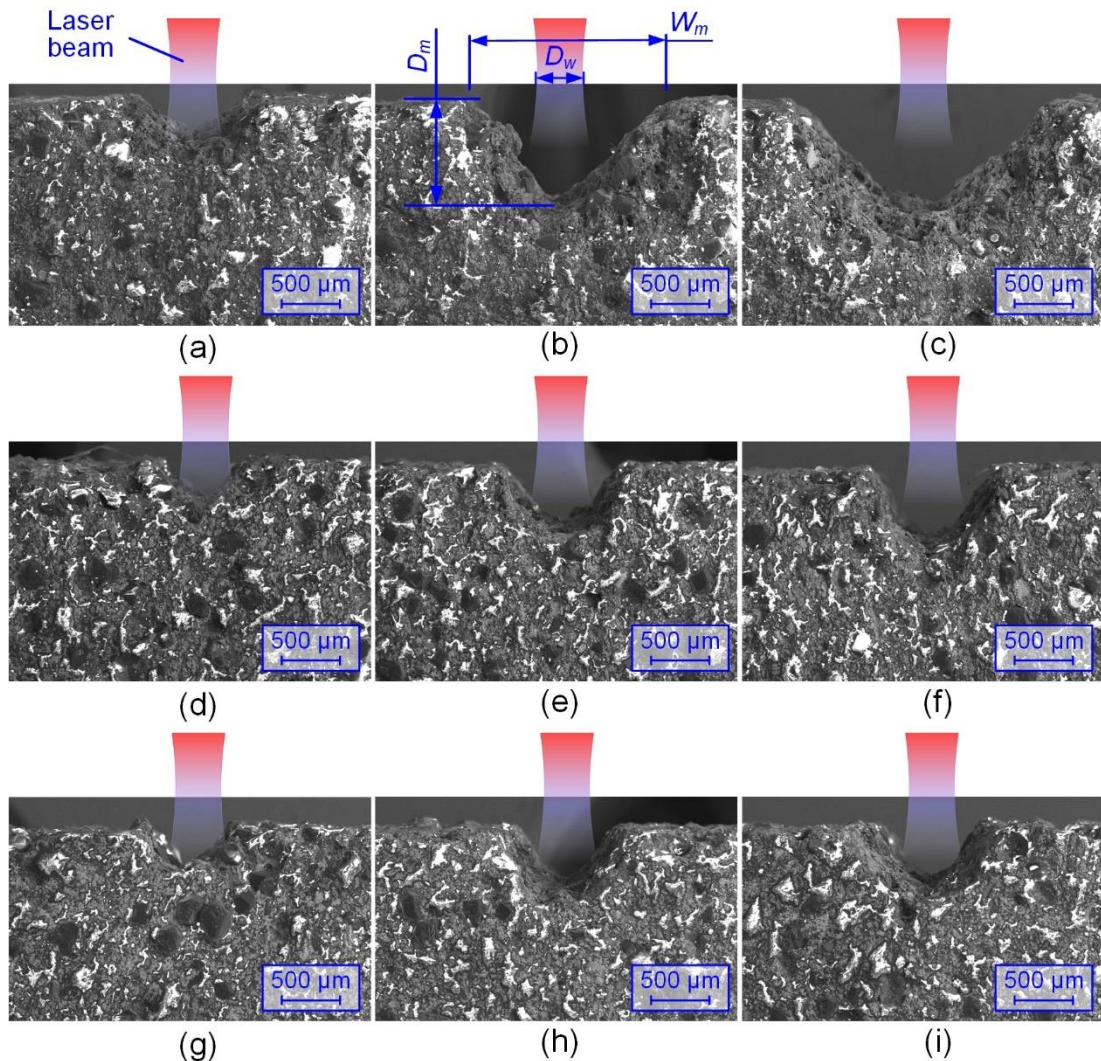


Figure 4.22 Application for heat-affected zone control on resin-bond diamond grinding wheels. Section views of the ablation result from the feed rate of 3.0 mm/s under laser powers of (a) 24 W, (b) 36 W and (c) 48 W; section views of the ablation result from the feed rate of 6.0 mm/s under laser powers of (d) 24 W, (e) 36 W and (f) 48 W. Section views of the ablation result from the feed rate of 8.0 mm/s under laser powers of (d) 24 W, (e) 36 W and (f) 48 W.

Figure 4.22 a, b&c showed the section views of the ablation result from the feed rate of 3 mm/s under laser powers of 24 W, 36 W and 48 W, while **Figure 4.22** d, e&f show the section views of the ablation result from the feed rate of 6 mm/s under laser powers of 24 W, 36 W and 48 W. Wherein, W_m is the width of the ablation trench, D_m is the depth of ablation trench, and D_w is the waist

diameter of the laser beam. Generally, it showed that the heat-affected zone was extended with laser power and decreased with the feed rate. To quantify the evaluation results, making the result understandable. Two evaluation indexes were defined: (i) the ratio of W_m/D_w was defined as an index to judge the heat-affected zone that the lower the ratio, the lower the heat-affected zone; (ii) the aspect ratio D_m/W_m was defined to measure the quality of the ablation that the higher the aspect ratio, the higher of the ablation quality.

Figure 4.23a shows that the heat-affected zone reduced with the feed rate under all the trial laser powers, especially the effects was more significant in higher laser power. **Figure 4.23b** shows that the aspect ratio was increased with the feed rate, and it also showed that the effect was more noticeable when the laser power was higher. Both indexes showed that the ablation quality was improved when the laser power and feed rate increased, which was consistent with the simulation results. Therefore, the application of simulation results was proved by the demonstration.

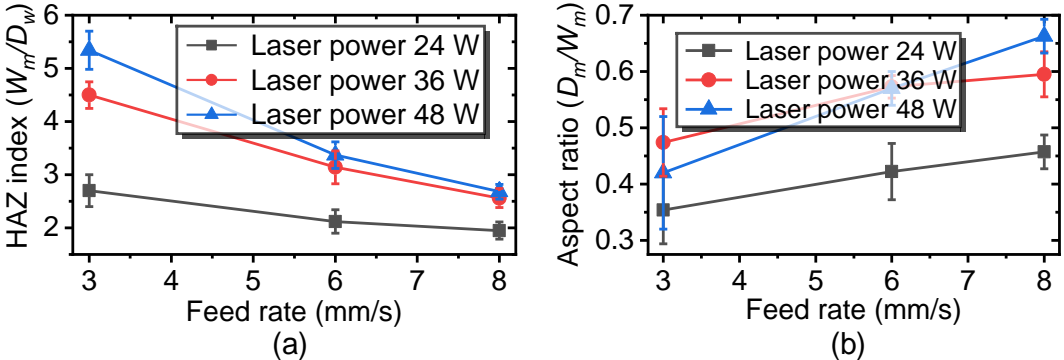


Figure 4.23 Evaluation of the ablation results on resin-bond diamond grinding wheels. (a) The heat-affected zone index (W_m/D_w ratio) and (b) aspect ratio (D_m/W_m ratio) change with feed rate under different laser power.

4.6 Conclusions and Discussions

To better understand the laser ablation process, a mathematical model is established to study the unsteady-state conduction in the composite. The time-dependent temperature field distribution and ablation depth changes with the laser power and feed rate in the heat-affected zone are revealed. Finally, an application is performed to illustrate the usefulness of the study. The key conclusions can be summarised as follows:

(1) By using the finite element difference method, a mathematical model considering the laser focus size, the laser beam energy intensity distribution along with propagation direction, and the heat conduction and convection in the ablation process is established. Both the time-dependent temperature field distribution in the heat-affected zone and ablation depth can be predicted by this model.

(2) The simulation results show that laser power (ranges from 24 W to 60 W) affects little on the shape of temperature field distribution, but it improves the core temperature of the heat-affected zone as laser power increases. Besides, the temperature field narrows with the feed rate (ranges from 3.0 mm/s to 6.0 mm/s). Therefore, it indicates that a higher laser power with a higher feed rate is expected to optimise the ablation.

(3) According to the dynamic temperature field from the simulation model, the section topography of the ablated slot can be generally predicted. Besides,

the heat-affected zone range can also be estimated using the model.

Based on the conclusions drawn from the study, an application is conducted to validate the results. It showed that ablation laws in the simulation are well consistent with the experiments. However, the computed ablation depth is inconsistent with the realistic situation greatly. Two reasons may account for this phenomenon: (i) the material failure temperature is set as a constant for the purpose of simplifying the model, so the complex failure characteristics of the organic substance are not considered; (ii) some invalid structures in the ablation zone likely have the same characters with the normal structures that make the SEM cannot precisely detect the actual ablation depth.

Chapter 5

On the Establishment of the Electromechanical Ablation System and Motion Evaluation

5.1 Introduction

To generate precise textured and profiled grinding wheels, the effect of laser power and feed rate on the diamond grinding wheels has been investigated by modelling simulation in Chapter 4. To further validate results and make the simulation work be realised in the experiment. This chapter aims to build an experimental platform for successfully conducting the further plan. With these, an electromechanical ablation system considering positioning, ablation, cleaning and measurement is expected to be made. Besides, the system's performance will be evaluated to meet all the further experimental requirements. The detailed system design and component selection idea are presented in this work. Since circumferential positioning is the main motion for the positioning system, the positioning accuracy, speed accuracy, acceleration performance and adjusting time for the motion will be evaluated. Finally, a complete performance evaluation of the system will be performed by an application demonstration.

5.2 Establishment of the Ablation System Prototype

Figure 5.1 shows the overview of the designed laser ablation system, which includes a commercial laser beam system (see **Figure 5.1a**), a custom positioning system (see **Figure 5.1b**) and an electromechanical control system (see **Figure 5.1c**). This electromechanical system design principle is to use

the existing commercial hardware to the maximum. In addition, two special control functions (mechanical shaped tools start and laser distance sensor communication) are designed by using Labview software with MyRIO 1900 (NI company) control board. The detailed design information for each part is shown below.

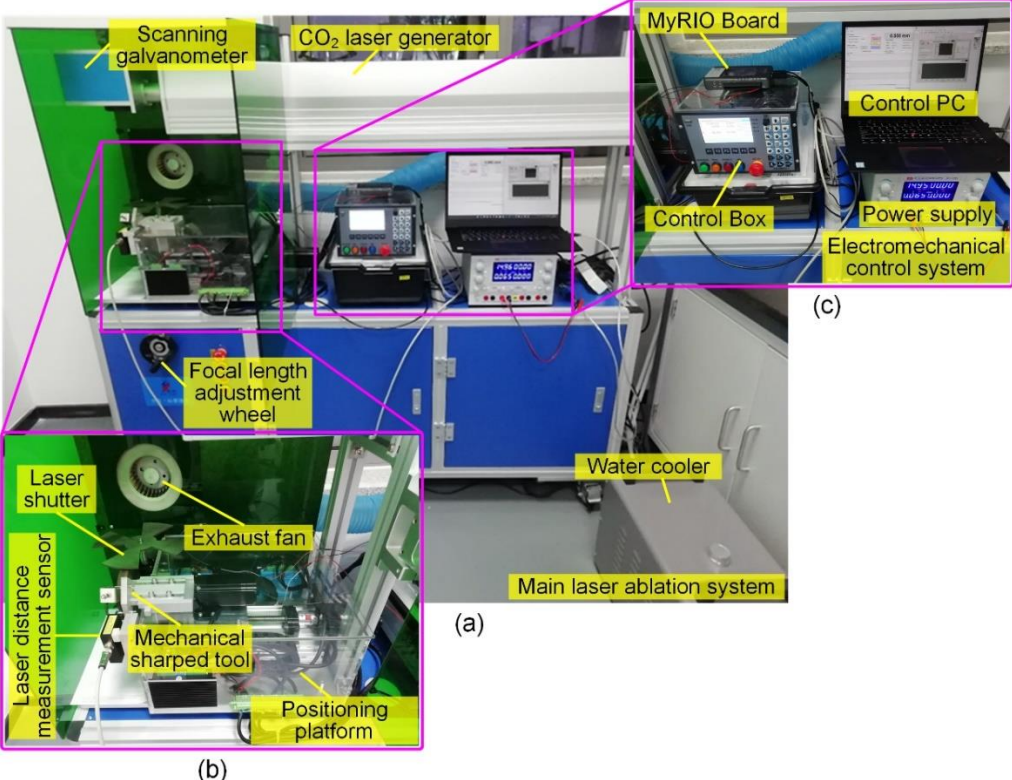


Figure 5.1 Overview of the newly designed ablation system. (a) The main ablation system; (b) the positioning; (c) the electromechanical control system.

5.2.1 Positioning Platform

1) The initial version of the platform

Based on the requirement of the positioning system, the linear and angular motions and positions of the grinding wheels were accurately controlled by the specially-made positioning system. The Solidworks and physical models of the positioning system are shown in **Figure 5.2 a&b**. It consisted of the controller (BR010-11T8X2M, BenT CNC Automation Equipment Company), the driver

(ZD-M42, Philips Company), the stepper motor (42HS4013A4CE, Sumtor Company), the reducer (SK4248-19.2, Yixing Technology Company) and other auxiliary hardware, enabling the 2-axis simultaneous motions (which were the translational and the rotational motions separately along and around the wheel axis). The positioning system has the translational and rotational motion accuracies of 10 μm and 0.05 deg based on the G-code-based SIEMENS NC system. In addition, the translational and rotational motion speeds were separately within the ranges of 0~100 mm/s and 0~15 deg/s.

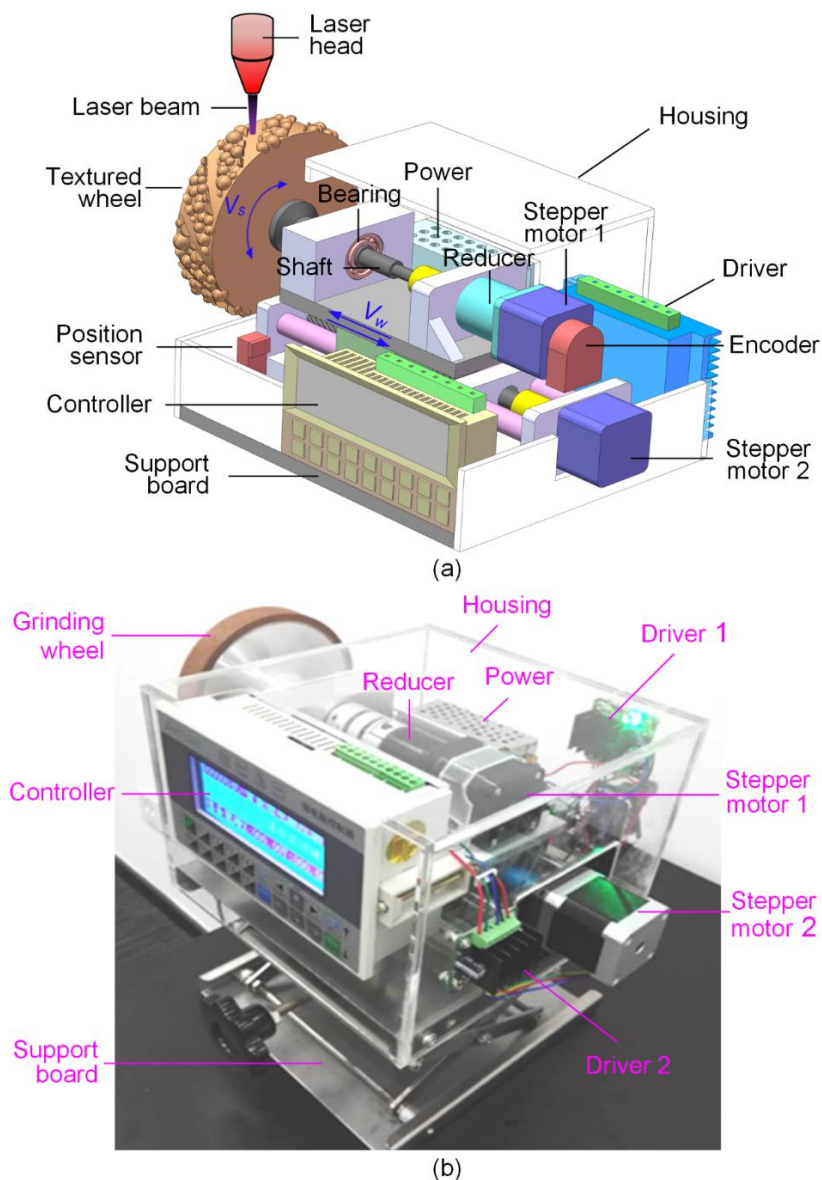


Figure 5.2 Initial version of the design. (a) Solidworks model and (b) the physical

prototype.

The small footprint is one of the advantages of this platform that makes it easy to be moved or placed in the workspace of a laser machine. Therefore some basic experiments can be completed with this design. However, the disadvantages are apparent (i) it has a limited movement range because of the small size, (ii) a low response speed, and inevitable backlash due to the relatively weak power has to be assisted by a reducer. Besides, this platform has no ability for laser beam manipulating and no ability to clean and measure the ablated slots.

2) The improved version of the platform

To make up for the shortcomings of the initial design, **Figure 5.3** a&b shows the Solidworks and physical models of the enhanced design of the platform. The platform contains an adjustable supporter, movement stages, laser beam shutter, mechanical shaped tool, and laser distance measurement sensor. The adjustable supporter has four adjustment screws, with which the height, angle, and stability of the platform can be custom adjusted. The movement stages include a linear movement stage and a rotational movement stage. The linear movement stage is driven by a commercialised motor-screw-slide system, which is rigidity and has a large motion range of 100 mm, and 10 μm in linear accuracy. The grinding wheel on the rotational stage is directly driven by a 57-servo motor through a shaft with a minimum rotational angle of 0.036° and a maximum torque of 3.5 N·M. The movement stages enable the grinding wheel to achieve a maximum linear move speed of 2,000 mm/s and a maximum rotational speed of 2,500 mm/s.

The laser beam shutter is made of stainless steel with graphite inserts and driven by a 42-step motor, which can make the switch time within 0.05 s. According to the experts and engineers from Han's machine, they usually use graphite and ceramic to stop the laser beam pass through. However, these materials are brittle and easy to be damaged. Therefore, here fabricated the shutter blades with the materials and embedded this brittle blade into an alloy-based matrix. Hence, the excellent strength and high-temperature resistance of the shutter could be achieved by this method. The mechanical-shaped tool is set with a diamond tip, which is controlled by a solenoid. Both the contact state and contact force can be controlled by the solenoid. The mechanical-shaped tool also can be adjusted from an axial direction by a manual method to adapt the grinding wheel position.

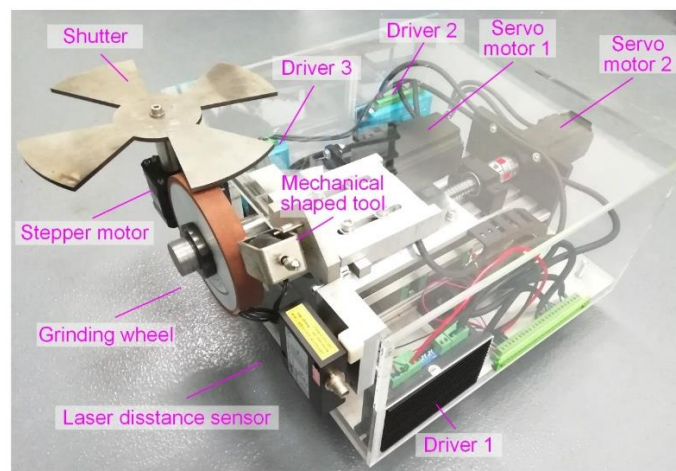
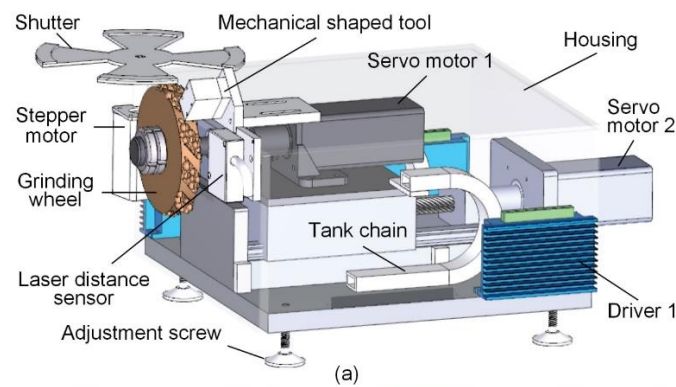


Figure 5.3 Improved version of the platform. (a) Solidworks model and (b) the

physical prototype.

The depth measurement is performed by a commercial laser distance measurement sensor, which is worked based on the red-light triangular reflection of a semiconductor laser. It has a measurement range of 10 mm with a resolution of 0.001 mm, and the maximum sampling rate is 921,600 Hz.

The overall view of the whole positioning platform is shown in **Figure 5.4**. It includes a positioning platform and a control box connected by several control cables. Compared to the initial version, the enhanced design has two special motion parts (stepper motor controlled laser shutter and solenoid controlled mechanical sharpened tool) for laser beam on-off control and grinding wheels cleaning, apart from the linear move and rotation of the initial version. Besides, a laser distance measurement sensor is added to monitor the ablation depth.

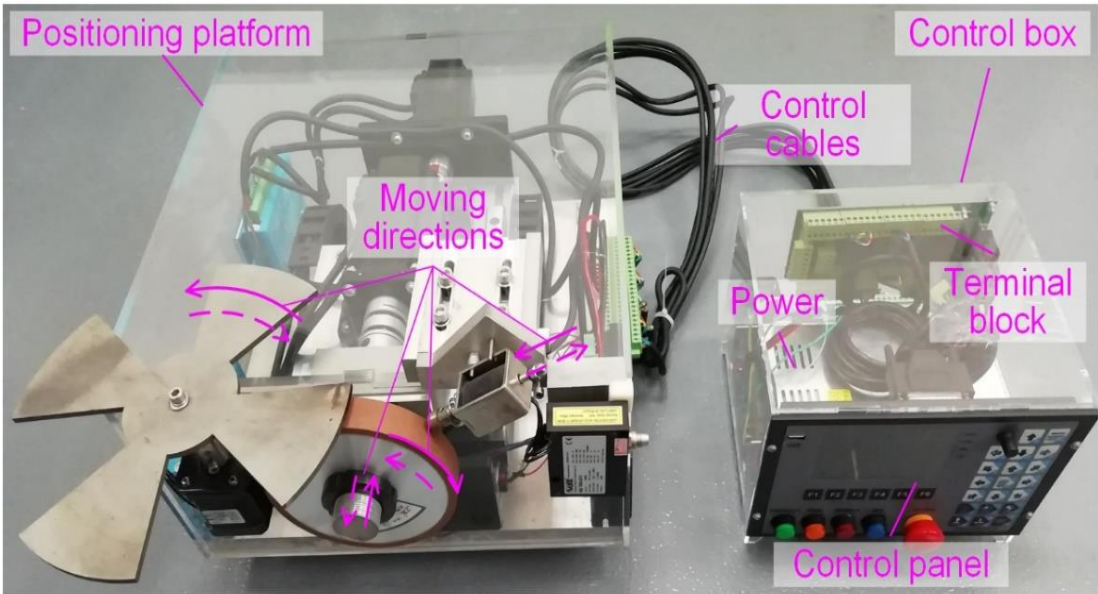


Figure 5.4 Overall view of the whole positioning platform.

5.2.2 Laser Beam Generation System

The main body of the laser generating system is a commercial CO₂ laser

carving machine provided by Ketai Company, which mainly includes a CO₂ laser generator, control system and cooling system. The typical wavelength for this kind of laser is 10.6 μm. With the collateral software kit, the power of the laser beam can be adjusted between 10 W to 100 W, and the emission frequency can be adjusted between 20 Hz to 200,000 Hz. After the focusing of the lens, the minimum focal spot size could be 0.3 mm with a focal length of 280 mm. Besides, the distance between the focus lens and the target can be adjusted by turning the handwheel.

5.2.3 Electromechanical Control System

The control system contains a custom control box, a MyRIO control board (1900, NI Company), a regulated power supply and a high-performance laptop (X1 Extreme, Lenovo Company). The custom control box comprises a motion control board and a 600 W power supply that is mainly responsible for the motion of the positioning system and the laser shutter. The MyRIO control board, the power supply, and the high-performance laptop play the role of controlling and coordinating the whole system. These tasks contain the feedback of the laser ablation depth on the grinding wheel, the wheel rotation speed, and the working state of the mechanical shaped tool. All these tasks' states can be presented on the screen of the high-performance laptop.

5.3 Positioning Evaluation

The custom positioning system is the most crucial part of the ablation system to be evaluated as other parts are commercial products that the market has proved the performance. There are two designs for the positioning system, but

the backlash cannot be avoided in the initial one due to the existence of a reducer. Therefore, it can only be used for some basic positioning without demanding requirements. The improved one is aimed to solve the shortcomings of the previous version, and it needs to be working in demanding conditions. Therefore, a serial test should be performed on the improved version for better application. Ablation accuracy is highly affected by precise motion and circumferential positioning. Thus, the positioning accuracy, speed accuracy, acceleration performance and adjusting time are evaluated.

5.3.1 Positioning Accuracy

Figure 5.5 shows the positioning for different moving distances at various speeds. Generally, the grinding wheel in the positioning system can reach the corresponding move distance under all the moving speeds. Besides, all the figures indicate the good linearity of the moving distance with time, except for the positioning for moving 1 mm (see details in **Figure 5.5a**). To be specific, the positioning in **Figure 5.5** (a) shows a high non-linearity in the higher speeds (like the speed of 20 - 100 mm/s). Especially, it presents a near exponential rise trend when the feed rate increases to 100 mm/s and takes more time to recover from the overshoot to a sound stage. Meanwhile, an overshoot is also found in each figure representing different moving distances. Notably, the higher the moving speed, the higher the overshoot.

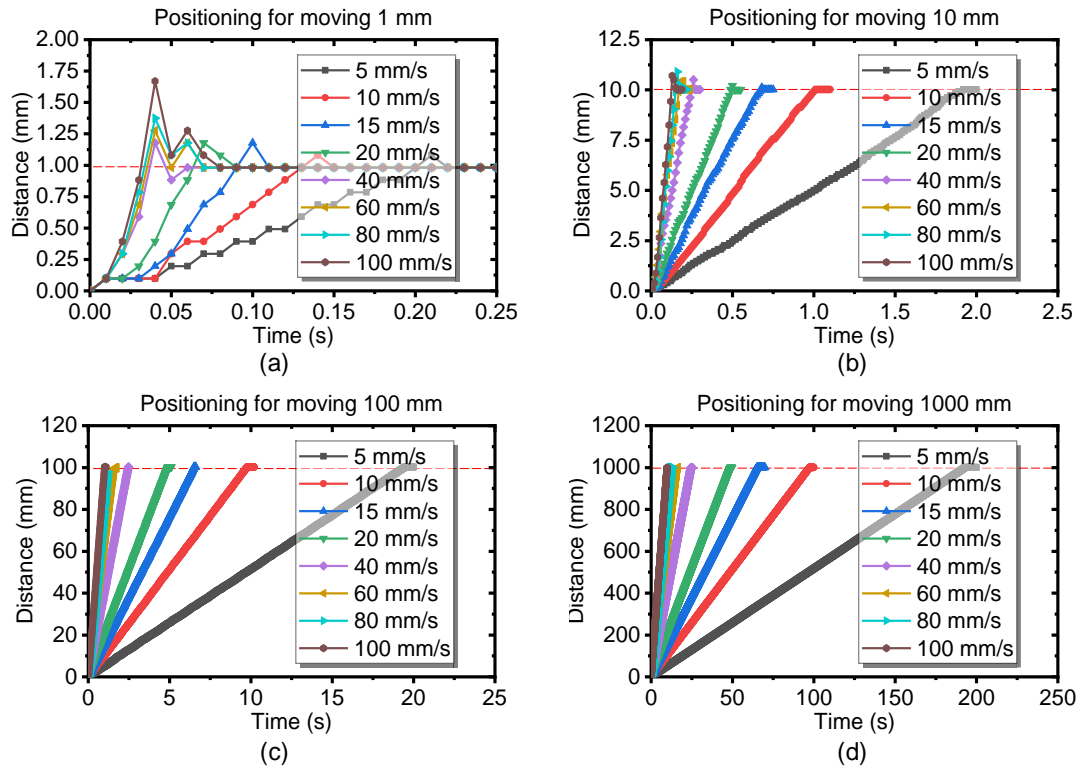


Figure 5.5 Positioning for different moving distances under various speeds. Positioning for moving distance of (a) 1 mm, (b) 10 mm, (c) 100 mm and (d) 1,000 mm.

Figure 5.6 shows the stable error and maximum overshoot for different moving distances under various speeds. It reveals that the actual moved distance is not fully consistent with the corresponding idea distance. With the increase in moving distance, the stable errors fluctuated and became larger. When positioning for moving 1 mm (see **Figure 5.6a**) and 10 mm (see **Figure 5.6b**), the stable errors are small and almost keep unchanged, but when positioning for moving 100 mm (see **Figure 5.6c**) and 1,000 mm (see **Figure 5.6d**), the stable error becomes fluctuating and growing. However, the maximum overall stable errors for each figure are within ± 0.2 mm. Remarkably, no signs show the stable errors keep increasing with the increase of the moving distance when compared with **Figure 5.6 (c)** and **Figure 5.6 (d)**.

The maximum overshoots are generally increased with the growth of moving speeds, especially for the relatively short-distance positioning. The maximum overshoot for most situations is below 0.5 mm, but it near approaches 1 mm for some extreme cases (see details in **Figure 5.6b**). This is likely due to the initial force of the moving parts, making the motion hard to be immediately stopped at a higher speed.

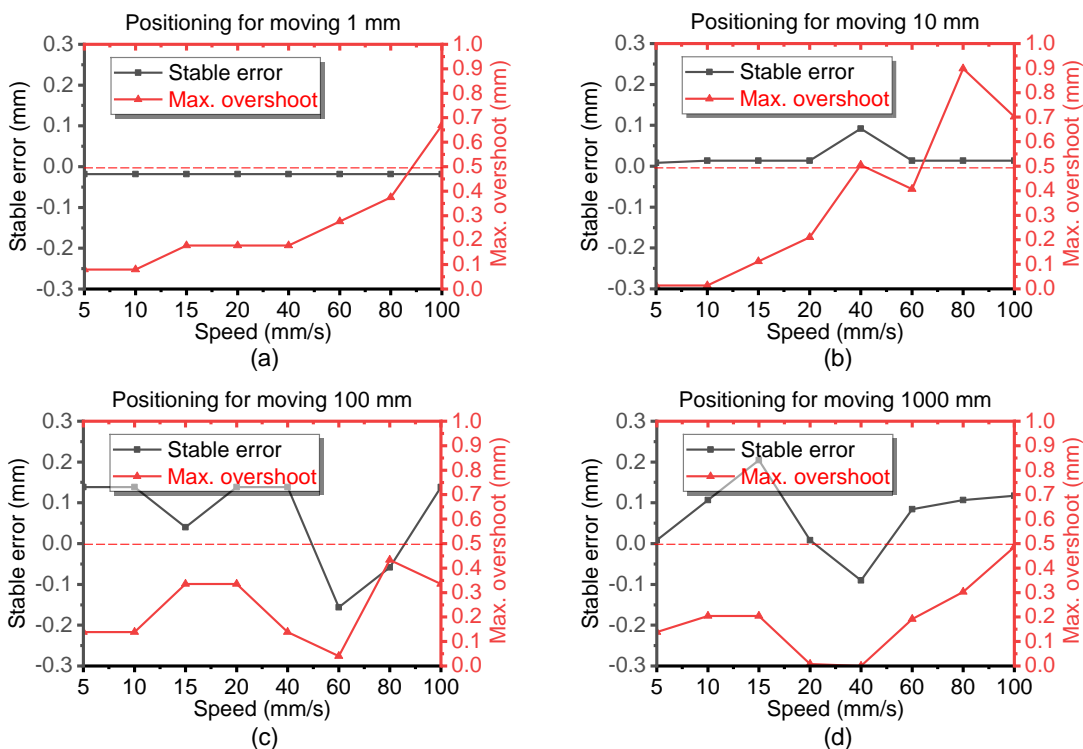


Figure 5.6 Stable error and maximum overshoot for different moving distances under various speeds. Positioning for moving distance of (a) 1 mm, (b) 10 mm, (c) 100 mm and (d) 1,000 mm.

5.3.2 Speed Accuracy

Figure 5.7 represents that the moving speed varies with time under different conditions. Generally, all the moving speeds experienced a short acceleration in the first stage (within about 0.5 s) and then gradually reached the stable stage. However, both the figures show the fluctuations of the moving speeds

even in the stable stages. Besides, both the figures show the cases where the actual speed exceeds the set speed in the acceleration stage. For example, in the lower feed rates (see **Figure 5.7a**), when the set moving speed is 1.0 mm/s, the system is even always over 1.0 mm/s and takes several steps to slow down.

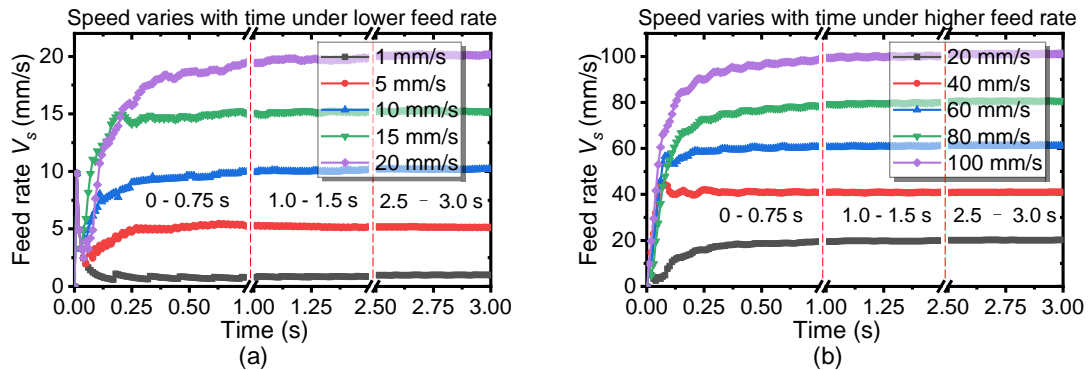


Figure 5.7 Moving speed varies with time under different conditions. Moving speed varies with time under (a) lower and (b) higher feed rates.

Figure 5.8 reveals that the stable error and percentage vary with speeds under different conditions. It shows that the stable error is increased with the growth of moving speed under both conditions. Differently, a larger increase degree is found in the higher moving speed. To be specific, the maximum stable error is about 0.2 mm/s in the lower speed group (see details in **Figure 5.8a**), while this figure for the higher speed group is reached 1.3 mm/s (see details in **Figure 5.8b**).

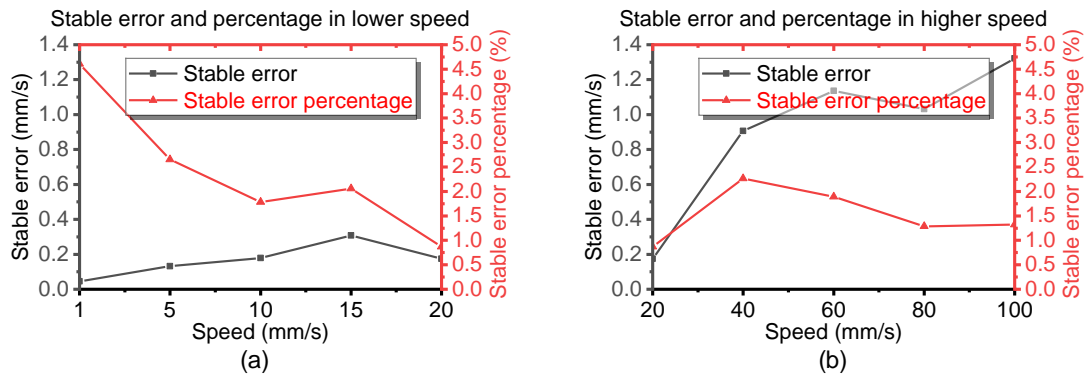


Figure 5.8 Stable error and percentage vary with speed under different conditions. Stable error and percentage under (a) lower and (b) higher feed rate.

As for stable error percentage, it has an obvious drop in the relatively lower moving speed from around 4.5% at 1.0 mm/s to about 1.0% at 20 mm/s (see details in **Figure 5.8a**). However, this figure for higher moving speed is almost kept around at 1.5% (see details in **Figure 5.8b**). Therefore, it indicates the stable errors will be raised with the increase in moving speed, but the stable error percentages are within the limited range.

5.3.3 Acceleration Performance

(1) Acceleration performance under relative lower speed

Figure 5.9 shows the acceleration performance at a relatively lower speed. Generally, all figures show the moving speeds experienced a sudden big acceleration at the first few milliseconds and then gradually reduced to around 0 mm/s² in the end. The maximum acceleration rates for each speed are almost the same (slightly below 1,000 mm/s²). But the acceleration processes for the different speeds show a slight difference. It seems the ratio of positive to negative acceleration time increased with moving speed.

To be specific, the acceleration for the speed of 1.0 mm/s, the positive acceleration accounts for a few percentages in the acceleration process. Typically, a sudden positive acceleration with a long-time negative acceleration (see details in **Figure 5.9a**). When the moving speed increases to 5.0 mm/s, both the positive and negative acceleration increase, but the negative acceleration amplitudes are smaller than the positive (see details in **Figure 5.9b**). When the moving speed exceeds 10.0 mm/s, most of the accelerations in the figures are presented to be positive and fluctuate in the range of 0-100 mm/s² (see details in **Figure 5.9c - Figure 5.9e**).

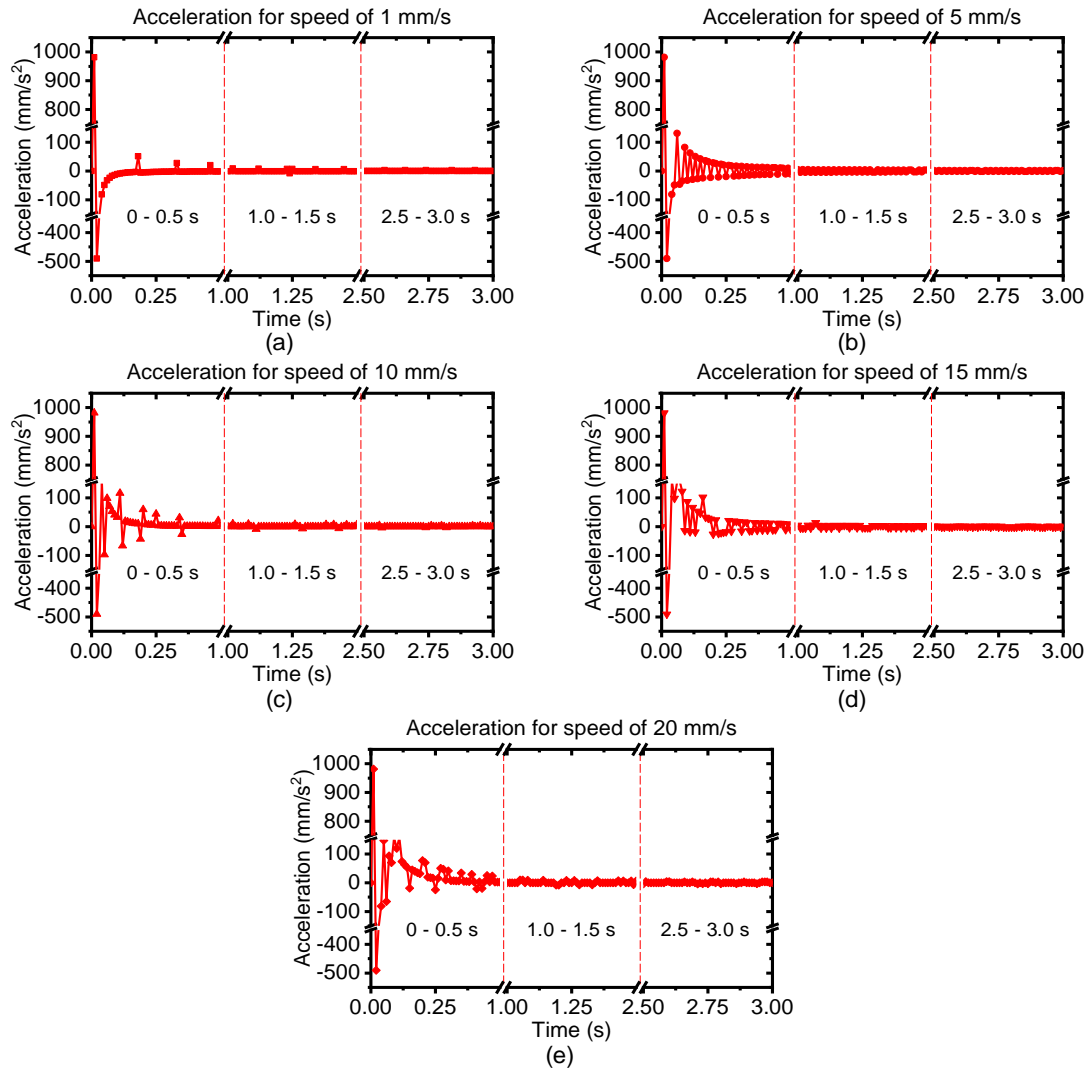


Figure 5.9 Acceleration performance under relatively lower speed. Acceleration performance for moving speed of (a) 1 mm/s, (b) 5 mm/s, (c) 10 mm/s, (d) 15 mm/s and 20 mm/s.

(2) Acceleration performance under relative higher speed

Figure 5.10 shows the acceleration performance at a relatively higher speed. Overall, the figures under relatively higher speed show the same trend as those under relatively lower speed. However, the maximum acceleration rates are slightly bigger than those under relatively lower speeds. Especially, the maximum acceleration has exceeded 1,200 mm/s² when the moving speed is 100 mm/s. Meanwhile, the fluctuation of the acceleration is more violent with the increase of the moving speeds (see details in **Figure 5.10 a-e**).

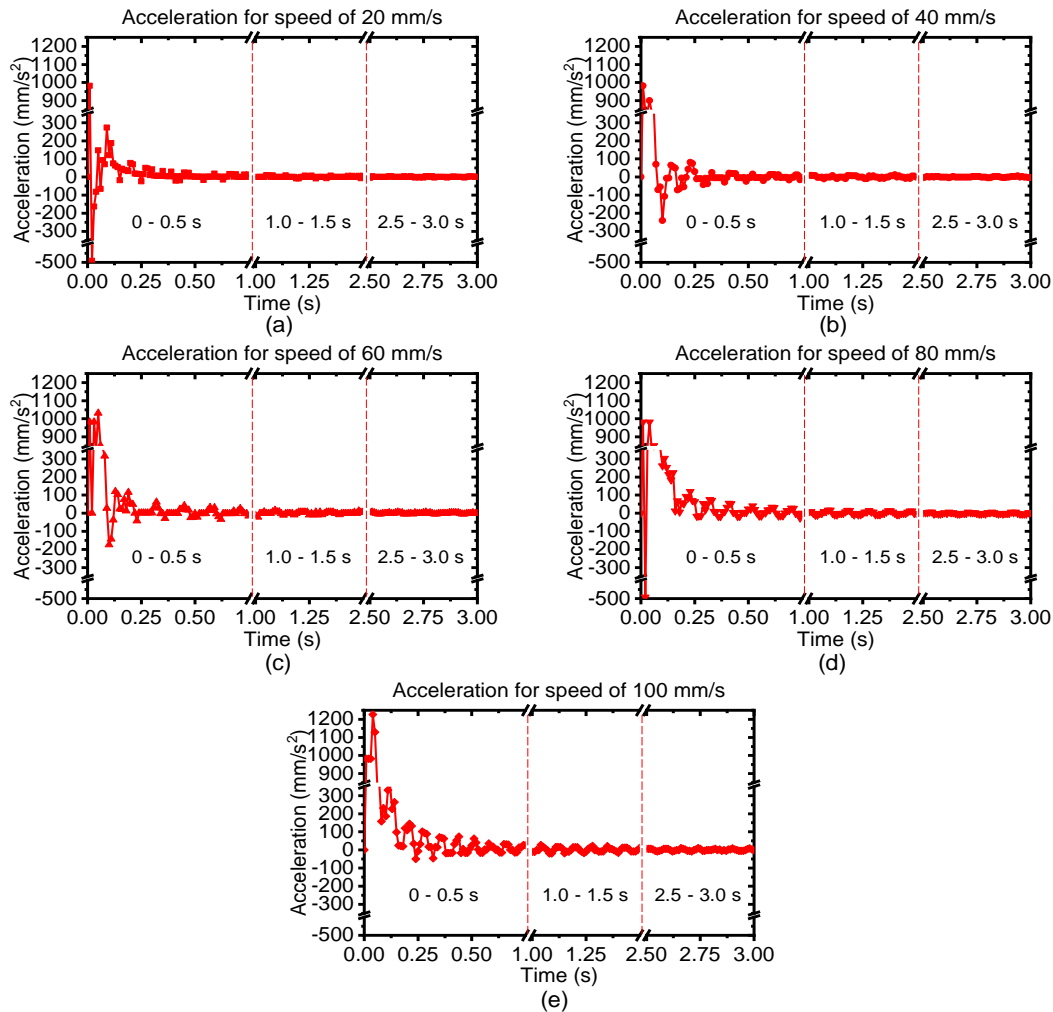


Figure 5.10 Acceleration performance under relative higher speed. Acceleration performance for moving speed of (a) 20 mm/s, (b) 40 mm/s, (c) 60 mm/s, (d) 80 mm/s and 100 mm/s.

Overall, the acceleration performance has the same characteristics under a relatively lower speed. However, it shows a more significant fluctuation under somewhat higher speed, and the fluctuations continuously exist with time. Especially, it shows a sporadic leap when the speed is below 60.0 mm/s (see **Figure 5.10 a-c**), but it starts to show an obviously cyclic acceleration similar to sine after the speed exceeds 80.0 mm/s (see **Figure 5.10 d-e**). This is likely due to the step-feeding nature of the stepper motor and the intervention of the PID controller system. The higher the speed, the higher the requirement for the controller. Therefore, the increased speed leads to continuously fluctuations in the acceleration.

5.3.4 Adjusting Time

Figure 5.11 shows the adjusting time for the positioning system motion regarding moving a certain distance, speed adjustment, and acceleration adjustment.

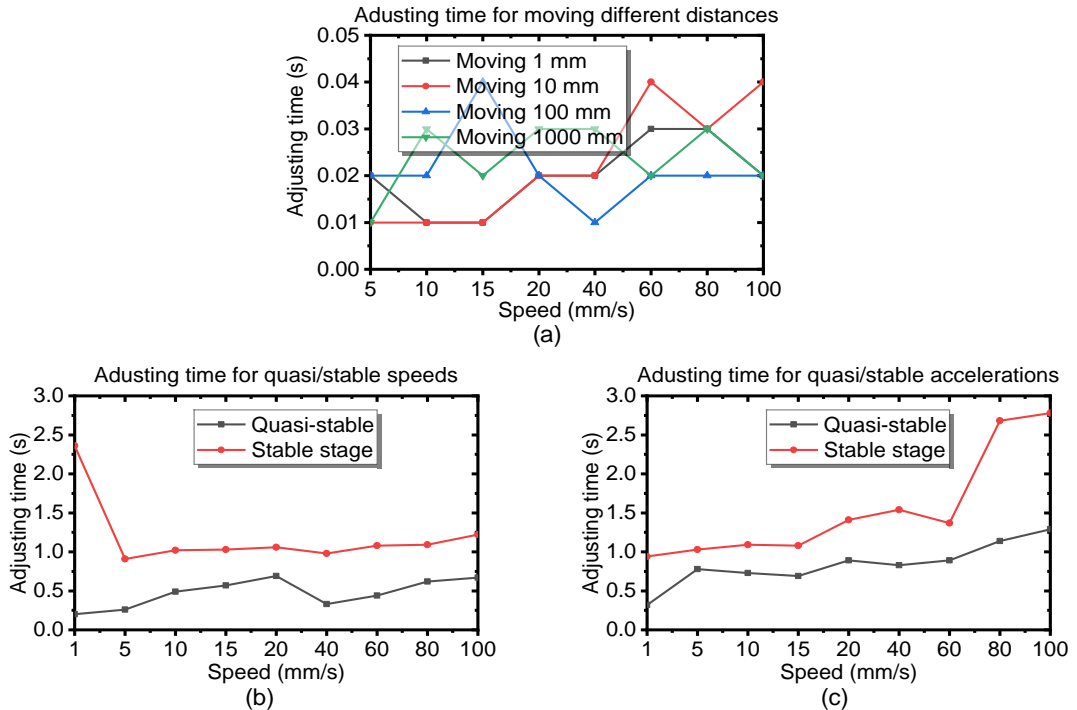


Figure 5.11 Adjusting time for the positioning system motion. Adjusting time for (a) moving different distances, (b) quasi/stable speeds and quasi/stable accelerations.

Figure 5.11a shows the adjusting time for moving different distances is slightly increased with the moving speed growing, especially for the short distance positioning, e.g., 1 mm or 10 mm. The mentioned adjusting time for moving certain distances is defined by the time that the aimed point on the grinding wheel first reaches the set position to stop. This is likely because more overshoots will happen at higher moving speeds, leading to more time being needed to fix the larger fluctuations. However, all the positioning processes can be completed within 0.05 s. This result may attribute to the stability of the system that ensures the positioning process rapidly responded to the system.

Figure 5.11b shows the adjusting time for quasi/stable speeds, where the

quasi-stable speed is defined as speeds with 10% - 5% errors compared to the target speed, while the stable speed is referred to as speeds within 5% errors to target speed. It indicates the adjusting time to the quasi-stable stage is slightly increased with the moving speeds growing, and the adjusting time range is around 0.25 s – 0.5 s. This is likely because the higher moving speeds suffered from more fluctuations and hence experienced more adjusting time. Interestingly, the adjusting time to the stable stage is about 1.0 s for all moving speeds except for 1.0 mm/s, where the adjusting time has exceeded 2.25 s (more than one time over that for other speeds). This phenomenon is due to the nature (creeping characteristics at low speed) of the step servo motor.

Figure 5.11c shows the adjusting time for quasi/stable accelerations, where the quasi-stable acceleration is defined as accelerations fluctuating between 5 mm/s² to 10 mm/s², while the stable acceleration is defined as speeds within 5 mm/s². It shows that the adjusting times for both quasi-stable and stable stage accelerations are increased with the moving speed. However, the adjusting time for the quasi-stable stage is ranged from 0.25 s to 1.25 s, while this figure for the stable stage is wide (from about 1.0 s to around 2.75 s). It is worth mentioning that the adjusting time for the stable stage only fluctuates between 1.0 s to 1.5 s when the moving speed is below 60 mm/s. After the moving speed of 60.0 mm/s, the adjusting time for the stable stage experienced a sudden increase from 1.25 s to 2.75 s. This is likely due to the high moving speed causing the vibration of the positioning system, which needs more time for the system to recover to stability.

5.4 Applications

As mentioned in the literature review, researchers were mainly working on generating regular textures on flat abrasive tools despite the potential application value of other textures. This is mainly because the lack of effective

dressing strategies and precise positioning platforms make it hard to remove target materials controllably.

Figure 5.12 presents the ablated diamond grinding wheels with irregular-shaped textures, which plays the role of the function test for the electromechanical ablation platform. **Figure 5.12a** shows the grinding wheel with continuously changed slots, indicating precise positioning and rapid response performance. The uniform intervals between the patterns and the sharpened junction tip for junction can only be achieved with these two super performances. **Figure 5.12b** shows the grinding wheel with sine-line-shaped slots, which is highly needed for the reliable linkage of the rotational and axial movement accuracy and rapid response time. The uniform slot topography and interval can be guaranteed with a reliable linkage. Besides, the ablated structures will not be damaged when the laser beam moves to other slots, thanks to the rapid response time.

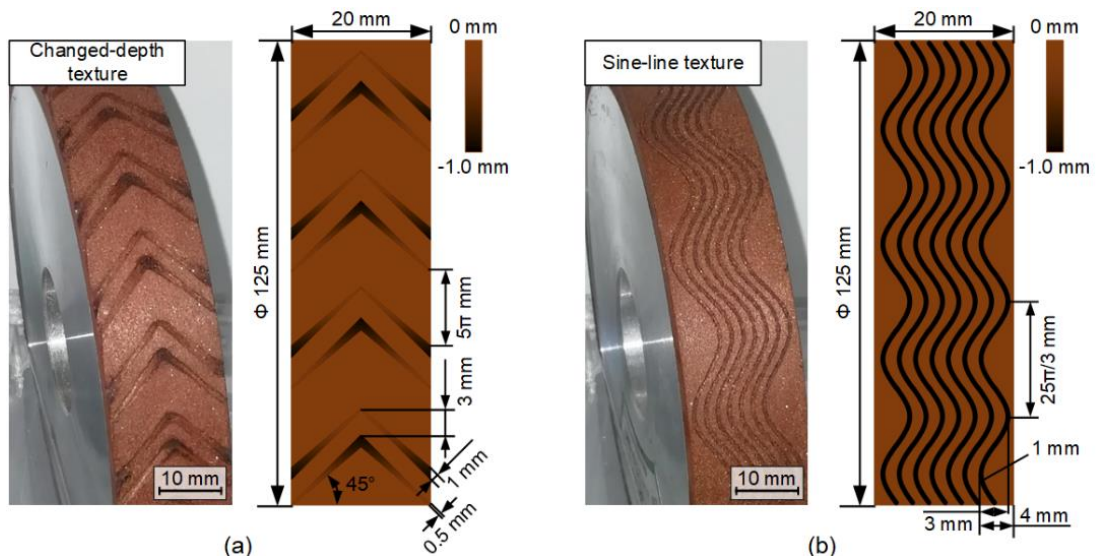


Figure 5.12 Ablated diamond grinding wheels with irregular-shaped textures. Grinding wheels with (a) continuously changed depths and (b) sine-line textures.

5.5 Conclusions and Discussions

According to the need for further experiment, an electromechanical ablation

system considering positioning, ablation, cleaning, and measurement is established. The performances of the custom-made positioning system are evaluated. Finally, an application to demonstrate the whole system's performance is made. The key conclusions of this chapter can be summarised as follows:

(1) An electromechanical ablation system is established by fully considering the experimental need. Most commercial parts are selected as possible to fill the needs of reliability.

(2) Rigorous testing has been performed, and it shows the overshoots and speed errors increased with the feed rates, but the maximum positioning errors are within ± 0.2 mm, the maximum speed errors percentage is around 4.5% at lower speed and is almost kept around at 1.5% at higher speed.

(3) Under both lower and higher speeds, the acceleration increased to its maximum in a few milliseconds and gradually reduced to around 0 mm/s². Meanwhile, the acceleration fluctuations increase with the moving speed.

(4) Despite the moving distance, the adjusting time for the positioning system can be completed with 0.05 s. The adjusting time to the stable stage is about 1.0 s for all moving speeds except for 1.0 mm/s, where the adjusting time has exceeded 2.25 s. The adjusting time for the stable stage fluctuates between 1.0 s to 1.5 s when the moving speed is below 60.0 mm/s.

(5) A demonstration of the application of the electromechanical ablation system is conducted. Grinding wheels with continuously changing depths and sine-line textures are created. Despite the imperfections of the system, most of the planned experiments are sure to be smoothly progressed.

Chapter 6

Generation of Textured Diamond Abrasive Tools by Continuous-Wave CO₂ Laser: Understanding the Laser Parameter Effects and Optimisation

6.1 Introduction

Textured Diamond Abrasive Tools (TDATs) have attracted multitudes of attention from academic scholars and industrial engineers due to their reported superior grinding performances. However, the absence of appropriate fabrication technologies can still be considered the bottleneck of broad applications of TDATs. This chapter aims to utilise the continuous-wave CO₂ laser to produce passive-grinding structures on the diamond abrasive tool surfaces, considering the superior advantages of the laser source, including (i) the high machining efficiency resulting from both the high average laser power and the stabilised laser beam quality due to the continuous-wave nature, (ii) the good ablated surface quality thanks to the good match between the long CO₂ laser wavelength and the absorbable light spectrum of non-metallic materials containing abrasives and bonds, and (iii) the superior cost efficiency because of the absence of the pulse-laser generator and any modulation magnifier. Not only the theoretical analysis of the non-metallic multi-material ablation threshold for TDATs but also the experimental investigation of the effects of both the laser power and the beam feed rate on both the topographies and morphologies of the produced structures are studied. Furthermore, the different structure generation mechanisms under different

laser parameters are analyzed, based on which the strategy for selecting proper ablation parameters is provided. Various examples of the produced textured wheels are given to prove the study's significance and feasibility. The presented work is anticipated to be not only meaningful to provide an academic reference to the research field of ultra-high precision machining but also helpful to provide a new method for industries to produce textured grinding wheels in an efficient and low-cost way.

6.2 Experimental Strategy

The standard commercial diamond abrasive grinding wheels (D120N75B771/8, 3M Company) were used in all the trials in this study (see more details in **Table 3.3**). The laser beam was generated by the continuous-wave carbon dioxide generator (LE900, Hongfan Tech. Company) with a maximum power of 60 W, a wavelength of 10.6 μm , a circular focus with a diameter of 0.3 mm, and a focal length of 12.5 mm.

The linear and angular motions and positions of the ablated diamond wheels were accurately controlled by the specially-made positioning system having the translational and rotational motion accuracies of 1 μm and 0.05 deg based on the G-code-based SIEMENS NC system. As seen in **Figure 6.1a**, the positioning system consisted of the controller (BR010-11T8X2M, BenT CNC Automation Equipment Company), the driver (ZD-M42, Philips Company), the stepper motor (42HS4013A4CE, Sumtor Company), the reducer (SK4248-19.2, Yixing Technology Company) and other auxiliary hardware, enabling the 2-axis simultaneous motions (which were the translational and the rotational motions separately along and around the wheel axis). The translational and

rotational motion speeds were separately within the ranges of 0~100 mm/s and 0~15 deg/s.

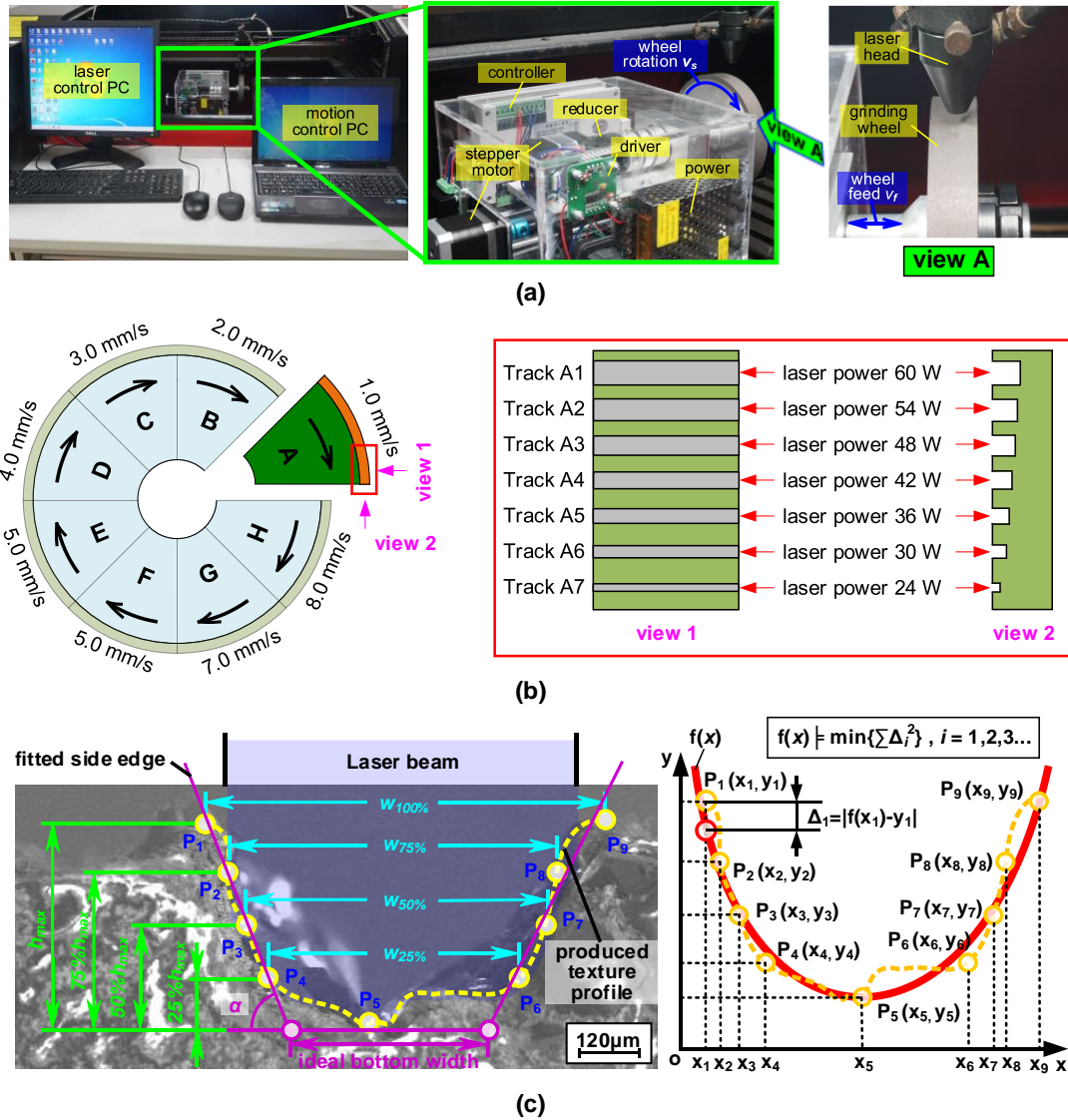


Figure 6.1 Experiment methodology. (a) Experimental setup including the laser and motion control PCs (left), the specially-designed positioning system (middle) and the laser ablation system setup (right), (b) the ablation strategy where the wheel was equally divided into eight segments (A-H) and in each segment there were seven ablated tracks along the wheel axis direction (X1-X7 where X refers to A-H). The laser feed rate was incrementally increased from segment A to H, while the laser power was incrementally increased from track X1 to X7, and (c) the quadratic function fitting by the least square method based on the nine key points (P1-P9).

Because this paper aims to study the effects of laser parameters on the ablated

surface topography and morphology, wide ranges of both the laser power and feed rate were employed. To make all the results comparable, all the laser ablation texturing trials using seven different levels of laser power and eight levels of laser feed rates were produced on one diamond wheel surface in the air atmosphere. As seen in **Figure 6.1b**, the whole wheel was equally divided into eight segments (see segments A to H) along with the wheel circumferential direction and in each segment there were seven ablated tracks along the wheel axis direction (see track X1 to X7 where X refers to A-H). The laser feed rate was incrementally increased from segment A to H, while the laser power was incrementally increased from track X1 to X7 (where X refers to A-H). The used parameters are given in **Table 6.1** in detail.

Table 6.1 The employed laser processing parameters in the trials.

Trial No.	laser power (W)	laser feed rate (mm/s)	Segment No.	Track No. in each segment
1-7		1.0	A	A1-A7
8-14		2.0	B	B1-B7
15-21	60,54,	3.0	C	C1-C7
22-28	48,42,	4.0	D	D1-D7
29-35	36,30,	5.0	E	E1-E7
36-42	24	6.0	F	F1-F7
43-49		7.0	G	G1-G7
50-56		8.0	H	H1-H7

After the laser ablation texturing, the diamond wheel was firstly carefully cut into eight segments (A-H) by the wire-EDM machine (MV2400S, Mitsubishi Electric Company), and the two cross-sections of each segment were carefully polished by the alumina with the sizes of #600 (2 hours), #1200 (2 hours), and #2000 (2 hours). Each segment then was cleaned by the ultrasonic distilled

water bath for 1 hour and air-dried at room temperature. Next, various analyses based on Scanning Electron Microscope (SEM) (174C CZ, ZEISS Company), Energy Dispersion Spectrum (EDS) (174C CZ, ZEISS Company), and Cu-K α X-Ray Diffraction (XRD) (D8 Advance, Bruker Company) were performed to observe and measure the ablated surface structure topographies and morphologies respectively.

The ablated structure topography was evaluated by (i) fitting the nine key points on the observed cross-section profiles based on the least square method to obtain the quadratic function (the red line in **Figure 6.1c** right), and (ii) comparing the four indicators, including top and bottom width, depth and tilt angle based on the fitted quadratic function (see the annotations in **Figure 6.1c**, left). For step (i), the key points included one deepest valley point (where the depth was H_{max} , see the Point P5), two endpoints (see the Point P1 and P9), and six intersecting points between the cross-section profile and the horizontal lines having the depth of 25%, 50% and 75% of H_{max} (see the Point P2-P4 and P6-P8). For step (ii), the top width and depth can be separately defined as the distance of the two endpoints (P1 and P9) and the vertical distance of the endpoint (P1 or P9) to the deepest valley point (P5). The tilt angle was obtained by fitting the key points on one side (P6-P9 for the right side and P1-P4 for the left side). The bottom width was the length of the interception between the two fitted tilt lines and the horizontal line passing the deepest point (P5).

6.3 Experimental Results on the Ablated Structure Topography

6.3.1 Effects of Laser Powers

Figure 6.2 shows the significant effects of laser power on the ablated structure topography: the power increase, in general, would lead to both the linearly-increasing top width (from 808.31 μm to 1850.30 μm with the slope of 16 $\mu\text{m}/\text{W}$) and the depth (from 297.44 μm to 1012.79 μm with the slope of 25 $\mu\text{m}/\text{W}$) and the nonlinearly-increasing bottom width (from 378.34 μm to 857.66 μm) and side edge tilt angle (from 55.08° to 69.38°). The large difference in the ablated slot top width and depth under different laser powers indicated the continuously effective ablation thanks to (i) the good match between the long CO₂ laser wavelength (10.6 μm) and the absorbable light spectrum of both artificial diamonds (around 4.3 μm) and resin (around 7.8 μm) atoms in the provided fluence range, and (ii) the well-focalized and stable CO₂ laser beam during the whole ablation process even after a layer of the wheel material with the thickness of 1000 μm (the largest valley depth in **Figure 6.2a**) was removed.

One noticeable observation here would be the critical laser power region (see **Figure 6.2c**), in which the rising power led to not the increasing but the decreasing top width (see **Figure 6.2c**) and the side edge tilt angle (see **Figure 6.2d**). This interesting phenomenon might be explained by the following competing active and negative ablation processes: in the active ablation, the increasing laser power not only resulted in intensive radiation fluence leading to oxidation, graphitization, melt and even gasification but also generated the thermal shock to diamond leading to breakage. Therefore, substantial material

removal was achieved in this phase. However, the over-increased laser power would lead to the negative ablation phase as well because the powerful laser enables (i) the generation of substantial micro-particles (including micro-diamond fragments, micro graphite particles, or other ash-like materials), either covering the ablated spots and hindering the laser absorption due to the high reflectivity, or suspending in the air leading to the laser beam scattering, and (ii) airfield ionization (multi-photon ionization, impact ionization and tunnelling ionization) leading to the laser beam defocusing effects. It can be seen from **Figure 6.2c** and **Figure 6.2d** that the critical laser power region for the resin-bonded diamond wheel might be probably within the range from 36 W to 42 W. Please note that the data in **Figure 6.2c** and **Figure 6.2d** are the average values of the multiple measurements while the error bars refer to the standard deviation.

Besides, **Figure 6.2b** shows the varying cross-section shapes of the ablated structures, from the inverted triangle (see A and B in **Figure 6.2b**), via the semi-circle (see C, D, and E in **Figure 6.2b**), to the shallow crater (see F in figure 3b) when the laser power was decreased. There is no surprise for the semi-circle and shallow crater shapes because they fit well with the ideal Gauss distribution of the power density within the laser beam when normal levels of laser power were used. However, when the laser power was over-increased, intensive air ionization, large ablation depth, and substantial micro-particles would take place, resulting in the non-Guass-shaped cross-section profile due to the significant re-focusing effect [269].

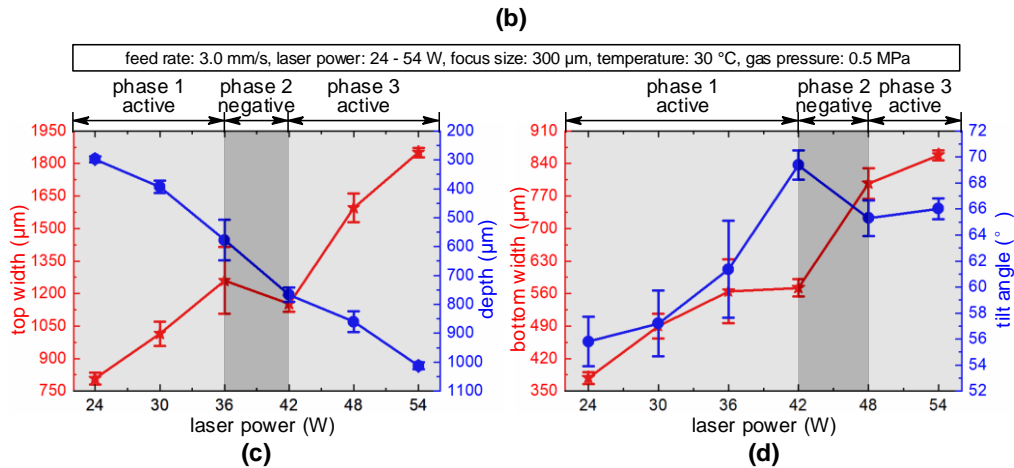
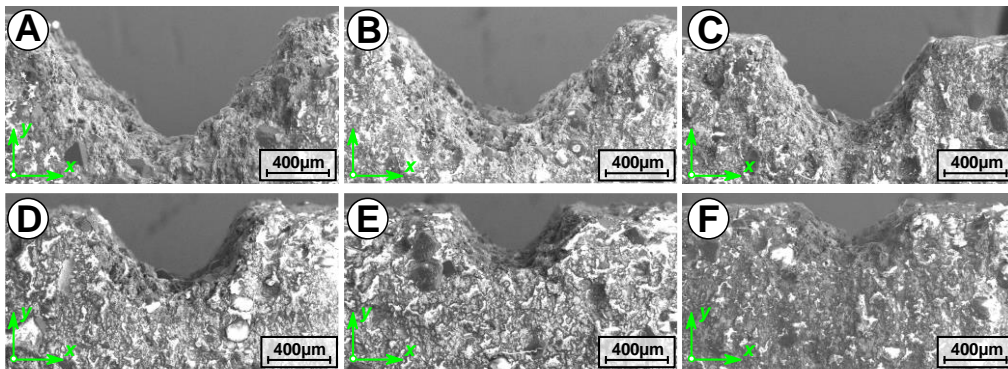
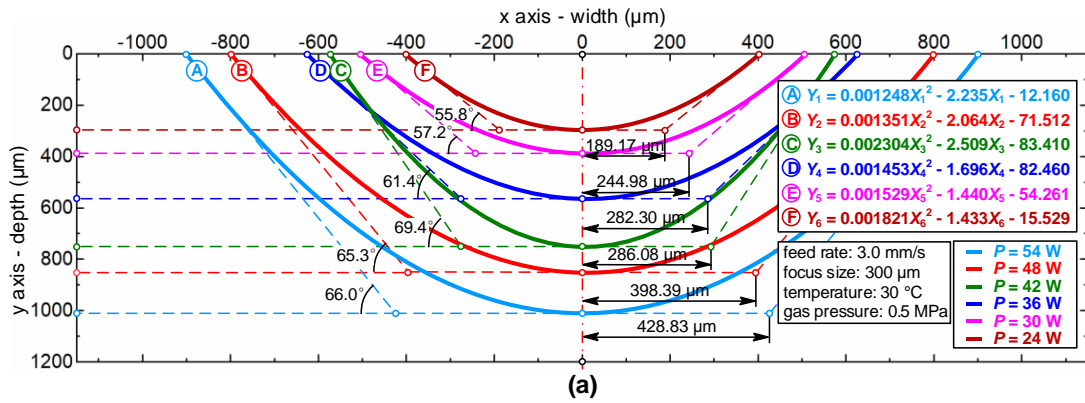


Figure 6.2 The effects of laser power on the ablated structure topography. (a) The fitting profile of the ablated structure cross-section profile when the feed rate was 3.0 mm/s and the laser powers were 54 W (specimen A), 48 W (specimen B), 42 W (specimen C), 36 W (specimen D), 30 W (specimen E), and 24 W (specimen F), (b) the SEM micrographs of the cross-sections of the specimens from A to F, and the effects of laser power on the (c) top width (red) and depth (blue), and (d) bottom width (red) and side edge tilt angle (blue).

6.3.2 Effects of Laser Feed Rates

Figure 6.3 shows the dominant influence of laser feed rate on the ablated

structure topography. The increased feed rates generally led to the decreasing top width (from 1850.30 μm to 761.90 μm), depth (from 1012.79 μm to 521.63 μm with a slope of 25 $\mu\text{m}/\text{W}$), bottom width (from 857.66 μm to 382.3 μm), but the increasing side edge tilt angle (from 64.25° to 71.01°). The relationships between the four geometrical parameters and the laser feed rate showed clearly nonlinear features (see **Figure 6.3 c&d**).

The critical feed rate region can also be observed in **Figure 6.3 c&d**, similar to the critical laser power region. In this region, the increased feed rate resulted in not only the relatively constant depth (see **Figure 6.3c**) but also the decreasing side edge tilt angle (see **Figure 6.3d**). The statement based on the competing active and negative ablation in **Figure 6.3** can also be applied here to explain this observation, and the only difference is in the previous statement the high laser power led to the active ablation while in this case the low feed rate did because of the incubation effect [270]. What is even more interesting here would be the encouragingly good match of the laser fluence of both the critical laser power region (from 36 W to 48 W) and the feed rate region (from 4.0 mm/s to 6.0 mm/s).

Similar to **Figure 6.2b**, **Figure 6.3b** illustrates the cross-section profile of the ablated structures, where the profile shapes kept relatively constant, only changing from the inverted triangle (see A, B, D in **Figure 6.2b**) to the semi-circle (see E and F in **Figure 6.2b**) when the feed rate was increasing. The inverted triangle shape might probably be because of the significant re-focusing effect resulting from the high laser power density induced by the low feed rate, while the semi-circle shape was attributed to limited material removal

behaviours due to the high feed rate. The only abnormal observation here would be the semi-circle-shaped ablation profile in specimen C in **Figure 6.3**, which might be because the employed laser feed rate in this case (5.0 mm/s) was within the critical feed rate region and therefore the opposite effect took place.

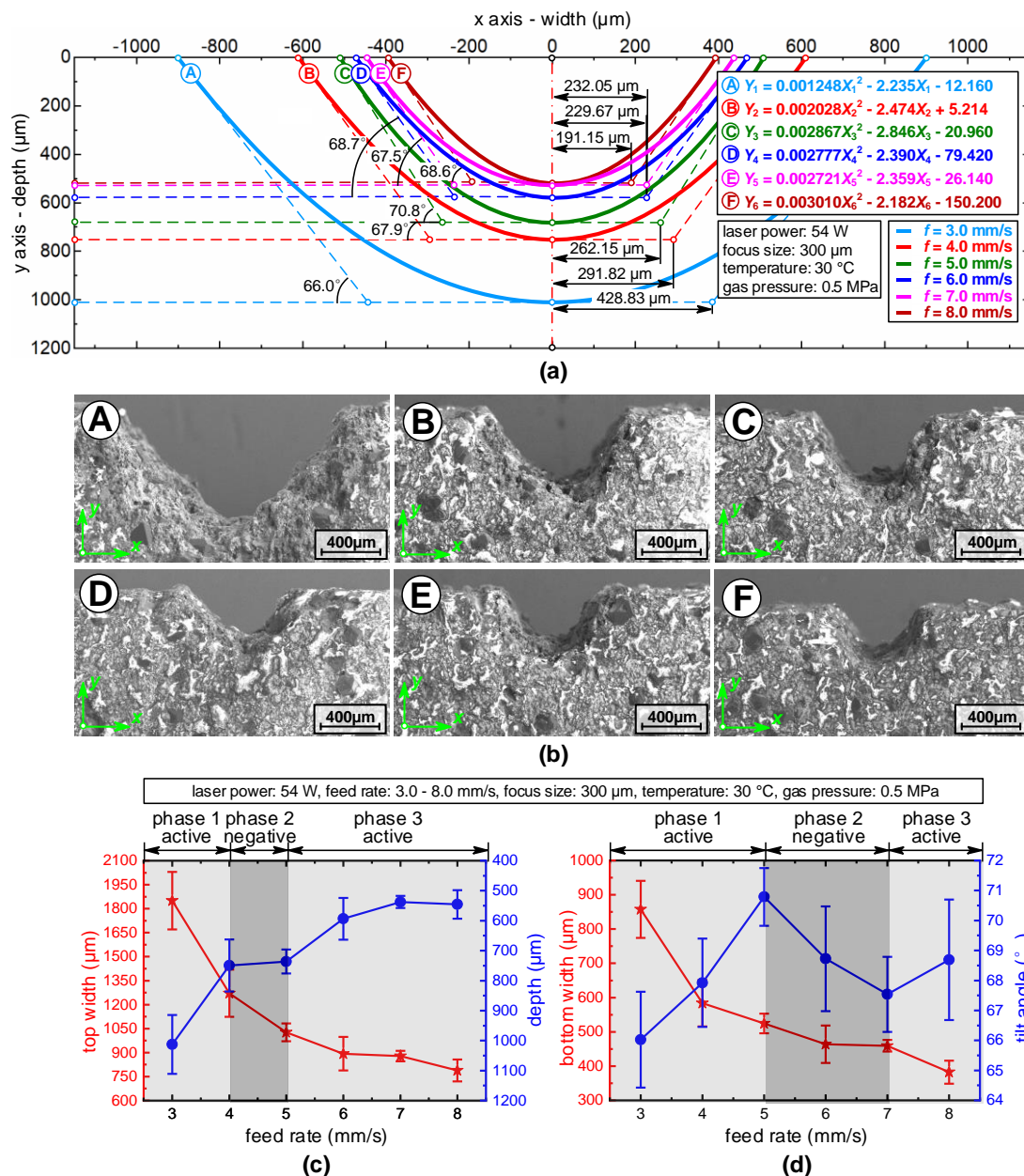


Figure 6.3 The effects of laser feed rate on the ablated structure topography. (a) The fitting profile of the ablated structure cross-section profile when the laser power

was 54 W and the feed rates were 3.0 mm/s (specimen A), 4.0 mm/s (specimen B), 5.0 mm/s (specimen C), 6.0 mm/s (specimen D), 7.0 mm/s (specimen E), and 8.0 mm/s (specimen F), (b) the SEM micrographs of the cross-sections of the specimens from A to F, and the effects of feed rate on the (c) top width (red) and depth (blue), and (d) bottom width (red) and side edge tilt angle (blue).

6.4 Experimental Results on the Ablated Structure Morphology

6.4.1 Effects of Laser Powers

Figure 6.4 shows the effects of laser power on the ablated structure morphologies. Both the types and the numbers of the observed morphologic features tended to be increased with the increasing laser power. This might be because of both (i) the increasingly complex and aggressive thermal, optical, electric, and mechanical cross-interactions between the laser beam, the abrasives, the resin bond and the air and (ii) the nonlinear and steep temperature gradient from the ablated surface to the subsurface covering an increasing area and leading to various material behaviours. The observed features can be mainly categorized into three groups according to different material behaviours of the diamond abrasives, including (i) exposure/loosening, (ii) deterioration and (iii) breakage.

The exposure/loosening was the dominant feature of the ablated abrasive tool morphologies when the low laser power was used (see specimen A in **Figure 6.4** when the laser power was 24 W). The abrasive exposure/loosening referred to the reduced abrasive-holding structure of the resin bond generated by the laser ablation and was mostly observed on the ablated wheel surface. The generation of the loosening structure might be because the low laser power can result in the bond melting, rather than the material removal, and generate the ash-like structure after the resolidification (see specimen A). It might, therefore, predict that the loosening features negatively (i) generated

the ineffective abrasives which cannot remove materials in grinding due to the limited abrasive retainment, (ii) increased the uncertainties of the ultra-high-precision grinding process accuracy due to the loose abrasives on the wheel surface, and (iii) raised the possibility of the undesired abrasive fall-off before the diamond normally worn out.

The exposure/loosening was the dominant feature as well, although the laser power was increased from 24 W to 42 W. However, the noticeable observation here would be the absence tendency of the loosening features (see the specimen **Figure 6.4B**) and the rising generation of the abrasive exposure feature. This phenomenon might be explained by the full resin bond material removal by the gasification induced by the medium laser power, rather than just the melting and resolidification in the low laser power. The exposure features are anticipated to (i) actively increase the functional cutting abrasives with favourable grain protrusion heights, leading to sharper grinding edges and therefore more superior tool grinding ability, and (ii) the intact diamond geometry with the appreciable portion buried beneath the resin bond, leading to better grain holding ability and longer tool durability.

Parallel to the exposure/loosening features, the unique morphology featured by abrasive breakage started to appear when the high laser power of 54 W was employed (see the specimen **Figure 6.4C**), where the clear pieces of evidence of the diamond fragments can be identified. This breakage probably resulted from the poor diamond heat resistance, i.e. the diamond material would break easily due to the non-uniformly distributed thermal deformation. A very interesting observation here can be the breakage feature locations, i.e. most of the broken diamonds can be found 300 μm ~ 400 μm beneath the ablated surface instead of on the surface.

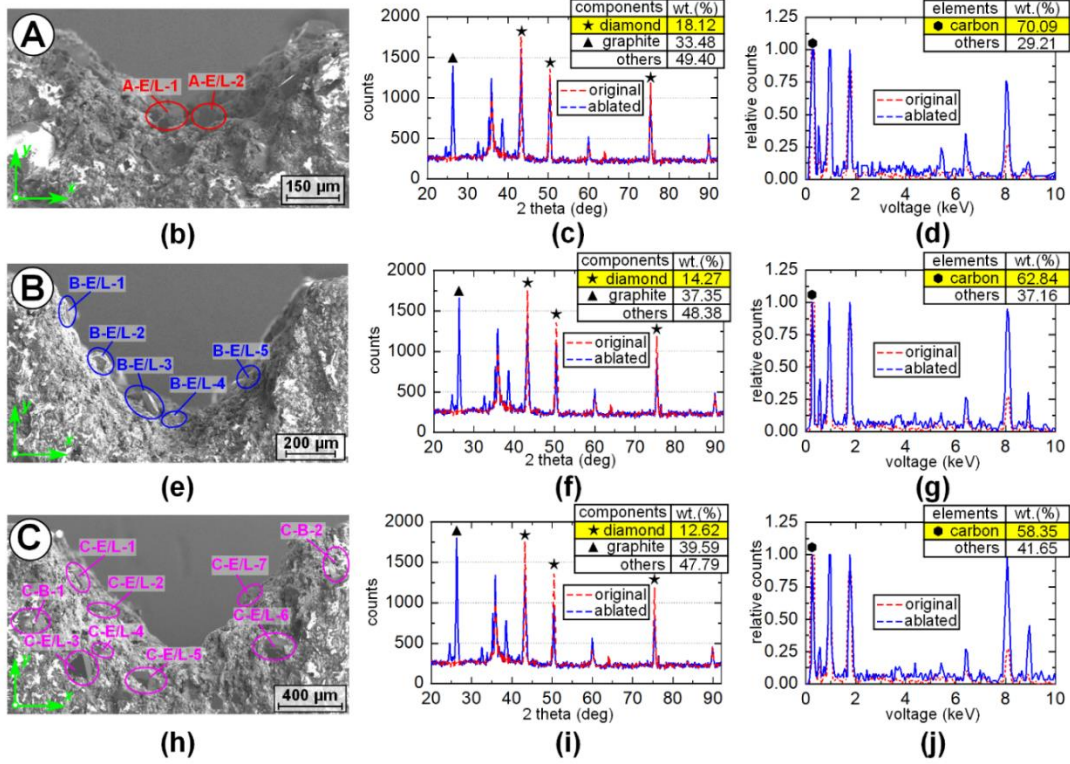
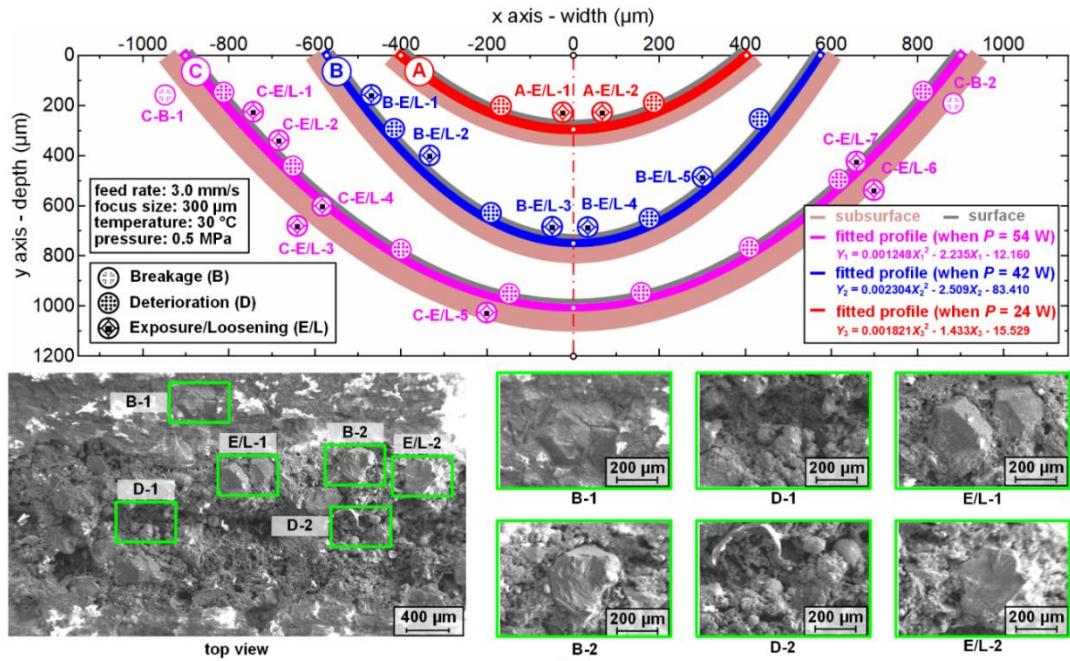


Figure 6.4 The effects of laser power on the ablated structure morphology. (a) The fitted profile of the ablated structure cross-section profile when the feed rate was 3.0 mm/s and the laser power was separately 24 W (specimen A), 42 W (specimen B), 54 W (specimen C) and the SEM micrographs of the top views from specimen C, and the SEM micrographs, the XRD patterns, and the EDS analysis results of the specimen A (b, c, d), B (e, f, g) and C (h, i, j).

The reason might be: that the diamonds on the ablated surface were fully burned out because (i) the employed laser energy density was 3.40×10^5 W/cm² higher than the diamond ablation threshold and (ii) the air atmosphere facilitated the diamond oxidation. On the contrary, the diamonds beneath the surface suffered a relatively mild thermal shock in the oxygen-poor environment, leading to incomplete ablation and breakage, and therefore the broken diamond fragments properly preserved by the resin bond can be clearly observed.

Except for the physical features mentioned above (i.e. loosening, exposure, and breakage), the chemical deterioration of both the diamonds and the resin bond can also be found in all levels of laser power. Not only did the diamond was deteriorated into graphite (see c, f, i in **Figure 6.4**, where the diamond weight percentage reduced from 18.12% via 14.27% to 12.62%), but also the organic resin bond was oxidized into the various carbides (e.g. CO, CO₂, etc.) (see d, g, j in **Figure 6.4** where the carbide weight percentage reduced from 70.09% via 62.84% to 58.35%) when the laser power was increased.

6.4.2 Effects of Laser Feed Rates

Figure 6.5 presents the effects of feed rates on the ablated structure morphology. The numbers of the morphologic features of the ablated surface tended to be increased with the reduced laser beam feed rate. This might be because of (i) the increasingly intensive laser fluence, leading to the substantial heat accumulation, material removal behaviours, and air ionization, and (ii) the large thermal affected zone and the complex material behaviours within the zone.

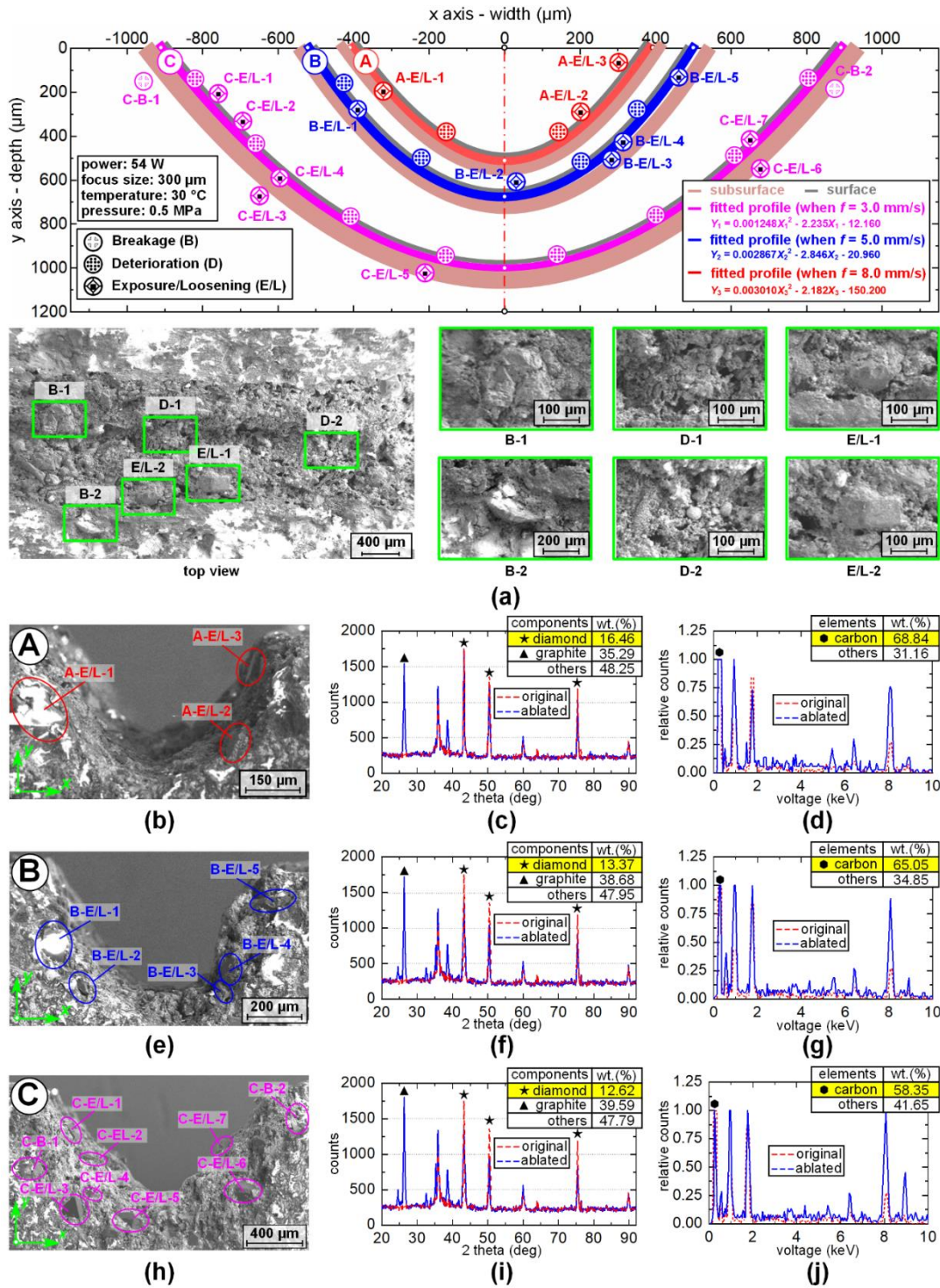


Figure 6.5 The effects of feed rates on the ablated structure morphology. (a) The fitting profile of the ablated structure cross-section profile when the laser power was 54 W and the feed rate was separately 8.0 mm/s (specimen A), 5.0 mm/s (specimen B), 3.0 mm/s (specimen C) and the SEM micrographs of the top views from specimen C; and the SEM micrographs, the XRD patterns, and the EDS analysis results of the specimen A (b, c, d), B (e, f, g) and C (h, i, j).

The diamond exposure features happened in all the levels of the feed rates from 3.0 mm/s via 5.0 mm/s to 8.0 mm/s when the laser power was kept at 54 W. Based on the loosening and breakage features, the effects of the feed rates tended to be unstable: on the one hand, the low feed rate of 3.0 mm/s resulted in the presence of the abrasive breakage due to the increasing laser energy accumulation; on the other hand, the fast feed rate of 8.0 mm/s did not lead to the presence of the abrasive loosening (see **Figure 6.5b**), somehow indicating the larger influence of the laser power on the ablated structure morphology in comparison with the feed rates. Regarding the deterioration feature, the low feed rate led to the high possibility of the diamond-to-graphite transformation, which can be evidenced by **Figure 6.5** (c, f, i), where the diamond weight percentage reduced from 16.46 % via 13.37 % to 12.62 %. This transformation was performed because of (i) the laser-induced high temperature and (ii) the relatively low atmospheric pressure in comparison with the critical graphite-to-diamond transformation pressure [271].

6.5 Applications

6.5.1 Laser Ablation Parameters Selection for Texturing Diamond Abrasive Tools

Based on the understanding of the laser parameter effects on both topographies and morphologies, the ambition of this section can be considered meaningful. As it is the usage of the knowledge above to properly select ablation parameters so that the passive-grinding textures having limited undesired thermal defects can be produced, because to the best knowledge of us most of the previous studies chose the laser ablation parameters by the trial-and-error principle and very limited theoretical guidance was given yet.

The parameter selection strategy can be explained based on **Figure 6.6**,

where the vertical and horizontal axes are separately the energy fluence and the laser feed rate. The whole diagram can be divided into three domains according to both the diamond and resin ablation thresholds calculated by **Equation (3.1)**, i.e. (i) the non-ablation domain, where neither the bond resin nor the diamond abrasive can be ablated, (ii) the resin-ablated domain, where only the resin is ablated while the diamond is not, and (iii) the full-ablation domain, where both the resin and the diamond were ablated. The energy fluence corresponding to different employed laser power when different feed rates are used can be plotted in **Figure 6.6** as well based on **Equation (3.2)**.

Based on the above, reasonable laser parameters can probably be selected. On the one hand, the ablation parameters within the full domain can be recommended because only the ablated diamonds can enable the diamond-covered resin to be removed so as to create the passive-grinding textures. On the other hand, the usage of high laser power should also be employed because of the efficient ablation material removal evidenced by enough ablation depth allowing enough coolants to be transported into the grinding zone to lower the grinding temperature. Considering the employment of the maximum laser power of the employed generator (60 W) might lead to an unstable laser beam due to fluctuation, only 90% of the maximum power should be used. This concludes that the parameter within the recommended domain in **Figure 6.6** can be reasonable. It can also note from the observed ablated morphology that a high feed rate can help to minimize the thermally affected zone where very limited diamond loosening structures can be found and therefore can give the TDATs good machining ability. This observation ends with the conclusion that the laser parameter at the intersecting point C in **Figure 6.6** can be considered the relatively suitable ablation parameters, i.e. the laser power of 54 W and the feed rate of 5.5 mm/s.

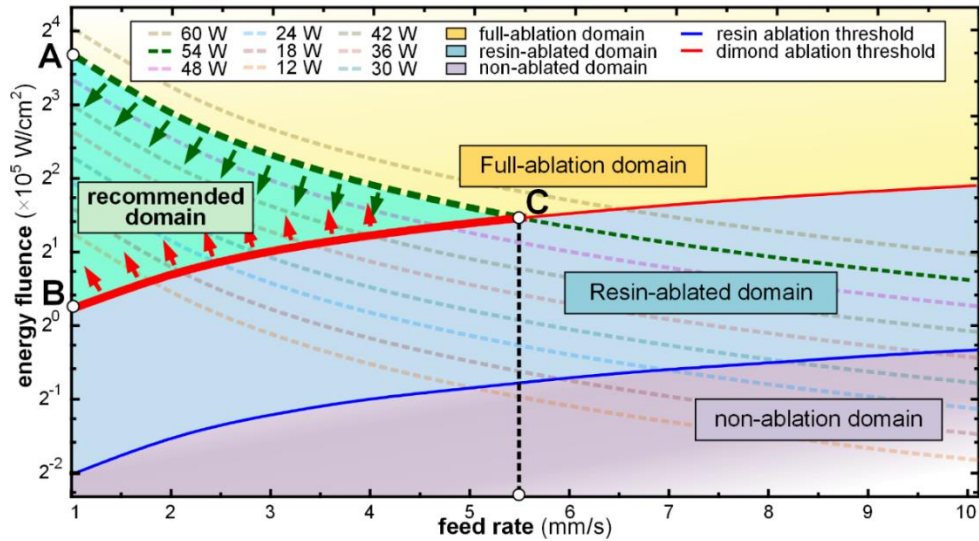


Figure 6.6 Diagram for the selection of laser ablation parameters for proper diamond grinding wheel texturing.

6.5.2 Precise Generation of Textures on Flat Grinding Wheels

Figure 6.7a presents the ablated diamond grinding wheels having different-shaped textures by using the laser parameters selected by the proposed method. Various textures, including tilt line, parallelogram, hexagon, triangle, and rectangle, were successfully obtained with high shape and dimensional accuracy, to a large extent proving the proper selection of the processing parameters based on the proposed strategy. However, little pieces of evidence of the poor ablated surface integrities such as micro-cracks at the edges can still be found, which might be due to the unstable ablation process induced by the motion system vibration and the air atmosphere.

Figure 6.7b presents the comparison with the unsuccessful examples of the wheels ablated by the improper parameters, further indicating the effectiveness of the proposed method. Although there was little variance of the feed rate (changed from the previous 5.5 mm/s to the current 2.0 mm/s) while the power kept constant (54 W), the obtained geometries were completely different. Neither clear texture geometries nor the sharp edges can be clearly

recognized. The neighbouring bond and abrasives appeared to be weak and loosened as well, implying the large loss of the grinding ability of the tools.

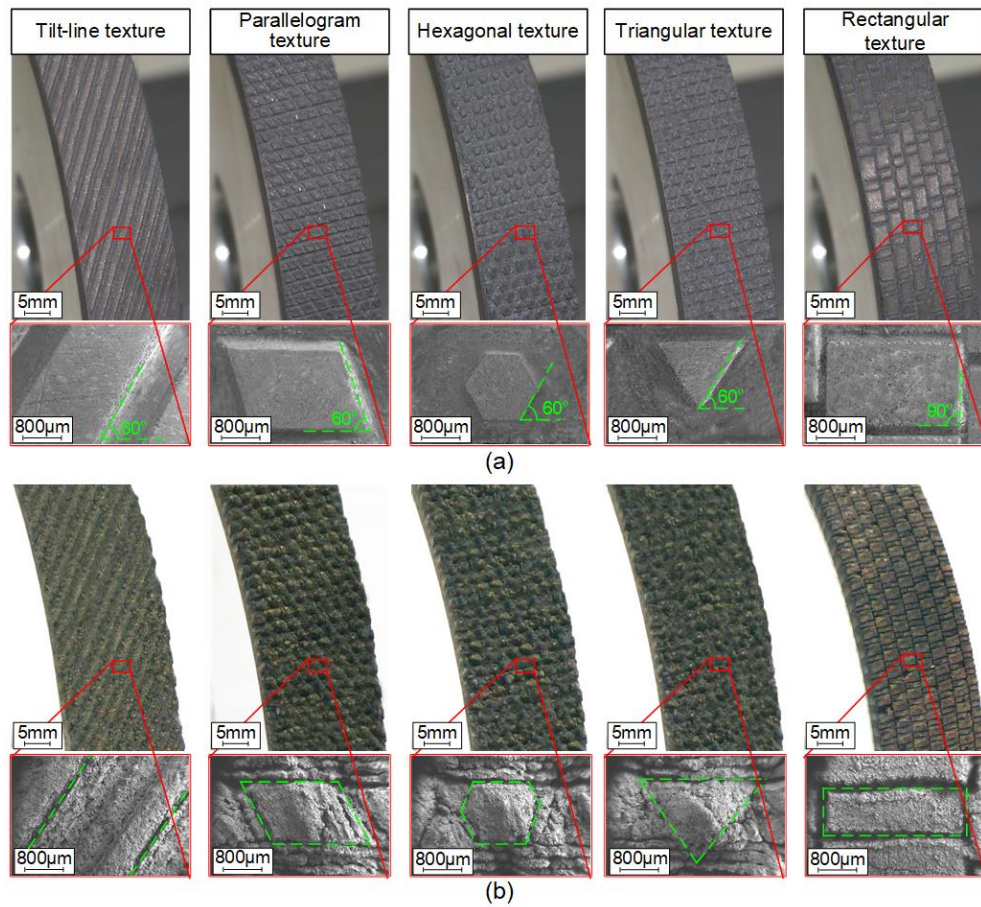


Figure 6.7 Ablated diamond abrasive tools with different-shaped textures (including tilt line, parallelogram, hexagonal, triangular, and rectangular structures). (a) The parameters selected by the proposed method (the laser power of 54 W and the feed rate of 5.5 mm/s) and (b) the improper parameters (the laser power of 54 W and the feed rate of 2.0 mm/s).

6.6 Conclusions and Discussions

Unlike most previous studies using pulse laser, this paper utilised the continuous-wave CO₂ laser to create passive-grinding structures on the diamond abrasive tool surfaces. The key findings and conclusions of this study might include:

- (1) The employment of the resin ablation threshold did not generate satisfying texture structures on the tool surface, implying the laser ablation

mechanism of multi-material non-metallic structure was more complex than the ablation of any individual single-material components.

(2) The increasing laser power resulted in the increase of all the geometrical parameters of the ablated structures, including top/bottom width, depth, and side edge tilt angle. Decreasing feed rate showed similar effects except for the decreasing tilt angle. The interesting critical ranges of both laser power and feed rate were found, where they showed the opposite effects on the ablated topographies due to the competing active and negative ablation processes.

(3) There were three basic morphological features on the ablated tools, including (i) diamond exposure/loosening when using low laser power (e.g., 24 W) and low feed rate (e.g., 3.0 mm/s), (ii) diamond breakage when using large laser power (e.g., 54 W) and low feed rate (e.g., 3.0 mm/s), and (iii) the diamond-to-graphite deterioration no matter what the parameters were.

(4) The strategy to select proper laser ablation parameters for texturing diamond abrasive tools was also proposed based on the observations and knowledge above. The successful fabrication of the diamond abrasive tools with different-shaped textures proved the feasibility and reasonability of the method.

With this, the reported findings are anticipated to be not only meaningful to provide the academic reference to the multi-material laser ablation process but also offer a promising method to produce textured grinding wheel considering the CO₂ laser advantages, including high machining efficiency, stabilised laser beam quality, low cost, and more importantly, a good match between the CO₂ laser wavelength and the absorbable light spectrum of diamond abrasives and resin bonds.

Chapter 7

Generating Profile Diamond Grinding Wheels by Single Pass of High-Power Fibre Laser: Understanding the Ablation Law with High Laser Power and Predictive Model Establishment

7.1 Introduction

Non-flat surfaces, such as step shafts, crankshafts, and aerospace craft engine blade tenon, are widely used in various industries, which usually need profile grinding as the finishing process to satisfy the demanding large batch precision requirement. However, the precise fabrication of these superhard profiled abrasive tools has kept an open question. Many scholars take advantage of laser processing technology for the manufacturing of superhard materials. However, most of the research is conducted on single, uniform material laser ablation. Besides, there is relatively little research on the ablation of non-uniform multi-materials and even less on the laser ablation law regarding non-uniform multi-materials ablation depth. As there is a complex interaction between the laser beam and diamond grinding wheel matrix, it is hard to remove the composite materials from the grinding wheel in a controllable way. Although some researchers manage to establish prediction models, the model is either only valid for lower laser power with a limited prediction range or established based on a femtosecond laser, for which it is hard to achieve a relatively higher average laser power, limiting its application in texturing structured abrasive wheels with high efficiency and precision. To

fill this gap, this work employs a 2,000 W fibre laser generator to investigate the laser ablation law regarding diamond abrasive wheels in terms of ablation depth and width with regards to the laser power, the duty cycle, and the feed rate. This is completed with the aim to generate profiled diamond grinding wheels, the corresponding predictive models for the selection of laser processing parameters and a further study of ablation law. The laser ablation depth and width change with various laser powers, feed rates, and duty cycles are investigated and analysed in this study. An analytical model regarding the laser ablation process on non-metallic, inhomogeneous materials is performed. The limitations and applicability of the model are also analysed. The evaluation results and experimental data show that corresponding predictive empirical models are established and experimentally validated. The presented work is anticipated to be not only meaningful to improve the efficiency of industrial structured abrasive wheel fabrications but also helpful in providing an academic reference for the research field of laser ablation law for the non-metallic composites.

7.2 Experimental Strategy

The main parameters influencing the ablation results include laser power, duty cycle, and feed rate [272, 273]. To clarify the effect of each parameter on the ablation results, in this study, the laser duty cycle was varied from 10% to 100% with an interval of 30%, the feed rate from 25 mm/s to 100 mm/s with an interval of 25 mm/s, and the laser power from 200 W to 2,000 W with an interval of 200 W (the experimental parameters are selected based on the fluence calculation above and previous work in reference [118]). To eliminate the influence of

material differences and make all the results comparable, all the ablation parameters mentioned are carried out on a single grinding wheel.

As shown in **Figure 7.1**, the grinding wheel used here is divided into eight segments, defined from segment A to segment H (see **Figure 7.1a**).

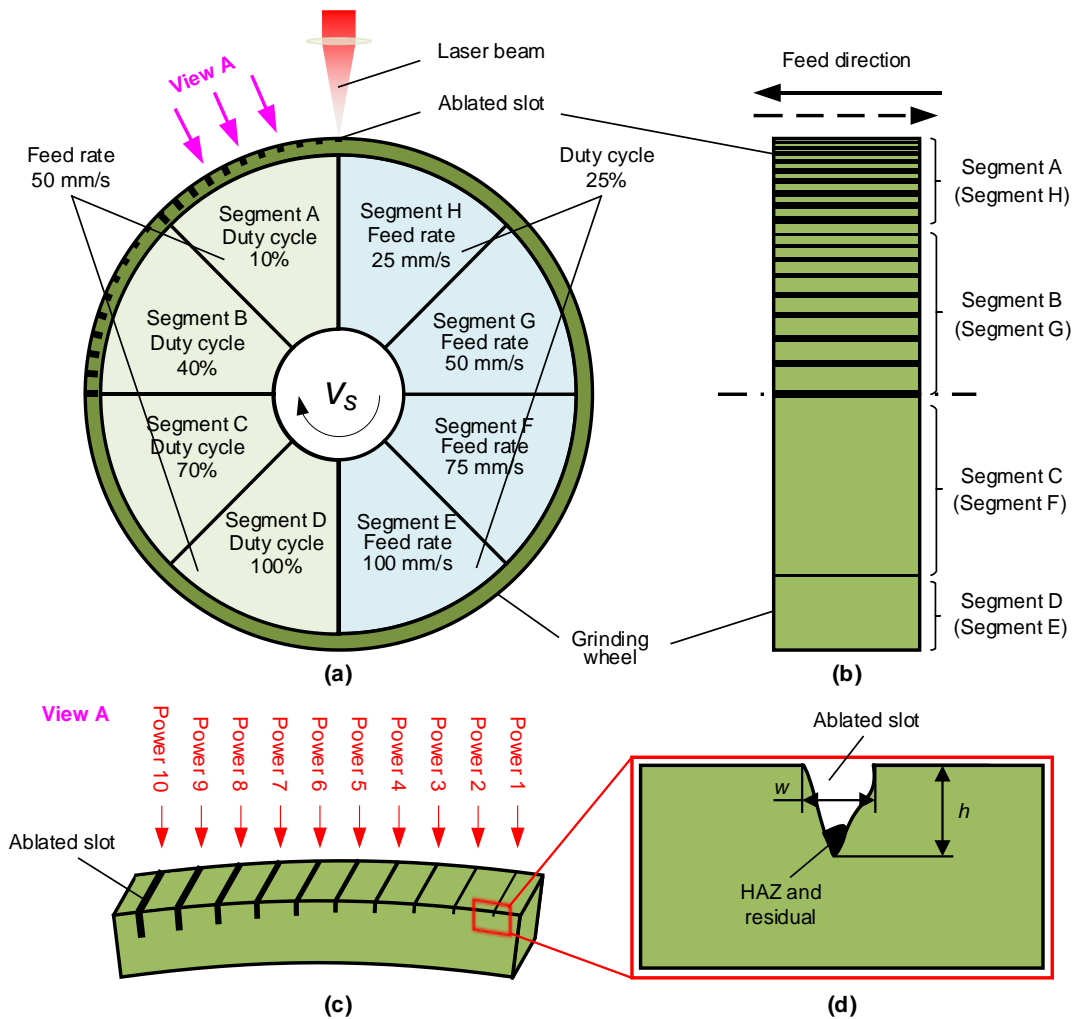


Figure 7.1 Experimental methodology. (a) The grinding wheel is divided into eight segments from segment A to segment H, for each segment includes ten laser power parameters, (b) the side view of the grinding wheel and (c) view A of the ablated area and (d) the measurement.

Among these segments, segments A to D are carried out under feed rate 50 mm/s with duty cycle changes from 10% to 100%, and segment E to segment H is carried out under a duty cycle of 25% with feed rate changes from 25

mm/s to 100 mm/s. On each segment, there are ten different laser powers from 200 W to 2,000 W involved (see **Figure 7.1c**). Therefore, a total of 80 experimental parameters were involved in the experiment. The feed rates are controlled by transverse motion, and the different slots are distributed by a fixed rotational angle of 4.5° (see **Figure 7.1b**). The strategy regarding the measurement and definition of the ablation result is shown in **Figure 7.1d**. The detailed experimental parameters are shown in **Table 7.1**.

Table 7.1 Details of the experimental parameters.

Trial No.	Feed rate (mm/s)	Power (w)	Duty cycle (%)	Trial No.	Duty cycle (%)	Power (w)	Feed rate (mm/s)
1-10	50	2000, 1800,	10	41-50	25	2000, 1800,	25
11-20		1600, 1400,	40	51-60		1600, 1400,	50
21-30		1200, 1000,	70	61-70		1200, 1000,	75
31-40		800, 600,	100	71-80		800, 600,	100
		400, 200				400, 200	

Standard commercial diamond abrasive grinding wheels (D120N75B771/8, 3M Company) were used in all the trials in this study (see more details in **Table 3.3**).

Han's laser machine (YLS-2000, IPG Photonics) was employed; X, Y, and Z axial ranges are 2000 mm, 1000 mm, and 100 mm, respectively. The laser beam (see **Table 3.2**) is generated by a fibre generator (IPG Tech. Company). A custom-made positioning system with a rotational resolution of 0.05 mm and an axial feed resolution of 0.01 mm was employed in the experiments; the experimental setup is shown in **Figure 7.2a**.

In the ablation process, the general setting was to keep the pulse repeat frequency at 3,000 Hz, the off-focus distance set to 0, and 0.5 Mpa compressed N₂ was employed as a shielding gas. The laser beam shot directly at the grinding wheel, and the grinding wheel firstly performed a transverse motion with a predefined feed rate and then was rotated by 4.5° to perform an ablation process on the next slot (as shown in **Figure 7.2b**).

After ablation, the diamond wheel was carefully cleaned using an ultrasonic distilled water bath for 1 hour and air-dried at room temperature. Then optical microscopy (NSZ-810, NOVEL OPTICS) was performed to observe and measure the ablated slots (as shown in **Figure 7.2 c&d**).

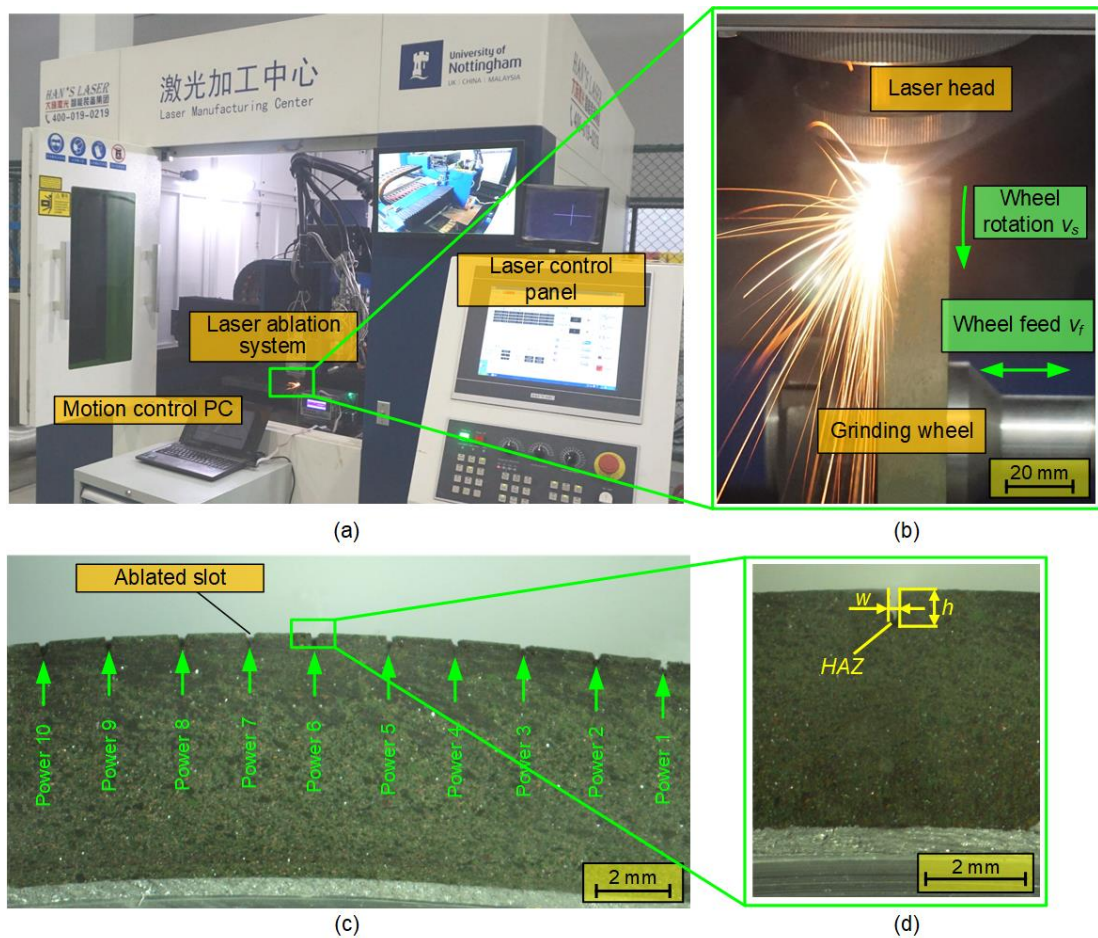


Figure 7.2 Experimental setup and procedure. (a) The experimental setup; (b) the ablation process; (c) the ablated slots; (d) the measurement diagram.

7.3 Experimental Results and Analysis

7.3.1 Effect of Duty Cycle Changes under Different Laser Power on the Ablation Law

Figure 7.3 shows both that the ablation depth and width increase with the duty cycle. In contrast to the influence on ablation width, the duty cycle has a greater effect on the ablation depth. For the whole, the ablation depth (see Figure 7.3a) varies from a minimum value of about 0 mm to a maximum value of around 4.5 mm, while the value for ablation width (see Figure 7.3b) is around 0.25 mm with a deviation of about 0.1 mm. In particular, the duty cycle has more impact on the ablation depth for higher laser power (i.e. 1,800 W) compared with lower laser power (200 W), while it has little effect on the ablation width. At 1,800 W, the ablation depth changes from around 1.0 mm to about 4.5 mm, with an increase in the duty cycle from 10% to 100%. Meanwhile, the figure for ablation width changes by less than 0.1 mm in the same condition.

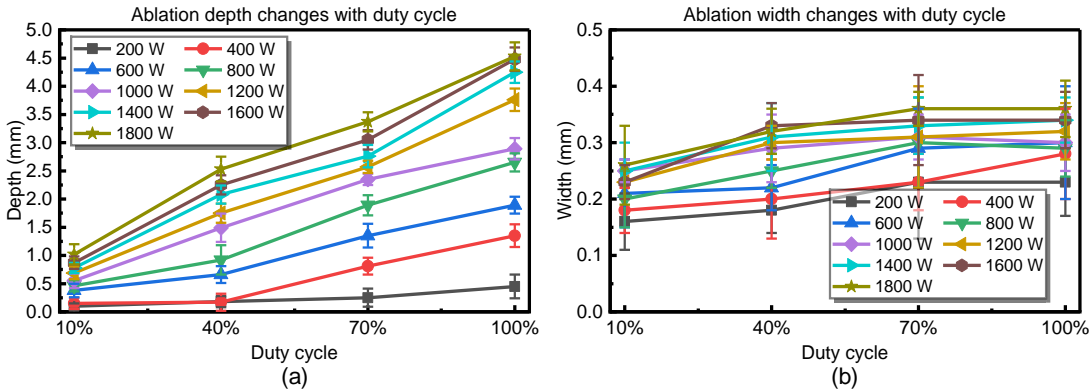


Figure 7.3 Influence of duty cycle changes under different laser power on the ablation law. (a) Influence on ablation depth and (b) influence on ablation width.

The fact that the duty cycle and laser power have a more significant effect on the ablation depth rather than width may be attributed to the directivity of the laser beam and the physical diameter of the laser beam focal spot, which allows the energy to remove more target materials along the laser propagation

direction. The duty cycle has a greater effect on the ablation depth when the laser power is high. This is mainly because heat accumulation is closely affected by the duty cycle and laser power; the heat accumulation process intensifies with increasing duty cycle and laser power, which causes the deterioration of the materials and failure. With the assistance of compressed gas and auto-adjustment of the focal plane, the target materials are more easily removed.

7.3.2 Effect of Feed Rate Changes under Different Laser Power on the Ablation Law

Figure 7.4 shows both that the ablation depth and width are slightly reduced with an increased feed rate. Similarly to the law presented in Figure 7.3, the feed rate also has a more significant impact on the ablation depth than the width. By contrast, for given laser power, the ablation results do not vary violently with feed rate changes. For instance, a maximum change of less than 2 mm of ablation depth (see Figure 7.4a) is observed in this experiment, while the figure for ablation width (see Figure 7.4b) is almost unchanged (observed variance within 0.05 mm).

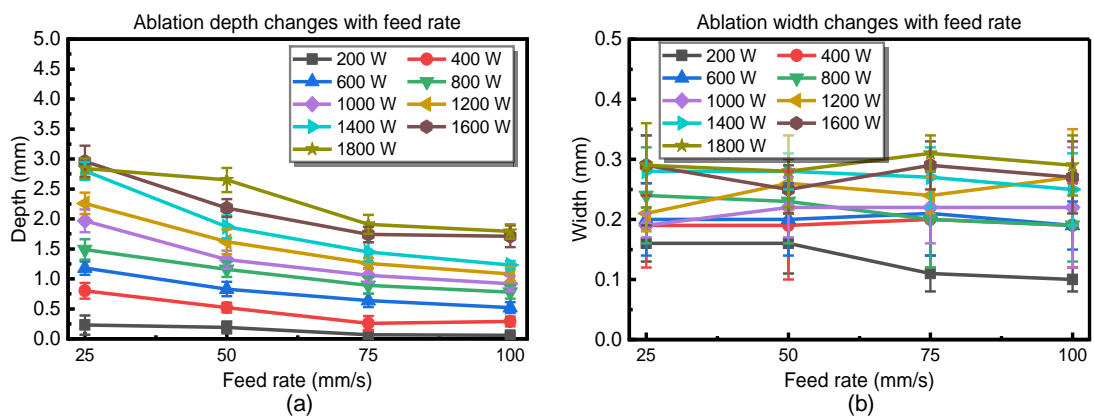


Figure 7.4 Influence of feed rate changes under different laser power on the ablation law. (a) Influence on ablation depth and (b) influence on ablation width.

The fact that the ablation depth is slightly reduced with the increase of feed rate and decrease of laser power may be due to the laser energy fluence change. It is clear that the laser energy fluence is affected by both the laser power and feed rate, and it will be decreased with an increase in feed rate and a decrease in laser power. As such, the target materials become harder to remove when the employed laser power and feed rate make the laser beam intensity close to or slightly above the materials' removal threshold. The interesting phenomenon observed for the ablation width (kept almost unchanged with the increase of feed rate) may result from the ablation width is mainly determined by the laser beam focal spot diameter and the heat-affected zone. As the focal spot diameter is fixed and the heat affects zone experiences limited change under a given laser power, the ablation width varies little with the feed rate.

7.3.3 Effect of Laser Power Changes under Different Duty Cycles on the Ablation Law

With the increase in laser power, **Figure 7.5** shows an increase in both the ablation depth and width (see **Figure 7.5b**). Notably, the laser power affects the ablation depth (see **Figure 7.5a**) dramatically for higher duty cycles (the ablation depth changes from less than 0.25 mm to above 3.5 mm when the duty cycle is 70%) than that in the low duty cycle (less than 1.0 mm change is found when the duty cycle is 10%). In terms of the figure for ablation width, only a maximum of about 0.2 mm change is found when the duty cycle is 10%.

Similarly to the reasons presented in **section 7.3.1**, more heat would be likely accumulated in a short time with the increase of duty cycle and laser power.

The accumulated heat deteriorates the materials around the laser beam, which causes both the ablation depth and width to increase. Therefore, both the ablation depth and width increase with either the laser power or duty cycle.

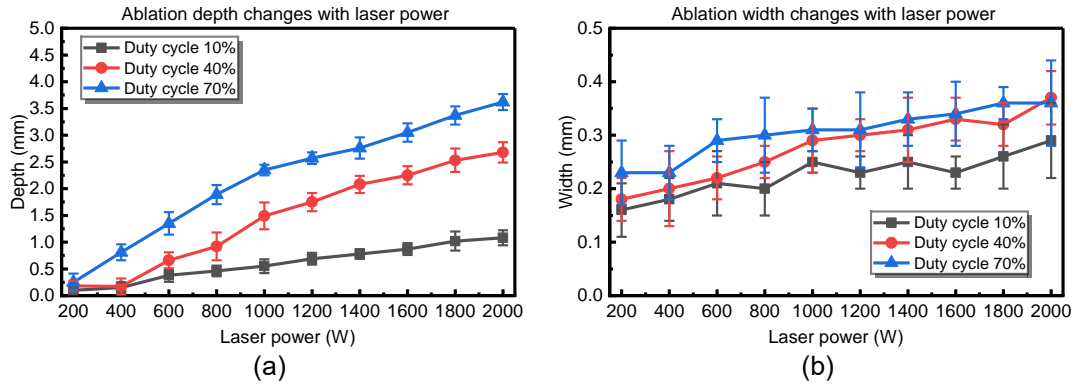


Figure 7.5 Influence of laser power changes under different duty cycles on the ablation law. (a) Influence on ablation depth and (b) influence on ablation width.

7.3.4 Effect of Laser Power Changes under Different Feed Rates on the Ablation Law

Overall, **Figure 7.6** shows a similar trend to **Figure 7.5**, e.g. the increasing trend with the rise of laser power. However, it is worth mentioning that the feed rate changes do not significantly affect the ablation results. To be specific, a maximum change of less than 1.5 mm for ablation depth (**Figure 7.6a**) is found with the feed rate changing from 75 mm/s to 25 mm/s (a range of 50 mm/s). More significantly, the ablation width (**Figure 7.6b**) is almost unchanged with a 50 mm/s feed rate variance.

As the explanations above have shown, as the laser power increases, more heat is accumulated in the ablation area in a short time, and this energy removes the materials either by deteriorating the materials or thermal impact, causing both the ablation depth and width increase. Due to the directivity of the laser beam, there is more effective on the ablation depth. As for the effect

of feed rate on ablation, with the feed rate increase, the laser fluence decreases, reducing incident energy and hence ablation depth. Meanwhile, the ablation width is mainly dictated by the diameter of the focused laser spot, and since the spot diameter is fixed in this research, the ablation width is hardly affected by the feed rate.

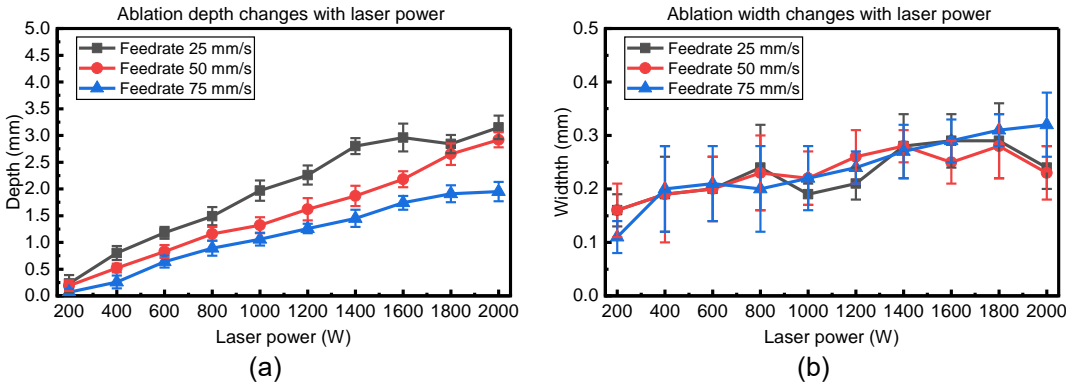


Figure 7.6 Influence of laser power changes under different feed rates on the ablation law. (a) Influence on ablation depth and (b) influence on ablation width.

7.4 Analytical Modelling Analysis

7.4.1 Modelling Process Background

Currently, the most relevant physical modelling approaches in the previous studies could be referred to as the method based on melt pool geometry. Because this is the only method that has been used for inhomogeneous non-metallic materials (concrete) despite it being performed under a relatively low laser power (maximum 120 W) [202].

7.4.2 Model Description

1) Principle

For the background mentioned above, the model established based on melt pool geometry is presented. In this laser ablation process, the temperature

distribution in the workpiece can be described by **Equation (7.1)** [251]:

$$\rho c_p \frac{\partial T}{\partial t} - \nabla \cdot (K \nabla T) + \nabla \cdot (U \rho c_p T) = Q \quad (7.1)$$

where the temperature at (x, y, z, t) is T (K), and t is the time (second), K is the thermal conductivity ($\text{W}\cdot\text{m}^{-1}\text{K}^{-1}$) of material, ρ is the density of the material ($\text{Kg}\cdot\text{m}^{-3}$), the material's thermal capacity is c (J/kg/m), U is the velocity of the heat fluid flow as a reference to (x, y, z) system coordinating stationary with respect to the beam of laser, while the heat source and sinks in the workpiece are denoted by Q (W/m^3).

In the process, radiation, conduction and convection heat transfer are involved. Energy may be reflected back to the environment when the laser beam reaches the workpiece surface, representing radiation heat transfer. The energy could be absorbed and cause the workpiece to fail or deteriorate, standing for conduction heat transfer. The rest of the energy may be dissipated from the interaction zone of the laser beam and material with the effect of fluid flow, referring to convection heat transfer. Given its boundary and initial condition, a well-known approach to solving the heat conduction function of **Equation (7.1)** is by using Green's functions [251].

2) Calculation of the ablated profile

A simple analytical model can be derived by considering the heat flow down the centreline of the melt pool as approximately one dimensional. This assumption implies that the melt pool is extensive and flat, though in practice, it is nearly parabolic (see **Figure 7.7**) [252].

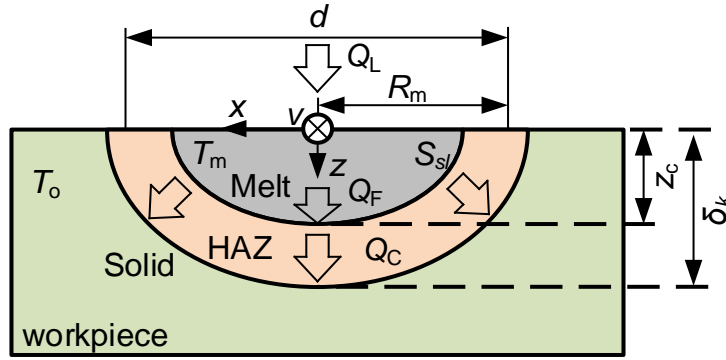


Figure 7.7 Diagram for melt pool geometry and energy flows in a quasi-stationary situation [202].

In the figure, d is the laser beam diameter, v is laser beam move speed, Q_L is the absorbed laser energy, R_m is the melt pool radius, Q_F is beside the melt pool required energy, Q_C is the heat conduction energy conveyed from the liquid-solid boundary of the melt pool into the unmelt material, z_c is the melt pool depth, δ_k is the heat affect zone depth, T_o is the initial sample piece temperature, T_m is the melting temperature.

The solid-liquid interface parabolic form is defined by **Equation (7.2)** [202]:

$$z = z_c \left(\frac{x^2 + y^2}{R_m^2} - 1 \right) \text{ for } x^2 + y^2 \leq R_m^2 \quad (7.2)$$

By assumption of a matched diameter of the melt pool and the laser beam, the total energy required for processing is higher than the latent heat of fusion and neglecting T_o , z_c can be expressed as **Equation (7.3)** [202]

$$z_c = \left(\frac{2A}{\rho c_p C_1 T_m \sqrt{\alpha}} \right) \frac{P_L}{\sqrt{d v}} \quad (7.3)$$

Wherein, A is the absorptivity of the material under process to Nd: YAG fibre laser (%), α is the material thermal diffusivity ($*10^{-6}m^2/s$), ρ is the material

density (kg/m^3), c_p is the material thermal capacity (J/kg/K), C_1 is constant, T_m is the material melting temperature (K), d is the laser spot diameter (m), v is the traverse speed (m/sec), and P_L is laser power (W).

The details of the material properties are shown in **Table 3.7**, which are provided by the Ningbo Institute of Materials Technology & Engineering, CAS.

7.4.3 Calculation Results and Analysis

Figure 7.8 shows the overall tendencies of calculated ablation profiles under various laser powers, and feed rates are consistent with the experimental data. It revealed that the calculated ablation depth increased with the laser power increasing when the feed rate kept the same (see **Figure 7.8** a, b, and c). Meanwhile, the ablation depth decreased with an increased feed rate (see **Figure 7.8** d, e, and f). However, it is worth mentioning that the errors between the calculated and experimental depth increased with the increase of both laser power and feed rate. Three main reasons may account for this: (i) the interactions between the laser beam, and the materials are far more violent than expected, and more behaviours (e.g., materials failed by thermal impact wave) have occurred in the process; (ii) the laser machine used in these experiments has the ability to auto-adjust the focal plane, avoiding the impact of defocusing, and the ability to eject compressed N_2 gas blows away the residue in the ablation area, allowing the laser beam to reach the bottom of the slot; (iii) the measured width is also an important parameter to calculate the ablated profile in this model, however, the aspect ratio of the melt pool has been changed by reason (ii), which will inevitably affect the ablation results.

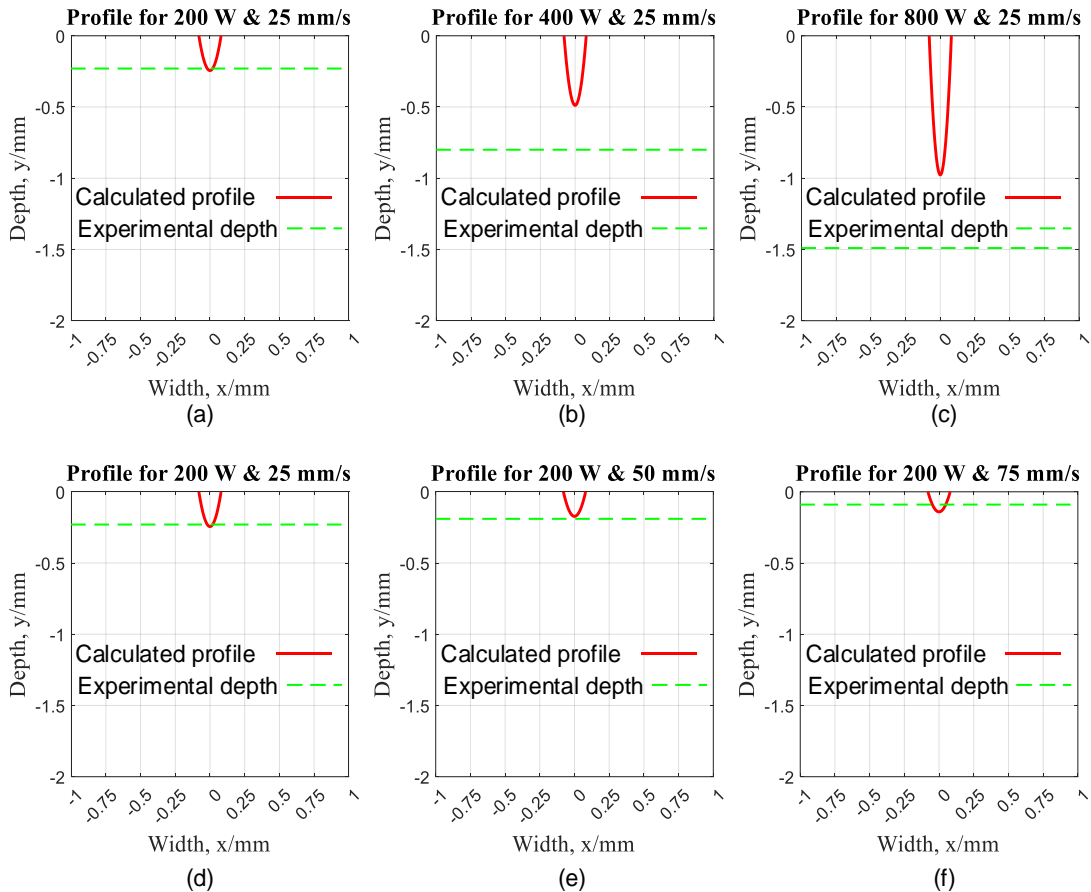


Figure 7.8 The calculation results of the theoretical model. The ablated profile for laser powers of (a) 200 W, (b) 400 W and (c) 800 W under a feed rate of 25.0 mm/s. The ablated profile for feed rate of (d) 25.0 mm/s, (e) 50.0 mm/s and (f) 75.0 mm/s under laser power of 200 W.

Two other issues should be addressed: (i) this model is established based on the hypothesis that the ablated profile obeys the law of the parabolic equation. However, the hypothesis became untenable with the auto-adjust of the laser focal plane and the disappearance of the residues in the melt pool; (ii) Due to the limitations of the model, the effect of the duty cycle on the ablation results can not be evaluated in this model. For the reasons mentioned above, it is difficult to establish an analytical model considering multiple aspects, like materials removed by thermal impact wave, auto-adjust laser beam focal plane, and melt pool residues blown away by compressed gas. Meanwhile, the

analytical model also can not be used for investigating the duty cycle effect on the ablation results. Therefore, creating a prediction model by the analytical method in this study has limitations that an empirical model may overcome.

7.5 Empirical Modelling Analysis

By studying the experimental results, the ablation law shows a clear tendency that no mutation data and no violent changes happened in the figures, which indicates the possibility to establish an empirical prediction model. With the ambition to effectively predict the ablation results in this study, the surface response prediction model is investigated in the following work. This model is often employed to solve practical problems because the response estimation results can approach the actual response surface and achieve a satisfactory prediction [248].

7.5.1 Model Description

As the ablated result is affected independently by laser power, duty cycle, and feed rate in the experiment, a second-order estimation regression equation is employed to establish the surface response prediction model of the ablation result.

The second-order regression prediction model of the laser power and the duty cycle/feed rate interaction of the two factors is given by **Equation (7.4)**.

$$f(x_1, x_2) = \varepsilon + \beta_1 x_1 + \beta_2 x_2 + \beta_{12} x_1 x_2 + \beta_{11} x_1^2 + \beta_{22} x_2^2 \quad (7.4)$$

where x_1 is the laser power (W), and x_2 is the duty cycle D_c (%) /feed rate f (mm/s).

The ablation results under laser power 2,000 W, duty cycle 100%, and feed rate 100 mm/s are reserved to verify the prediction model, while the rest of the ablation results are used to establish the corresponding predictive models.

7.5.2 Modelling Results

1) Ablation Depth Changes with the Duty Cycle under Varying Laser Power

The ablation depth is the dependent variable, the laser power x_1 and the duty cycle x_2 are the independent variables. Using the experimental data under feed rate 50 mm/s, the laser powers are 200, 400, 600, 800, 1,000, 1,200, 1,400, 1,600, 1,800, and 2,000 W, and the duty cycles are 10%, 40%, 70%, and 100%. By fitting **Equation (7.4)**, the second-order regression prediction model regarding the ablation depth changes with duty cycle and laser power is expressed as **Equation (7.5)**:

$$f_1(x_1, x_2) = -0.4708 + 0.0011x_1 + 0.009367x_2 - 2.888e^{-7}x_1^2 + 2.086e^{-5}x_1x_2 - 7.222e^{-5}x_2^2 \quad (7.5)$$

where x_1 is the laser power (W), and x_2 is the duty cycle D_c (%).

After the calculation, the goodness of the fit is also checked (as shown in **Table 7.2**). The results (see No.1 in **Table 7.2**) show that the confidence levels of the model exceeds 95%, which illustrates the high accuracy of the prediction results. Meanwhile, the SSE, the RMSE, and the correlation coefficient R^2 are 0.6232, 0.1611 and 0.981, respectively, which indicates that the fitting results are reliable and the correlation between the predicted values and measured

values is strong.

Figure 7.9 shows ablation depth changes with duty cycle and laser power. The ablation depth increases with the rising laser power and duty cycle (see **Figure 7.9a**). In the higher laser power (see **Figure 7.9b**) and larger duty cycle (see **Figure 7.9c**), the ablation depth has a larger variation range than that in the lower laser power.

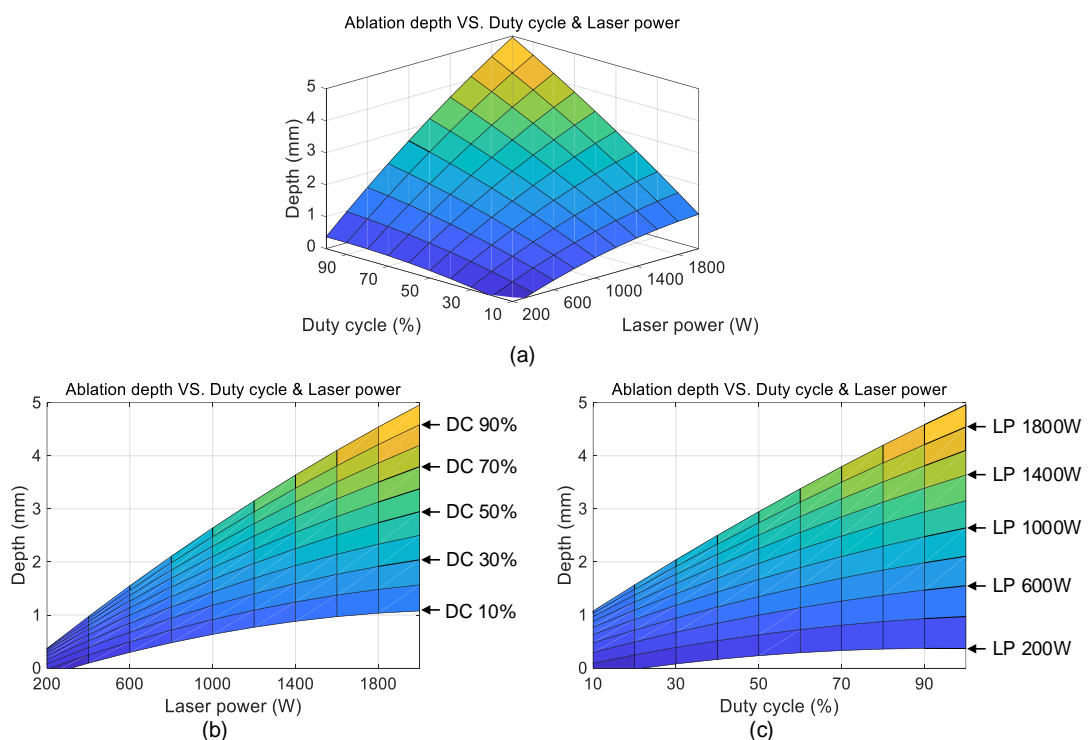


Figure 7.9 Ablation depth changes with duty cycle under different laser power. (a) The overview of the prediction result; (b) the influence of laser power on ablation depth; (c) the influence of duty cycle on ablation depth.

2) Ablation width changes with duty cycle under varying laser power

By using the same principle, the ablation width is the dependent variable in this section, and the independent variables (the laser powers x_1 and the duty

cycles x_2) are the same as that in **section 1**). By fitting **Equation (7.4)**, the second-order regression prediction model regarding the ablation width changes with duty cycle and laser power is expressed as **Equation (7.6)**:

$$f_2(x_1, x_2) = 0.08589 + 0.0001416x_1 + 0.0025x_2 - 2.841e^{-8}x_1^2 + 5.051e^{-8}x_1x_2 - 1.444e^{-5}x_2^2 \quad (7.6)$$

In checking the goodness of fit, **Table 7.2** (see No.2) shows that the confidence levels of the model exceed 95%. Additionally, the SSE, the RMSE, and the correlation coefficient R^2 are 0.007217, 0.01734 and 0.9349, respectively, which means the effectiveness of the prediction model.

In the prediction model, **Figure 7.10a** indicates an ablation width slightly rises with the laser power and duty cycle increase. Both **Figure 7.10b** and **Figure 7.10c** show that the ablation width has a relatively narrow variation range.

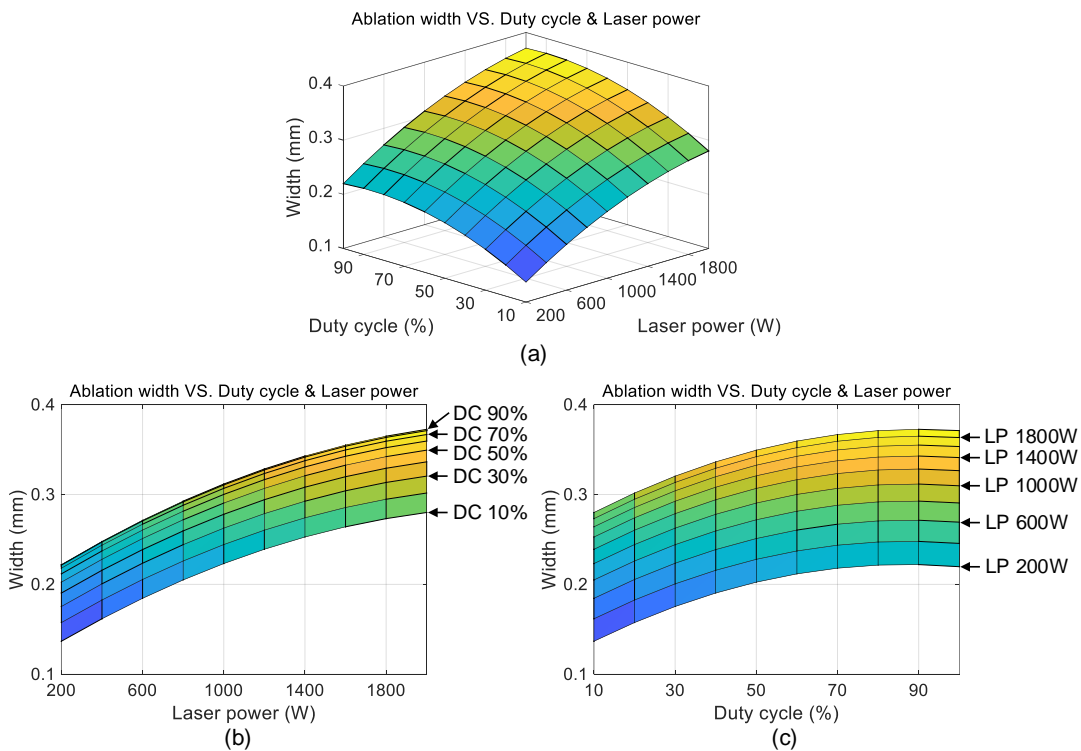


Figure 7.10 Ablation width changes with duty cycle under different laser power. (a) The overview of the prediction result; (b) the influence of laser power on ablation

width; (c) the influence of duty cycle on ablation width.

3) Ablation depth changes with feed rate under varying laser power

Similarly, the ablation depth is the dependent variable, the laser power x_1 and the feed rate x_2 are the independent variables. Using the experimental data under duty cycle 25%, the laser powers are 200, 400, 600, 800, 1,000, 1,200, 1,400, 1,600, 1,800, and 2,000 W, and the feed rates are 25, 50, 75, and 100 mm/s. By fitting **Equation (7.4)**, the regression prediction model regarding the ablation depth changes with feed rate and laser power is expressed as

Equation (7.7):

$$\begin{aligned} f_3(x_1, x_2) = & 0.08689 + 0.002443x_1 - 0.005973x_2 - 3.087e^{-7}x_1^2 \\ & - 8.224e^{-6}x_1x_2 - 8.8e^{-6}x_2^2 \end{aligned} \quad (7.7)$$

Table 7.2 (see No.3) showed that the confidence level of the model also exceeds 95% in the goodness fit checking. The SSE, the RMSE, and the correlation coefficient R^2 are 1.041, 0.2083 and 0.9544, respectively. Although the SSE is a little higher than the other fit result, the correlation coefficient R^2 still indicates the acceptability of the prediction model.

Figure 7.11 represented the ablation depth changes with feed rate under different laser power, which indicated the ablation depth increases with the growth of laser power and the dropping of the feed rate (see **Figure 7.11a**). Notably, the ablation depth has a narrow change range under a certain laser power (see **Figure 7.11b**), and has a wide change range under a certain feed rate (see **Figure 7.11c**).

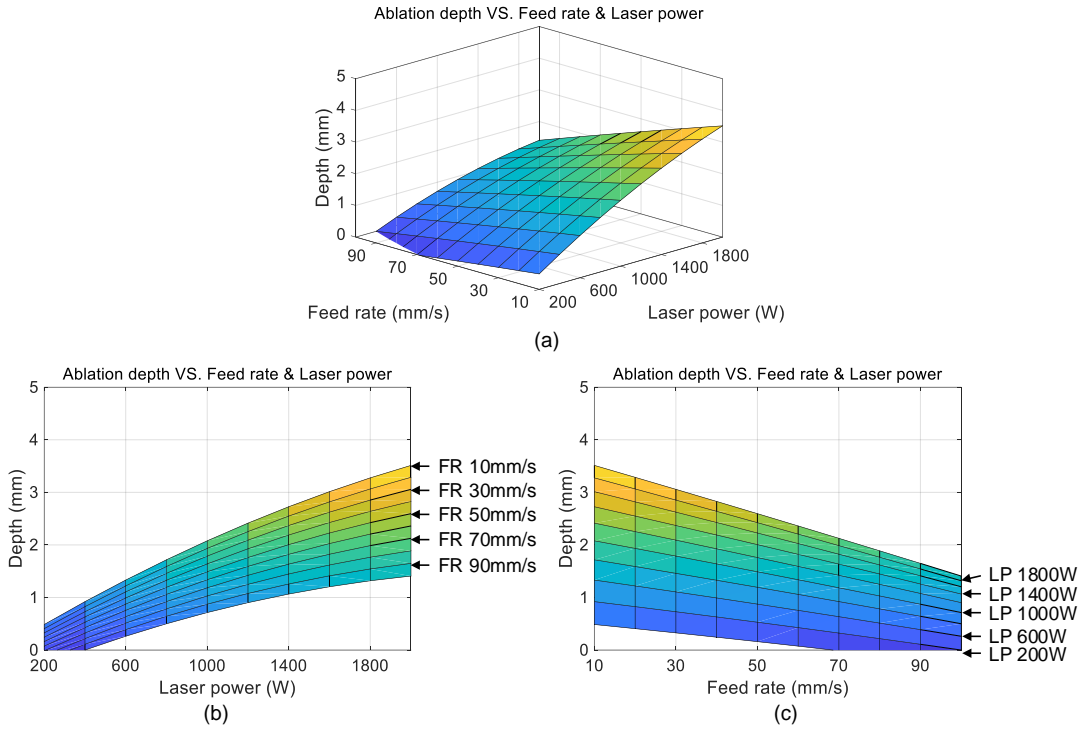


Figure 7.11 Ablation depth changes with feed rate under different laser power. (a) The overview of the prediction result; (b) the influence of laser power on ablation depth; (c) the influence of feed rate on ablation depth.

4) Ablation width changes with feed rate under varying laser power

The ablation width was the dependent variable in this section, and the independent variables (the laser powers x_1 and the feed rates x_2) were the same as that in **section 3**). By fitting **Equation (7.4)**, the second-order regression prediction model regarding the ablation width changed with feed rate and laser power was expressed as **Equation (7.8)**

$$f_4(x_1, x_2) = 0.1694 + 0.0001055x_1 - 0.001173x_2 - 3.346e^{-8}x_1^2 + 7.758e^{-7}x_1x_2 + 4.8e^{-6}x_2^2 \quad (7.8)$$

As shown in **Table 7.2** (see No.4), the correlation coefficient R^2 is 0.7944, the lowest value among the four prediction models, which means the prediction model may be weak to reflect the actual situation. However, considering the SSE and RMSE are small (0.01429 and 0.0244, respectively), and the confidence level is over 95%, which indicates the model is stable and has little

variation error. Besides, the ablation width has a relatively narrow change range, so the prediction model is acceptable.

Figure 7.12 represented the ablation depth changed with feed rate under different laser power, which showed the ablation depth increased with the growth of laser power and the dropping of the feed rate (see **Figure 7.12a**). Notably, the ablation depth had a narrow change range under a certain laser power (see **Figure 7.12b**) and had a wide change range under a specific feed rate (see **Figure 7.12c**).

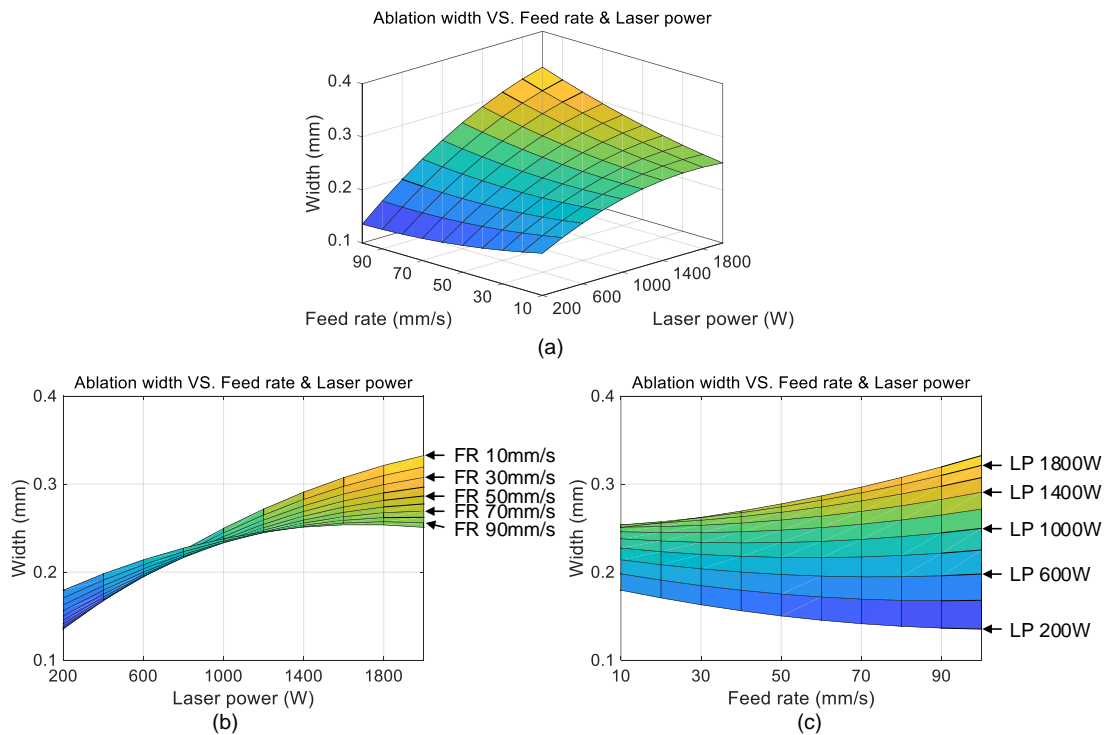


Figure 7.12 Ablation width changes with feed rate under different laser power. (a) The overview of the prediction result; (b) the influence of laser power on ablation width; (c) the influence of feed rate on ablation width.

Table 7.2 Goodness of fit for the prediction models.

No.	Prediction Models	SSE	RMSE	R-square	Confidence level
1	$f_1(x_1, x_2)$	0.6232	0.1611	0.981	> 95%
2	$f_2(x_1, x_2)$	0.007217	0.01734	0.9349	> 95%
3	$f_3(x_1, x_2)$	1.041	0.2083	0.9544	> 95%
4	$f_4(x_1, x_2)$	0.01429	0.0244	0.7944	> 95%

7.6 Prediction Results Validation

7.6.1 Validation of Ablation Results under the Laser Power of 2,000 W

Figure 7.13a and Figure 7.13b showed the validation results under the laser power of 2,000 W and the feed rate of 50 mm/s. Overall, the tendency of the predicted ablation result to change with the duty cycle was well consistent with the experimental result. Figure 7.13c and Figure 7.13d showed the comparison of predicted, and experimental values regarding ablation results changed with feed rate under the laser power of 2,000 W and the duty cycle of 25%. According to the calculation result, the Bias for the ablation depth (see Figure 7.13a) and width (see Figure 7.13b) prediction were 0.0109 and 0.0039, respectively. The RMSEs for the figures were 0.1464 and 0.0240, while the Std.Res. for the prediction was 0.1459 and 0.0235.

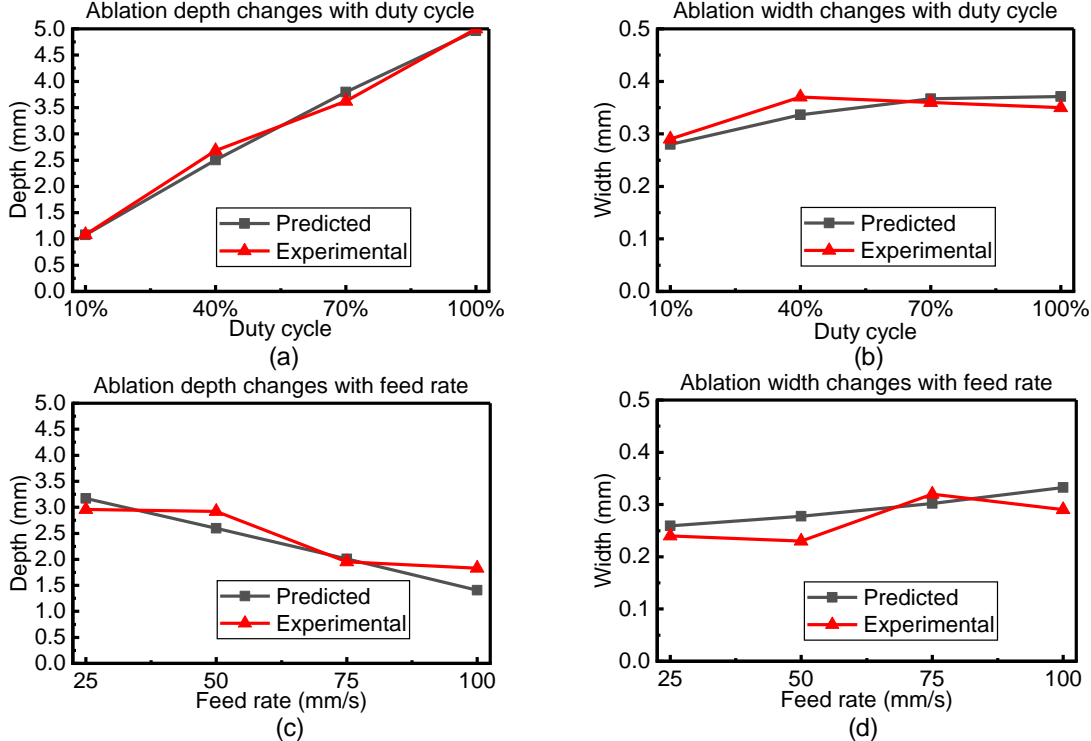


Figure 7.13 Validated results under the laser power of 2,000 W. (a) Ablation depth and (b) width changed with duty cycle. (c) Ablation depth and (d) width changed with feed rate.

A maximum discrepancy of 0.42 mm was found in the depth prediction model when the feed rate was 100 mm/s (see **Figure 7.13c**), and a maximum relative error of 0.05 mm appeared in the width prediction model when the feed rate was 50.0 mm/s (see **Figure 7.13d**). However, the overall trend for the prediction model and the experimental value was the same.

7.6.2 Validation of Ablation Results Changed with Laser Power under the Duty Cycle of 100%

Figure 7.14 showed the predicted and experimental ablation results changed with laser power under a duty cycle of 100% and a feed rate of 50 mm/s. Generally, the predicted value was consistent with the experimental result, especially for the ablation width prediction. It showed that the prediction result for the ablation depth, on the whole, was slightly smaller than the experimental result and the maximum relative error was 0.61 mm when the laser power was 1,200 W (see **Figure 7.14a**). As the figure for ablation width, the maximum relative error was 0.35 mm, when the laser power was 400 W.

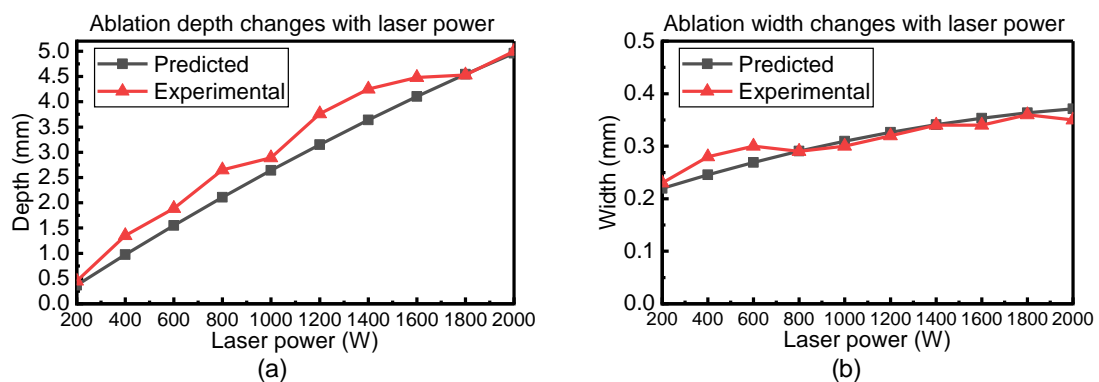


Figure 7.14 The validation of ablation results changed with laser power changes under the duty cycle of 100%. (a) Ablation depth and (b) ablation width.

7.6.3 Validation of Ablation Results Changed with Laser Power under the Feed Rate of 100 mm/s

Generally, **Figure 7.15** shows the tendency agreement between the predicted and experimental results under a feed rate of 100.0 mm/s and a duty cycle of 25%. Interestingly, the overall predicted value for the ablation depth was smaller than the experimental value, while the figure for the ablation width was inverse. For example, the maximum relative error for the ablation depth was 0.51 mm when the laser power was 1,600 W, and for the ablated width was 0.04 mm when the laser power was 2,000 W.

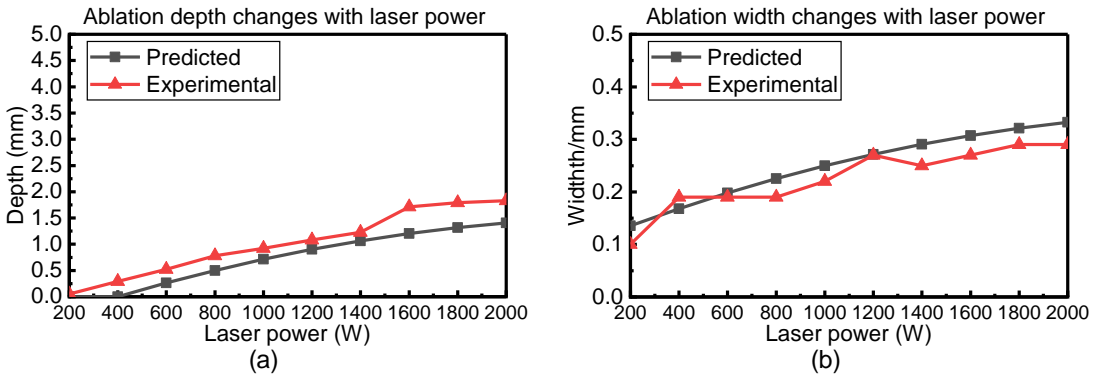


Figure 7.15 The validation of ablation results changed with laser power changes under the feed rate of 100 mm/s. (a) Ablation depth and (b) ablation width.

7.7 Error Analysis

The Root Mean Squared Error (RMSE), Bias, and Standard Deviation of Residues (Std.Res.) for the prediction models from **Figure 7.13** to **Figure 7.15** were shown in **Figure 7.16**. Overall, the trend of the experimental results can be reflected by the predictive model, which provided help for ablation parameter selection. Despite the fact that not all the experimental data can be precisely predicted, the predicted error was acceptable. As shown in the table that both the maximum RMSE (0.4096) and Bias (0.3215) of ablation depth

were found in **Figure 7.14**, and the maximum Std.Res. (0.3027) was found in **Figure 7.13c**. The minimum RMSE (0.1464) and Bias (0.0109) for the ablation depth and width appeared in **Figure 7.13a** and **Figure 7.13b**, and the minimum Std.Res. was shown in **Figure 7.15**. As the data for ablation width, the maximum RMSE (0.0398) and Bias (0.240) of ablation width were found in **Figure 7.13d** and **Figure 7.15**, respectively, while the minimum Std.Res appeared in **Figure 7.14**.

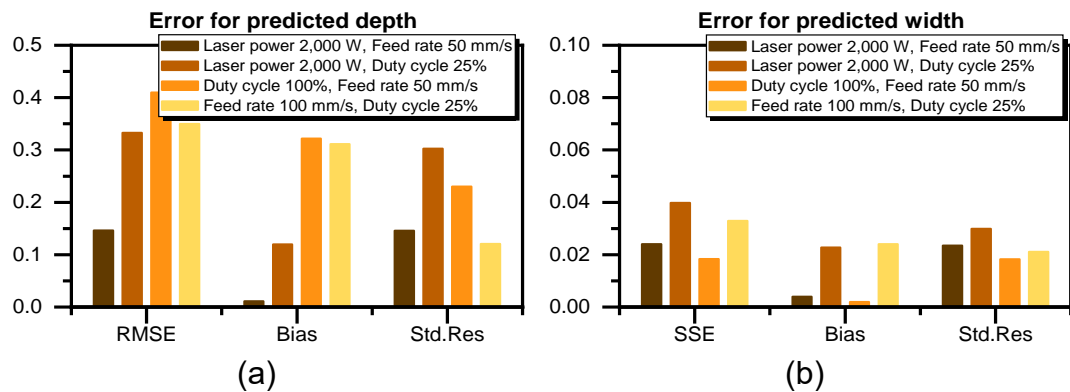


Figure 7.16 The errors for prediction. (a) Ablation depth and (b) ablation width.

Generally, three main reasons may be related to explaining the issues: (i) when comparing the data in the figures, it can be found that the signal-to-noise ratio was not big enough due to the complexity of non-metallic multi-material laser ablation. Hence, a certain random error happens, and the error ratio will become obvious in the prediction model. (ii) The prediction model was established within limited experimental data, three groups of duty cycles, and nine groups of feed rates, the relatively low quantity of experimental data resulting in a less good fit (see **Figure 7.14**). Besides, as the endpoint (which has a strong influence on the fitting results) was not involved in establishing the prediction model, the error is inevitable when the data was used for the model validation. (iii) The second-order regression function was employed

here to establish the prediction model, which was an empirical prediction model that could not be used to satisfy all the experimental data.

7.8 Applications

Based on the understanding of the ablation law, a rough application regarding manufacturing curved surfaces was demonstrated, which was the usage of the knowledge above to select proper ablation parameters for the slots. The ablation strategies can be explained in **Figure 7.17a**, where the grinding wheel from the same batch as had been described in **Table 3.3** was used for the application demonstration and the laser power (from 200 W to 2,000 W) was used as a variable to achieve a wide range of ablation depth. The laser power changes for each laser beam while other ablation parameters were kept unchanged. Between the two adjacent laser beam tracks, a 0.3 mm (approximately the maximum ablation width) interval was used to minimise the possible effect and maximise the removal of the residues between the two adjacent tracks. According to the designed profile, the laser power for each laser beam track was carefully selected based on the predictive model. **Figure 7.17b** shows the ablated two slots on the grinding wheel. After cleaning the ablated grinding wheel with a hairbrush, the cross-section of the grinding wheel (a sample taken from the wheel and polished) and the comparison between the measured and designed profile were presented in **Figure 7.17c**. The comparison results showed the RMSE, Bias and Std.Res. were 0.2867, 0.0296, and 0.2588, respectively.

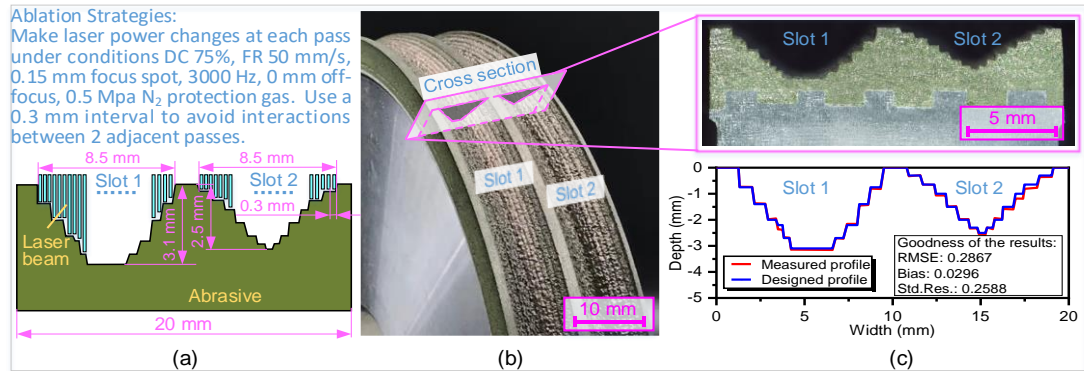


Figure 7.17 An application example. (a) The ablation scheme; (b) the ablated curved grinding wheel; (c) the cross-section of the curved grinding wheel and the comparison between the measured and designed profile.

Overall, the demonstrated application revealed the high-quality results of the applied empirical model considering the precise profiles and the reserved microstructures generated by such a high laser power (2,000W). Meanwhile, benefitting from the high laser power, the achieved results in the high-efficiency process indicate that it potentially can be directly used in industrial applications. As for the errors, three main reasons are proposed: (i) changing laser power is used as the unique variable for different ablation depths, which causes some of the designed depth in the profile to be approximated; (ii) to minimise the possible effect and to maximise the removal of residue between two adjacent tracks, and the intervals had been set to 0.3 mm; this consistent interval value can not meet each requirement, especially for the ablation of the microstructures; (iii) the random distribution of the diamond grits in abrasives, making discrepancies inevitable.

7.9 Conclusions and Discussions

By controlling the laser power, the duty cycle, and the feed rate, the laser ablation law on the diamond grinding wheel was investigated. Predictive

models were established by analysing the limitations and applicabilities of the analytical and empirical models. Based on the empirical model, an application to generate profiled diamond grinding wheels was demonstrated. The main conclusions drawn from the paper can be summarized as follows:

(1) Both the ablation depth and width increased with the duty cycle and laser power and decreased with feed rate. However, the ablation results were not significantly affected by feed rate changes by comparison. The ablation depth varies to a lesser extent under a fixed laser power, while it has a wide variance under a fixed feed rate.

(2) In contrast with the influence on ablation width, the duty cycle had a greater effect on the ablation depth. In particular, the ablated depth had a larger variation range under higher laser power than at lower power with duty cycle changes, while the ablation width had a relatively narrow variation range.

(3) Taking advantage of the empirical model, the predictive models regarding single laser pass ablated width and depth changed with laser power, duty cycle, and feed rate had been established. The experimental validation for the prediction models had also been performed. Overall, the ablation law can be revealed by the empirical models despite the inevitable errors.

An application to generate profiled diamond grinding wheel is performed to demonstrate the usefulness of the study. It shows the RMSE, Bias and Std.Res. values for the designed and measured profile were 0.2867, 0.0296, and 0.2588, respectively, which illustrates the acceptability of the empirical model.

Chapter 8

Generating Profile Diamond Grinding Wheels by Multiple Pass of Fibre Laser: On the Understanding of Laser Ablation Law with Pass Number and Feed Rate

8.1 Introduction

To generate profiled diamond grinding wheels in a precise and efficient way is not accessible due to the limitation of existing dressing techniques to super-hard composite materials. A single-pass dressing technique has been presented using a 2,000 W fibre laser generator in *Chapter 7*, and the laser ablation law regarding ablation depth and width with regards to the laser power, the duty cycle, and the feed rate has been explored. An application to generate profiled diamond grinding wheel with micro-steps is demonstrated. However, it takes time and effort and is error-prone when dressing structures with multiple scales, as it needs to frequently stop the process to adjust the laser power and duty cycle. Besides, it is hard to achieve a relatively smooth surface efficiently and cost-effectively due to the limited resolution. This chapter plans to explore the possibility of using a different way to fabricate profiled diamond grinding wheels. This work uses a 2,000 W fibre laser to experimentally investigate the morphology and topography changes with the number of laser passes and feed rate. A parameter selection diagram for better ablation results will be built, and an attempt to generate curved diamond grinding wheels will be performed by using this diagram. The presented work is expected to be meaningful when considering the selection of optimum dressing strategies for

producing profiled grinding wheels.

8.2 Theoretical Analysis

Laser multi-pass ablation refers to a laser beam repeatedly passing on the same slot. As the threshold for multi-pass is affected not only by the optical and thermal properties of the materials but also by the incubation effect, the behaviours are more unpredictable than only progresses regarding homogenous materials ablation; single-pass ablation could be found in the previous studies.

Based on Beer's law, ablation occurs when a unit composite absorbs an amount of energy that makes the material undergo permanent deterioration. The minimum energy required for the ablation to occur was defined as threshold fluence, expressed in **Equation (8.1)** [274].

$$F_{th} = \frac{\rho\Omega_{vap}}{\alpha A} \quad (8.1)$$

where $\rho\Omega_{vap}$ is the enthalpy of evaporation per unit volume, $1/\alpha$ is the characteristic absorption of materials, and A is the absorptance of the material.

Since the laser beam repeatedly impacts the same region in multi-pass ablation, the incubation effect should be considered. Therefore, the situation for multi-pass ablation is similar to multi-shot ablation, and the threshold could be written as **Equation (8.2)** [274].

$$F_{th} = F_{th}(1) \times N^{S-1} \quad (8.2)$$

where $F_{th}(1)$ is the threshold fluence for one pass, N is the pass number, and

S is the incubation coefficient, which can be determined by fitting the experimental data. Due to the incubation coefficient being always smaller than one, the threshold fluence will decrease when the pulse number increases. **Figure 8.1** shows two ablated slots with the same output energy fluence (44.4 J/mm^2 , which can be calculated by **Equation (3.2)**) but in different pass numbers. Since the threshold fluence decreased with the laser beam passes, the ablation depth with more pass numbers **Figure 8.1b** is larger than the one with fewer pass numbers **Figure 8.1a**. It indicates that multi-pass ablation on composite materials could be more complex when considering the weight variation of incubation effects. Therefore, the ablation law regarding multi-pass ablation should be studied by experimental works.

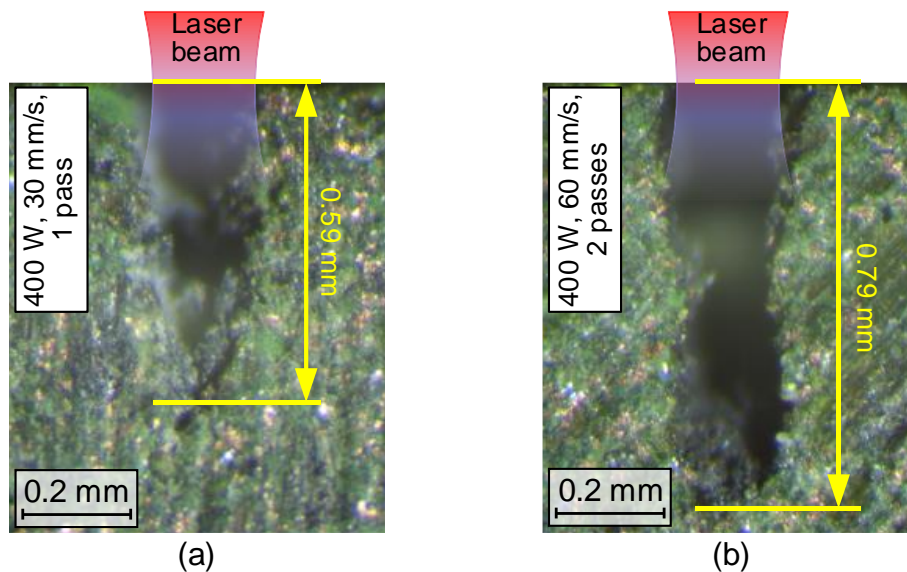


Figure 8.1 Section view of the ablated slots under the same output fluence but different conditions. (a) 400 W, 30 mm/s, 1 pass and (b) 400 W, 60 mm/s, 2 passes.

8.3 Experimental Strategy

The standard commercial diamond abrasive grinding wheels (D120N75B771/8, 3M Company) with resin bond (see details in **Table 3.3**) are used as non-

metallic multi-material in all the trials of the experiment. An Nd: YAG fibre laser generator (Han's machine) with a maximum power of 2,000 W, a wavelength of 1.06 μm , a focus diameter of 0.15 mm and a focal length of ± 5 mm was used (see **Figure 8.2a**). Again, the custom precise positioning system was employed here to conduct the experiments (see **Figure 8.2b**), and the relative position of the laser nozzle and the grinding wheel was shown in **Figure 8.2c**.

In order to study the effects of multi-pass laser ablation, a wide range of pass numbers and feed rates with a fixed laser power of 400 W was used. The laser power was based on the principle that the laser can generate a clear slot but not cut through the grinding wheels.

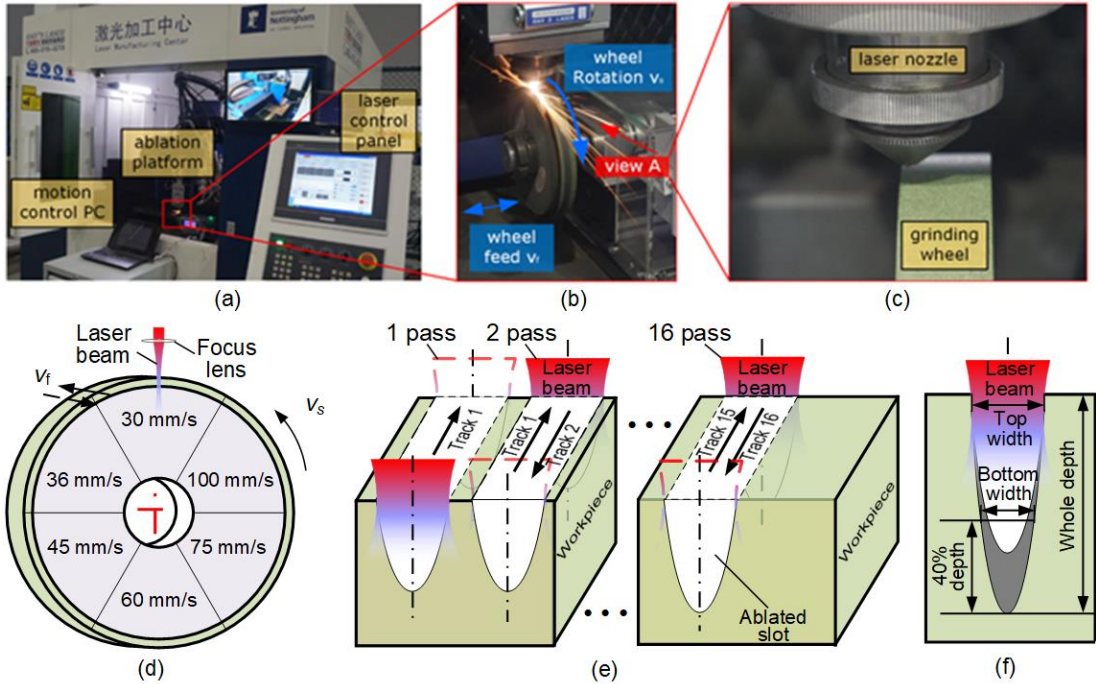


Figure 8.2 Experimental strategy. (a) The experimental setup consists of a fibre laser machine process centre, a customized positioning system and a control PC; (b) a detailed view of the ablation process; (c) a detailed view of the laser nozzle and grinding wheel; (d) parameters for the trail; (e) definition of pass number; (f) measurement strategy for ablated grooves.

To make the ablation results comparable, six different feed rates with sixteen different pass numbers were deployed on one abrasive wheel, as shown in **Figure 8.2** (d). A laser pass was defined as one laser track scanned over the surface of the grinding wheel (see **Figure 8.2e**). The detailed experimental parameters are shown in **Table 8.1**.

Table 8.1 Details of the experimental parameters.

Trial No.	Laser power (W)	Pass number	Feed rate(mm/s)
1-16	400		30
17-32			36
33-48		1, 2, 3, 4, 5, 6, 7,	45
49-64		8, 9, 10, 11, 12,	60
55-80		13, 14, 15, 16	75
81-96			100

After the ablation process, the diamond wheel was firstly carefully cut into six segments by EDM (MV2400S, Mitsubishi Electric Company). The two sides of each segment were carefully polished by the alumina with the sizes of #240 (1 hour), #400 (1 hour), and #1200 (2 hours). Then all the segments were cleaned by the ultrasonic distilled water bath for 1 hour and air-dried at room temperature. Both the optical microscope (NSZ-810, NOVEL OPTICS) and Scanning Electron Microscope (SEM, 174C CZ, ZEISS Company) were employed to evaluate the ablated structures, respectively. To assess the topography and morphology precisely, both the top width and bottom width were recorded. As the bottom shape of the ablated slot is near round, the bottom width was hard to define here. Therefore, the bottom width was defined as the width at 40% of the ablation depth from the bottom in this work.

8.4 Experimental Results and Analysis

8.4.1 Ablation Width Affected by Laser Pass Number and Feed Speed

Figure 8.3 shows that the ablation width was affected by laser pass number and feed speed. It revealed that the top width was wider than the bottom width. Besides, the top width had a wider fluctuation, while the fluctuation at the bottom width was smaller than the top width. It may be due to the top wide being affected by the variation of the output of laser power that breakage has happened for some parts around the top when multiple passes are performed. Meanwhile, as the grinding wheel materials absorb some of the laser energy, the energy decreases at the bottom.

In all trailed parameters, the pass number affected little the slot width, and the top width and bottom width fluctuated in a certain range. This may be due to the auto-adjust of the laser head that made the off-focus effect have little effect on the ablation width.

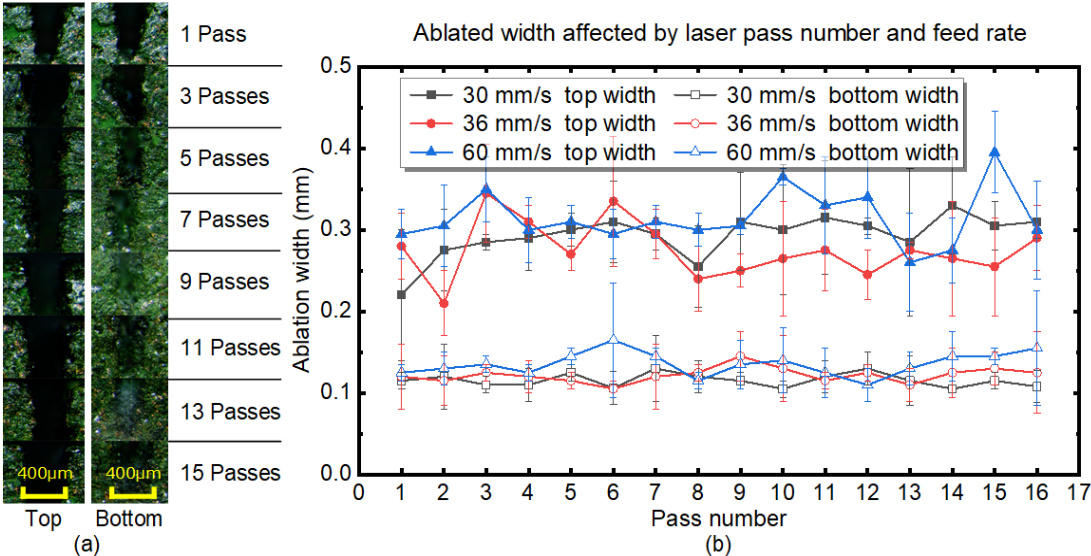


Figure 8.3 Ablation width affected by laser pass number and feed speed. (a) Optical micrographs from the side view of the ablated grooves with the pass number

of 1, 3, 5, 7, 9, 11, 13, 15 at the laser power of 400 W and the feed speed of 30 mm/s; (b) top width and bottom width from 1 pass to 16 passes at a feed speed of 30 mm/s, 36 mm/s and 60 mm/s.

8.4.2 Ablation Depth Affected by Laser Pass Number and Feed Speed

Figure 8.4a-c shows the slot depth was increased with laser beam pass number and decreased with the feed rate. The increase rate was reduced with the pass number, while the heat-affected zone was gradually ascended. It can be inferred that the ablated depth was likely kept unchanged to a value with the laser pass number continuing to increase, which can be fitted by the Logarithmic curve. The observed phenomena were likely caused by the sidewall absorbing a part of energy when the laser passes the slot. Meanwhile, the laser energy will also lose for the defocus. The sidewall of the slot became smoother when the feed rate increased, which provided a promising way to lower the heat-affected zone. It may be thanks to the rapid laser pass having a relatively smaller fluence value hence the heat-affected zone was smaller due to less heat will be accumulated.

Figure 8.4d shows that the larger pass speed could cause deeper depth when the laser fluence is the same. It can be easily found that the laser fluence had a more dramatic effect on ablation depth than the passing speed. It may be that the same fluence for higher speed means the laser passes more times or has higher energy. Meanwhile, compared with higher laser single pass, lower laser power with multi-pass could make the ablation depth deeper, heat effect smaller, and less heat accumulation.

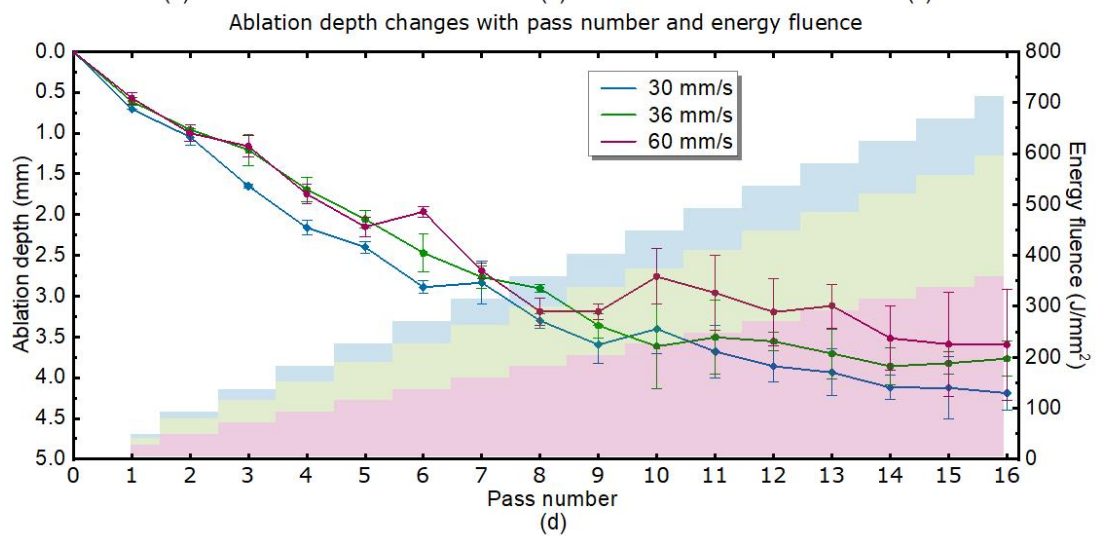
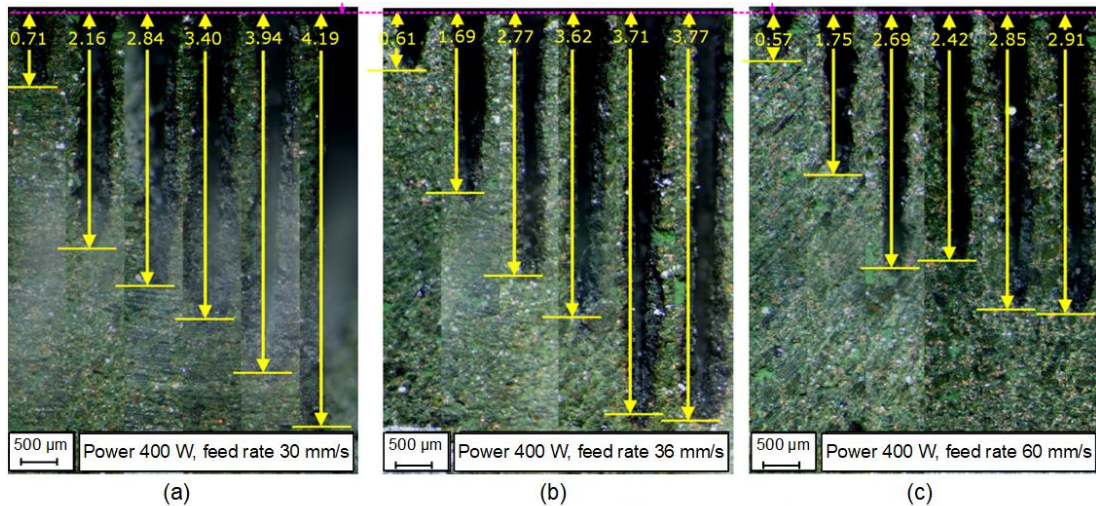


Figure 8.4 Effect of laser pass number and feed speed on the depth of the ablated structure. (a), (b) and (c) the optical micrographs from one side of the ablated grooves with the pass number of 1, 4, 7, 10, 13, 16 at the same laser power of 400 W and various feed speeds of 30 mm/s, 36 mm/s, 60 mm/s. (d) the effects of laser pass number, feed speed and energy fluence (right) on the ablation depth (left) when the feed rate was 30 mm/s (blue), 36 mm/s (green), 60 mm/s (red).

8.4.3 Ablation Morphology Affected by Laser Pass Number and Feed Speed

Figure 8.5 (a) shows three types of diamond abrasives in the ablated structure morphologies: (i) exposure/loosening, (ii) breakage and (iii) deterioration. These three types of morphology could not be observed in the un-ablated areas.

The exposure/loosening structure refers to the most part of an abrasive grit being out of the resin bond. This structure might be generated by the small thermal effect, resulting in the melting of only the resin bond. The adverse effects of loosening abrasives in the grinding process could be the inefficient materials removal rates and the increased uncertainties of grinding accuracy. The ineffective materials removal rates are due to the limited abrasive retainment. The increased grinding accuracy uncertainties are caused by the loose abrasives scratching the grinding surface and undesired abrasive fall-off before the abrasive is normally worn out in the ultra-high-precision grinding process.

The breakage structure refers to the split of the abrasives within the resin bond. This structure was mostly observed at the mid slot boundary, which might be generated by a short-time strong impact rather than the thermal effects of the laser beam with high energy density. Compared with exposure and loosening structure, the breaking abrasives and loosening bond had a better situation, as the breakages would not fall off in large pieces, and the sharp edges are helpful to the grinding process.

The deterioration structure refers to the deteriorated powder-like diamond abrasives blended with the resolidified resin bond that cannot be generally recognised. This structure is generated by the direct radiation of a laser beam with an intensive energy density, and both the abrasives and resin bonds within the slot have seriously deteriorated. The grinding ability is totally lost for this structure.

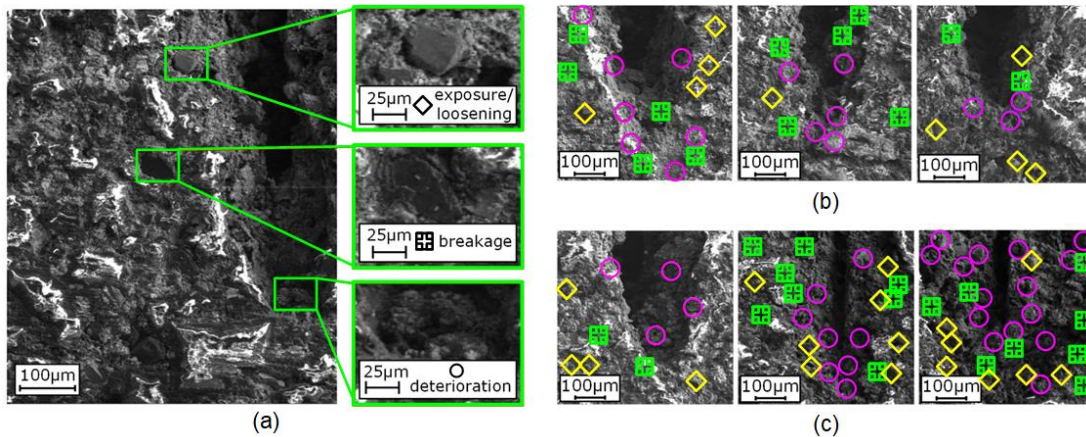


Figure 8.5 Bottom morphology affected by laser pass number and feed rate. (a) Definition of morphology characters; (b) bottom morphology with four passes under the feed speed of 30 mm/s, 36 mm/s and 60 mm/s; (c) bottom morphology with the feed rate of 30 mm/s under the pass numbers of 1, 8 and 15.

Figure 8.5b shows the effects of feed rates of 30 mm/s, 36 mm/s, and 60 mm/s on the morphology of the ablated structure under four laser passes. It indicates that the counted characters number decreased with the feed rate increasing. With the feed rate rising, the laser fluence dropped, and more grits around the bottom of the groove presented the morphology characteristics of exposure/loosening, which reveals the thermally affected region is reduced. In addition, more other two characteristics, like deterioration and breakage, are observed around the bottom of the slot when the feed rate is relatively slower.

Figure 8.5c shows the effects of laser pass numbers of 1, 8, and 15 on the morphology of the ablated structure under a feed rate of 30 mm/s. It shows both the number and morphology characters increased and spread to the side of the slot with the pass number increasing, and more deterioration characters are detected around the slot as well.

8.4.4 Parameters Selection for Multi-pass Ablation of Abrasive Tools

Based on the previous results about multi-pass laser ablation, an ideal ablation product of the grinding wheel was a combination of high shape accuracy and low burned region. The ablation parameters could be selected according to **Figure 8.6**, where the ablation depth changed with the pass number is limited by over ablated and non-ablated domains. The over ablated domain has such a burned region (more than 50 μm thickness) that affects the ablation performance, which is derived from large pass number (more than 14) or/and slow feed speed. The less ablated domain has little efficiency, and very little material could be removed, resulting from the poor laser energy fluence. The recommended domain has a large depth variation range for the selection of desired ablation depth with relative higher efficiency. A variety of ablation depths could be achieved by selecting the ablation parameters in the diagram.

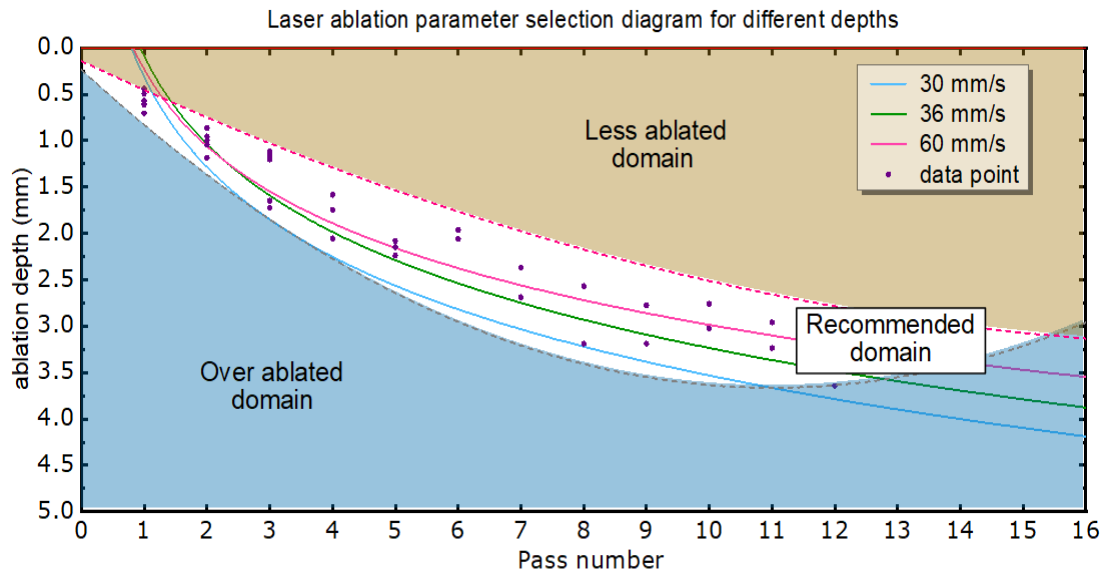


Figure 8.6 Diagram for laser ablation parameter selection for different ablation depths.

8.5 Applications

Figure 8.7 presents an application of the ablation parameter selection diagram. The ablation strategies can be explained in **Figure 8.7a**, where the basic ablation parameters are the same except for the pass number. The pass number is selected according to ablation depth under a feed rate of 36 mm/s. This feed rate is selected according to the fact that it is located in the centre of the recommended domain, which is less likely to be over/less ablated. The pass number is selected based on the designed profile and ablation parameter selection form. The interval between the two adjacent passes of 0.3 mm is selected to avoid the interactions of the slot and minimise the residuals to fit the profile as possible. **Figure 8.7b** shows the overall view of the optical image of the ablated grinding wheel. **Figure 8.7c** shows the optical image of the ablated grinding wheel cross-section and the comparisons of the measured profile and the designed profile.

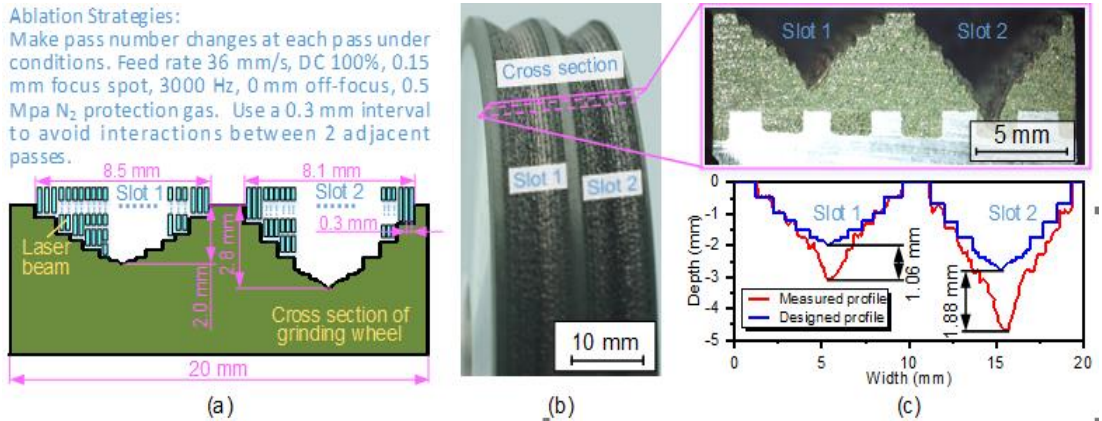


Figure 8.7 An application example. (a) The ablation scheme; (b) the ablated curved grinding wheel; (c) the cross-section of the curved grinding wheel and the comparison between the measured (red) and designed (blue) profile.

Surprisingly, the result is not consistent with the parameter selection diagram. It shows that the error is increased with the ablation depth, where the error is

1.06 mm when the ablation depth is aimed at 2 mm (slot 1), while the error is 1.88 mm when the target is aimed at 2.8 mm (slot 2). It indicates that the ablation process for curved grinding wheels is far more complex than expected. There are several reasons that may account for the results: (i) the higher laser power makes the energy rapidly accumulated in the bottom of the grooves making the bottom temperature increase, and the increased temperature induces the incubation effect that reduces the ablation threshold; (ii) the curved and deep narrow bottom makes the heat hard to be dispersed to the surrounding environment, which enhanced the incubation effect; (iii) the good quality of the positioning platform that makes multiple passes available on target slot.

8.6 Conclusions and Discussions

The laser ablation law on composite materials is investigated by controlling the feed rate and pass number of the laser beam on the diamond grinding wheel. Based on the understanding of the ablation law, a diagram for laser ablation parameter selection for different ablation depths is built. Then, an application for the diagram to generate profiled diamond grinding wheels is demonstrated. The main conclusions drawn from this chapter can be summarised as follows:

(1) Compared to the bottom width, the top width is larger and has a wider fluctuation. Both the top width and bottom width fluctuate in a certain range, and the pass number affects little the slot width.

(2) Slot depth is increased with laser beam pass number and decreased with the feed rate. However, the increase rate is reduced with the pass number,

while the heat-affected zone is gradually extended.

(3) Due to the heat accumulation and incubation effect, the HAZ is increased with the increase of the laser beam passes number and the decrease in feed rate. Besides, both the types and amounts of the morphology characters are increased with the laser beam passes number growing and decreased with the feed rate climbing.

Finally, according to the instruction of the parameter selection diagram, an application to generate profiled diamond grinding wheel by changing the moving speed of the grinding wheel and the passing number of the laser beam is attempted. However, from the view of ablation shape accuracy, the ablated surface for the curved grinding wheels is far from accurate. Meanwhile, it is also hard to obtain a smooth surface due to more rotational speeds that should be involved to improve the ablation resolution. That indicates that more superior strategies are highly expected to be developed in the ablation process.

Chapter 9

Generating Precise Non-flat Diamond Grinding Wheels via a Combination of CO₂ Laser Ablation: Understanding the relationship between Overlap Rate and Feed Rate on Composite Materials

9.1 Introduction

Non-flat structures are essential features in key mechanical functional surfaces such as aero-space engine blade tenons, optical components, screw rods and machine tool guide rails etc., which usually require profile grinding as the finishing process to meet demanding working requirements. However, the precise manufacturing of profile grinding wheels remains challenging as it is hard to remove the super hard materials within the grinding wheel in a controllable way. Dressing the target wheel by laser ablation appears promising; however, the interactions between the laser energy beam and target composite materials are quite complex, especially the combined behaviours among a series of adjacent ablation tracks are hard to understand when concerning the ever-changing Overlap Rates (ORs) and feed rates in the ablation process. In the previous two Chapters, it has been tried to remove materials by single pass and multiple passes, respectively, but neither of them cannot obtain a smooth surface.

This chapter aims to investigate the methodologies of generating precise non-flat profile grinding wheels (including stepped and curved surfaces) via CO₂

laser ablation. In this study, the nature of the laser beam and the characteristics of the beam energy distribution will be analysed. The shapes for the laser ablation under various ORs and feed rates will be theoretically analysed and experimentally validated. Based on the results, empirical prediction models regarding ablation depth, width, and topography changing with ORs and feed rates could be established. Finally, based on the research results, an attempt to fabricate high-resolution non-flat surfaces by using the developed strategies will be demonstrated. The presented work provides a novel approach for manufacturing non-flat grinding wheels.

9.2 Theoretical Analysis

9.2.1 Laser Ablation Process

In the ablation process, the laser beam is focused by a focus lens, and the focused spot is kept still on the top surface of the resin bond diamond grinding wheel (see **Figure 9.1a**). The grinding wheel can be precisely controlled by servo motors to perform rotational and transversal motions. As the focused laser beam has a huge energy density, especially at the focal spot where the targeted materials will be deteriorated and be removed by the intensive energy (View A in **Figure 9.1a**), thus a slot related to the energy beam is generated.

However, for a certainly focused laser beam, it has a focus site (see **Figure 9.1b**) or focal plane (View A in **Figure 9.1a**) along the laser beam propagation direction, and the power density in the site is the highest. With the defocusing distance increase, the centre laser power density becomes weaker and weaker (see **Figure 9.1c**), and the energy fluence is unable to remove the

materials eventually [249, 275]. However, the energy beam kept heating the slot boundary, and the Heat Affect Zone (HAZ) was inevitably formed. As the bond agency is made of resin, which has a relatively lower creep deterioration temperature point, HAZ also makes the ablation depth changes since the material deterioration may be happened because of the heating.

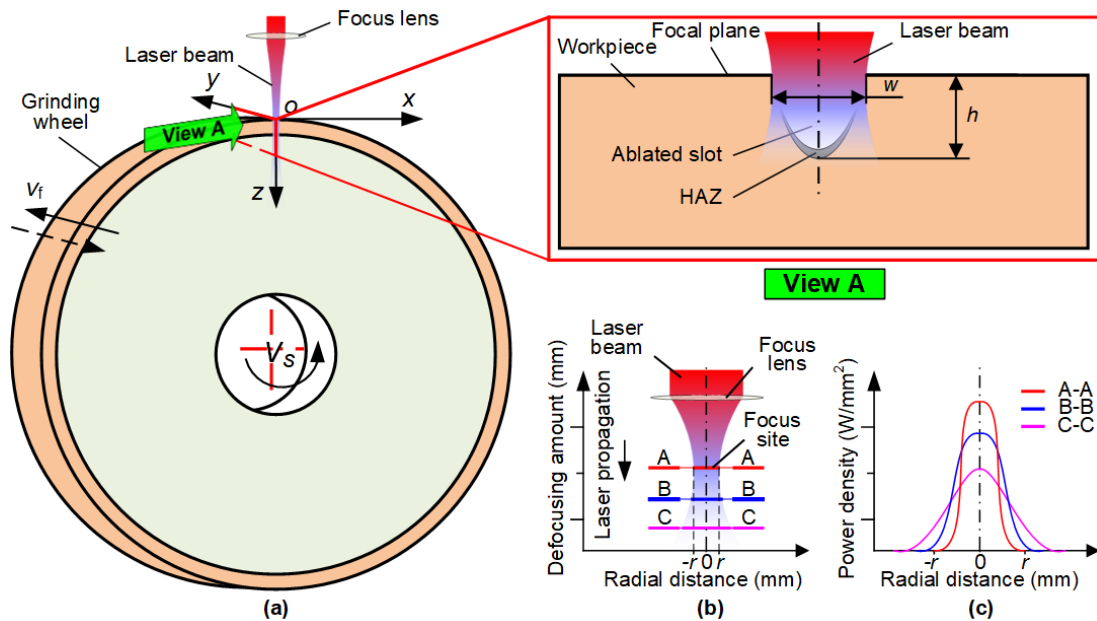


Figure 9.1 The ablation process. (a) Ablation process diagram and the character of the ablated slot (View A); (b) general shape of a focused laser beam; (c) energy distribution at a certain cross-section along the laser propagation direction [276].

9.2.2 Parallel Overlap

Given that various energy fluences over the ablation threshold of the target material can be obtained by controlling the overlap ratio of the laser spot, various ablation behaviours could happen in the process with the overlap ratio changing [277, 278]. When there is no overlap (see the definition in **Figure 9.2a**) in the ablation process, each laser spot is independent as little heat will be accumulated and no base shape discrepancy between the two adjacent spots (see case 1 in **Figure 9.2a**). When the overlap is introduced (see case

2 in **Figure 9.2a**), both the heat accumulation and base shape discrepancy start to affect the ablated topography. With the overlap ratio and ablation time increasing, the material removal behaviour tends to be more seriously affected, and larger HAZ and deeper ablation depth have been found in previous studies [7, 278]. However, the ablated topographies in the stable stage are kept the same (see **Figure 9.2e**) under a certain overlap ratio as the heat accumulation has a balance point.

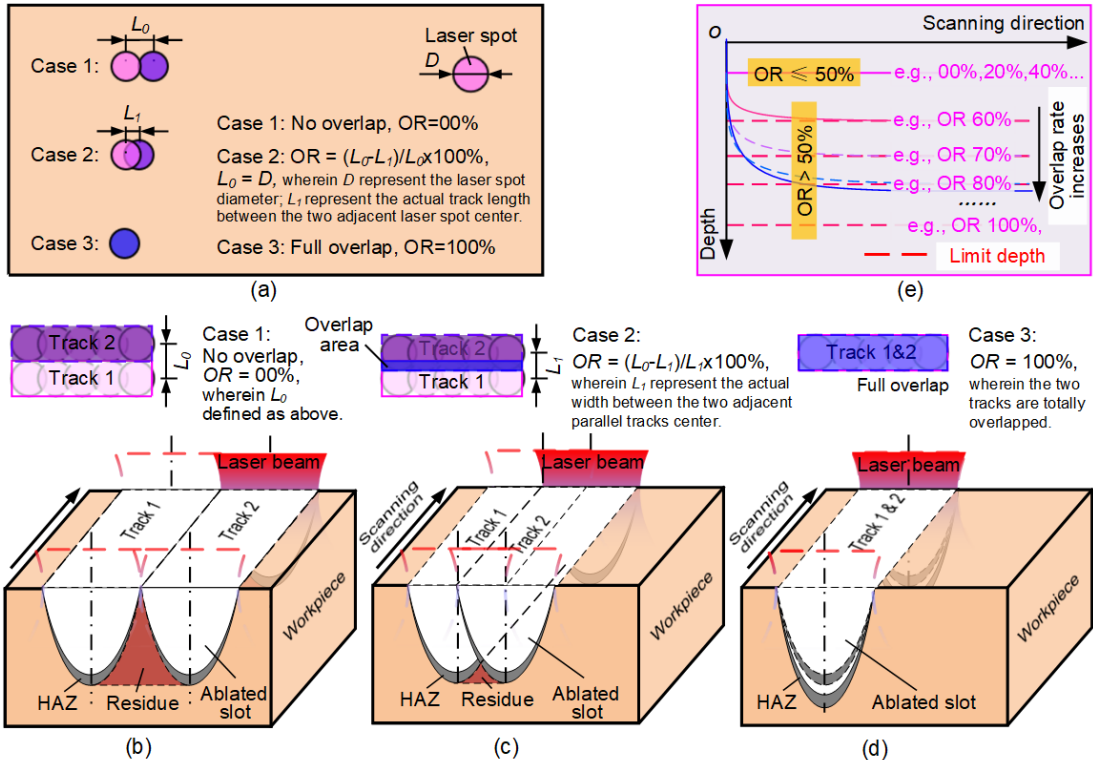


Figure 9.2 Definition of overlap ablation. (a) The overlap ratio definition in single pass ablation; (b), (c) and (d) in multi-pass parallel overlap ablation; (e) the diagram of ablation depths change tends with ORs change (see Figure 9.3 and Figure 9.4).

In the parallel overlap ablation (or line overlap [279]), the laser ablation process is performed along with the previous ablated slot. The overlap ratio in different cases is defined in **Figure 9.2 b, c&d**. As no parallel overlap happen when the distance between the adjacent tracks is over the spot diameter, the ablation

track intervals between the two slots are normally equal to or smaller than the diameter of the spot. By the methodology of analogy, it can be found that the parallel overlap ablation is an extension of single-pass overlap ablation from an array to a matrix. Differently, as heat generated in track one usually has little effect on track 2, most of the heat-related issues (including the incubation effect [280]) rarely happen in parallel overlap ablation. Therefore, the topography in parallel overlap ablation is little affected by the heat accumulation but is close affected by the base shape and overlap ratio of two laser tracks.

Based on the theoretical analysis above, here further predicted the topographies of five parallel overlap passes (the ablated slots do not change much after five passes, see **Figure 9.3**) under various cases from OR 00% to OR 100% with an interval of 20%, as showing below.

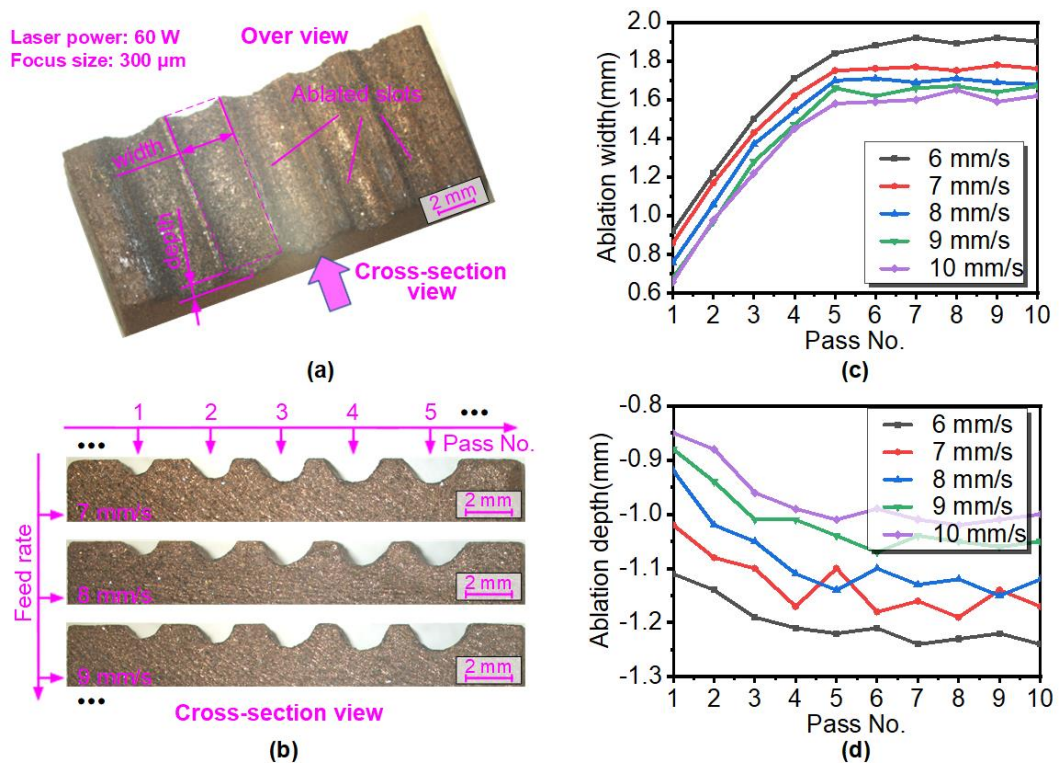


Figure 9.3 Ablation results after multiple passes. (a) and (b) the physical model of

the ablated samples; (c) and (d) The ablation width and depth changes with feed rate and pass number under laser power 60 W.

(1) When the OR is lower or equal to 50%, like in the case of OR 00% (see **Figure 9.4a**), as no overlap happened between the two adjacent tracks, the two tracks have little effect on each other. Hence, the superposition of the two tracks will not cause ablation depth changes. For the case OR 20% (see **Figure 9.4b**) and the case OR 40% (see **Figure 9.4c**), although a certain amount of overlap has occurred, the power density in the bottom of the slot is low due to defocusing effect (especially off the centre of the laser beam), which indicates the ablation depth of the superposed two tracks will not be dramatically changed. Thus, the ablation depth is not likely to change significantly when the OR is less than 50%.

(2) When the OR exceed 50%, the ablation process starts to slightly increase the ablation depth (see **Figure 9.4d** to **Figure 9.4f**) due to (i) the relative higher power density in the current beam centre being close to the previous ablated slot bottom, (ii) the previous ablated slot enables the current laser beam directly reach to the bottom of the slot. Finally, when the OR increases to 100% (two tracks are fully overlapped), the residues between the two tracks disappear (see **Figure 9.4f**). Meanwhile, the final ablated depth of the fully overlapped ablation will not be equal to the sum of the independent ablation depths since the power density in the section changes along the laser beam propagation direction.

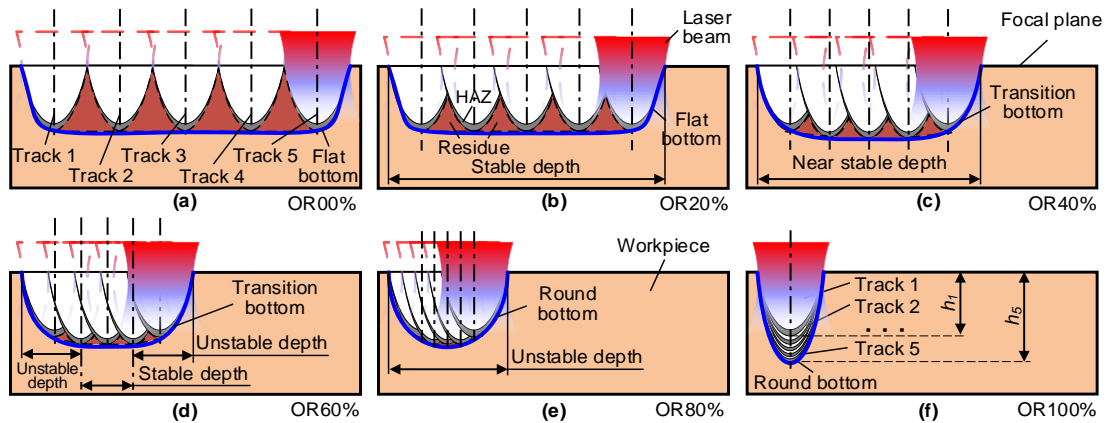


Figure 9.4 Diagram of parallel overlap ablation. (a) No overlap (OR 00%); (b) less than half overlap (OR 20%); (c) less than half overlap (40%); (d) over than half overlap (60%); (e) over than half overlap (80%); (f) total overlap (100%).

Theoretically, with the overlap rate (OR) increase (track intervals decrease), the ablation residue is reduced from the highest level at OR 00% to the lowest at OR 100%. Actually, when taking into consideration the size effect, heat accumulation, and heat impact, the ablation residues between the tracks are hard to be detected. Three major reasons may account for the issue, (i) the residual between the two tracks usually has a small volume and a big heat convection surface area, the size effect makes these small structures easily to be heated, (ii) the heat accumulation process is easier to happen in the bottom of the ablation, which furthermore heated these small structures, and (iii) these small structures are also can be damaged by the intensively transient heat impact. The disappearing of the ablation residues would likely interest the ablation results that a flat, transition and round bottom can be obtained by employing the ORs that are much smaller than 50% (see **Figure 9.4a** and **Figure 9.4b**), near around 50% (see **Figure 9.4c** and **Figure 9.4d**), and much bigger than 50% (see **Figure 9.4e** and **Figure 9.4f**), respectively.

In conclusion, due to the nature of laser beam energy distribution, the ablated topography types are very limited for a single track, especially the bottom shapes. However, as both the nature of the laser beam energy distribution and the laser parallel overlap rate would have a crucial effect on the ablated profile (the dominant effect of overlap ablation can be changed by controlling the ORs), the ablated topography (including the width, depth, and shape) can be largely extended by overlap ablation. With this, it is clear that some general applications regarding non-flat grinding wheels (e.g., the stepped/free-form surface) can be obtained by selecting the appropriate ORs.

9.3 Experimental Strategy

The layout of the experimental system is shown in **Figure 9.5a**, which involves a laser machine (including laser control PC and laser machine body), a positioning system (including motion body and motion controller), and a laser distance sensor (including laser distance sensor and PC). The specific parameters of the laser (LE900, Hongfan Tech. Company) are shown in **Table 3.1**. The linear and circular motions and positions for the ablation process were accurately controlled by the specially-made positioning system (see **View A** in **Figure 9.5a**), which has the translational and rotational motion accuracies of 1 μm and 0.009 deg based on the G-code-based NC system. The translational and rotational motion speeds were separately within the ranges of 0~1,500 mm/s and 0~1,800 deg/s. The radial runout error of the grinding wheel is precisely detected by the laser distance sensor and manual-adjusted till the maximum runout error is within 0.01 mm. The details of the grinding wheels (D125N75B771/8, 3M Company) used in the trials are shown in **Table 3.3**.

A commercial red semiconductor laser distance sensor (MSE-TS803-60/10, Moduloc System Engineering Ltd.) is used in this study (see more details in **Table 9.1**).

Table 9.1 Details of the laser distance sensor.

Range (mm)	Linearity (F.S)	Resolution (F.S)	Temperature drift (F.S /°C)	Frequency (Hz)
10	±0.05%	0.01%	0.02%	Max. 9400

As this paper aims to study the effects of ORs on the ablated depth under various feed rates, wide ranges of both the OR and feed rate were employed. To make the results comparable, all the trials using six different levels of ORs and six levels of laser feed rates were performed on one diamond wheel surface in the air atmosphere. As shown in **Figure 9.5b**, the whole wheel was equally divided into six segments (see sample A to F) along with the wheel circumferential direction, and in each sample, there were six ablated tracks along the wheel axis direction (OR 00% - OR 100% with an interval of 20%). The laser feed rate was incrementally increased from segment A (5.0 mm/s) to F (10.0 mm/s), while the track OR was incrementally increased from the OR 00% to OR 100%, and there are five parallel passes for each OR (see **View B** and **View C** in **Figure 9.5b**). The used parameters are given in **Table 9.2**.

Table 9.2 Employed laser parameters in the trials.

Trial No.	ORs(%)	Feed rate (mm/s)	Seg. No.	Trial No.	ORs(%)	Feed rate (mm/s)	Seg. No.
1-6	100,80,	5.0	A	19-24	100,80,	8.0	D
7-12	60,40,	6.0	B	25-30	60,40,	9.0	E
13-18	20,00	7.0	C	31-36	20,00	10.0	F

After the laser ablation process, the diamond grinding wheel was firstly cut into six samples (A-F) by the wire-EDM machine (MV2400S, Mitsubishi Electric Company), and the two cross-sections of each sample were carefully polished by the polisher (Yuzhou Company) with alumina sizes of #320 (1 hour), #600 (1 hour) and #1,200 (2 hours). After that, each sample was cleaned with a hairbrush and ultrasonic distilled water bath for 1 hour and then air-dried at room temperature. Then the optical microscopy (NSZ-810, NOVEL OPTICS) was performed to observe and measure the ablated slots (see **Figure 9.5c**), where the ablated top width (W), the bottom depth (H), and the topography are recorded. Then the second-order regression prediction model is established based on the ablated top width and bottom depth. Besides, the topography was fitted by the nine key points on the observed cross-section profiles based on super-Gaussian and polynomial functions. The nine key points include one deepest valley point (where the depth was h , see the Point P5), two endpoints (see the Point P1 and P9), and six intersecting points between the cross-section profile and the horizontal lines having a depth of 20%, 60% and 90% of h (see the Point P2 - P4 and P6 - P8). The top width and bottom depth are separately defined as the distance of the two endpoints (P1 and P9) and the vertical distance of the endpoint (P1 or P9) to the deepest valley point P5 see **View D in Figure 9.5c**.

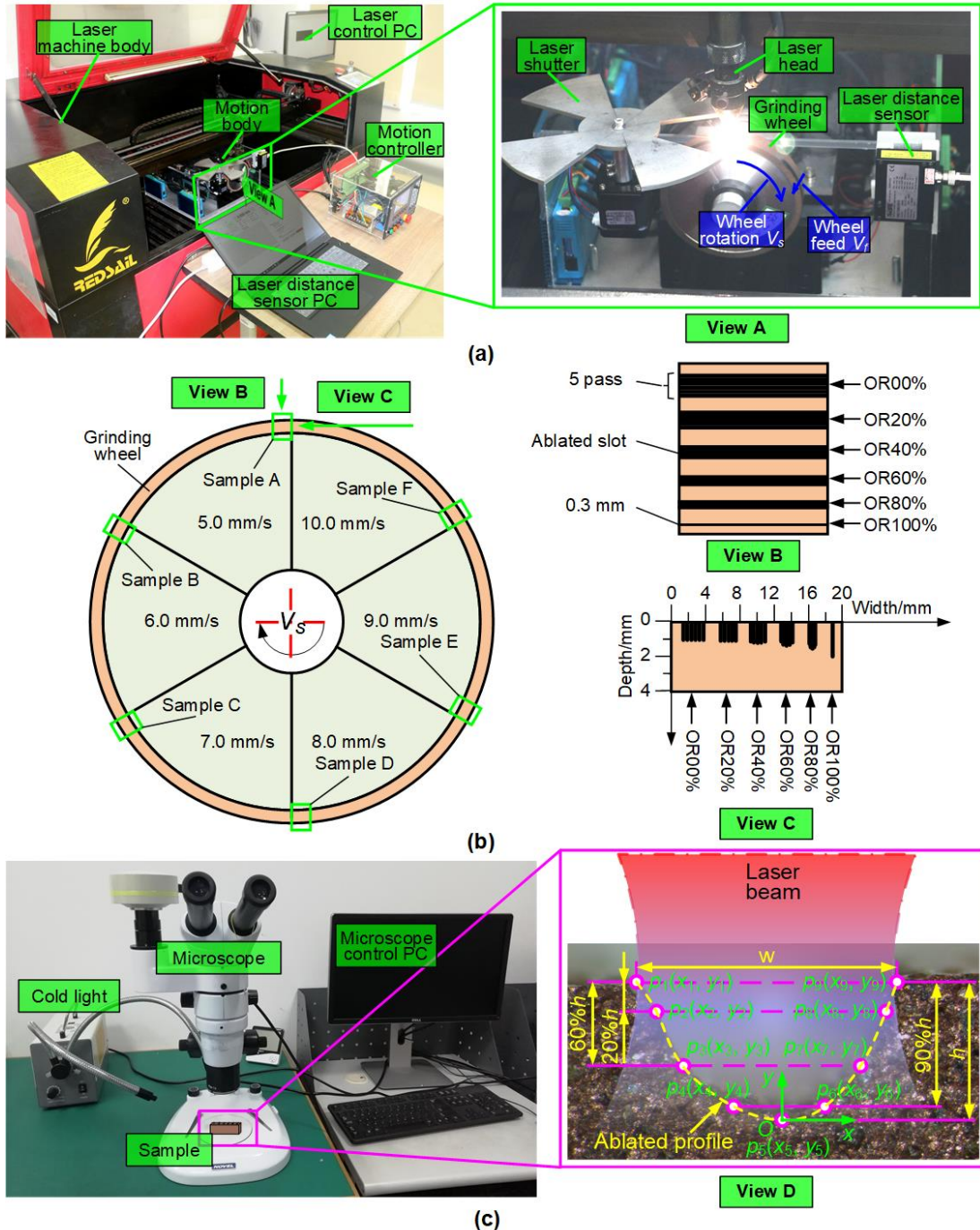


Figure 9.5 Experiment methodology. (a) Experimental setup including the laser machine (left) and the specially-designed positioning system (right); (b) the ablation strategy where the wheel was equally divided into six segments (A-F) and in each segment there were six ablated tracks along the wheel axis direction (OR 00% - OR 100% with an interval of 20%, where OR refers to Overlap Rate). The laser feed rate was incrementally increased from segment A (5 mm/s) to F (10 mm/s), while the tracks OR was incrementally increased from the OR 00% to OR 100% and there are five parallel passes for each OR; (c) the measurement system for the ablated slots,

and the nine key points that the ablated width (W), depth (H) and topography are based on being recorded.

9.4 Experimental Results and Analysis

The detailed ablation results (for 60 W laser power) with duty cycle and feed rate change are recorded and analysed, where the Overlap Rate (OR) changes from 00% to 100% with an interval of 20% and Feed Rate changes from 5.00 mm/s to 10.00 mm/s with an interval of 1.00 mm/s. Both the data for ablated top width (TW) and bottom depth (BD) have been collected, and the ablated topography is analysed as well. Based on the data, the ablation law regarding TW and BD change with overlap rate and feed rate is achieved, and then the corresponding empirical prediction model is established.

9.4.1 Effect of Feed Rates and Overlap Rates on the Ablated Topography

As expected, nearly no residuals can be found in the whole cases of the experimental process thanks to the strong laser heat that destroyed the micro-structures between the two passes. Besides, the feed rates seem to change little of the ablated bottom shape, but they narrow the ablation width and shallow the ablation depth with the feed rates increase under certain OR (see feed rate 5.0 mm/s in **Figure 9.6a** to feed rate 10.0 mm/s in **Figure 9.6f**). This phenomenon may account that the feed rate changes the energy intensity on the whole, but the energy distribution state in the laser beam cross-section is kept unchanged, which is determined by the nature of the laser beam. As the laser energy distribution in a certain laser beam cross-section does not change, the ablated profile will not change as well. However, due to the whole energy

intensity becoming weak, both the ablation width and depth were reduced.

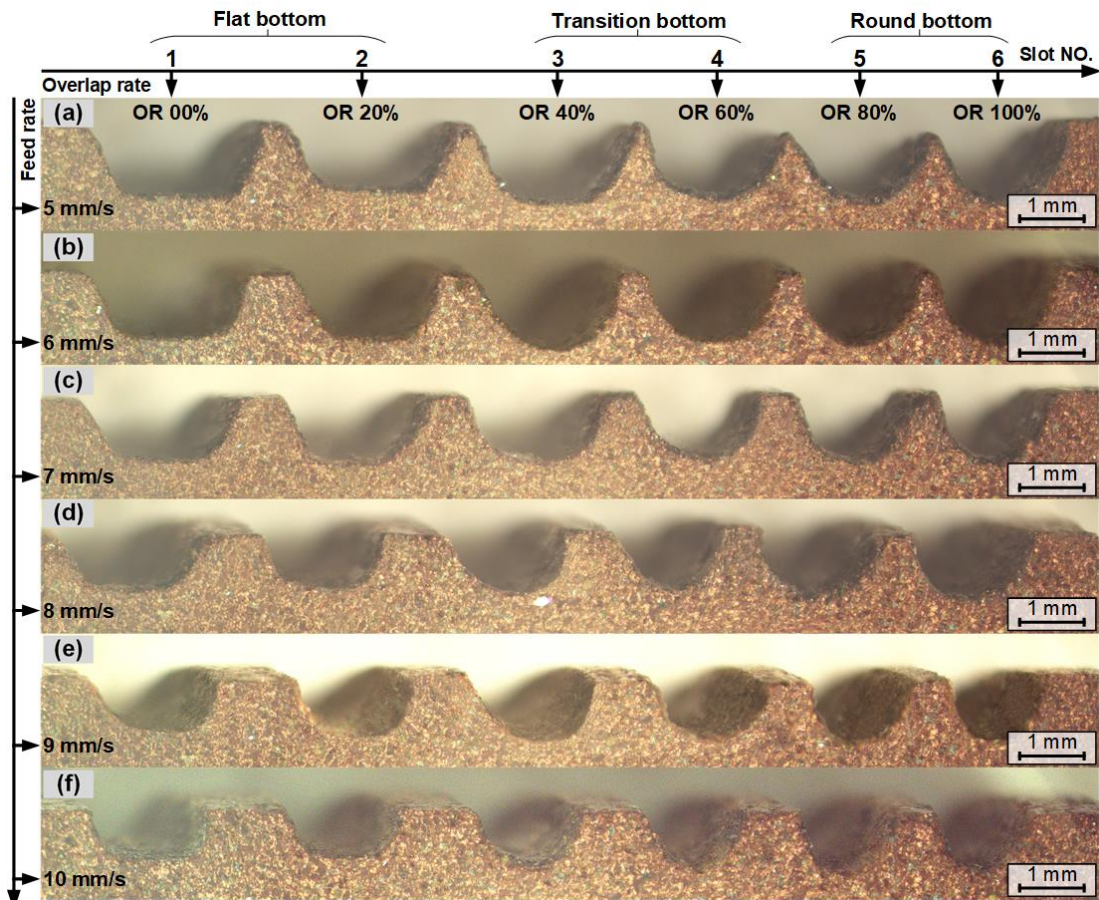


Figure 9.6 Influence on the ablated topography under varying feed rates and overlap rates. (a)-(f) refer to feed rate of 5.0 mm/s, 6.0 mm/s, 7.0 mm/s, 8.0 mm/s, 9.0 mm/s, 10.0 mm/s, respectively. Slot No. 1-No. 6 refer to the overlap rate from 00% to 100% with an interval of 20%, where OR 00% and OR 20% showed a flat bottom, OR 40% and OR 60% showed a transition bottom, and OR 80% and OR 100% showed a round bottom.

Interestingly, the topography of the ablated slot bottom changes with the OR under the whole used feed rates, from flat bottom, via transition bottom, to round bottom (see slot 1 to slot 6 in **Figure 9.6**). To be specific, when the OR is far less than 50%, the bottom of the slots tend to be flat, while they tend to be round when the OR is far over 50%, and they tend to be transition bottom when the OR is near 50%. This is likely due to the dominating effect of overlap

that when the neighbouring two laser passes are far (say far less than 50%), the current laser pass has little effect on the previous one. As a result, each pass's ablation process is relatively independent, and the removal depth is the same. With the OR becoming large, the neighbouring two passes become close, especially the intensive energy distributed in the laser beam centre overlapped, the ablation depth will change dramatically as the laser beam in the current pass will reach the bottom directly since the previous pass has removed part of the materials.

9.4.2 Effect of Overlap Rate Changes on the Ablation Law under Different Feed Rates

Figure 9.7a shows that the ablation width decreases with the ORs increase under all the feed rates. However, the overlap rate affects ablation width in a different way under various feed rates. The ablation width has a wide variation range under lower feed rates. The ablation width decreased 1.06 mm (from 2.86 mm to 1.80 mm) for 5.0 mm/s when the OR changed from 00% to 100%, while the data for 10.0 mm/s only decreased 0.35 mm (from 2.00 mm to 1.65 mm). There is no doubt that the ablation width decreased with the ORs increase as the reduced parallel track intervals make the effective sum width of the tracks narrow. Due to more heat would be accumulated at a low feed rate that enlarges the heat affect zone, which would further extend the ablation width. Thus, it makes the variation range larger in the low feed rate than that in the high.

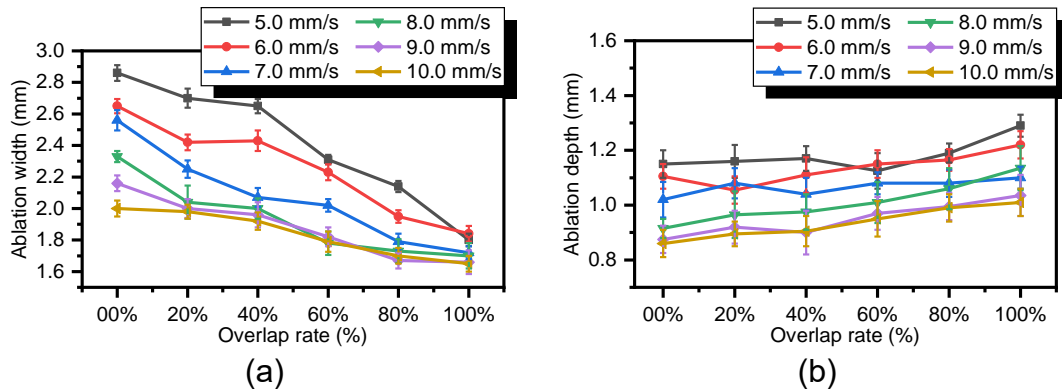


Figure 9.7 Influence of overlap rate changes on the ablation law under different feed rates. (a) The effect of overlap rate on ablation width; (b) the effect of overlap rate on ablation depth.

As the figure for ablation depth, **Figure 9.7b** shows it overall has a climbing tendency with the overlap rate increased at any feed rates, and deeper ablation depth can be achieved under a lower feed rate as expected. Surprisingly, the overlap rate seems to affect equally the ablation depth (A 0.15 mm average fluctuation is found for each feed rate). Interestingly, the ablation depth is kept almost unchanged when the overlap rate is lower than 50%, and when the overlap rate is over 50%, the ablation depth begins to grow obviously. It is not hard to understand the phenomenon, as the two adjacent tracks have little effect on each other when the overlap rate is low. With the overlap rate increase, the mutual effect between the two adjacent tracks becomes intensive, which causes the ablation depth to begin to change dramatically. However, for the limited ablation depth change, it is likely due to the dual role of the defocusing effect of the laser beam that is determined by its nature and the narrowed ablation slot caused by the increased overlap rate.

9.4.3 Effect of Feed Rate Changes on the Ablation Law under Different Overlap Rates

Figure 9.8a shows that the ablation width decreases with the feed rates increase under all the ORs. To be different, the feed rate effect ablation width more violently under a lower overlap rate that a maximum fluctuation of 0.86 mm is found for OR 00% when the feed rate changes from 5 mm/s to 10 mm/s, while the figure for OR 100% only decreased 0.15 mm from 1.80 mm to 1.65 mm, which almost keep unchanged. Undoubtedly, as the heat-affected zone will be decreased with the feed rate increase due to less heat will be accumulated in the ablated area. Meanwhile, with the overlap rate increase, the effect scope gets narrow. Hence the feed rate negatively correlates to the ablation width, and a moderate fluctuation range appears in a higher overlap rate.

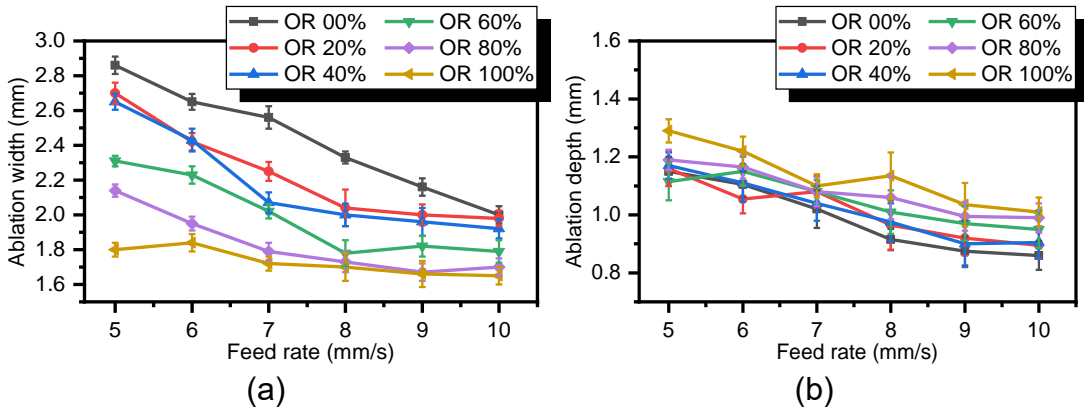


Figure 9.8 Influence of feed rate changes on the ablation law under different overlap rates. (a) The effect of feed rate on ablation width; (b) the effect of feed rate on ablation depth.

Figure 9.8b shows the whole trend of ablation depth reduced slightly with the feed rate growing under the trialled ORs, and higher ablation depth appears in low feed rate with high OR (a maximum drop of 0.3 mm is found in feed rate 5

mm/s with OR 100%). Interestingly, the feed rate seems to affect the ablation depth under the trailed ORs almost equally. To be specific, the average drop for all trails is 0.24 mm with a maximum variation of 0.06 mm. It is easy to be understood that the ablation depth is reduced with the feed rate increase, as the increased feed rate reduces the laser energy fluence, which is crucial to the ablation process. As for the effect of feed rate work on the ablation depth, it is likely due to the feed rate changed laser energy fluence, which has a similar impact on the ablation cases with various ORs. Meanwhile, the defocusing effect of the laser beam that determined by its nature and the narrowed ablation slot caused by the increased overlap rate. As a result, the ablation depth drops at a similar trend with the feed rate increases under the trailed ORs, and the ablation depth appears deeper in a low feed rate with a high OR.

In short, the experimental results are consistent with the theoretical analysis. The profiles of the ablated topography are close related to the OR. By controlling the OR changes from 00% to 100%, the bottom shape of the slots can be changed from flat to round. Meanwhile, the feed rate changes little of the profile, but both the ablation width and depth are reduced with the feed rate increase. With the law, the possibility of generating desired stepped and curved surfaces by selecting the proper processing parameters can be validated.

9.5 Establishment of Empirical Prediction Model

As the ablated results are determined by the overlap rate and feed rate in this study, a second-order regression equation is employed to establish the

prediction model. The effectiveness of this model in solving practical problems has been proved in the previous study, which has shown a pleasant result [248]. The standard form of a second-order regression prediction model of two interaction factors is given by **Equation (9.1)**

$$f(x_1, x_2) = \varepsilon + \beta_1 x_1 + \beta_2 x_2 + \beta_{12} x_1 x_2 + \beta_{11} x_1^2 + \beta_{22} x_2^2 \quad (9.1)$$

where x_1 is the overlap rate (%), and x_2 is the feed rate (mm/s).

9.5.1 Prediction Model for Ablated Width and Depth

By fitting the data with the second-order regression prediction model, the ablation width changes with overlap rate and feed rate are expressed as **Equation (9.2)**

$$f_1(x_1, x_2) = 4.739 - 1.666e^{-2}x_1 - 4.578e^{-1}x_2 + 5.357e^{-6}x_1^2 + 1.223e^{-3}x_1x_2 + 1.875e^{-2}x_2^2 \quad (9.2)$$

where x_1 represents the overlap rate (%), x_2 represents the feed rate (mm/s), and $f_1(x_1, x_2)$ represents the ablation width (mm).

Figure 9.9a shows the overview prediction result of ablation width changes with overlap rate and feed rate, which indicates the ablation width decreases with both the overlap rate and feed rate increase. **Figure 9.9 b&c** show the side view of overlap rate and feed rate influence on the ablation width, respectively. They show the overlap rate linearly affect the ablation width while the feed rate non-linearly affects the ablation width.

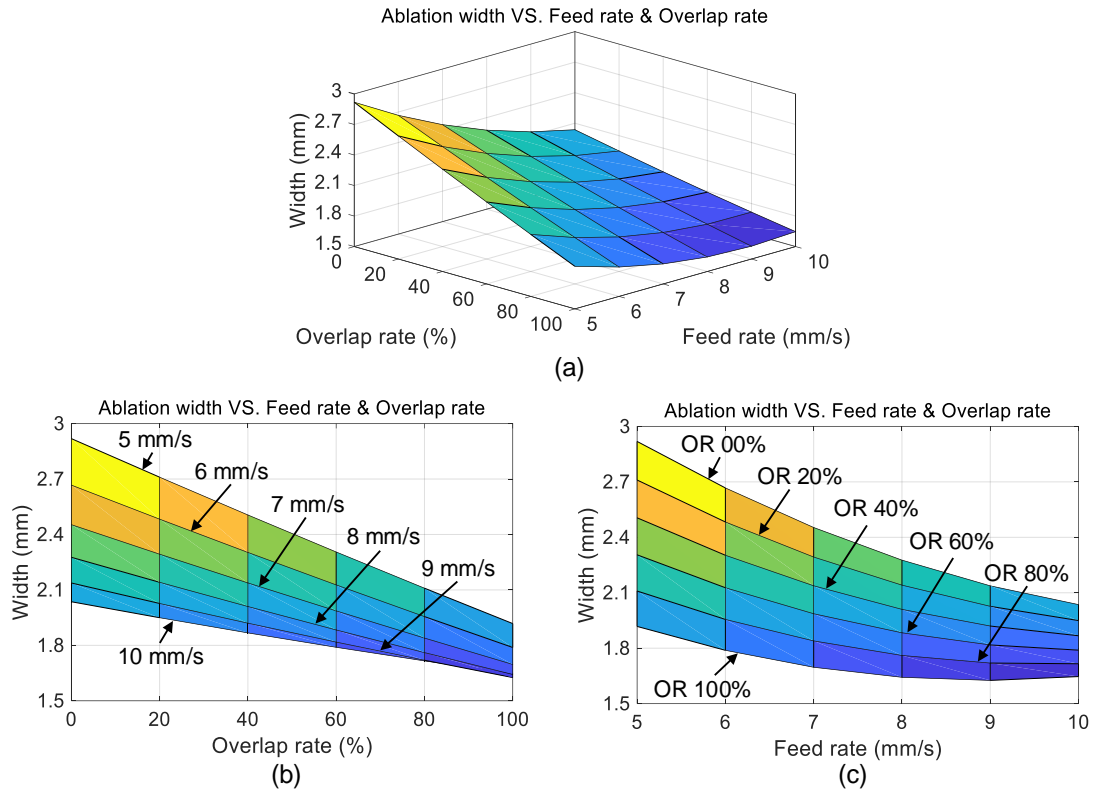


Figure 9.9 Ablation width changes with overlap rate and feed rate. (a) The overview of the prediction result; (b) the influence of overlap rate on ablation width; (c) the influence of feed rate on ablation width.

By using the same fitting method, the second-order regression prediction model regarding the ablation depth changes with overlap rate and feed rate is expressed as **Equation (9.3)**

$$f_2(x_1, x_2) = 1.605 - 8.652e^{-4}x_1 - 1.055e^{-1}x_2 + 1.213e^{-5}x_1^2 + 1.343e^{-4}x_1x_2 + 3.065e^{-3}x_2^2 \quad (9.3)$$

where x_1 represents the overlap rate (%), x_2 represents the feed rate (mm/s), and $f_2(x_1, x_2)$ represents the ablation depth (mm).

Figure 9.10a shows the overview prediction result of ablation depth changes with overlap rate and feed rate, which indicate the ablation depth reduces with the feed rate increase and the decrease of overlap rate. **Figure 9.10 b&c** show the side view of overlap rate and feed rate influence on the ablation depth, respectively. They indicate that both the overlap rate and feed rate non-linearly

affect the ablation depth, and the ablation depth has a larger fluctuation range under a given overlap rate than that under a given feed rate.

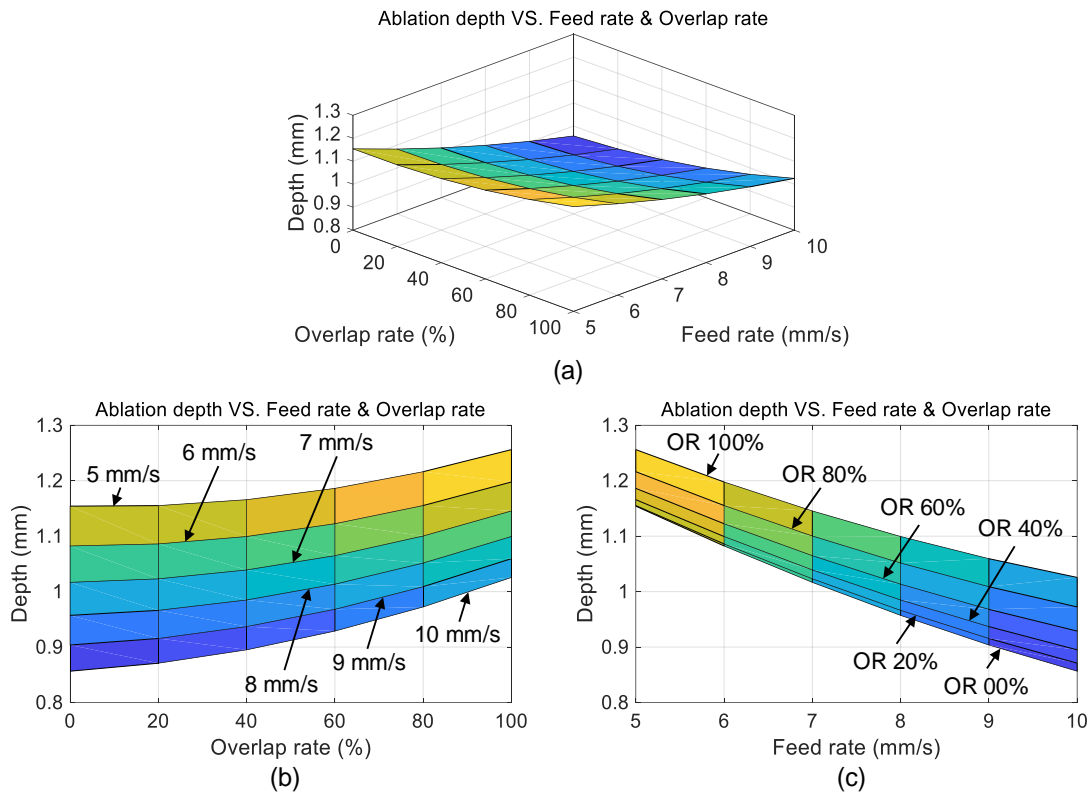


Figure 9.10 Ablation depth changes with overlap rate and feed rate. (a) The overview of the prediction result; (b) the influence of overlap rate on ablation depth; (c) the influence of feed rate on ablation depth.

The goodness of fit of the two empirical prediction models is evaluated as shown in **Table 9.3**. It shows the Sum of Squares due to Error (SSE) and the Root Mean Squared Error (RMSE) tend to be zero. Both the two prediction models' confidence level is over 95%, and the Coefficient of determination (R-square) for the two models is 0.9693 and 0.9411, respectively. These signs indicate the predicted results are credible and desirable.

Table 9.3 Goodness of fit for the prediction models.

No.	Prediction Models	SSE	RMSE	R-square	Confidence level
1	$f_1(x_1, x_2)$	0.1168	0.0624	0.9693	> 95%
2	$f_2(x_1, x_2)$	0.02373	0.02812	0.9411	> 95%

9.5.2 Prediction Model for Ablated Topography

Figure 9.11 shows the fitted profile of each ablated topography with 95% confidence bounds, where Figure 9.11a - Figure 9.11d are fitted by the Super Gauss formula as their bottom tends to be flat, Figure 9.11e is fitted by unary quartic polynomial due to the round bottom and the slight asymmetry profile, and Figure 9.11f is fitted with quadratic polynomial for its round bottom and symmetry profile.

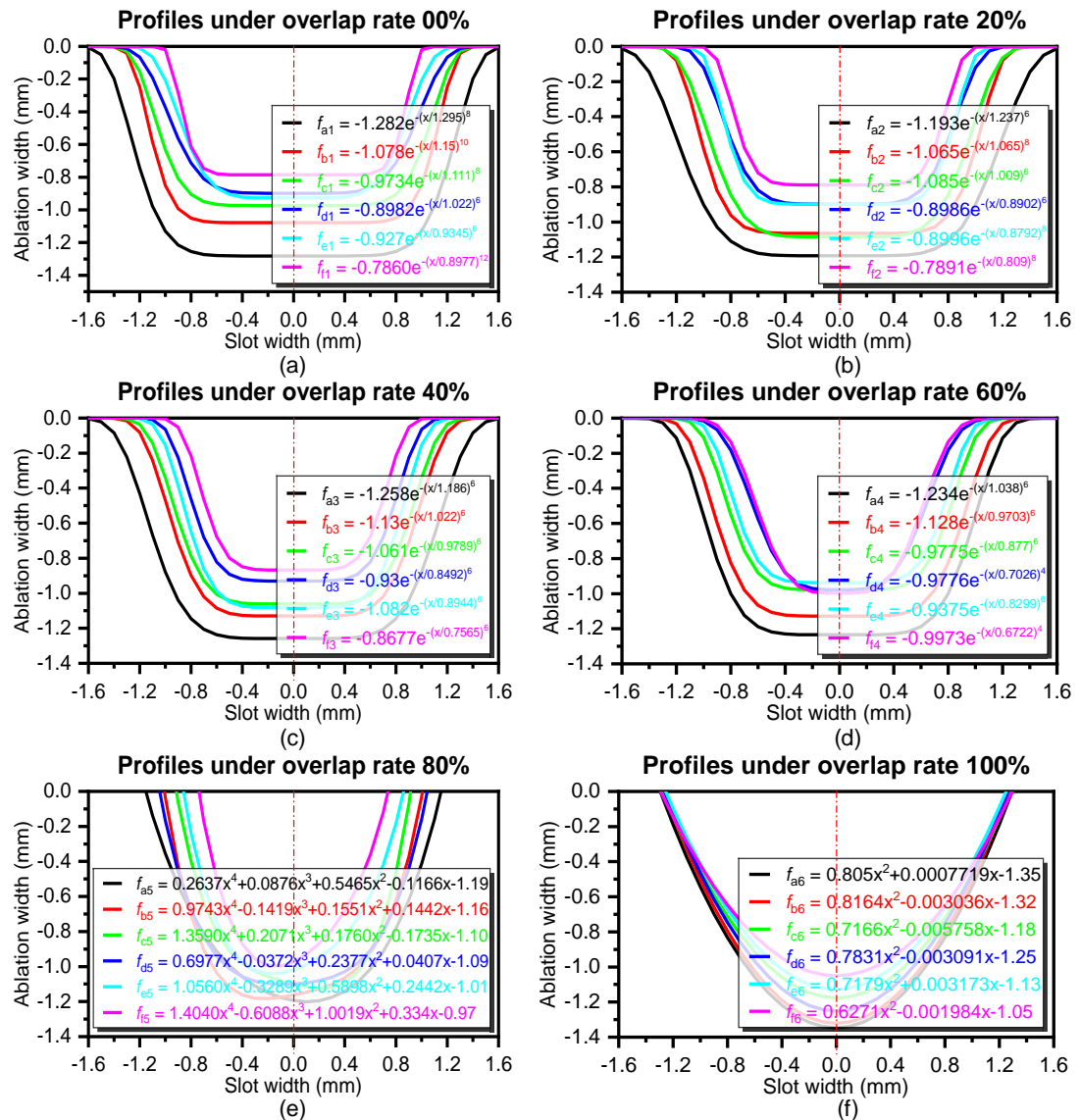


Figure 9.11 The fitted profile of the ablated topography with 95% confidence bounds. (a), (b) flat bottoms generated by overlap rates 00% and 20% (fitted by

Super Gauss Formula); (c), (d) transition bottoms generated by overlap rates 40% and 60% (fitted by Super Gauss formula); (e), (f) round bottoms generated by overlap rates 80% and 100% (fitted by Polynomial). Wherein, the alphabetic subscript (a-f) and numeric subscript (1-6) in the fitting functions (f_{xx}) represent feed rates (5.0 mm/s - 10.0 mm/s, increased by 1.0 mm/s) and ORs (00% - 100%, increased by 20%), respectively.

With the overlap increases, it shows that the whole ablation widths become narrow, and the ablation depths become deep. Meanwhile, the bottom shapes gradually change from flat to round. As expected, these fundamental characteristic trends are consistent with the experimental results. To further understand the correctness of the prediction model, the goodness of fit for each profile is also analysed, as shown in **Figure 9.12**. Despite there being also some worst situations where the R-square results are lower than 90%, these figures all show the acceptance of the prediction model. To be specific, the maximum SSE and RMSE are 0.142 (see **Figure 9.12a**) and 0.154 (see **Figure 9.12b**), respectively. Meanwhile, the R-square in most of the cases are over 96% (see **Figure 9.12c**), even in the worst situation, the lowest R-square result is 89% (located in OR 40% in **Figure 9.12c**). Actually, the worst predictions are all distributed in the process situation OR 40% and OR 60%, e.g. 89%, 91% shown in process situation OR 40%, and 94%, 95% shown in process situation OR 60%, this is likely due to the sake of irregular transition bottom shape caused the poor fit of the prediction results.

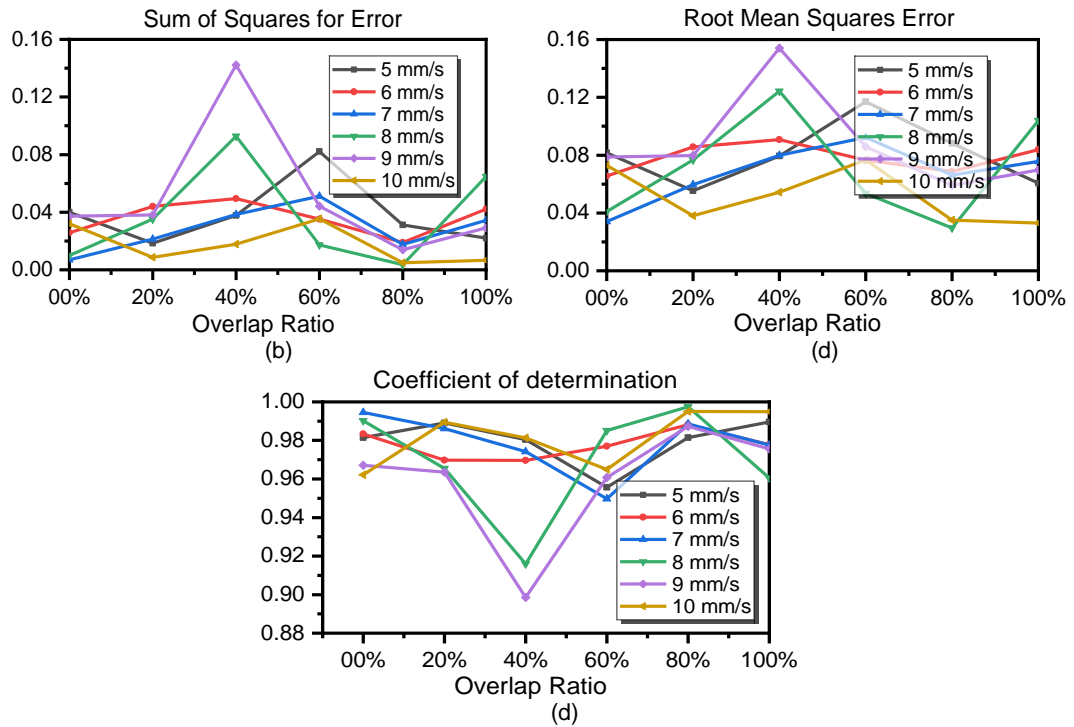


Figure 9.12 Goodness of the fitted profiles. (a)-(c) the Sum of Squares for Error (SSE), Root Mean Square Error (RMSE), and Coefficient of Determination (R-square) changes for each feed rate under various overlap rates, respectively.

9.6 Applications

Based on the research results, an attempt to manufacture two kinds of high-resolution non-flat surfaces (multi-steps and free forms) by controlling the overlap rate and feed rate is demonstrated, which is the usage of the knowledge above to select proper ablation parameters for the generation of the desired profile.

The ablation strategies can be explained in **Figure 9.13**, where the laser power of 60 W is employed throughout the experiments, the Focal plane (FP), overlap rate and feed rate are taken as the variables to achieve a wide range of ablation topography. Wherein the overlap rate and feed rate are respectively controlled by axial moving speed and rotational speed of the grinding wheel manipulated by a precision positioning system, while other ablation

parameters are kept unchanged. According to the designed profile, a series of processing parameters is carefully selected for each feature based on the predictive models.

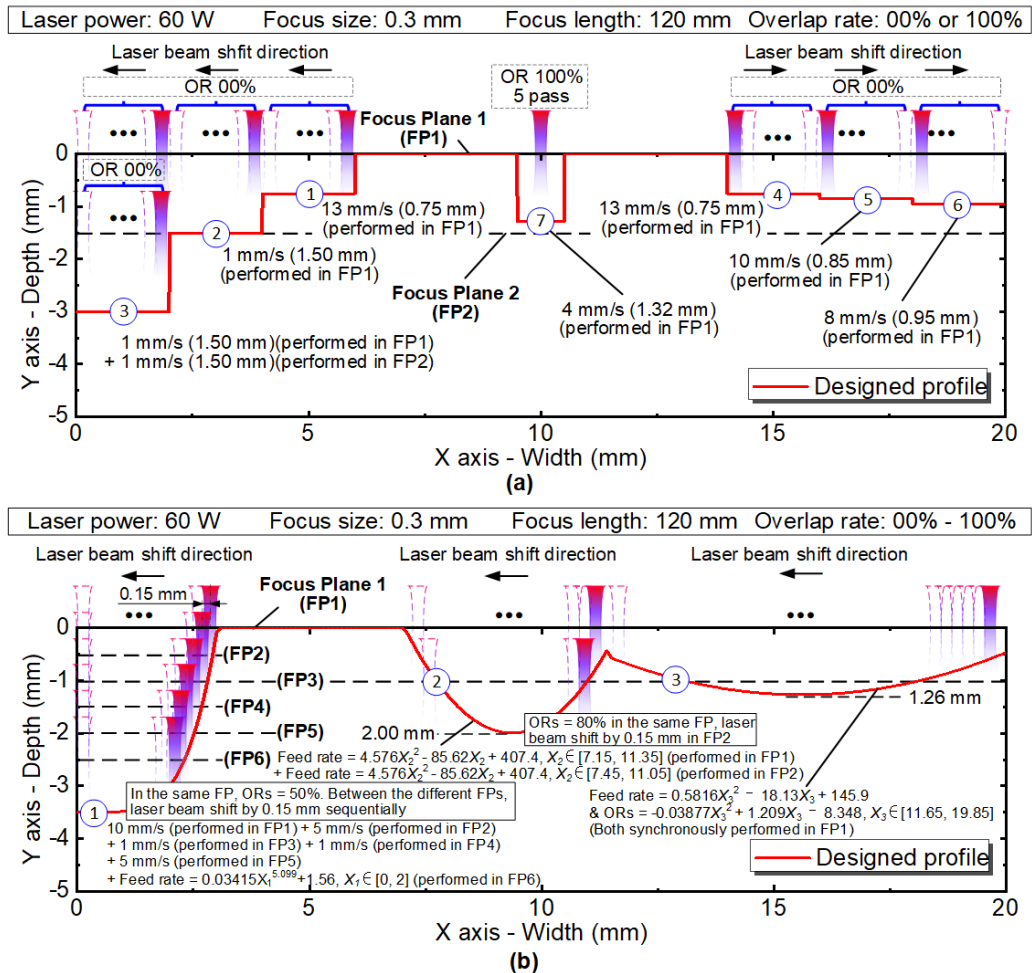


Figure 9.13 Planned ablation strategies for designed non-flat grinding wheels. (a) Strategies on multi-steps wheel featured with large-span macro-steps (steps tagged with No. 1, 2 and 3), deep-narrow slot (slot tagged with No. 7) and high-resolution micro-steps (steps tagged with No. 4, 5 and 6); (b) curved-surfaces wheel featured with exponential (surfaces tagged with No. 1), parabolic (surfaces tagged with No. 2) and arcuate (surfaces tagged with No. 3) generatrix.

To be specific, **Figure 9.13a** shows the details of strategies on a multi-step wheel, which featured large-span macro-steps (steps tagged with No. 1, 2 and 3), a deep-narrow slot (slot tagged with No. 7) and a high-resolution micro-steps (steps tagged with No. 4, 5 and 6). Wherein, steps tagged with No. 1 to

No. 6 are carried out under an overlap rate of 00%, while step tagged with No. 7 is carried out under an overlap rate of 100% for five repeated passes. Meanwhile, except for the step tagged with No. 3 is ablated in two different focal planes (the ablated surface in focal plane 1 is carefully cleaned before the ablation process in focal plane 2), all the other steps are ablated in focal plane 1. **Figure 9.13b** reveals the strategies on a curved-surfaces wheel featured with exponential (surface tagged with No. 1), parabolic (surface tagged with No. 2) and arcuate (surface tagged with No. 3) generatrix. Wherein, exponential generatrix (surface tagged with No. 1) is generated with six times FP change. In the first 5 FPs, an overlap rate of 50% (the adjacent two passes will not cause the ablation depth to increase dramatically) is employed in the same FP and the laser beam shift by 0.15 mm (the radius of the focus spot) sequentially between the FPs to adjust the positions and focal planes. Additionally, several fixed scanning speeds are assigned to the laser beam in different focal planes (10.0 mm/s, 5.0 mm/s, 1.0 mm/s, 1.0 mm/s, 5.0 mm/s and a function-controlled speed which is formulated according to the errors between the current and the target ablation depth, respectively). The parabolic generatrix (surface tagged with No. 2) is generated with two times FP change, and both the two FPs (FP1 and FP3) use the same ORs of 80% (the ablated profile achieved in this OR is similar to the target profile) and the same functional feed rate designed according to the target profile. Differently, the arcuate (surface tagged with No. 3) generatrix is generated in the same FP, while the feed rate and ORs are synchronously changed along the target profile to get the final ablation result (the maximum depth of this profile is

capable enough for one-time ablation forming). It is worth mentioning that the ablated surfaces are carefully cleaned with a hairbrush to minimize the effect of attachments when multiple FPs are employed. A 0.15 mm length is reserved for both the ends in each focal plane as the HAZ will remove the unwanted materials.

After the whole ablation process, the achieved grinding wheel is carefully cleaned with a hairbrush and ultrasonic distilled water bath for an hour, and a sample is taken from the wheel and polished. Then the cross-section profile of the grinding wheel sample is photographed by optical microscopy and measured by a laser distance measurement sensor, the comparisons between the measured and designed target profiles are presented in **Figure 9.14**.

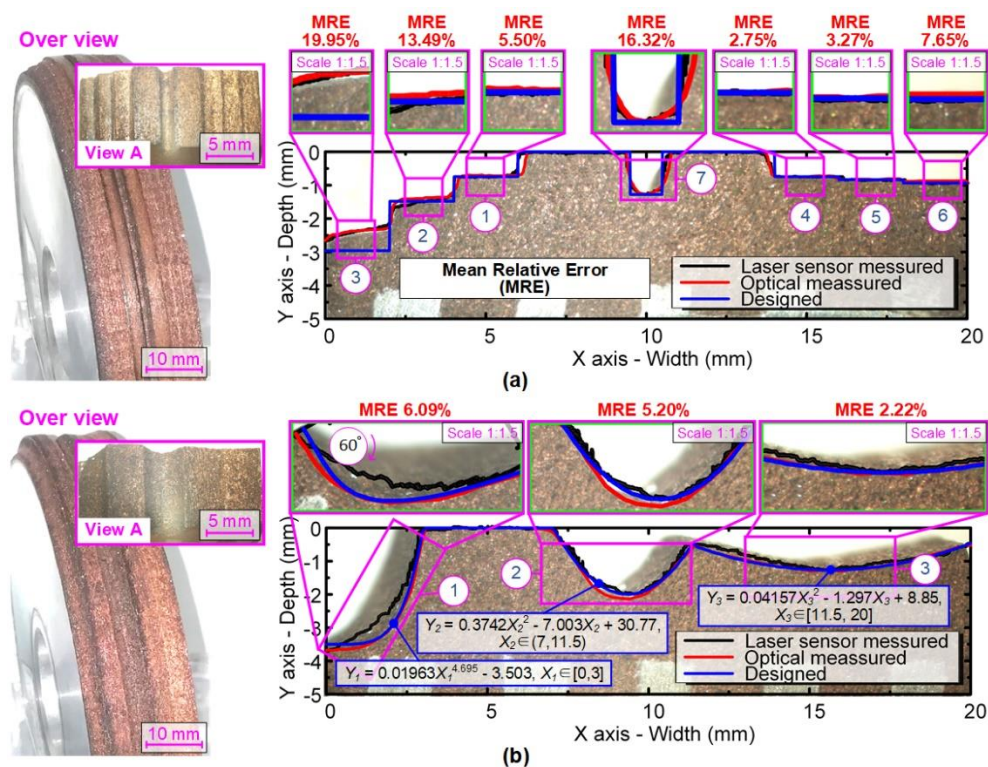


Figure 9.14 Ablation results using proposed strategies. (a) Multi-steps profile wheel featured with large-span macro-steps (steps tagged with No. 1, 2 and 3), deep-narrow slot (slot tagged with No. 7) and high-resolution micro-steps (steps tagged with

No. 4, 5 and 6); (b) curved-surfaces profile wheel featured with exponential (surfaces tagged with No. 1), parabolic (surfaces tagged with No. 2) and arcuate (surfaces tagged with No. 3) generatrix.

Figure 9.14a shows the Mean Relative Error (MRE) for the comparison of the optical measurement and designed results of the multi-step profile wheel. It shows the errors increased with steps aimed at deeper ablation depth, like step tagged with No. 3 aimed -3 mm has the error of 19.95% (the maximum error), step tagged with No. 2 aimed -1.5 mm has the error of 13.49%, while steps tagged with No. 1 and No. 4 both aimed -0.75 mm achieved the errors of 3.06% and 2.75% respectively. For these steps achieved in the same focal plane tagged with No. 1, No. 2, No. 4, No. 5 and No. 6, the errors are likely to stem from the off-focus effect of the laser beam, causing the imperfect of the prediction model. Meanwhile, the step tagged with No. 7 also suffers from the nature of the laser beam energy distribution as described in **Figure 9.1c**. For step tagged with No. 3 achieved with the adjustment of the focal plane may be suffered from both the off-focus effect and the potential graphitisation effect due to the heat effect from the previous pass that makes the target materials hard to remove.

As inspired by the ablation results from **Figure 9.14a** that the errors can be restrained when the ablation depth is shallow. Therefore, **Figure 9.14b** shows the results after adjusting the ablation strategies that performed the ablation process using multiple focal planes to control the ablation depth for each ablation step. Amazingly, the overall error for the results of the curved surfaces

is dramatically decreased, where the most significant error is 7.03% for the curved surface 1 and followed by 6.83% for the surface 2. In contrast, the results with the least error are in surface 3, with only a 2.2% error. The errors from surfaces 1 and 2 that are likely due to the adjustment of the focal plane make the laser energy easily arrive at the target materials, which causes some of the materials over removed with the laser beam multiple passes on the ablated surfaces. The pleasant result from the surface 3 could attribute to (i) the relatively small ablation depth makes it no necessary to change the focal plane, (ii) the synchronously change of both the feed rate and ORs that makes it capable of covering all the designed key points, and (iii) the relatively smooth profile makes the platform possible to response all the set processing parameters.

Overall, the measured results by both the optical microscopy and the laser distance measurement sensor showed great consistency with the proposed model (as shown in **Figure 9.14**). However, discrepancies were found between the two different measurement methodologies, especially in the measured results for surface 1 in **Figure 9.14b** - the maximum discrepancy exceeds 28%. Two reasons may account for the discrepancies: (i) the profile boundaries can be easily recognised by the optical method, but as some deteriorated material is still attached to the matrix, they cannot be distinguished by the laser measurement sensor. Therefore, the measurement accuracy for the laser distance measurement sensor is closely related to the

quality of cleaning applied to the HAZ; (ii) the surface tagged with No. 1 in **Figure 9.14b** featured the largest ablation depth and curved surface, and is manufactured with multiple focal plane changes and feed rate parameter adjustments, leading to a larger and less predictable HAZ.

9.7 Conclusions and Discussions

In this study, both theoretical and experimental work is carried out to investigate the possibilities of manufacturing a high-resolution profiled grinding wheel by controlling the focal plane, ORs and feed rate change. Generally, the key conclusions drawn from the paper can be summarised below:

(1) The nature and the characteristics of the laser beam ablation are analysed. Based on the analysis, the possibilities of manufacturing the profiled grinding wheel by controlling the ORs are theoretically analysed and experimentally proved. It revealed that for the given laser conditions, the ablation depth would not be obviously increased when the overlap rate is below 50% for the nature of laser beam energy super-Gauss distribution, and even if the overlap rate is 100%, the ablation depth will also not be continuously increased due to the off-focus effect.

(2) The ablation law regarding ablated depth, width, and topography changes with overlap rate and feed rate is studied, and the corresponding empirical prediction models are established. Meanwhile, the errors for the prediction models are also analysed. It shows that the ablation depth is kept

almost unchanged when the overlap rate is lower than 50%, and the ablation depth begins to grow obviously when the overlap rate is over 50%. The average drop for all feed rates is 0.24 mm with a maximum variation of 0.06 mm under the trailed ORs, indicating the feed rates affect the ablation depth almost equally. In the worst situation, the established prediction model still has the R-square result of 89%, which indicates the effectiveness of the model.

(3) An application attempt to generate precise non-flat surfaces like stepped surfaces and curved surfaces using the CO₂ laser generator has been demonstrated, which showed that the developed strategies could achieve the amazing result in this study. It shows that with the synchronous change of both the feed rate and ORs, a relatively smooth profile with a relative error of 2.22% can be achieved without extra focus plane changes (an effective way to avoid unexpected errors resulting from the off-focus effect when deeper ablation depth is required).

Chapter 10

Research outcomes and further work

10.1 Summary of research findings and conclusions

Based on the understanding of the research background, a system research plan for the precise manufacturing of textured and profiled grinding wheels is scheduled for this project. The research covers the methodologies of theoretical analysis, modelling simulation and experimental investigation and the contents from the platform establishment, via laser ablation law study, to the application of the research results. By the completion of this research work, the key findings and conclusions could be summarised as follows:

(1) Known as high-performance abrasive tools, textured and profiled diamond grinding wheels are highly needed for the end-tech equipment components. Though laser ablation has been considered a promising way, the precise removal of target materials in the specific area remains an open question. To fill the gaps, a systematic study on this project is made from the aspects of theoretical analysis, modelling simulation and experimental investigation after around analysis of the methodologies.

(2) By using the heat transfer theory, the temperature field distribution of the heat-affected zone during the ablation process is simulated. It shows that the material removal rate as well as the ablation depth and width are increased with laser power and decreased with feed rate. However, an optimum ablation result can be achieved with the proper selection of feed rate and laser power.

(3) An electromechanical ablation system is established, which enables the functions of the grinding wheel positioning, laser beam manipulating, and ablation depth measurement. Besides, the performance of the ablation system

is evaluated. It indicates the maximum positioning errors are within ± 0.2 mm, the maximum speed errors percentage is around 4.5% and reduces with speed (almost kept around at 1.5% when the speed is above 60 mm/s). Furthermore, the adjusting time for the positioning system can be completed with 0.05 s under all the experimental parameters. Finally, grinding wheels with continuously changing depths and sine-line textures are created using the system.

(4) Both the ablated topographical and morphological characteristics changing with continuous-wave CO₂ laser power and feed rate are studied. Based on the understanding of the ablation law, a parameter selection diagram for the optimum ablation strategy of the diamond grinding wheels is made. An example representing the application of the parameter selection diagram is demonstrated (grinding wheels with various textures are fabricated), which indicates the usefulness of the study.

(5) The laser ablation law regarding laser power, duty cycle and feed rate effect on the resin-bond diamond grinding wheel is investigated using a fibre laser. It shows that the ablation depth increases with the laser power and duty cycle, and reduces with the feed rate, while the ablation width varies little. The empirical predictive models are established by analysing the limitations and applicabilities of the analytical and empirical models. Finally, an application to generate profiled diamond grinding wheels by single-pass of the fibre laser beam is demonstrated based on the empirical model, which shows the good results of the strategy.

(6) To improve the ablation efficiency, the effect of feed rate and pass number of a fibre laser beam on the laser ablation law is investigated. It shows that the slot depth increases with the laser beam pass number and decreases

with the feed rate. However, the increase rate is reduced with the pass number, while the heat-affected zone is gradually extended. Meanwhile, the top slot width is affected little by the pass number. Both the types and amounts of the morphology characters are increased with the laser beam passes number growing and decreased with the feed rate climbing. Based on the understanding of the ablation law, a diagram for laser ablation parameter selection for different ablation depths is built. Finally, an application for the diagram to generate profiled diamond grinding wheels is demonstrated, which shows that the errors increase with the ablation depth.

(7) To manufacture the high-resolution profiled grinding wheel, the possibilities by controlling the focal plane, ORs and feed rate change are investigated in both theoretical and experimental work, and the corresponding empirical prediction models are established. It reveals that the ablation depth increased little with the overlap when the overlap rate is below 50%, and it will be dramatically increased until its summit after that. The bottom shape of the ablated topography is largely affected by the overlap rate compared to the feed rate. Overall, the ablated results can be reflected by the established prediction model that shows an R-square result of 89% even in the worst situation. An application attempt to generate precise non-flat surfaces like stepped surfaces and curved surfaces by using the CO₂ laser generator has been demonstrated, which shows a relatively smooth profile with a relative error of 2.2% can be achieved with the synchronous change of the feed rate and ORs.

10.2 Further work

This research work has presented a systematic study on the precise fabrication of the textured (e.g., the regular group consist of tilt-line, parallelogram, hexagonal, triangle, rectangle textures and the irregular group

consisting of sine-line slots and slots with changed topography) and profiled (e.g., multi-stepped and freeform curved) diamond grinding wheels. A laser beam manipulating platform and an ablation process modelling are also presented, which could predict the temperature distribution in the heat-affected zone during the ablation process and guarantee the effective implementation and validation of the experimental strategies. Despite the research achievements that have been made, the practical applications of the outcomes are still not thoroughly investigated to achieve optimised results. Some of the main possible future work can be summarised as follows:

(1) The simulation performed in chapter 5 reveals the temperature distribution changes with feed rate and laser power in the heat-affected zone during the ablation process. However, an adjusting time is needed for the ablation process to reach a stable ablation because of the heat conducted in materials. With further investigation of the model, it should be able to find some ways to minimise the adjusting time for the ablation to get to the sound stage.

(2) The final achieved profiled grinding wheels in Chapter 9 provide an amicable solution only for non-flat grinding wheels aimed at limited ablation depth. How to make the research results applicable in a deeper ablation depth has not been studied. A further study could be done by investigating laser type and focal spot length.

(3) Both textured and profiled grinding wheels are achieved in this research. However, the grinding performance of the textured and profiled grinding wheels has not been studied. A potential work could be done to evaluate the grinding wheel from the grinding performance. With the practical test on the grinding wheel, a better understanding of the generation strategies could be achieved.

References

- [1] L. Zheng, *Abrasives - fierce competition at the middle and low end, and the industry may change*. 2021, CINDA SECURITIES CO.,LTD.
- [2] W.F. Zheng, *Heat dissipation and cooling problem of resin diamond grinding wheel*. 2016 [cited 2016 July 22]; Available from: <https://club.1688.com/threadview/48323794.htm>.(In Chinese)
- [3] H.N. Li and D. Axinte, *Textured grinding wheels: A review*. Int. J. Mach. Tool. Manuf., 2016. **109**: p. 8-35.
- [4] W. Ding, et al., *Diamond Wheel Dressing: A Comprehensive Review*. J. Manuf. Sci. & Eng., 2017. **139**(12): p. 121006-121006-25.
- [5] S.D. Milić, et al., *Detailed Study of Fluid Flow and Heat Transfer in the Abrasive Grinding Contact Using Computational Fluid Dynamics Methods*. J. Manuf. Sci. & Eng., 2013. **135**(4): p. 041002-041002-13.
- [6] H.N. Li and D. Axinte, *On the inverse design of discontinuous abrasive surface to lower friction-induced temperature in grinding: An example of engineered abrasive tools*. Int. J. Mach. Tool. Manuf., 2018. **132**: p. 50-63.
- [7] C. Beausoleil, et al., *Deep and high precision cutting of alumina ceramics by picosecond laser*. Ceramics International, 2020. **46**(10): p. 15285-15296.
- [8] C. Walter, et al., *Laser-structured grinding tools - Generation of prototype patterns and performance evaluation*. Journal of Materials Processing Technology, 2014. **214**(4): p. 951-961.
- [9] J.C. Hernandez-Castaneda, et al., *An experimental investigation of laser drilling nitrile butadine (NBR) rubber*. International Journal of Advanced Manufacturing Technology, 2020. **108**(4): p. 1139-1152.
- [10] M. Moradi, et al., *Simulation, statistical modeling, and optimization of CO2 laser cutting process of polycarbonate sheets*. Optik, 2021. **225**: p. 164932.
- [11] J.S. Shin, et al., *Underwater laser cutting of stainless steel up to 100 mm thick for dismantling application in nuclear power plants*. Annals of Nuclear Energy, 2020. **147**: p. 107655.
- [12] S.W. Chang, et al., *Microstructure and dissolution of UO₂ pellet after cutting by fiber laser*. Optics and Laser Technology, 2020. **132**: p. 106493.
- [13] T. Nguyen and L.C. Zhang, *Performance of a new segmented grinding wheel system*. Int. J. Mach. Tool. Manuf., 2009. **49**(3): p. 291-296.
- [14] T.B. Yu, et al., *Experimental investigation on grinding characteristics of optical glass BK7: with special emphasis on the effects of machining parameters*. Int. J. Adv. Manuf. Tech., 2016. **82**(5): p. 1405-1419.
- [15] H.N. Li, et al., *Evaluation of grinding-induced subsurface damage in optical glass BK7*. J. Mater. Process. Tech., 2016. **229**: p. 785-794.
- [16] Y.J. Zhao, et al., *Intelligent assessment of subsurface cracks in optical glass generated in mechanical grinding process*. Adv. in Eng. Sof., 2018. **115**: p. 17-25.
- [17] H.N. Li and D. Axinte, *Textured grinding wheels: A review*. International Journal of Machine Tools & Manufacture, 2016. **109**: p. 8-35.

- [18] A.K. Dubey and V. Yadava, *Laser beam machining - A review*. International Journal of Machine Tools & Manufacture, 2008. **48**(6): p. 609-628.
- [19] P. Parandoush and A. Hossain, *A review of modeling and simulation of laser beam machining*. International Journal of Machine Tools & Manufacture, 2014. **85**: p. 135-145.
- [20] A.N. Samant and N.B. Dahotre, *Laser machining of structural ceramics—A review*. Journal of the European Ceramic Society, 2009. **29**(6): p. 969-993.
- [21] P.W. Butler-Smith, et al., *Preferentially oriented diamond micro-arrays: A laser patterning technique and preliminary evaluation of their cutting forces and wear characteristics*. International Journal of Machine Tools & Manufacture, 2009. **49**(15): p. 1175-1184.
- [22] K.C. Yung, et al., *UV laser cutting of beech plywood*. International Journal of Advanced Manufacturing Technology, 2021. **112**(3-4): p. 925-947.
- [23] P.W. Butler-Smith, et al., *Ordered diamond micro-arrays for ultra-precision grinding—An evaluation in Ti-6Al-4V*. International Journal of Machine Tools and Manufacture, 2011. **51**(1): p. 54-66.
- [24] S. Malkin, *Grinding Technology*. Dearborn, USA, 2008.
- [25] Rockler, *Norton White Aluminum Oxide Grinding Wheels-6" Grinding Wheels*, I. Rockler Companies, Editor. 2022.
- [26] K. North, *Silicon Carbide Grinding Wheels*, I. Kingsley North, Editor. 2022.
- [27] Baoletao, *Durable Diamond Grinding Wheel Cup 100*10mm 180 Grit Cutter Grinder Grinding Wheels for Carbide Metal Stone Polishing*, DHgate, Editor. 2016.
- [28] Woodcraft, *120g 8" x 1" CBN Grinding Wheel with 5/8" Arbor*, WOODCRAFT, Editor. 2022.
- [29] Tools, *Sigma 100mm Long Life Diamond Grinding Wheel M14 Tread 72*, P.T. Tools, Editor. 2022.
- [30] P. Plainte. *Why Select Gear Grinding with cBN?* 2019 [cited 2022 April 6]; Available from: <https://www.nortonabrasives.com/en-us/resources/expertise/why-select-gear-grinding-cbn>.
- [31] W.B. Rowe, *Principles of Modern Grinding Technology*. 2014.
- [32] J. Webster and M. Tricard, *Innovations in Abrasive Products for Precision Grinding*. CIRP Annals, 2004. **53**(2): p. 597-617.
- [33] I.D. Marinescu, et al., *Handbook of Machining with Grinding Wheels*. 2006: CRC Press.
- [34] F. Klocke, et al., *Capability Profile of Hard Cutting and Grinding Processes*. CIRP Annals, 2005. **54**(2): p. 22-45.
- [35] Uama, *Markings for Identifying Grinding Wheels and Other Bonded Abrasives*. 1982.
- [36] Abrasive. *Natural and Synthetic Industrial Diamond Products for Industry*. 2018; Available from: <https://indab.com/products/>.
- [37] Realtec, *CBN Grits & Mircron Powers*, Hunan Real Tech Superabrasive & Tool Co., Editor. 2022.

- [38] I.D. Ohmori, *Tribology of abrasive machining processes*. 2013, USA: Elsevier.
- [39] H.W.H. Beth, *Segmental grinding wheel*. 1925, 1,526,953: USA. p. 4.
- [40] Y.S. Lv, *An investigation on a tin fixed abrasive polishing pad with phyllotactic pattern for polishing wafer*. Journal of China Ordnance, 2012. **8**(3): p. 7.
- [41] K. Yamaguchi, I. Horaguchi and Y.Sato, *Grinding with directionally aligned SiC whisker wheel – loading-free grinding*. Precision Eng. **22**(2): p. 6.
- [42] K. Yamaguchi, *Development of diamond-like carbon fibre wheel*. Precision Eng. **28**(4): p. 6.
- [43] J. Aurich, D. Hellmann and H. Roelawski, *Interne Schleifölzufuhr beim Hochleistungsschleifen, Entwicklung eines Grundkörperprototyps mit internen, strömungsdynamisch ausgelegten Schleifölkanälen*. wtWerkstattstechnikonline. **96**: p. 2.
- [44] J.D. Kim, et al., *Development of discontinuous grinding wheel with multi-porous grooves*. International Journal of Machine Tools and Manufacture, 1997. **37**(11): p. 14.
- [45] A. Malshe, et al., *Bio-inspired functional surfaces for advanced applications*. CIRP Annals, 2013. **62**(2): p. 607-628.
- [46] M. Pacella, et al., *An assessment of the wear characteristics of microcutting arrays produced from polycrystalline diamond and cubic boron nitride composites*. Journal of Manufacturing Science and Engineering, 2016. **138**(2): p. 16.
- [47] P.W. Butler-Smith, et al., *Preferentially oriented diamond micro-arrays: A laser patterning technique and preliminary evaluation of their cutting forces and wear characteristics*. Int. J. Mach. Tool. Manuf., 2009. **49**(15): p. 1175-1184.
- [48] Y. Zhou, et al., *Effects of novel rotary-abrasive finishing pad textures on the controlled 2-body abrasive wear of Type 304 stainless steel*. Wear, 2016. **348-349**: p. 89-97.
- [49] H. Dai, et al., *A numerical study of ultraprecision machining of monocrystalline silicon with laser nano-structured diamond tools by atomistic simulation*. Applied Surface Science, 2017. **393**: p. 405-416.
- [50] B. Zhang and Y. Fu, *Grinding of brittle materials with brazed diamond grinding wheel*. The International Journal of Advanced Manufacturing Technology, 2013. **67**(9): p. 2845-2852.
- [51] M.M. Islam, et al., *Convex diamond patterns by grinding with a wheel which is dressed by a rounded tool*. Journal of Mechanical Science and Technology, 2016. **30**(4): p. 1865-1873.
- [52] C. Walter, et al., *Laser-structured grinding tools – Generation of prototype patterns and performance evaluation*. J. Mater. Process. Tech., 2014. **214**(4): p. 951-961.
- [53] J.C. Aurich and B. Kirsch, *Improved coolant supply through slotted grinding wheel*. CIRP Annals, 2013. **62**(1): p. 363-366.
- [54] M. Rabiey, *Dry grinding with CBN wheels, the effect of structuring*. 2011, University of Stuttgart.
- [55] J.C. Aurich, et al., *Development of a Superabrasive Grinding Wheel With Defined Grain Structure Using Kinematic Simulation*. CIRP Annals, 2003. **52**(1): p. 275-280.

- [56] H.N. Li and D. Axinte, *Textured grinding wheels: A review*. International Journal of Machine Tools and Manufacture, 2016. **109**: p. 8-35.
- [57] D.K. Aspinwall, et al., *Profiled Superabrasive Grinding Wheels for the Machining of a Nickel Based Superalloy*. CIRP Annals, 2007. **56**(1): p. 335-338.
- [58] C.G. Fang, et al., *Analysis and Compensation for Gear Accuracy with Setting Error in Form Grinding*. Advances in Mechanical Engineering, 2015. **21**(3): p. 716-723.
- [59] X.R. Liu and Z.H. Wang, *Research on High-Precision Form Grinding Technology of Gear Based on Ambient Temperature Adaptability*. Mathematical Problems in Engineering, 2018. **2018**: p. 1-13.
- [60] D.T. Nguyen, et al., *Design of grinding wheel profile for new micro drill flute*. Transactions of the Canadian Society for Mechanical Engineering, 2018. **42**(2): p. 116-124.
- [61] L.J. Tao, et al., *A correction method of screw rotor profile error based on parameter adjustment for grinding wheel dresser*. Advances in Mechanical Engineering, 2018. **10**(9): p. 1-7.
- [62] Q. Miao, et al., *Grinding force and surface quality in creep feed profile grinding of turbine blade root of nickel-based superalloy with microcrystalline alumina abrasive wheels*. Chinese Journal of Aeronautics, 2021. **34**(2): p. 576-585.
- [63] S.S. Chen, et al., *Curvature effect on surface topography and uniform scallop height control in normal grinding of optical curved surface considering wheel vibration*. Optics Express, 2021. **29**(6): p. 8041-8063.
- [64] S. Wang, et al., *Ultra-precision raster grinding of monocrystalline silicon biconical free-form optics using arc-shaped diamond grinding wheels*. Journal of Manufacturing Processes, 2020. **58**: p. 1064-1074.
- [65] W. Wang, et al., *Envelope grinding of micro-cylinder array lenses using a near arc-profile wheel without on-machine precision truing*. Journal of Materials Processing Technology, 2021. **289**.
- [66] S.Y. Chen, et al., *Fast registration of 3D point clouds with offset surfaces in precision grinding of free-form surfaces*. International Journal of Advanced Manufacturing Technology, 2018. **97**(9-12): p. 3595-3606.
- [67] Z.X. Zhang and Z.H. Fong, *A novel tilt form grinding method for the rotor of dry vacuum pump*. Mechanism and Machine Theory, 2015. **90**: p. 47-58.
- [68] V.T. Thang, et al., *Evaluation of grinding wheel wear in wet profile grinding for the groove of the ball bearing's inner ring by pneumatic probes*. Journal of Mechanical Science and Technology, 2018. **32**(3): p. 1297-1305.
- [69] G. Li, et al., *A function-oriented active form-grinding method for cylindrical gears based on error sensitivity*. International Journal of Advanced Manufacturing Technology, 2017. **92**(5-8): p. 3019-3031.
- [70] T. Jin, et al., *Temperature distributions in form grinding of involute gears*. International Journal of Advanced Manufacturing Technology, 2017. **88**(9-12): p. 2609-2620.
- [71] J. Yi, et al., *The temperature field study on the three-dimensional surface moving heat source model in involute gear form grinding*. International Journal of Advanced Manufacturing Technology, 2019. **103**(5-8): p. 3097-3108.

- [72] J. Yi, et al., *Theoretical and experimental analysis of temperature distribution during full tooth groove form grinding*. Journal of Manufacturing Processes, 2020. **58**: p. 101-115.
- [73] J. Yi, et al., *Estimation of residual stresses in gear form grinding using finite element analysis and experimental study based on grinding force and heat flux distribution models*. International Journal of Advanced Manufacturing Technology, 2019. **104**(1-4): p. 849-866.
- [74] J.X. Su, et al., *Numerical simulation and experimental analysis of temperature field of gear form grinding*. International Journal of Advanced Manufacturing Technology, 2018. **97**(5-8): p. 2351-2367.
- [75] L. Wang, et al., *Experimental study and theoretical analysis of the form grinding of gears using new type micro-crystal corundum grinding wheels*. International Journal of Advanced Manufacturing Technology, 2017. **92**(5-8): p. 1659-1669.
- [76] X. Li, et al., *Grinding of fir tree slots of powder metallurgy superalloy FGH96 using profiled electroplated CBN wheel*. International Journal of Advanced Manufacturing Technology, 2021. **115**: p. 311–17.
- [77] Z.C. Zhao, et al., *An investigation on high-efficiency profile grinding of directional solidified nickel-based superalloys DZ125 with electroplated CBN wheel*. International Journal of Advanced Manufacturing Technology, 2016. **83**(1-4): p. 1-11.
- [78] J.Y. Liao, et al., *Modeling of curved diamond wheel errors for improvement of freeform grinding accuracy*. International Journal of Advanced Manufacturing Technology, 2019. **103**(5-8): p. 1879-1892.
- [79] Y.H. Zhang, et al., *Research on wear detection of wheel in precision NC curve point grinding*. International Journal of Advanced Manufacturing Technology, 2008. **35**(9-10): p. 994-999.
- [80] V.K. Starkov, et al., *Comparative analysis of performance of cubic boron nitride and microcrystalline alumina tools in profile grinding of form cutters*. Journal of Superhard Materials, 2014. **36**(1): p. 43-48.
- [81] J. Xie, et al., *Form-truing error compensation of diamond grinding wheel in CNC envelope grinding of free-form surface*. International Journal of Advanced Manufacturing Technology, 2010. **48**(9-12): p. 905-912.
- [82] J. Xie, et al., *Dispersed grinding wheel profiles for accurate freeform surfaces*. International Journal of Machine Tools & Manufacture, 2011. **51**(6): p. 536-542.
- [83] J. Xie, et al., *Study on a 5-axis precision and mirror grinding of glass freeform surface without on-machine wheel-profile truing*. International Journal of Machine Tools & Manufacture, 2016. **109**: p. 65-73.
- [84] J.H. Yang, et al., *A path planning method for error region grinding of aero-engine blades with free-form surface*. International Journal of Advanced Manufacturing Technology, 2015. **81**(1-4): p. 717-728.
- [85] J.D. Qi and B. Chen, *Elastic-contact-based tool-path planning for free-form surface in belt grinding*. Advances in Mechanical Engineering, 2019. **11**(1).
- [86] V. Bogutsky, et al., *Calculating the profile of intermittent grinding wheel for the sharpening teeth of the broach*. International Conference on Modern Trends in Manufacturing Technologies and Equipment (Icmtmte 2018), 2018. **224**.
- [87] Y. Ichida, *Profile Grinding of High-Speed Steel using Ultrafine-Crystalline cBN*

- Wheels*. Journal of Advanced Mechanical Design Systems and Manufacturing, 2008. **2**(3): p. 385-395.
- [88] Z.M. Liu, et al., *A Novel Optimization Design Method of Form Grinding Wheel for Screw Rotor*. Applied Sciences, 2019. **9**(23).
- [89] A.M.O. Mohamed, et al., *Application of shallow circumferential grooved wheels to creep-feed grinding*. Journal of Materials Processing Technology, 2013. **213**(5): p. 700-706.
- [90] A.M.O. Mohamed, et al., *A novel method for grooving and re-grooving aluminum oxide grinding wheels*. The International Journal of Advanced Manufacturing Technology, 2014. **73**(5-8): p. 715-725.
- [91] J.F.G. Oliveira, et al., *A novel dressing technique for texturing of ground surfaces*. CIRP Annals, 2010. **59**(1): p. 361-364.
- [92] E.J.D. Silva, et al., *Strategies for production of parts textured by grinding using patterned wheels*. CIRP Annals, 2013. **62**(1): p. 355-358.
- [93] B. Denkena, et al., *Grinding with patterned grinding wheels*. CIRP Journal of Manufacturing Science and Technology, 2015. **8**: p. 12-21.
- [94] T. Tawakoli and A. Daneshi, *T-Dress, A Novel Approach in Dressing and Structuring of Grinding Wheels*. Advances in Abrasive Technology Xv, 2012. **565**: p. 217-221.
- [95] J.C. Aurich, et al., *Hydraulic design of a grinding wheel with an internal cooling lubricant supply*. Prod. Eng., 2011. **5**(2): p. 119-126.
- [96] B. Guo, et al., *Precision grinding of optical glass with laser micro-structured coarse-grained diamond wheels*. J. Mater. Process Tech., 2014. **214**(5): p. 1045-1051.
- [97] M. Wu, et al., *The influence of the focus position on laser machining and laser micro-structuring monocrystalline diamond surface*. Optics and Lasers in Eng., 2018. **105**: p. 60-67.
- [98] J.C. Aurich, et al., *High-performance dry grinding using a grinding wheel with a defined grain pattern*. CIRP Annals, 2008. **57**(1): p. 357-362.
- [99] Y. Lyu, et al., *Improved performance of electroplated grinding wheels using a new method of controlled grain size sorting*. J. Manuf. Proc., 2017. **30**: p. 336-342.
- [100] H. Yu, et al., *A biomimetic engineered grinding wheel inspired by phyllotaxis theory*. Journal of Materials Processing Technology, 2018. **251**: p. 267-281.
- [101] R.P. Upadhyaya and J.H. Fiecoat, *Factors Affecting Grinding Performance with Electroplated CBN Wheels*. CIRP Annals, 2007. **56**(1): p. 339-342.
- [102] J. Chen, et al., *Investigation on induction brazing of revolving heat pipe grinding wheel*. Materials & Design, 2017. **116**: p. 21-30.
- [103] G. Huang, et al., *Fundamental aspects of ultrasonic assisted induction brazing of diamond onto 1045 steel*. Journal of Materials Processing Technology, 2018. **260**: p. 123-136.
- [104] A.K. Chattopadhyay, et al., *On performance of brazed bonded monolayer diamond grinding wheel*. CIRP annals, 1991. **40**(1): p. 347-350.
- [105] J. Chen, et al., *Grinding characteristics in high speed grinding of engineering ceramics with brazed diamond wheels*. Journal of Materials Processing

Technology, 2010. **210**(6-7): p. 899-906.

- [106] W.F. Ding, et al., *Interface characteristics and fracture behavior of brazed polycrystalline CBN grains using Cu–Sn–Ti alloy*. Materials Science and Engineering: A, 2013. **559**: p. 629-634.
- [107] A. Bilbao-Guillerna, et al., *Waterjet and laser etching: the nonlinear inverse problem*. Royal Society Open Science, 2017. **4**(7): p. 161031.
- [108] S. Wang, et al., *Investigation on kerf taper in abrasive waterjet machining of aluminium alloy 6061-T6*. Journal of Materials Research and Technology, 2021. **15**: p. 427-433.
- [109] P. Karmiris-Obratański, et al., *Experimental Study on the Correlation of Cutting Head Vibrations and Kerf Characteristics during Abrasive Waterjet Cutting of Titanium Alloy*. Procedia CIRP, 2021. **101**: p. 226-229.
- [110] Z. Liao, et al., *Dual-processing by abrasive waterjet machining—A method for machining and surface modification of nickel-based superalloy*. Journal of Materials Processing Technology, 2020. **285**: p. 116768.
- [111] Y. Zhang, et al., *Hole characteristics and surface damage formation mechanisms of Cf/SiC composites machined by abrasive waterjet*. Ceramics International, 2022. **48**(4): p. 5488-5498.
- [112] J.N. Nyaboro, et al., *Fluid-structure interaction modeling of the abrasive waterjet drilling of carbon fiber reinforced polymers*. Journal of Manufacturing Processes, 2020. **58**: p. 551-562.
- [113] D. Liu, et al., *Material removal mechanisms of ceramics turned by abrasive waterjet (AWJ) using a novel approach*. Ceramics International, 2021. **47**(11): p. 15165-15172.
- [114] P.B. Arab and T.B. Celestino, *A microscopic study on kerfs in rocks subjected to abrasive waterjet cutting*. Wear, 2020. **448-449**: p. 203210.
- [115] N.P. Singh, et al., *Modelling of abrasive waterjet kerf in a double-layered structure*. Journal of Manufacturing Processes, 2021. **69**: p. 514-531.
- [116] D. Axinte, et al., *Abrasive waterjet turning—An efficient method to profile and dress grinding wheels*. International Journal of Machine Tools & Manufacture, 2009. **49**(3-4): p. 351-356.
- [117] F. Morczinek and M. Putz, *An investigation of abrasive waterjet machining of cubic boron nitride (CBN) with a softer abrasive material*. Procedia CIRP, 2020. **95**: p. 6-11.
- [118] H.N. Li, et al., *Generation of textured diamond abrasive tools by continuous-wave CO₂ laser: Laser parameter effects and optimisation*. Journal of Materials Processing Technology, 2020. **275**.
- [119] B. Guo, et al., *Precision grinding of optical glass with laser micro-structured coarse-grained diamond wheels*. Journal of Materials Processing Technology, 2014. **214**(5): p. 1045-1051.
- [120] B. Guo, et al., *Surface micro-structuring of coarse-grained diamond wheels by nanosecond pulsed laser for improving grinding performance*. Int. J. Prec. Eng. & Manuf., 2014. **15**(10): p. 2025-2030.
- [121] Z. Zhang, et al., *Mechanisms of femtosecond laser ablation of Ni₃Al: Molecular dynamics study*. Optics and Laser Technology, 2021. **133**: p. 106505.

- [122] R. Zhang, et al., *Evolution of micro/nano-structural arrays on crystalline silicon carbide by femtosecond laser ablation*. Materials Science in Semiconductor Processing, 2021. **121**: p. 105299.
- [123] J.W. Cai, et al., *Experimental study of diamond ablation based on femtosecond laser*. Optik, 2020. **217**: p. 164838.
- [124] P.W. Butler-Smith, et al., *Ordered diamond micro-arrays for ultra-precision grinding—An evaluation in Ti–6Al–4V*. Int. J. Mach. Tool. Manuf., 2011. **51**(1): p. 54-66.
- [125] D. Sun, et al., *Surface integrity of water jet guided laser machining of CFRP*. Procedia CIRP, 2018. **71**: p. 71-74.
- [126] H.R.F. Shahri and R. Mahdavinejad, *Prediction of temperature and HAZ in thermal-based processes with Gaussian heat source by a hybrid GA-ANN model*. Optics & Laser Technology, 2018. **99**: p. 363-373.
- [127] S. Sattel. *How Do Lasers Work*. 2016 November 29 2021]; Available from: <https://www.autodesk.com/products/eagle/blog/how-lasers-work/>.
- [128] A. Back. *Breathing Life into a Vintage Gas Laser*. 2014 [cited 2014 2014-03-07]; Available from: <https://www.rs-online.com/designspark/breathing-life-into-a-vintage-gas-laser>.
- [129] Scientific. *Dye Lasers & Accessories*. 2012 [cited 2012; Available from: <http://www.warsash.com.au/products/lasers/DYE-LASERS.php>.
- [130] Semiconductors. *Tailoring dopants in semiconductors - LEDs and lasers*. Available from: <http://www.webexhibits.org/causesofcolor/11AA.html>.
- [131] M. Hashemzadeh, *Investigations into fibre laser cutting*. 2014.
- [132] M. Weschler. *How laser works*. 2006 [cited 2006 29 November 2021]; Available from: <https://science.howstuffworks.com/laser.htm>.
- [133] D. Bergström, *The absorptance of metallic alloys to Nd:YAG and Nd:YLF laser light*. 2005.
- [134] G. Fomitchev, *Absorption wavelength spectrum for different materials: glass, metal and others*. 2021 [cited 2021 2021-11-12]; Available from: <https://endurancelasers.com/absorption-wavelength-spectrum-for-different-materials/>.
- [135] A. Mahrle and E. Beyer, *Theoretical aspects of fibre laser cutting*. Journal of Physics D: Applied Physics, 2009. **42**(17): p. 175507.
- [136] J. Powell, et al., *Fibre laser cutting of thin section mild steel: An explanation of the 'striation free' effect*. Optics and Lasers in Engineering, 2011. **49**(8): p. 1069-1075.
- [137] A.F.H. Kaplan, *Local absorptivity modulation of a 1 μ m-laser beam through surface waviness*. Applied Surface Science, 2012. **258**(24): p. 9732-9736.
- [138] A.F.H. Kaplan, *Absorptivity modulation on wavy molten steel surfaces: The influence of laser wavelength and angle of incidence*. Applied Physics Letters, 2012. **101**(15): p. 151605.
- [139] D. Petring, et al., *How beam quality power and wavelength influence laser cutting and welding processes*. in *Proceedings of LAMP2009 - the 5th international congress on laser advanced materials processing*. 2009. Kobe, Japan;: Fraunhofer.

- [140] D. Bergström, et al., *The absorptance of steels to Nd:YLF and Nd:YAG laser light at room temperature*. Applied Surface Science, 2007. **253**(11): p. 5017-5028.
- [141] V.M. Fomin, et al., *Similarity of heat fluxes upon laser oxygen cutting of steel*. Doklady Physics, 2011. **56**(1): p. 12-15.
- [142] V.M. Fomin, et al., *Energy conditions of gas laser cutting of thick steel sheets*. Journal of Applied Mechanics and Technical Physics, 2011. **52**(3): p. 340-346.
- [143] A. Otto and M. Schmidt, *Towards a Universal Numerical Simulation Model for Laser Material Processing*. Physics Procedia, 2010. **5**: p. 35-46.
- [144] J. Powell and A. Kaplan. *Laser cutting: From first principles to the state of the art*. Laser Institute of America.
- [145] T. Sims. *Understanding laser machines – how can I select the right laser source for my application*. 2020 [cited 2020 2020-05-26]; Available from: <https://www.controllaser.com/blog/2018/11/22/how-can-i-select-the-right-laser-source-for-my-application/>.
- [146] B.C. Gahan and B. Shiner, *New High-Power Fiber Laser Enables Cutting-Edge Research*. Laser Technology, 2004: p. 29-31.
- [147] E. Beyer, et al. *High-power laser materials processing*. Laser Institute of America.
- [148] J. Powell, *CO2 laser cutting*. Vol. 214. 1993: Springer.
- [149] A.H. Hamad, *Effects of Different Laser Pulse Regimes (Nanosecond, Picosecond and Femtosecond) on the Ablation of Materials for Production of Nanoparticles in Liquid Solution*. 2016, InTech.
- [150] V.G. Niziev and A.V. Nesterov, *Influence of beam polarization on laser cutting efficiency*. Journal of Physics D: Applied Physics, 1999. **32**(1999): p. 7.
- [151] R. Weber, et al., *Effects of Radial and Tangential Polarization in Laser Material Processing*. Physics Procedia, 2011. **12**: p. 21-30.
- [152] P. Pasquet, et al., *Laser cleaning of oxide iron layer: Efficiency enhancement due to electrochemical induced absorptivity change*. Applied Physics A: Materials Science & Processing, 1999. **69**(7): p. S727-S730.
- [153] J. Ion, *Laser Processing of Engineering Materials: Principles, Procedure and Industrial Application*. 2005.
- [154] Z.H. Xiao, *Fibre laser cutting of mild steel*, in *Department Council of Mechanical Engineering*. 2007, Lapperanta University of Technology.
- [155] W.M. Steen and J. Mazumder, *Laser material processing*. 2010: springer science & business media.
- [156] W. O'neill, et al. *High power high brightness industrial fiber laser technology*. Laser Institute of America.
- [157] H. Hügel, *New solid-state lasers and their application potentials*. Optics and Lasers in Engineering, 2000. **34**(4-6): p. 213-229.
- [158] L.D. Scintilla, et al., *Primary losses in disk and CO2 laser beam inert gas fusion cutting*. Journal of Materials Processing Technology, 2011. **211**(12): p. 2050-2061.
- [159] L.D. Scintilla, et al. *Experimental investigation on the cut front geometry in the*

inert gas laser fusion cutting with disk and CO2 lasers. Laser Institute of America.

- [160] W. Suder. *Study of fundamental parameters in hybrid laser welding*. 2011.
- [161] D. Li, et al., *Multi-state objects depth acquisition based on binocular structured light*. Optics and Lasers in Engineering, 2019. **121**: p. 521-528.
- [162] H. Hu, et al., *A combined binary defocusing technique with multi-frequency phase error compensation in 3D shape measurement*. Optics and Lasers in Engineering, 2020. **124**: p. 105806.
- [163] M. Kytö, et al., *Method for measuring stereo camera depth accuracy based on stereoscopic vision*. IS&T/SPIE Electronic Imaging. Vol. 7864. 2011: SPIE.
- [164] M.H. Chiu, et al., *Small absolute distance measurement with nanometer resolution using geometrical optics principles and a SPR angular sensor*. Sensors and Actuators A: Physical, 2008. **141**(1): p. 217-223.
- [165] M. Norgia, et al., *Self-mixing instrument for simultaneous distance and speed measurement*. Optics and Lasers in Engineering, 2017. **99**: p. 31-38.
- [166] Z. Duan, et al., *Absolute distance measurement based on multiple self-mixing interferometry*. Optics Communications, 2017. **389**: p. 270-274.
- [167] R. Wang, et al., *A point and distance constraint based 6R robot calibration method through machine vision*. Robotics and Computer-Integrated Manufacturing, 2020. **65**: p. 101959.
- [168] Q. Fu, et al., *Laser distance measurement by triangular-wave amplitude modulation based on the least squares*. Infrared Physics & Technology, 2020. **104**: p. 103146.
- [169] M. Medhat, et al., *Distance measurement using frequency scanning interferometry with mode-hopped laser*. Optics & Laser Technology, 2016. **80**: p. 209-213.
- [170] J. Kim, et al., *A method to estimate the absolute ultrasonic nonlinearity parameter from relative measurements*. Ultrasonics, 2017. **77**: p. 197-202.
- [171] Y. Shi, et al., *Design and testing of a linear encoder capable of measuring absolute distance*. Sensors and Actuators A: Physical, 2020. **308**: p. 111935.
- [172] S. Feng, et al., *Surface quality evaluation of single crystal 4H-SiC wafer machined by hybrid laser-waterjet: Comparing with laser machining*. Materials Science in Semiconductor Processing, 2019. **93**: p. 238-251.
- [173] C. Leone, et al., *Investigation of CFRP laser milling using a 30W Q-switched Yb:YAG fiber laser: Effect of process parameters on removal mechanisms and HAZ formation*. Composites Part A: Applied Science and Manufacturing, 2013. **55**: p. 129-142.
- [174] C. Leone and S. Genna, *Heat affected zone extension in pulsed Nd:YAG laser cutting of CFRP*. Composites Part B: Engineering, 2018. **140**: p. 174-182.
- [175] A. Belhadj, et al., *Simulation of the HAZ and magnetic properties of laser cut non-oriented electrical steels*. Journal of Magnetism and Magnetic Materials, 2002. **248**(1): p. 34-44.
- [176] E. Haddadi, et al., *Experimental and parametric evaluation of cut quality characteristics in CO2 laser cutting of polystyrene*. Optik, 2019. **184**: p. 103-114.
- [177] A. Solati, et al., *Combined GA-ANN approach for prediction of HAZ and bearing*

- strength in laser drilling of GFRP composite*. Optics & Laser Technology, 2019. **113**: p. 104-115.
- [178] D. Kumar and S. Gururaja, *Investigation of hole quality in drilled Ti/CFRP/Ti laminates using CO2 laser*. Optics & Laser Technology, 2020. **126**: p. 106130.
- [179] Z. Shang, et al., *On modelling of laser assisted machining: Forward and inverse problems for heat placement control*. International Journal of Machine Tools and Manufacture, 2019. **138**: p. 36-50.
- [180] H. Zhu, et al., *Heat transfer and material ablation in hybrid laser-waterjet microgrooving of single crystalline germanium*. International Journal of Machine Tools and Manufacture, 2017. **116**: p. 25-39.
- [181] A. Bharatish, et al., *Characterization of hole circularity and heat affected zone in pulsed CO2 laser drilling of alumina ceramics*. Optics & Laser Technology, 2013. **53**: p. 22-32.
- [182] A.C. Popescu, et al., *Investigation and in situ removal of spatter generated during laser ablation of aluminium composites*. Applied Surface Science, 2016. **378**: p. 102-113.
- [183] T. Wu, et al., *Fabrication of trapezoidal cross-sectional microchannels on PMMA with a multi-pass translational method by CO2 laser*. Optik, 2019. **183**: p. 953-961.
- [184] A. Salama, et al., *Understanding the self-limiting effect in picosecond laser single and multiple parallel pass drilling/machining of CFRP composite and mild steel*. Materials & Design, 2016. **107**: p. 461-469.
- [185] Q. Chen, et al., *Characterization of hole taper in laser drilling of silicon nitride ceramic under water*. Ceramics International, 2018. **44**(11): p. 13449-13452.
- [186] V. Tangwarodomnukun, et al., *Laser ablation of titanium alloy under a thin and flowing water layer*. International Journal of Machine Tools and Manufacture, 2015. **89**: p. 14-28.
- [187] N. Iwatani, et al., *Optimization of near-infrared laser drilling of silicon carbide under water*. International Journal of Heat and Mass Transfer, 2014. **71**: p. 515-520.
- [188] Y. Wang, et al., *Study on immersion waterjet assisted laser micromachining process*. Journal of Materials Processing Technology, 2018. **262**: p. 290-298.
- [189] Y.Z. Liu, *Coaxial waterjet-assisted laser drilling of film cooling holes in turbine blades*. International Journal of Machine Tools and Manufacture, 2020. **150**: p. 103510.
- [190] X. Li and Y. Guan, *Theoretical fundamentals of short pulse laser-metal interaction: A review*. Nanotechnology and Precision Engineering, 2020. **3**(3): p. 105-125.
- [191] A. Parthiban, et al., *Modeling on surface cut quality of CO2 laser cutting for Austenitic Stainless steel sheet*. Materials Today-Proceedings, 2020. **21**: p. 823-827.
- [192] H. Karbasi. *COMSOL Assisted Simulation of Laser Engraving*. 2010.
- [193] W. Frei, *Modeling Laser-Material Interactions in COMSOL Multiphysics*, in *COMSOL Blog*. 2015.
- [194] Q. Ge, et al., *Mechanisms of laser energy absorption and melting behavior*

- during selective laser melting of titanium-matrix composite: role of ceramic addition. *Journal of Physics D: Applied Physics*, 2021. **54**(2021): p. 12.
- [195] P. Wongchadukul, et al. *Simulation of temperature distribution in different human skin types exposed to laser irradiation with different wavelengths and laser irradiation intensities*. 2019.
- [196] J. Ma, et al., *Thermal damage in three-dimensional vivo bio-tissues induced by moving heat sources in laser therapy*. *Scientific Reports*, 2019. **9**(1).
- [197] H.E. Orimi, et al., *Experimental investigation of texturing complex geometry using high repetition Nano laser and comparison with the simulated COMSOL model*. *Laser-Based Micro- and Nanoprocessing Xii*, 2018. **10520**.
- [198] J.W. Ma, et al., *Solution of maximum laser ablation depth based on dynamic energy distribution model*. *Materials and Manufacturing Processes*, 2019.
- [199] L.E. Criales, et al., *Effect of Fluence and Pulse Overlapping on Fabrication of Microchannels in PMMA/PDMS Via UV Laser Micromachining: Modeling and Experimentation*. *Materials and Manufacturing Processes*, 2015. **30**(7): p. 890-901.
- [200] D. Cha and D. Axinte, *Transient thermal model of nanosecond pulsed laser ablation: Effect of heat accumulation during processing of semi-transparent ceramics*. *International Journal of Heat and Mass Transfer*, 2021. **173**.
- [201] J. Li, et al., *Analytical modelling of full single-track profile in wire-fed laser cladding*. *Journal of Materials Processing Technology*, 2021. **290**.
- [202] A.A. Peligrad, et al., *A melt depth prediction model for quality control of laser surface glazing of inhomogeneous materials*. *Optics & Laser Technology*, 2001. **33**(1): p. 7-13.
- [203] M.S. Salim, et al., *Novel improvement glazing depth measurement model for concrete surface treated by CO2 laser*. *Optik*, 2017. **142**: p. 412-420.
- [204] C.L. Chen, et al., *Modeling and high-precision control of a ball-screw-driven stage*. *Precision Engineering*, 2004. **28**(4): p. 483-495.
- [205] S.T. Wu, et al., *Vibration control of a flexible beam driven by a ball-screw stage with adaptive notch filters and a line enhancer*. *Journal of Sound and Vibration*, 2015. **348**: p. 71-87.
- [206] T. Campbell and J.F.X. Jones, *Design and implementation of a low cost, modular, adaptable and open-source XYZ positioning system for neurophysiology*. *HardwareX*, 2020. **7**: p. e00098.
- [207] C.G. Zhou, et al., *Experimental analysis of the wear coefficient of double-nut ball screws*. *Wear*, 2020. **446-447**: p. 203201.
- [208] T. Fujimoto, *LINEAR MOTOR DRIVING DEVICE*, N. Corporation, Editor. 1988: Japan. p. 5.
- [209] J. Li, et al., *Stepping piezoelectric actuators with large working stroke for nano-positioning systems: A review*. *Sensors and Actuators A: Physical*, 2019. **292**: p. 39-51.
- [210] H. Huang, et al., *A novel driving principle by means of the parasitic motion of the microgripper and its preliminary application in the design of the linear actuator*. *Review of Scientific Instruments*, 2012. **83**(5): p. 055002.
- [211] C. Li, et al., *Recession in a linear stepper motor based on piezoelectric actuator*

- and electrorheological claspers*. Smart Materials and Structures, 2012. **21**(12): p. 125008.
- [212] S.C. Kim and S.H. Kim, *Precise rotary motor by inchworm motion using dual wrap belts*. Review of Scientific Instruments, 1999. **70**(5): p. 2546-2550.
- [213] S. Song, et al., *Piezoelectric inchworm rotary actuator with high driving torque and self-locking ability*. Sensors and Actuators A: Physical, 2018. **282**: p. 174-182.
- [214] J. Li, et al., *A piezoelectric-driven rotary actuator by means of inchworm motion*. Sensors and Actuators A: Physical, 2013. **194**: p. 269-276.
- [215] D. Saravanakumar, et al., *A review on recent research trends in servo pneumatic positioning systems*. Precision Engineering, 2017. **49**: p. 481-492.
- [216] R. Beerens, et al., *Reset integral control for improved settling of PID-based motion systems with friction*. Automatica, 2019. **107**: p. 483-492.
- [217] A. Bisoffi, et al., *To stick or to slip: A reset PID control perspective on positioning systems with friction*. Annual Reviews in Control, 2020. **49**: p. 37-63.
- [218] J. Jiang, et al., *State-of-the-Art control strategies for robotic PiH assembly*. Robotics and Computer-Integrated Manufacturing, 2020. **65**: p. 101894.
- [219] J. Takahashi, et al., *Passive Alignment Principle for Robotic Assembly Between a Ring and a Shaft With Extremely Narrow Clearance*. IEEE/ASME Transactions on Mechatronics, 2016. **21**(1): p. 196-204.
- [220] H. Park, et al. *Dual arm peg-in-hole assembly with a programmed compliant system*. in *2014 11th International Conference on Ubiquitous Robots and Ambient Intelligence (URAI)*. 2014.
- [221] P.D. Labrecque, et al., *uMan: A Low-Impedance Manipulator for Human–Robot Cooperation Based on Underactuated Redundancy*. IEEE/ASME Transactions on Mechatronics, 2017. **22**(3): p. 1401-1411.
- [222] T. Fukukawa, et al., *Precise assembly of ring part with optimized hollowed finger*. ROBOMECH Journal, 2016. **3**(1): p. 16.
- [223] N. Mol, et al. *Nested compliant admittance control for robotic mechanical assembly of misaligned and tightly toleranced parts*. in *2016 IEEE International Conference on Systems, Man, and Cybernetics (SMC)*. 2016.
- [224] J.C.P. Ibarra and A.A.G. Siqueira. *Impedance Control of Rehabilitation Robots for Lower Limbs, Review*. in *2014 Joint Conference on Robotics: SBR-LARS Robotics Symposium and Robocontrol*. 2014.
- [225] I.F. Jasim, et al. *Model-Free Robust Adaptive Control for flexible rubber objects manipulation*. in *2015 IEEE 20th Conference on Emerging Technologies & Factory Automation (ETFA)*. 2015.
- [226] K. Wang. *Fuzzy Sliding Mode Joint Impedance Control for a tendon-driven robot hand performing peg-in-hole assembly*. in *2016 IEEE International Conference on Robotics and Biomimetics (ROBIO)*. 2016.
- [227] S. Wen, et al., *Elman Fuzzy Adaptive Control for Obstacle Avoidance of Mobile Robots Using Hybrid Force/Position Incorporation*. IEEE Transactions on Systems, Man, and Cybernetics, Part C (Applications and Reviews), 2012. **42**(4): p. 603-608.
- [228] T.P. Nascimento and M. Saska, *Position and attitude control of multi-rotor aerial*

- vehicles: A survey*. Annual Reviews in Control, 2019. **48**: p. 129-146.
- [229] S. Martínez, et al., *Note: Fast, small, and low vibration mechanical laser shutters*. The Review of scientific instruments, 2011. **82**: p. 046102.
- [230] G.H. Zhang, et al., *Fast Compact Laser Shutter Using a Direct Current Motor and 3D Printing*. REVIEW OF SCIENTIFIC INSTRUMENTS 2015.
- [231] C.D. Colquhoun, et al., *Note: A simple laser shutter with protective shielding for beam powers up to 1 W*. Review of Scientific Instruments, 2018. **89**(12): p. 126102.
- [232] W. Bowden, et al., *Note: A high-performance, low-cost laser shutter using a piezoelectric cantilever actuator*. REVIEW OF SCIENTIFIC INSTRUMENTS, 2017. **88**(1): p. 016102.
- [233] H. Deng, et al., *Online, efficient and precision laser profiling of bronze-bonded diamond grinding wheels based on a single-layer deep-cutting intermittent feeding method*. Optics and Laser Technology, 2016. **80**: p. 41-50.
- [234] H. Deng, et al., *Optimization of efficiency and uniformity of bond removal during laser sharpening*. International Journal of Advanced Manufacturing Technology, 2019. **103**(5-8): p. 3087-3096.
- [235] H. Deng and Z. Xu, *Laser dressing of arc-shaped resin-bonded diamond grinding wheels*. Journal of Materials Processing Technology, 2021. **288**.
- [236] W. Zhou, et al., *Dual-laser dressing concave rectangular bronze-bonded diamond grinding wheels*. Diamond and Related Materials, 2022. **123**.
- [237] B. Guo, et al., *Water assisted pulsed laser machining of micro-structured surface on CVD diamond coating tools*. Journal of Manufacturing Processes, 2020. **56**: p. 591-601.
- [238] X.H. Zhang, et al., *Grinding performance improvement of laser micro-structured silicon nitride ceramics by laser macro-structured diamond wheels*. Ceramics International, 2020. **46**(1): p. 795-802.
- [239] X.H. Zhang, et al., *Precision grinding of silicon nitride ceramic with laser macro-structured diamond wheels*. Optics and Laser Technology, 2019. **109**: p. 418-428.
- [240] J.J. Wu, et al., *A method for obtaining the fraction of absorbed energy of material based on laser shock processing experiment and simulation*. International Journal of Advanced Manufacturing Technology, 2021.
- [241] B. Guo, et al., *Improvement of precision grinding performance of CVD diamond wheels by micro-structured surfaces*. Ceramics International, 2018. **44**(14): p. 17333-17339.
- [242] M.T. Wu, et al., *The influence of the focus position on laser machining and laser micro-structuring monocrystalline diamond surface*. Optics and Lasers in Engineering, 2018. **105**: p. 60-67.
- [243] N. Lasemi, et al., *Pulsed laser ablation and incubation of nickel, iron and tungsten in liquids and air*. Applied Surface Science, 2018. **433**: p. 772-779.
- [244] H.Q. Dou, et al., *Femtosecond laser ablation of Al-Mg alloy in vacuum and air*. Applied Surface Science, 2018. **447**: p. 388-392.
- [245] H.O. Jeschke and M.E. Garcia, *Theoretical description of the ultrafast ablation of diamond and graphite: dependence of thresholds on pulse duration*. Applied Surface Science, 2002. **197**: p. 107-113.

- [246] A.F. Mohammed, et al., *Ablation threshold measurements and surface modifications of 193 nm laser irradiated 4H-SiC*. Chemical Physics Letters, 2018. **713**: p. 194-202.
- [247] M. Hashida, et al., *Ablation threshold dependence on pulse duration for copper*. Applied Surface Science, 2002. **197**: p. 862-867.
- [248] Z.H. Ding, et al., *A Model of Surface Residual Stress Distribution of Cold Rolling Spline*. Mathematical Problems in Engineering, 2017. **2017**(2017): p. 1-21.
- [249] J. Wu, et al., *Effect of beam profile on heat and mass transfer in filler powder laser welding*. Journal of Materials Processing Technology, 2018. **258**: p. 47-57.
- [250] D.L. Shealy and J. Hoffnagle, *Laser beam shaping profiles and propagation*. 2006. **45**(21): p. 5118-5131.
- [251] H.S. Carslaw and J.C. Jaeger, *Conduction of heat in solids*. 1959, Oxford: UK: Clarendon Press.
- [252] G.R.B.E. Römer, *Modelling and control of laser surface treatment*, in *Faculty of Engineering Technology*. 1999, University of Twente.
- [253] S. Malkin, *Grinding Technology Theory and Applications of Machining with Abrasives*. 2002, Shenyang: Northeast University.
- [254] *Specific heat of substances chart*. Available from: <https://amesweb.info/Materials/Specific Heat of Substances.aspx>.
- [255] *Diamond*. Available from: <https://en.wikipedia.org/wiki/Diamond>.
- [256] Toolbox, *Thermal Conductivity of selected Materials and Gases*. 2003.
- [257] *What is the specific heat capacity of epoxy resin?* ; Available from: <https://zhidao.baidu.com/question/551132847.html>.
- [258] *Epoxy resin*. Available from: <https://baike.baidu.com/item/%E7%8E%AF%E6%B0%A7%E6%A0%91%E8%84%82/1076812?fr=aladdin>.
- [259] *Specific heat of copper*. Available from: <https://amesweb.info/Materials/Specific-Heat-of-Copper.aspx>.
- [260] *Density of copper*. Available from: <https://amesweb.info/Materials/Density of Copper.aspx>.
- [261] Toolbox, *Thermal Conductivity of Metals, Metallic Elements and Alloys*. 2005.
- [262] Y. Qi, et al., *Magnolol-based bio-epoxy resin with acceptable glass transition temperature, processability and flame retardancy*. Chemical Engineering Journal, 2020. **387**: p. 124115.
- [263] H.N. Li and D. Axinte, *On a stochastically grain-discretised model for 2D/3D temperature mapping prediction in grinding*. International Journal of Machine Tools and Manufacture, 2017. **116**: p. 60-76.
- [264] J.P. Holman, *Heat transfer*. 1986: McGraw-hill.
- [265] M. Alimardani, et al., *Three-dimensional numerical approach for geometrical prediction of multilayer laser solid freeform fabrication process*. Journal of Laser Applications, 2007. **19**(1): p. 14-25.
- [266] C.S. Baird, *Electromagnetic radiation*. Access Science, 2019.

- [267] J.F. Ready, et al., *LIA handbook of laser materials processing*. 2001.
- [268] J. Li, et al., *Analytical modelling of full single-track profile in wire-fed laser cladding*. Journal of Materials Processing Technology, 2021. **290**: p. 116978.
- [269] A.K. Shukla, et al., *Laser assisted wet texturing of flexible polyethylene terephthalate substrate using Nd³⁺:YAG laser for photovoltaics devices*. Mater. Sci. and Eng.: B, 2017. **226**: p. 78-85.
- [270] K. Zimmer, et al., *Reducing the incubation effects for rear side laser etching of fused silica*. Appl. Surf. Sci., 2014. **302**: p. 42-45.
- [271] M.D. Feudis, et al., *Diamond graphitization by laser-writing for all-carbon detector applications*. Diamond and Related Mater., 2017. **75**: p. 25-33.
- [272] J.Y. Min, et al., *Application of laser ablation in adhesive bonding of metallic materials: A review*. Optics and Laser Technology, 2020. **128**: p. 106188.
- [273] S. Ravi-Kumar, et al., *Laser Ablation of Polymers: A Review*. Procedia Manufacturing, 2019. **34**: p. 316-327.
- [274] J. Byskov-Nielsen, et al., *Ultra-short pulse laser ablation of metals: threshold fluence, incubation coefficient and ablation rates*. Applied Physics A, 2010. **101**(1): p. 97-101.
- [275] D.L. Shealy and J.A. Hoffnagle, *Laser beam shaping profiles and propagation*. Applied Optics, 2006. **45**(21): p. 272944773.
- [276] D.L. Shealy and J.A. Hoffnagle, *Beam shaping profiles and propagation*. in *SPIE Conf. Laser Beam Shaping VI, Proc.* 2005.
- [277] N. Bellini, et al., *Increasing laser pulse overlap restricts picosecond laser ablation of thin metal films near ablation threshold*. Applied Physics A-Materials Science & Processing, 2017. **123**(5).
- [278] F.B. Wang, et al., *Analysis of overlapping rate of spot derived from ablated monocrystalline silicon by femtosecond laser*. Journal of Laser Applications, 2020. **32**(3).
- [279] G. Schnell, et al., *Effect of Laser Pulse Overlap and Scanning Line Overlap on Femtosecond Laser-Structured Ti6Al4V Surfaces*. Materials, 2020. **13**(4).
- [280] K. Zimmer, et al., *Reducing the incubation effects for rear side laser etching of fused silica*. Applied Surface Science, 2014. **302**: p. 42-45.